

Institut für Veterinär-Physiologie  
des Fachbereichs Veterinärmedizin  
der Freien Universität Berlin

und

Biophysikalische Analytik  
Deutsches Rheuma-Forschungszentrum (DRFZ), Berlin  
- ein Institut der Leibniz-Gemeinschaft -

Vector-analyzed fluorescence lifetime microscopy  
approach: new insights into cell metabolism and calcium  
signaling, *in vitro* and *in vivo*

Inaugural-Dissertation  
zur Erlangung des Grades eines

Ph.D. of Biomedical Sciences

an der  
Freien Universität Berlin

vorgelegt von

**Ruth Leben**

Master of Engineering  
aus Potsdam, Deutschland

**Berlin 2021**

Journal-Nr.: 4269

**Gedruckt mit Genehmigung  
des Fachbereichs Veterinärmedizin  
der Freien Universität Berlin**

**Dekan:** Univ.-Prof. Dr. Uwe Rösler

**Erste Gutachterin:** Univ.-Prof. Dr. Raluca A. Niesner

**Zweite Gutachterin:** Univ.-Prof. Dr. Susanne Hartmann

**Dritte Gutachterin:** Prof. Dr. Petra Knaus

**Deskriptoren (nach CAB-Thesaurus):** cell structure, metabolism, fluorescence microscopy, NADH, NADPH, enzyme activity, neutrophiles

**Tag der Promotion:** 23.11.2021

## Abstract

Title: Vector-analyzed fluorescence lifetime microscopy approach: new insights into cell metabolism and calcium signaling, *in vitro* and *in vivo*

The ability to dynamically observe functional processes at the (sub-) cellular level holds a high potential to answer open questions in medical biology, e.g. immunology. The ubiquitous co-enzymes nicotinamide adenine dinucleotide (NADH) and its phosphorylated variant (NADPH) play a major role in metabolic processes, for instance in the production of the energy carrier ATP, or in the generation of reactive oxygen species (ROS) for cellular defense against invading pathogens. Since these two co-enzymes are autofluorescent, they provide an endogenous sensor to study those basic mechanisms label-free *in vitro* and *in vivo* using multi-photon microscopy. When NADH/NADPH bind to another enzyme to catalyze one of these processes, the molecular structure of the assembled enzyme compartment changes and thus (in contrast to their emission wavelengths) their fluorescence lifetime, meaning the time the molecule remains in the excited state before it emits light. However, the evaluation and interpretation of NAD(P)H fluorescence lifetime images (FLIM) in real biological environments are challenging. Here, the method of phasor analysis has been adopted and applied to stimulated/non-stimulated ROS-producing lymphocytes. This way it was possible to directly image the temporal dynamics of NADPH oxidase activation and its requirement for triggering NETosis in phagocytosing neutrophils. In order to meet the growing demand for a systematic interpretation of NAD(P)H-FLIM measurements, especially to reflect the complex distribution and activity of NAD(P)H-dependent enzymes, the phasor approach was extended by the analysis of the phase vectors involved. For this purpose, *a priori* knowledge about the specific fluorescence lifetimes of the most abundant enzymes in tissue was created by measuring NADH or NADPH with the respective enzyme in solution. Applied to 3T3-L1 cell line or the data of phagocytosing neutrophils, this method reveals insights into the enzyme composition and its enzymatic activity, which was shown to be even more complex than the pure FLIM images suggest. In addition to NAD(P)H-FLIM, the phasor approach and the vector analysis application to extract further information from the FLIM images was applied to Förster resonance energy transfer (FRET). The CD19<sup>+</sup> lymphocytes of the reporter mouse line YellowCaB, carry the genetically encoded calcium-sensitive FRET-construct TN-XXL. In the presence of calcium ions, a second messenger of signal transduction, this construct is folded and the donor quenched. The fluorescence lifetime of the donor is shortened proportionally to the cytosolic Ca<sup>2+</sup> concentration. Using vector analysis in the phase domain, maps of the absolute calcium ion concentration of the

different B-cell populations in the germinal center of the lymph node were generated and their cell-to-cell interaction visualized. Together, both NAD(P)H-FLIM and donor-FRET-FLIM, hold the power to map mechanisms in cellular metabolism, defense, and intercellular communication, providing new insights into their interaction.

## Zusammenfassung

Titel: Vektoranalytischer Fluoreszenz-Lebensdauer-Mikroskopie-Ansatz: neue Einblicke in den Zellstoffwechsel und die Kalzium-Signalübertragung, *in vitro* und *in vivo*

Funktionelle Prozesse auf (sub-) zellulärer Ebene dynamisch beobachten können, birgt ein hohes Potential ausstehende biomedizinische Fragestellungen z.B. der Immunologie beantworten zu können. Die ubiquitären Co-Enzyme Nicotinamid-Adenin-Dinucleotid (NADH) und seine phosphorylierte Variante (NADPH) spielen eine wichtige Rolle bei Stoffwechselprozessen, zum Beispiel bei der Produktion des Energieträgers ATP oder bei der Bildung reaktiver Sauerstoffspezies (ROS) zur zellulären Abwehr eindringender Krankheitserreger. Da diese beiden Co-Enzyme autofluoreszierend sind, liefern sie einen endogenen Sensor, um diese grundlegenden Mechanismen markierungsfrei *in vitro* und *in vivo* mittels Multiphotonenmikroskopie zu untersuchen. Wenn sich diese Co-Enzyme an ein weiteres Enzym binden, um einen dieser Prozesse zu katalysieren, verändert sich der molekulare Aufbau des Gesamtkonstrukts und damit (im Gegensatz zu ihrer Emissionswellenlänge) die Fluoreszenzlebensdauer, also die Zeit, die das Moleküle im angeregten Zustand verweilt, bevor es fluoresziert. Allerdings ist seit langem bekannt, dass sowohl die Auswertung als auch die Interpretation einer solchen Lebenszeitmessung in einer realen biologischen Umgebung eine Herausforderung ist. In der vorliegenden Arbeit wurde die Methode der phasor-Analyse übernommen und auf stimulierte/ nicht-stimulierte ROS-produzierende Lymphozyten angewendet. Auf diese Weise war es möglich, die zeitliche Dynamik der NADPH-Oxidase-Aktivierung und ihre Voraussetzung für die Auslösung der NETosis in phagozytierenden Neutrophilen direkt abbilden. Um den wachsenden Bedarf einer systematischen Interpretation von NAD(P)H-Fluoreszenzlebenszeitaufnahmen zu begegnen, speziell um die komplexe Verteilung und Aktivität der NAD(P)H-abhängigen Enzymen wiedergeben zu können, wurde die phasor-Anwendung um eine Analyse der beteiligten Phasenvektoren erweitert. Zu diesem Zweck wurde

durch die Messung von NADH oder NADPH mit dem jeweiligen Enzym in Lösung *a priori* Wissen über die spezifischen Fluoreszenzlebensdauern der am häufigsten im Gewebe vorkommenden Enzyme geschaffen. Angewendet auf die 3T3-L1 Zelllinie oder die Daten von phagozytierenden Neutrophilen, offenbart diese Methode Einblicke in die Enzymzusammensetzung und enzymatische Aktivität, die noch komplexer ist als die reinen FLIM-Bilder vermuten lassen. Neben NAD(P)H-FLIM kann die phasor-Anwendung und die Herangehensweise der Vektoranalyse zum Extrahieren weiterer Informationen aus den FLIM-Aufnahmen auch auf den Förster-Resonanzenergietransfer (FRET) angewendet werden. Die CD19<sup>+</sup> Lymphozyten der Reporter Mauslinie YellowCaB tragen genetisch kodiert das calciumsensitive FRET-Konstrukt TN-XXL. In Anwesenheit von Calciumionen, einem sekundären Botenstoff der Signaltransduktion, wird das Konstrukt gefaltet und der donor gequenched, dessen Fluoreszenzlebensdauer sich proportional zur zytosolischen Ca<sup>2+</sup> Konzentration verkürzt. Mit Hilfe der Vektoranalyse in der Phasenebene wurden hier Karten der absoluten Kalziumionenkonzentration verschiedener B-Zellpopulationen im Keimzentrum des Lymphknotens erstellt und auf diese Weise deren Zell-zu-Zell-Kommunikation sichtbar gemacht. Zusammen sind beide, NAD(P)H-FLIM und donor-FRET-FLIM, in der Lage, Mechanismen des Zellstoffwechsels, der zellulären Abwehr und der interzellulären Kommunikation abzubilden und eröffnen so neue Einblicke in deren Zusammenspiel.

# Contents

<b>ABSTRACT</b> .....	<b>I</b>
<b>ZUSAMMENFASSUNG</b> .....	<b>II</b>
<b>CONTENTS</b> .....	<b>IV</b>
<b>FIGURES</b> .....	<b>VII</b>
<b>ABBREVIATIONS</b> .....	<b>XI</b>
<b>1. INTRODUCTION</b> .....	<b>1</b>
1.1. MAINTAINING LIFE AND HEALTH ON A CELLULAR LEVEL.....	1
1.1.1. <i>Cellular energy metabolism</i> .....	1
1.1.2. <i>Metabolic challenges during the immune response</i> .....	3
1.1.3. <i>Calcium ions as second messenger</i> .....	10
1.2. FLUORESCENCE AND ITS LIFETIME .....	11
1.3. CELLULAR AUTOFLUORESCENCE BY NAD(P)H.....	16
1.4. MONITORING CELL SIGNALING BY ENERGY TRANSFER.....	19
1.5. A VIEW INSIDE - DEEP TISSUE MICROSCOPY .....	23
1.6. RESEARCH AIMS OF THIS THESIS.....	25
1.7. SELECTED PUBLICATIONS AND AUTHOR CONTRIBUTIONS.....	28
<b>2. METHODS</b> .....	<b>30</b>
2.1. TWO-PHOTON MICROSCOPE SETUP FOR FLIM .....	30
2.2. DATA ANALYSIS: THE PHASOR APPROACH .....	31
2.3. NAD(P)H-FLIM AND DONOR FRET-FLIM.....	34
2.4. SAMPLES .....	35
<b>3. RESULTS – VALIDATION OF THE FLIM-SYSTEM AND DATA ANALYSIS</b> .....	<b>37</b>
<b>4. RESULTS – LEBEN, R. ET AL., (2018)</b> .....	<b>38</b>

4.1.	ENDOGENOUS NAD(P)H-FLIM IDENTIFIES OXIDATIVE BURST IN INNATE IMMUNE CELLS VIA NOX2 .....	38
4.2.	NADPH OXIDASE ACTIVATION IS LOCALIZED IN THE PHAGOSOMES .....	39
4.3.	NADPH OXIDASE ACTIVATION PRECEDES NETOSIS.....	40
4.4.	UNPUBLISHED DATA – “LONG-LIFETIME SPECIES” FOUND IN 3T3-L1 CELL LINE.....	41
<b>5.</b>	<b>RESULTS – LEBEN, R., ET AL., (2019) .....</b>	<b>43</b>
5.1.	NAD(P)H-FLIM ADEQUATELY DETERMINES FLUORESCENCE LIFETIMES USING THE PHASOR APPROACH ..	43
5.2.	THE PHASOR APPROACH ENABLES AN ENZYMES-BASED REFERENCE SYSTEM .....	44
5.3.	ASSIGNING NAD(P)H-FLIM DATA TO THE METABOLIC ENZYMES: A SYSTEMATIC ANALYSIS FRAMEWORK .....	45
5.4.	VALIDATION ON HOMOGENEOUS NAD(P)H-ENZYME MIXTURES .....	46
5.5.	SYSTEMATIC ANALYSIS IS SUITABLE IN STROMAL-LIKE 3T3-L1 CELLS.....	47
5.6.	UNPUBLISHED DATA – SYSTEMATIC VECTOR ANALYSIS APPLIED TO PHAGOCYTOSING NEUTROPHILS.....	48
<b>6.</b>	<b>RESULTS – ULBRICHT, C. ET AL., (2021) .....</b>	<b>50</b>
6.1.	FLUCTUATING CALCIUM LEVELS ARE OBSERVED <i>IN VIVO</i> .....	50
6.2.	PHASOR-ANALYZED DONOR FRET-FLIM TO CALCULATE ABSOLUTE CELLULAR $Ca^{2+}$ CONCENTRATION.....	51
6.3.	<i>IN VIVO</i> DONOR FRET-FLIM OF CYTOPLASMIC TN-XXL CONSTRUCT IN YELLOWCAB CELLS .....	52
6.4.	ABSOLUTE QUANTIFICATION OF CYTOPLASMIC $Ca^{2+}$ REVEALS ACTIVATION-DEPENDENT CALCIUM HETEROGENEITY IN B CELLS .....	55
6.5.	UNPUBLISHED DATA – HIGH DYNAMICS OF $Ca^{2+}$ SIGNALING BETWEEN B CELLS.....	55
<b>7.</b>	<b>DISCUSSION .....</b>	<b>57</b>
7.1.	PERFORMANCE OF THE MEASUREMENT SYSTEM AND STEADY-STATE ANALYSIS .....	57
7.2.	NAD(P)H AS FLUORESCENT ENDOGENOUS BIO-MARKER .....	58
7.3.	NAD(P)H-FLIM IN PHAGOCYTOSING NEUTROPHILS.....	59
7.4.	NAD(P)H BOUND TO NOX AND “LONG-LIFETIME SPECIES” AS INDICATORS OF OXIDATIVE BURST/ STRESS .....	60
7.5.	INDIVIDUAL LIFETIMES OF ENZYME-BOUND NAD(P)H.....	61
7.6.	SIGNAL-TO-NOISE RATIO IN NAD(P)H-FLIM.....	62

7.7.	SYSTEMATIC FRAMEWORK TO ANALYZE AND INTERPRET NAD(P)H-FLIM DATA .....	63
7.8.	DEEPER INSIGHTS IN NEUTROPHIL METABOLISM BY SYSTEMATIC ENZYME MAPPING .....	63
7.9.	DONOR FRET-FLIM REVEALS THE DYNAMICS OF $Ca^{2+}$ CONCENTRATION IN B CELLS .....	65
<b>8.</b>	<b>CONCLUSION AND FUTURE PROSPECTS .....</b>	<b>66</b>
<b>9.</b>	<b>REFERENCES .....</b>	<b>68</b>
	<b>ACKNOWLEDGMENT .....</b>	<b>76</b>
	<b>APPENDIX A .....</b>	<b>78</b>
A.1.	CONFERENCE CONTRIBUTIONS .....	78
A.2.	COMPLETE LIST OF PUBLICATIONS .....	79
A.3.	PRINTED VERSIONS OF SELECTED PUBLICATIONS .....	81
	<b>APPENDIX B .....</b>	<b>147</b>
B.1.	PYTHON SCRIPT .....	147
	<b>APPENDIX C .....</b>	<b>161</b>
C.1.	CURRICULUM VITAE .....	161
C.2.	FINANZIERUNGSQUELLEN, INTERESSENSKONFLIKTE, SELBSTSTÄNDIGKEITSERKLÄRUNG .....	162

## Figures

**Fig. 1:** Cellular energy metabolism in homeostasis; abbreviation see text. The four main processes in cellular metabolism to generate energy in form of ATP are glycolysis, fatty acid oxidation, citric cycle and electron transport chain. In these processes are the coenzymes NAD<sup>+</sup> and NADH (and their phosphorylated forms NADP<sup>+</sup>/NADPH) as electron carrier involved. ①

Fermentation, ② OxPhos..... 3

**Fig. 2:** Phagocytosis and activation of NADPH oxidase. (A) Scheme of phagocytosis: a) engulfing the pathogen, b) forming a phagosome, c) union of phagosome and lysosome to digest the inclusion, d) fragments are deinfected by ROS, e) remaining material is released to the extracellular space. (B) Resting (i) and activated (ii) NOX2 (Scheme taken from (Leben et al. 2018))..... 6

**Fig. 3:** Memory B cell and plasma blast generation in the lymphoid tissue. [Scheme taken from Fig. 1 in (Kurosaki et al. 2015) with permission from Springer Nature (Oct 12, 2020)].....9

**Fig. 4:** Simplified Jabłoński diagram depicting the molecular energy levels during spontaneous fluorescence and the non-radiative decay [19]. The thick horizontal lines represent the electronic singlet levels, the thin horizontal lines the vibrational levels. S<sub>0</sub> ... ground state, S<sub>1</sub> ... first energetic state, λ<sub>ex</sub> ... excitation wavelength, λ<sub>em</sub> ... emission wavelength, Γ... emissive rate, k<sub>nr</sub> ... rate of non-radiative decay..... 12

**Fig. 5:** Slice of rhizome of *Convallaria majalis* with acridin-orange-staining for fluorescence (DAPI, FITC/GFP, TEX RED, Cy5 and DIC) by MEDICAL & SCIENCE MEDIA, excited at 800 nm, detected without wavelength discrimination. (A) Intensity image, (B) intensity-weighted FLIM of the same field of view. Calibration bar is given in nanoseconds. Scale bar indicates 50 μm.....16

**Fig. 6:** NAD(P)H autofluorescence (A) The molecular structures of the redox couples NAD<sup>+</sup>/NADH and their phosphorylated forms NADP<sup>+</sup>/NADPH, reduction and oxidation reaction is shown in gray; grey, dashed encirclings indicate changed parts. (B) NAD(P)H fluorescence of unlabeled MC3T3 cells at day 10 of differentiation (unpublished data). Ex 760 nm (2PE), Em 466/40 nm. Scale bar indicates 50 μm. (C) Normalized one-photon excitation (violet) and emission (blue) spectra of NADH (data taken from Arizona Spectra Database “NADH(AB)” and “NADH(EM)” (Utzinger 2011))..... 17

**Fig. 7:** Simplified Jabłoński diagram of the Förster resonance energy transfer. (Same declaration abbreviation as in Fig. 4). ..... 19

**Fig. 8:** Conservation of energy and momentum. (A) Overlap integral  $J(\lambda)$  (gray area) of the donor emission spectrum (CFP) and the acceptor excitation spectrum (Citrine) (data taken from (Utzinger 2011)), (B) Angles of the transition dipoles and the resulting orientation factor  $k^2$ , nomenclature see (Eq. 14)..... **20**

**Fig. 9:** Scheme of the Troponin-C (TnC)-based FRET in presence of calcium ( $\text{Ca}^{2+}$ , red). The FRET-pair is CFP (donor) and citrine (acceptor). (Scheme taken from (Ulbricht et al. 2021)..... **21**

**Fig. 10:** Biological optical window. Absorption coefficient of hemoglobin (Hb), its oxidized form ( $\text{HbO}_2$ ) and water ( $\text{H}_2\text{O}$ ). (Figure taken from (Phan and Bullen 2010) with permission from John Wiley and Sons (Oct, 12, 2020))..... **23**

**Fig. 11:** Two-photon excitation. (A) Extension of the simplified Jabłoński diagram in Fig. 4, (B) excitation volume and focal plane (horizontal line) in one-photon (i) and two-photon (ii) excitation. ((B) taken from Fig 2 in (Soeller and Cannell 1999) with permission from John Wiley and Sons (Oct, 12, 2020))..... **24**

**Fig. 12:** Schematic two-photon microscope setup to perform time-domain FLIM. BS (beam splitter), GS (galvo scanner), DC (dichroic mirror), OBJ (objective), S (sample), IF interference filter), h-PMT (hybrid-PMT), PD (photon diode), PC (personal computer), TCSPC (time-correlated single photon counter). (Scheme taken from [Leben et al, 2018])..... **30**

**Fig. 13:** Normalized instrument response function of TCSPC measured by SHG of KDP crystals. Red circles: data points, blue line: Gaussian fit..... **31**

**Fig. 14:** Coordinate transformation of FLIM data from time domain to phase domain via a discrete Fourier transformation..... **32**

**Fig. 15:** Phasor approach to graphically represent exponential decays. Gray: phase vectors origin from mono-exponential temporal decays, orange: bi-exponential, green: tri-exponential. Modulations frequency is 80 MHz..... **33**

**Fig. 16:** Spectral excitation and emission properties and the selected wavelength to perform NAD(P)H FLIM and donor-FRET FLIM. (Data taken from Arizona Spectra Database “NADH(EM)”, “NADH+AD in H<sub>2</sub>O – DRBIO-2P”, “CFP (Tsien) (EM)”, “ECFP-Drobizehev-2P (2P)”, “Ti:Saph” (Utzinger 2011))..... **35**

**Fig. 17:** Validation of the FLIM measurement setup and data analysis: (A) SHG in KDP, (B) eGFP in HEK 293T cells (C) background noise in non-fluorescent medium. All (i) are the normalized intensity images, all (ii) the intensity-weighted FLIM images and all (iii) the corresponding phasor plots. Scale bars indicate 50  $\mu\text{m}$ ..... **37**

**Fig. 18:** NAD(P)H metabolism of (A) resting and (B) PMA-stimulated (activated) monocytes. Each: i) schema of enzymes involved in ROS catalyze, ii) intensity image, iii) fluorescence lifetime image, vi) pixel-based phasor plot; Scale bar indicates 20  $\mu\text{m}$ . “#” marks the fluorescence lifetime of oxidized lipids as defined by e.g. (Datta et al. 2015). (Space-saving and RGB redesign of Fig 2 in (Leben et al. 2018)).....**38**

**Fig. 19:** NAD(P)H-metabolism during phagocytosis. Selected frames of time-lapse NAD(P)H-FLIM data of healthy human PMN phagocytosing *S. aureus* pHrodo™ beads. (A) 0 min, (B) 32 min, (C) 64 min after co-culturing. i) merged intensity images of NAD(P)H and pHrodo fluorescence, ii) FLIM images, iii) pixel-based phasor plots. Scale bar indicates 20  $\mu\text{m}$ . “#” in all (iii) mark the fluorescence lifetime of oxidized lipids as defined by e.g. (Datta et al. 2015). (Space-saving and RGB redesign of Fig 3 in (Leben et al. 2018)).....**39**

**Fig. 20:** NET formation and cellular death. Comparison of neutrophil metabolism in presence (A) and absence (B) of *S. aureus* pHrodo™ beads. Each a) cells immediately after and b) 80 min/60 min after co-culturing with beads. The columns (i) merged intensities of DNA stain (green) and NAD(P)H (gray), (ii) NAD(P)H FLIM, (iii) phasor plots, “#” mark the fluorescence lifetime of oxidized lipids as defined by (Datta et al. 2015). (C) Intensities of DNA stain after applying shear forces. (i) and (ii) is the same image, (ii) has a high-contrast adjustment. All scale bars indicate 20  $\mu\text{m}$ . (Space-saving and RGB redesign of Fig 5 in (Leben et al. 2018))..... **41**

**Fig. 21:** Phasor-analyzed NAD(P)H-FLIM of mouse embryo 3T3-L1 preadipocytes at day 5, three fields of view in the same culture. **(A)** thresholded and intensity-weighted FLIM images, 512x512 pixel covering 200x200  $\mu\text{m}^2$  **(B)** corresponding phasor plots. Color bar in Aiii) applies to all 3 FLIM images (0-4 ns); scale bars in A are 20  $\mu\text{m}$ , # indicates “long-lifetime species”. (unpublished data).....**42**

**Fig. 22:** NADH, LDH, and FX11 solved in MOPS solution. (i) only 50  $\mu\text{M}$  NADH; (ii) 50  $\mu\text{M}$  NADH and 10  $\mu\text{M}$  LDH; (iii) 50  $\mu\text{M}$  NADH, 10  $\mu\text{M}$  LDH, and 10  $\mu\text{M}$  FX11; (iv) 50  $\mu\text{M}$  NADH, 10  $\mu\text{M}$  LDH, and 0.5 mM FX11; (v) 50  $\mu\text{M}$  NADH, 10  $\mu\text{M}$  LDH, and 1.0 mM FX11. (Fig 1D in (Leben et al. 2019)).....**44**

**Fig. 23:** Reference system of NAD(P)H fluorescence lifetimes and phase vectors in the free and enzyme-bound state. (A) Phasor plot (B) List of measured fluorescence lifetimes  $\tau_2$  of NADH or NADPH fully bound to enzymes. (C) Fluorescence lifetimes calculated from single images represented as gray dots, average values as black lines, standard error of the mean (s.e.m.) values over all pixels in all measured images per coenzyme/enzyme mixture as black boxes. The list was completed by our previously measured fluorescence lifetimes (Mossakowski et al. 2015). The color coding in (A) – (C) is consistent. (Fig 2 in (Leben et al. 2019))..... **45**

**Fig. 24:** Systematic analysis framework of NAD(P)H-FLIM data. (i) Radius surrounding the pixels that are assumed to represent free NAD(P)H, (ii) Angle similarity of the vectors free

NAD(P)H to data point (violet dashed) and free NAD(P)H to NADH bound to MDH, (iii) Applied to all measured enzyme-bound NAD(P)H lifetimes. (Fig 3A in (Leben et al. 2019)).....**46**

**Fig. 25:** Label-free NAD(P)H-FLIM reveals subcellular heterogeneity of enzyme activity but homogeneous metabolic activity in stromal-like 3T3-L1 cells. (A) Phasor plot, with enzyme-vectors. (B) Intensity-weighted (i) NAD(P)H-FLIM, (ii) Enzymatic activity map, (iii) Enzyme map. Scale bars indicate 50  $\mu\text{m}$ . (Fig 4 AB in (Leben et al. 2019) ).....**48**

**Fig. 26:** NAD(P)H-metabolism of healthy human neutrophils during phagocytosing *S. aureus* pHrodo™ after 20 min of co-culturing. (A) Phasor plot with free-to-enzyme vectors, (B) 125 x 125  $\mu\text{m}^2$  ROI, (i) NAD(P)H intensity, (ii) NAD(P)H-FLIM, (iii) enzyme map, (iv) activity map. All images/maps are intensity-weighted and background-thresholded (pixels with SNR < 15 were excluded). (C) 21 x 21  $\mu\text{m}^2$  magnified ROI marked in (B). Scale bar indicates 20  $\mu\text{m}$ . (Unpublished data)..... **49**

**Fig. 27:** Phasor approach to analyze donor FRET-FLIM of the TN-XXL construct. Unquen.” marks the position of the fluorescence lifetime of unquenched eCFP, “quen.” marks the position of the fluorescence lifetime of quenched eCFP..... **51**

**Fig. 28:** Still frame of a 60-minute 3D in vivo imaging of YellowCaB cells in the lymph node, including the germinal center (GC) and the medullary cords (MC) (A) Merged intensity images of the stained naïve (red), AG-specific B cells (green) and FDC (white), (B) donor FRET-FLIM (intensity weighted), (C) cell-based phasor plot with noise exclusion radius (green dashed), labeling as outlines in main text. Scale bar indicates 50  $\mu\text{m}$ .(Fig 4b in (Ulbricht et al. 2021)).....**52**

**Fig. 29:** Determination of the noise exclusion radius (green) for phasor analysis. (Supplement Fig S5 (Ulbricht et al. 2021))..... **53**

**Fig. 30:** Determination of the absolute  $\text{Ca}^{2+}$  concentration (A) Phase vector projections of single B cells over time onto FRET segment under consideration of background noise (i) naïve B cell, (ii) two AG-specific B cells, (iii) two plasma blasts. (B) 3D representation of  $\text{Ca}^{2+}$  concentration map, scale bar indicates 50  $\mu\text{m}$ . Arrows indicate cells with high  $\text{Ca}^{2+}$  concentration. (Fig 4 DE in (Ulbricht et al. 2021)).....**54**

**Fig. 31:** In vivo  $\text{Ca}^{2+}$ -dependent B cell signaling in the lymph node of YellowCaB mice (here in the medullary cord). (A) 35 x 35  $\mu\text{m}^2$  stills of a 32 min sequence of the donor FRET-FLIM shown in Fig 4 and supplementary movie S2 in (Ulbricht et al. 2021). (B) Still at 13 min (i) FLIM image marking the cell 1 (green), cell 2 (red) and cell 3 (blue), (ii) corresponding antigen staining indicating the AG-specific B cell (green), collagen is shown in white. (C)  $\text{Ca}^{2+}$  concentration in [nM] versus the time in [min] of the sequence, the period of direct cell contact was marked in gray. Color bar on the y-axis gives the color coding of donor FRET-FLIM data in (A) and (B).....**55**

## Abbreviations

$\tau$	fluorescence lifetime
2PM	two-photon microscopy
3D	three-dimensional
3T3-L1	mouse cell line
ADH	alcohol dehydrogenase
ADP	adenosine diphosphate
AG	antigen
AMP	adenosine monophosphate
APC	antigen presenting cell
ATP	adenosine triphosphate
BCR	B cell receptor
BS	beam splitter
Ca <sup>2+</sup>	calcium ion
CD	cluster of differentiation
Ch	channel
CTBP1	C-terminal binding protein 1
DC	dichroic mirror
DFT	discrete Fourier transformation
DNA	deoxyribonucleic acid
eCFP	enhanced cyan fluorescent protein
eGFP	enhanced green fluorescent protein
ETC	electron transport chain
FADH <sub>2</sub>	flavin adenine dinucleotide
FDC	follicular dendritic cells
FX11	LDHA inhibitor
FDC	follicular dendritic cell
FLIM	fluorescence lifetime imaging
FRET	Förster resonance energy transfer
FWHM	full width at half maximum

G6PDH	glucose-6-phosphate dehydrogenase
GaAsP	gallium arsenide phosphide
GAPDH	glyceraldehyde 3-phosphate dehydrogenase
GC	germinal center
GLUT1	glucose transporter 1
GRIN	gradient refractive index (optics)
GUI	graphical user interface
HADH	hydroxyacyl-coenzyme-A dehydrogenase
HEK 293T	human embryonic kidney 293 cells
IDH	isocitrate dehydrogenase
IF	interference filter
IL	interleukin
iNOS	inducible nitric oxide synthase
IR	infrared light
IRF	instrument response function
KDP	potassium dihydrogenphosphate
LASER	light amplification by stimulated emission of radiation
LDH	lactate dehydrogenase
LIMB	longitudinal intravital imaging of the bone marrow
LLS	long-lifetime species
LUT	look up table
MC	medullary cords
MDH	malate dehydrogenase
MHC-II	major histocompatibility complex class II
MOPS	3-(N-morpholino)propanesulfonic acid
NAD <sup>+</sup>	oxidized form of nicotinamide adenine dinucleotide
NADH	reduced form of nicotinamide adenine dinucleotide
NADP <sup>+</sup>	oxidized, phosphorylated form of nicotinamide adenine dinucleotide
NADPH	reduced phosphorylated form of nicotinamide adenine dinucleotide
nan	not a number
NET	neutrophil extracellular traps
NOX	NADPH oxidases family (NOX1-5, DUOX1,2)
O <sub>2</sub>	oxygen

$O_2^-$	ion superoxide
OxPhos	oxidative phosphorylation
PB	plasmablast
PC	personal computer
PDH	pyruvate dehydrogenase
PMA	phorbol-myristate-acetate
PMN	polymorph-nuclear cell
PMT	photomultiplier tube
PPP	the pentose phosphate pathway
RNA	ribonucleic acid
ROS	reactive oxygen species
SDH	sorbitol dehydrogenase
SHG	seconde harmonic generation
$S_n$	energetic levels
SNR	signal-to-noise ratio
TCR	T cell receptor
TCSPC	time-correlated single photon counting
TDC	time-to-digital converter
Ti:Sa	titanium:sapphire laser
TIFF	tagged image file format
TnC	troponin C
TN-XXL	troponin C Calcium biosensor
UV	ultraviolet light



## 1. Introduction

### 1.1. Maintaining life and health on a cellular level

Every living organism requires energy to maintain its body functions, thus to sustain its life and health. This energy is provided by a series of chemical and physical processes that take place in each cell of an organism to extract the energy needed from the chemical bonds between atoms and molecules of substrates that the organism regularly consumes. Through the enzymatic activity, these substrates (water, oxygen and nutrients i.e. glucose, fatty acids and proteins) are converted into intermediates, named metabolites, smaller and better manageable molecules, for instance amino acids, lipids, carbohydrates, and energy. The process of breaking down substrates is referred to as “catabolism”. From these metabolic intermediates, the cells form by the influence of enzymes new macromolecules, additional substrates such as growth factors, and energy input. These macromolecules are needed in order to maintain the cellular structure, to grow, to proliferate, or to differentiate. The process of building up is referred to as “anabolism”. Taken together, both biochemical processes form the entire cellular metabolism and are linked by metabolites and energy. (Löffler and Petrides 2019)

Every biochemical reactions is catalyzed by specific enzymes and can therefore can be highly controlled by the cell, which regulates its energy balance according to its current needs, the available substrate supply or in response to signals from other cells. These enzyme-catalyzed reactions thus enable organisms to react to their environment.

#### 1.1.1. Cellular energy metabolism

The required energy to perform metabolism is mainly driven by adenosine triphosphate (ATP), the “universal energy currency” of cells. The energy stored in the ATP molecule is released by hydrolysis, the enzymatic cleavage of phosphate bonds. Depending on whether one or two of the phosphates have been cleaved, adenosine diphosphate (ADP) and about 30 kJ/mol or adenosine monophosphate (AMP) and about 60 kJ/mol energy as well as free energy in form of heat are produced (Christen and Jaussi 2006). In eukaryotes these reactions mainly take place in the mitochondria.

Furthermore, cells are able to convert low-energy AMP/ADP into high-energy ATP, by either substrate-level phosphorylation or the respiratory chain. In substrate-level phosphorylation, a

phosphate group is enzymatically transferred to ADP via several conversion processes such as glycolysis and lactate generation (Krantz 2007). These anaerobic processes run in the cytoplasm and they are fast, but energetically inefficient. In glycolysis, a glucose molecule is converted into two ATPs (net), two NADH and two pyruvate molecules by glyceraldehyde 3-phosphate dehydrogenase GAPDH. NADH is a highly energetic molecule, which transports electrons to their destination. As depicted in Fig. 1, the pyruvate molecules are either added to the lactate generation catalyzed by lactate dehydrogenase LDH to maintain glucose, or they are added to the oxidative phosphorylation (OxPhos) in the mitochondria. In the aerobic mechanism of OxPhos energy is released by the reduction of oxygen to water to produce more ATP in an energetically much more efficient way than the cytosolic anaerobic processes. OxPhos includes two main processes: the citric acid cycle and the electron transport chain (ETC). Before, the two pyruvate molecules from the glycolysis are converted into acetyl-CoA by pyruvate decarboxylation catalyzed by pyruvate dehydrogenase (PDH), creating an additional NADH molecule. The acetyl-CoA is shuttled into the citric acid cycle where two further ATP, six further NADH and two FADH<sub>2</sub> molecules are generated. During this cycle, NAD<sup>+</sup> binds to such as isocitrate dehydrogenase (IDH) and malate dehydrogenase (MDH). In the final step of energy metabolism, all NADH and FADH<sub>2</sub> from the previous steps carry electrons to the electron transport chain (ETC) on the inner mitochondrial membrane. NADH and FADH<sub>2</sub> provide the energy to pump positively charged hydrogen nuclei (H<sup>+</sup>) from the inner mitochondrial matrix to the intermembrane space by a series of enzymes (complex I-IV) to create an electrochemical gradient. The H<sup>+</sup> strive to return to the matrix to compensate for the resulting pH gradient ( $pH = -\log_{10}a(H^+)$ ). The only way back is through the enzyme ATP synthase, so as they pass through it, mechanical work is done, driving its rotating mechanism, which fuses phosphates and ADP to produce ATP. One NADH molecule produces three ATP molecules, so that 30 ATP are formed from the ten NADH of the previous steps by this process alone. In addition, the two FADH<sub>2</sub> produce two ATP molecules each. Under ideal conditions, two ATP are produced by glycolysis and 34 ATP via the electron transport chain, thus during the entire process in a cell, a total of 36 ATPs are formed from a single glucose molecule in energy metabolism. (Löffler and Petrides 2019; Gaber et al. 2017; Blacker and Duchon 2016; Krantz 2007)

If ATP is the “universal energy currency”, NADH and FADH<sub>2</sub> are the “fuel” to generate it. All the processes outlined above take place simultaneously in every cell of an organism. So NAD<sup>+</sup> is permanently reduced to NADH and, vice versa, NADH is oxidized to NAD<sup>+</sup> in order to either store or release electrons for ATP-synthesis. The same applies to its phosphorylated variant NADPH in

reductive biosynthesis processes. In order to maintain these processes, NADH and NADPH continuously bind to various enzymes, for instance GAPDH, PDH, IDH, MDH, G6PDH, for their activation.

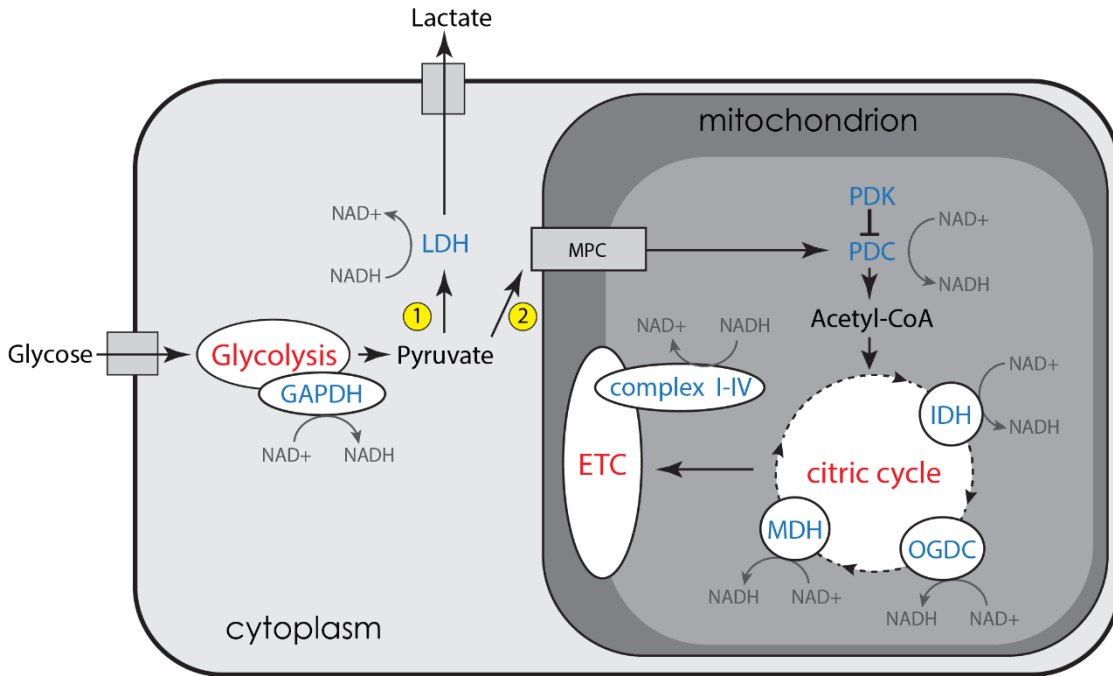


**Fig. 1: Cellular energy metabolism in homeostasis.** The four main processes in cellular metabolism to generate energy in form of ATP are glycolysis, fatty acid oxidation, citric cycle and electron transport chain. These processes involve the coenzymes NAD<sup>+</sup> and NADH (and their phosphorylated forms NADP<sup>+</sup>/NADPH) as electron carrier. Abbreviations: see text. ① Lactate generation (anaerobic glycolysis), ② OxPhos.

### 1.1.2. Metabolic challenges during the immune response

Complex organisms like mammals have a biological defence system - their immune system, which protects them from tissue damage and infection. Immune cells patrol the body via blood and lymph vessels and destroy and remove invading pathogens (such as fungi, viruses or bacteria), foreign substances and even cells of the organism, including damaged, diseased or aged ones. The immune system is a complex network of primary (e.g. thymus or bone marrow) and secondary lymphoid organs (e.g. lymph nodes, tonsils or spleen), cells (e.g. dendritic cells, macrophages, granulocytes, B- and T-cells) as well as soluble humoral factors (e.g. antibodies, cytokines, interleukins). It is classified into the innate immune system, which the organism is born with, and the adaptive immune system, which responds to new or altered pathogens to protect the organism

more effectively after an initial infection. The innate immune system is limited to unspecific, but rapid reactions, including physical barriers such as epithelial cells, inflammatory reactions or phagocytosis. In contrast, the adaptive immune system is able to give a specific immune response, which means that it recognizes pathogens and specifically forms cellular defense mechanisms and antigen receptors. It can also store and later retrieve this "memory" of pathogens already fought by memory T- and B-cells, so that the organism can gradually build up immunity to them. Together, the innate and adaptive immune system form a closely interconnected, well coordinated and very efficient defence system. (Schütt and Bröker 2011; Janeway Jr et al. 2012)

Resting/quiescent immune cells are metabolically relatively inactive, due to their minimal demand of biosynthesis and energy (Gaber et al. 2017). They are well-supplied with nutrients, water and oxygens by the blood and lymph vessel network in their host tissue and only need to maintain their homeostasis (Gaber et al. 2017).

Upon activation of the immune system for example by pathogen-derived or inflammatory signals, motile immune cells leave their origin and migrate to the source of infection, in order to drive the immune response. This process requires a dynamic adaptation of their energy metabolism. On their way through the different tissues to the site of infection, they are exposed to challenging environmental conditions, such as hypoxia or a change nutrient and water supply. Apart from that, their energy demand is increased and different immune cell subsets have different metabolic requirements. A high amount of energy is needed for cell migration, the required cell differentiation (e.g. monocytes to macrophages), rapid cell proliferation (clonal B-cell expansion) and of course the immune response itself, including the production of soluble factors like cytokines and antibodies, or phagocytosis and the resulting activation of NADPH oxidase (NOX) to produce reactive oxygen species (ROS). (Gaber et al. 2017)

(Warburg and Christian 1936) observed the change in energy metabolism from aerobic OxPhos in healthy cells to anaerobic glycolysis in cancer cells, something that normally only happens under oxygen deficiency, although the cancerous tissue was sufficiently oxygenated. This is nowadays called the Warburg effect. As noted in the previous section, glycolysis is energetically less efficient than OxPhos, since it generates only two ATP (net) from a single glucose molecule in contrast to 36 ATP molecules in OxPhos, however it is much faster. This inefficiency is balanced by an increased rate of glycolysis. The Warburg effect was also observed in leukocytes (Seelich et al. 1957; Remmele 1955), although Warburg himself contradicted this (Warburg et al. 1958). However, in 2002 it was shown that activated T cells do indeed use the Warburg metabolism,

which is evident by the increased expression of glucose transporter 1 (GLUT1) on the cell membrane and thus increased glucose uptake (Frauwirth et al. 2002; Medzhitov 2015). This finding was subsequently generalized to proliferating cells (Medzhitov 2015; Vander Heiden et al. 2009). Thus, nowadays it is known, that the Warburg metabolism occurs in many activated immune cells (Gaber et al. 2017). It allows them to anticipate energetic and biosynthetic needs associated with a sustained immune response.

### *First-line defence – macrophages and neutrophils*

The first-line defence cells of the innate immune system, the phagocytic macrophages and neutrophils, give the first nonspecific immune response to an infection (Janeway Jr et al. 2012). Among other functions, macrophages and neutrophils clean-up the infection via phagocytosis, neutrophils trap pathogens via NETosis, and macrophages present fragments of pathogens to other immune cells.

Stimulated by pro-inflammatory signals from damaged or infected cells, neutrophils and monocytes leave the blood vessel through the endothelium and migrate along a chemokine gradient towards the site of infection. In the tissue at the site of infection, the monocytes differentiate into macrophages. Neutrophils and macrophages are able to recognise pathogens, by typical surface molecules shared by many pathogens via pattern recognition. When phagocytes detect a pathogen, as depicted in Fig. 2 (A) they phagocytose it by engulfing the foreign object with a part of their cell membrane and tie a vesicle (phagosome) into their interior. Phagocytes have organelles called lysosomes, which are filled with digestive enzymes. During the process of phagocytosis the phagosome fuses with lysosomes and form a phagolysosome, thus the contents of the lysosomes are released into it and so the trapped pathogen gets digested. (Schütt and Bröker 2011; Janeway Jr et al. 2012)

In addition, macrophages and neutrophils produce ROS by the activation of NADPH oxidase (NOX2). When these cells are resting, the subunits of NOX2 gp91<sup>phox</sup> and p22<sup>phox</sup> form a membrane-associated component, whereas the cyclic hetero-trimer p67<sup>phox</sup>, p47<sup>phox</sup> and p40<sup>phox</sup> is located cytosolic (Fig. 2 (B i)) (Bedard and Krause 2007). After activation the cytosolic hetero-trimer translocates to the membrane-associated part under phosphorylation of p67 and the enzyme assembles into its activatable configuration (Fig. 2 (B ii)). Activation of NOX2 is initiated by binding NADPH to catalyse the oxidation of O<sub>2</sub> to the highly reactive O<sub>2</sub><sup>-</sup>. This is rapidly

transformed in a chain reaction to various ROS, which are released into to phagolysosome. This oxidative burst disintegrates the inclusions and the remaining fragments are released into the extracellular space. The mentioned NOX2 is part of the NOX family, a collective term covering all isoforms of NADPH oxidases, NOX1, NOX2, NOX3, NOX4, NOX5, DUOX1 and DUOX2, whereas NOX2 is the phagocyte NADPH oxidase (Bedard and Krause 2007).

The metabolism in activated neutrophils and macrophages relies primarily on the Warburg metabolism as a source of ATP, partly due to the rapidity with which ATP can be made available, but also because oxygen availability is limited due to the activity of NADPH oxidase (Pearce and Pearce 2013). The NADPH necessary to generate the oxidative burst is created by the pentose phosphate pathway in the cytosol (Pearce and Pearce 2013), which also consumes and limits oxygen supply.

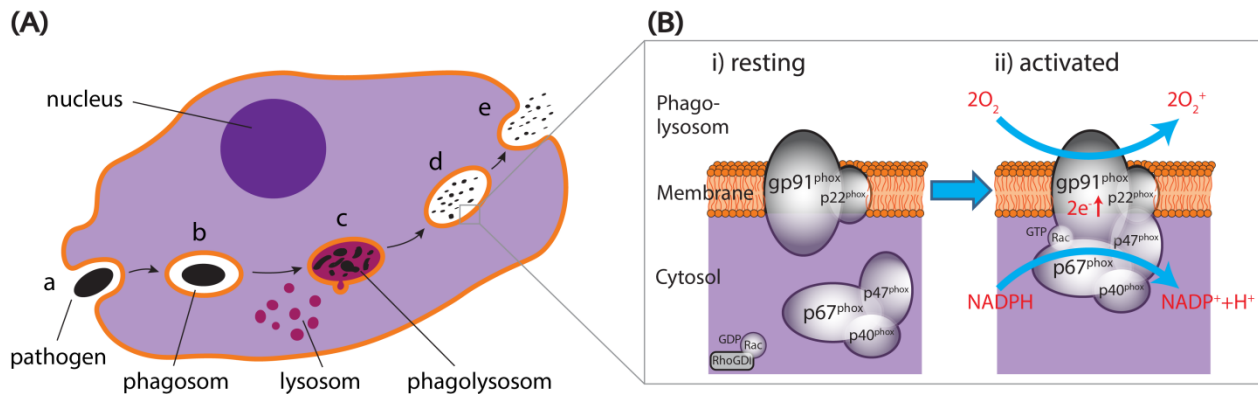


**Fig. 2: Phagocytosis and activation of NADPH oxidase. (A)** Scheme of phagocytosis: a) engulfing the pathogen, b) forming a phagosome, c) union of phagosome and lysosome to digest the inclusion, d) fragments are deinfected by ROS, e) remaining material is released to the extracellular space. **(B)** Resting (i) and activated (ii) NOX2 (Scheme taken from (Leben et al. 2018)).

Macrophage and neutrophil function is not limited to “cleaning up” the infection. Neutrophils are able to process a special kind of death pathway, which is different from the normal pathways like apoptosis (programmed/natural cell death) and necrosis (traumatic cell death) due to external damage. Neutrophils are the first cells to reach the site of infection, because they patrol in their final form through the blood vessels and do not differentiate into another cell type like monocytes to macrophages (Schütt and Bröker 2011). When activated and outnumbered by the pathogens they form neutrophil extracellular traps (NET) to immobilize and kill pathogens extracellularly, making them an easy target for other immune cells that will enter the inflamed tissue later

(Brinkmann et al. 2004). Those NETs are composed of cellular DNA from the dissolved nuclei and granular content of the neutrophils. (Schütt and Bröker 2011; Brinkmann and Zychlinsky 2007)

Both, macrophages and neutrophils initiate specific defence mechanisms by recruiting other immune cells (e.g. natural killer cells) to the site of infection by the secretion of signalling molecules such as interleukin IL-1 and IL-8, tumour necrosis factor alpha TNF- $\alpha$  (Schütt and Bröker 2011).

Next to their main function of being the first defence line against pathogens or debris, the innate immune cells such as macrophages and neutrophils may present antigen to T cells and, thus, are involved in the formation of immunological memory.

### *Second-line defence – focus on B cells*

After an initial response to a specific pathogen, the cells of the adaptive immune system create an immunological memory and thus form the second-line defence. Here, anti-gen presenting cells like macrophages, dendritic cells and B cells present in the secondary lymphoid tissue antigen to naïve T and B cells to activate them. In a selection process memory B and T cells as well as antigen-secreting plasma cells are formed. This leads to an enhanced immune response during a second infection with that pathogen.

Naïve B cells are mature B cells that migrated from their birthplace, the bone marrow, to a secondary lymphatic organ, but have not yet encountered antigens. B cell receptors, the membrane-bound precursor of the antibody, are formed by random recombination of antigen-binding, immunoglobulin-variable gene regions, during the maturation in the bone marrow (Schütt and Bröker 2011).

T-cells are formed in the bone marrow as well, but mature to the thymus, where they undergo a selection process. T cells differentiate into T-helper cells (CD4<sup>+</sup>), which alarm other immune cells with soluble messenger substances, or into T-killer cells (CD8<sup>+</sup>), which detect and kill malfunctioning or infected cells. Together they form the group of T-effector cells (Schütt and Bröker 2011).

As shown in Fig. 3, naïve T and B cells meet antigen-presenting cells (APC) in the secondary lymphoid tissues. APC present previously captured antigens by the MHC-II complex. When an antigen gets recognised by a randomly generated B cell receptors (BCR), the naïve B cell is

activated by a series of intracellular signals. The activated BCR is engulfed by receptor mediated cytolysis and the bound antigen molecule is then presented on the surface via MHC-II. Now the activated B cell is an APC as well, but cannot proliferate yet. Cell proliferation of the activated B cell requires co-stimulatory signals from T-helper cells (CD4<sup>+</sup>), to which the B cell presents antigen at the border of the T cell follicle and the B cell follicle. Both activated cell types get in contact via the MHC-II molecule of the B cell and the T cell receptor (TCR) which recognizes the MHC-II via the CD4 receptor. Co-stimulatory molecules like CD40 enhance B cell activation. The T-cell also secretes IL-2/4/5, which further stimulate the activated B cells to proliferate under clonal expansion. Some of these B cells undergo differentiation and become memory B cells or antibody producing short-lived plasma cells. Other activated B cells migrate to the germinal center (GC) of the secondary lymphoid organs where follicular dendritic cell (FDC) present native antigen on their surface, and T-helper cells mediate a refinement of the antibody selection in iterative cycles in a microevolutionary process. (Schütt and Bröker 2011; Janeway Jr et al. 2012)

B cells that have successfully passed this fate decision point differentiate into either memory B cells or long-lived plasma cells. These cells lack the BCR on their surface, presumably because the selection and refinement is completed and the receptor is no longer needed (Brynjolfsson et al. 2018). Plasma cells produce a high amount of this high-affinity antibody during a second infection or enter another round of antigen receptor diversification in the GC.

Antibodies are freely secreted into the blood by the plasma cells and form the humoral immune defence (Schütt and Bröker 2011). They evolutionary evolved to recognize and capture pathogens. Antibodies do not destroy pathogens, but activate a number of defence mechanisms. If the organism is repeatedly infected by an already defeated pathogen, these specific antibodies bind to the invading pathogen and mark them for the phagocytosing cells and the complement system (Schütt and Bröker 2011). Furthermore, antibodies neutralize viruses so that they can no longer penetrate a cell. In this way, the secondary immune response is much faster and more efficient than the innate immune response.

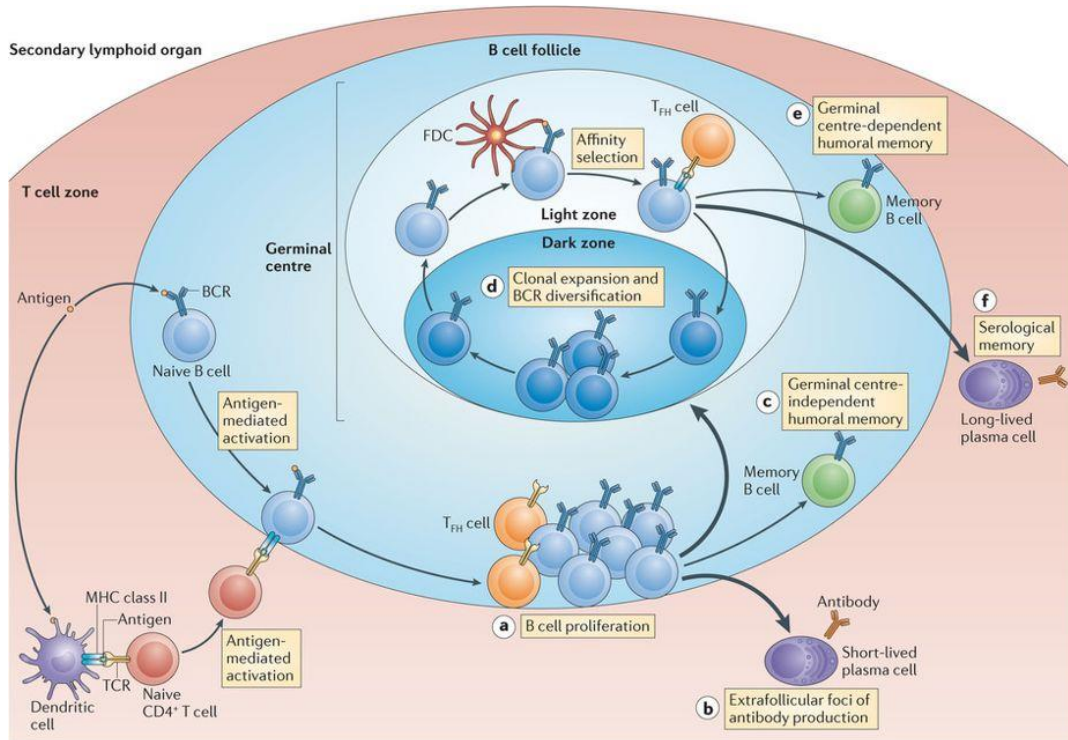


**Fig. 3: Memory B cell and plasma blast generation in the lymphoid tissue.**

[Scheme taken from Fig. 1 in (Kurosaki et al. 2015) with permission from Springer Nature (Oct 12, 2020)]

A lot is known about T cell metabolism, for example that naïve T cells show an engaged Warburg metabolism, when they recognize an antigen, in order to grow, proliferate and acquire specialized effector functions (Pearce and Pearce 2013). However, detailed information about metabolism in B cell subsets is scarce (Gaber et al. 2017), especially how metabolism directs the fate of healthy B cells. It is generally assumed that B cells share certain fundamental metabolic characteristics with T cells (Pearce and Pearce 2013), because naïve B cell also undergo a metabolic reprogramming and use aerobic glycolysis when activated (Gaber et al. 2017). Furthermore, B cells can differentiate into long-lived plasma cells, which survive within the bone marrow for years and at the same time synthesize large amounts of antibodies. It is not yet clear how longevity and high-performance biosynthesis are compatible with each other (Pearce and Pearce 2013).

### 1.1.3. Calcium ions as second messenger

Intercellular signalling is mediated by primary and secondary messengers. During an acute immune response as well as during the development of an immunological memory, multicellular actions are coordinated through cell signalling to ensure an effective present and future defence. Such intercellular signals occur in form of direct cell-to-cell contact or in the indirect exchange of substances, such as cytokines or hormones, over greater distances. Those substances are the “first messengers”. “Second messengers”, such as calcium ions ( $\text{Ca}^{2+}$ ), enable cells to internally process signals from their environment. Intercellular biochemical or electrical signals are transmitted and translated intracellularly in order to stimulate the appropriate response. Thus calcium plays an important role in the function of many different cell types. (Christen and Jaussi 2006; Janeway Jr et al. 2012)

Rapid calcium signaling is ensured by maintaining calcium membrane potentials. The free calcium ion concentration in a quiescent cell is low (10-100 nM) compared to their environment. By opening ion channels the  $\text{Ca}^{2+}$  concentration is increased by several powers of ten (up to 10 mM) (Engelke et al. 2007) due to the gradient, whereas the calcium ions originate from the surrounding environment or from the cell's interior i.e. endoplasmic reticulum or mitochondria. Depending on cell type, the increase in intracellular calcium concentration differs and triggers a variety of effects, for instance the contraction in muscle cell types or the exocytosis of neurotransmitters in neurons. Each cell type has its own set of ion channels, pumps and enzymes for processing these signals and maintaining a gradient between the intra- and extracellular space (Ulbricht 2018). Opening of the calcium channel is triggered by voltage changes across the cell membrane or ligands like inositol trisphosphate ( $\text{IP}_3$ ). The pumping and processing of calcium ions are active cell processes that consume energy in form of ATP (Engelke et al. 2007).

In lymphocytes, the increase of cytosolic  $\text{Ca}^{2+}$  is involved in signaling pathways that initiate transcription of target genes to regulate the cell fate, including proliferation, differentiation and survival (Engelke et al. 2007; Fenninger and Jefferies 2019). In B cells, the subunits of the B cell receptor  $\text{Ig}\alpha$  and  $\text{Ig}\beta$  extend into the cytoplasm for signal transduction. Initiated by the antigen stimulation, the calcium release activated channels (CRAC) are activated and intracellular  $\text{Ca}^{2+}$ , stored in the endoplasmic reticulum, are depleted, which leads to a signalling cascade and, if necessary, to a further  $\text{Ca}^{2+}$  influx from the extracellular space (Fenninger and Jefferies 2019). Depending on the differentiation status of the B cell, the calcium response is distinct. For example, the temporal extension in transitional (naïve) B cells is much shorter compared to marginal zone

B cells and mature B cells have a greater influx of calcium from the extracellular space than immature B cells (Hoek et al. 2006).

## 1.2. Fluorescence and its lifetime

Fluorescence is the absorption of radiative energy by a molecule and the subsequent spontaneous emission of light. Fluorescence lifetime is the time in which the molecule remains in the higher energetic state.

In 1917 A. Einstein described the quantum theory of radiation and distinguished three processes in radiative equilibrium, a closed system of radiative molecules (fluorophores) in which each molecule emits exactly as much radiation as it absorbed before (Einstein 1917). Those three processes are: a) the absorption of a photon, in which the photons energy is transferred to an absorbing molecule and the energetic state of the molecule changes to the excited state ( $S_1$ ) (Fig. 4); b) the spontaneous emission of a photon, the fluorescence, in which the molecule returns to the  $S_0$  state without external influence and the difference in energy  $\Delta E = S_1 - S_0$  is transferred to the emission photon, which is radiated in arbitrary direction (Fig. 4); and c) the stimulated emission of a photon, whereat the photon emission and the molecule's return to  $S_0$  energetic level is caused by another photon, the emission photon has the same direction, frequency and phase as the incident photon, which is not absorbed but amplified. The probability of such a process depends on the number of molecules  $N$ . A. Einstein introduced undefined constants, the Einstein coefficients, to describe the proportionality of these processes, whereat absorption and stimulated emission additionally depend on the spectral radiance  $u$ :

$$\text{for absorption:} \quad B_{01} \cdot N_1 \cdot u \quad (\text{Eq. 1})$$

$$\text{for spontaneous emission:} \quad A_{10} \cdot N_2 \quad (\text{Eq. 2})$$

$$\text{for stimulated emission:} \quad B_{10} \cdot N_2 \cdot u \quad (\text{Eq. 3})$$

$B_{01}, A_{10}, B_{10}$	... Einstein coefficients
$N_n$	... number of molecules
$u$	... spectral radiance

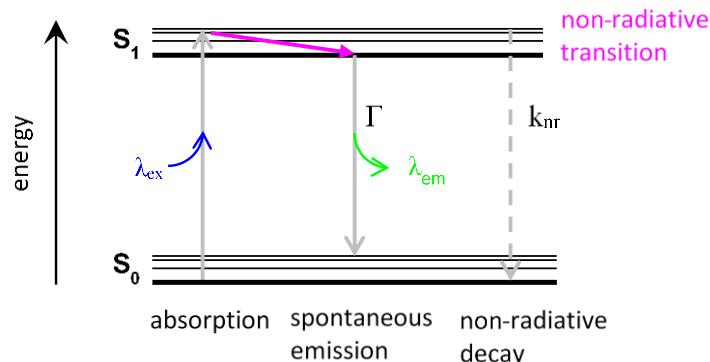


**Fig. 4:** *Simplified Jabłoński diagram depicting the molecular energy levels during spontaneous fluorescence and the non-radiative decay (Jabłoński 1935). The thick horizontal lines represent the electronic singlet levels, the thin horizontal lines the vibrational levels.  $S_0$  ... ground state,  $S_1$  ... first energetic state,  $\lambda_{ex}$  ... excitation wavelength,  $\lambda_{em}$  ... emission wavelength,  $\Gamma$  ... emissive rate,  $k_{nr}$  ... rate of non-radiative decay.*

The Einstein coefficients in equation (Eq. 1) to (Eq. 3) are substance-specific properties and are linked to each other by:

$$A_{10} = B_{01} \frac{8\pi h}{\lambda^3} \quad (\text{Eq. 4})$$

$\lambda$  ... wavelength  
 $h$  ... Planck's constant;  $h = 6.626 \cdot 10^{-34}$  Js

After a fluorophore has been excited by a photon with the exact wavelength  $\lambda_{ex}$ , i.e. which photon energy  $E_{ph}$  bridges the energetically forbidden range between the energetic levels, the molecule remains in the excited state (representative  $S_1$  in Fig. 4) for a certain time before it relaxes back to the ground state  $S_0$  by emitting a fluorescence photon. Kasha's rule describes that during this retention period the molecule relaxes non-radiatively to the lowest vibrational level of the  $S_1$  state (Kasha 1950). This retention period is commonly known as fluorescence lifetime  $\tau$  and is linked to the Einstein coefficients and under the exclusion of external influences it can be expressed as:

$$\tau = \frac{1}{A_{10}} \quad (\text{Eq. 5})$$

In order to account for the absence of a radiative equilibrium in natural systems Eq. 5 is modified, considering effects like atomic transitions. (Strickler and Berg 1962) rewrote the relationship

considering experimentally measured molar absorptivities and solvent effects such as the refractive index:

$$\Gamma = \frac{1}{\tau_n} = 2.88 \cdot 10^{-9} \cdot n^2 \cdot \frac{\int I(\tilde{\nu}) d\tilde{\nu}}{\int I(\tilde{\nu}) \tilde{\nu}^{-3} d\tilde{\nu}} \cdot \int \frac{\varepsilon(\tilde{\nu})}{\tilde{\nu}} d\tilde{\nu} \quad (\text{Eq. 6})$$

$\tau_n$	... natural radiative lifetime
$n$	... refractive index
$I$	... fluorescence emission
$\varepsilon$	... extinction coefficient
$\tilde{\nu}$	... wave number

The natural radiative lifetime  $\tau_n$  depends not only on intrinsic properties such as the molecule structure, which characterize its energetic level, but is also sensitive to outer influences such as the refractive index (Strickler and Berg 1962), the solvent polarity (Scott et al. 1970), the pH value (Niesner et al. 2005), the temperature (Lakowicz et al. 1992a) and the ion concentration (Celli et al. 2010) of the medium surrounding the fluorophore as well as binding to macromolecules. Thus the fluorescence lifetime is sensitive to the local chemical environment and can be used as a sensitive parameter to measure changes in it.

As depicted in Fig. 4 both the emissive rate  $\Gamma$  and the rate of non-radiative decay  $k_{nr}$  depopulate the excited state  $S_1$ , i.e. the fluorescence lifetime  $\tau$ , the time the molecule stays in the excited state, depends on them.

$$\tau = \frac{1}{\Gamma + k_{nr}} \quad (\text{Eq. 7})$$

$\Gamma$	... emissive rate
$k_{nr}$	... rate of non-radiative decay

The natural radiative lifetime  $\tau_n$  is linked to the fluorescence lifetime  $\tau$  via the fluorescence quantum field  $\Phi$ , which is given by the number of emitted photon relative to the number of absorbed photon:

$$\Phi = \frac{\tau}{\tau_n} \quad (\text{Eq. 8})$$

$\Phi$	... fluorescence quantum field
$\tau_n$	... natural radiative lifetime
$\tau$	... fluorescence lifetime

The fluorescence lifetime is an important measurement parameter to distinguish fluorophores with the same emission wavelength, but different lifetimes. In spontaneous fluorescence, in which the emission was not stimulated by a second photon or trapped in the triple state by intersystem crossing, this fluorescence lifetime amounts a few nanoseconds (Berezin and Achilefu 2010; Lakowicz 2013).

Fluorescence is a stochastic process, which follows first order kinetics, thus the intensity  $I$  of an entire fluorophore population decays mono-exponentially in time.

$$I(t) = I_0 e^{-t/\tau} \quad (\text{Eq. 9})$$

$I(t)$  ... emission intensity at time  $t$   
 $I_0$  ... initial emission intensity  
 $\tau$  ... fluorescence lifetime

There are two main methods to acquire fluorescence lifetime data: the phase domain and the time domain method. In phase domain the fluorophores are excited by sinusoidal modulated light, whose frequency is reciprocal to the lifetime of the investigated fluorophore (approx. 100 MHz). Thus the resulting emission light is also sinusoidal modulated at the same frequency, but due to the delay time in the excited state the phase is shifted  $\Delta\Phi$  and the amplitude (modulations depth  $M$ ) is decreased. Both can be used to calculate the fluorescence lifetime  $\tau_\Phi$  (Eq. 10) and/or  $\tau_M$  (Eq. 11). If the sample contains only a single fluorescent component  $\tau_\Phi$  and  $\tau_M$  are equal. When two or more fluorescent species of different lifetimes are involved,  $\tau_\Phi$  and  $\tau_M$  differ (Bastiaens and Squire 1999; Lakowicz 2013).

$$\tau_\Phi = \frac{\tan(\Delta\Phi)}{\omega} \quad (\text{Eq. 10})$$

$$\tau_M = \frac{\sqrt{\frac{1}{M^2} - 1}}{\omega} \quad (\text{Eq. 11})$$

$\tau_\Phi, \tau_M$  ... fluorescence lifetime (determin by  $\Phi$  or  $M$ )  
 $\omega = 2\pi f$  ... modulation frequency  
 $\Delta\Phi$  ... phase shift  
 $M$  ... reduction in the relative modulation depth  $M = (B/A)/(b/a)$

Alternatively, fluorescence lifetime is measured in time domain, whereat the fluorophores are excited by a pulsed laser source. The resulting fluorescence emission decays exponentially which

decay constant is the fluorescence lifetime (Bastiaens and Squire 1999; Lakowicz 2013). For  $n$  fluorophore species the decay curve is given by:

$$F(t) = A_1 e^{-t/\tau_1} + A_2 e^{-t/\tau_2} + \dots + A_N e^{-t/\tau_N} + C \quad (\text{Eq. 12})$$

$F(t)$	... fluorescence intensity at time $t$
$A_1, A_2, A_N$	... amplitudes of the lifetime components
$\tau_1, \tau_2, \tau_N$	... decay constants = fluorescence lifetimes
$C$	... a constant representing e.g. background light

Typically, the time domain measurements are performed by using a time-correlated single photon counter (TCSPC). The time between a start signal and a stop signal is measured by an internal time-to-digital converter (TDC). Most modern TCSPC devices measure in "reverse mode", in which the emission gives the start signal and the excitation the stop signal. For the calculation of the time between start and stop the repetition rate of the excitation laser is used. On average, only one emission pulse is released per 100 excitation pulses, i.e. much less frequently. If the excitation pulse would give the start signal, the time measurement would be strongly distorted, because it would be stopped much too late. The spontaneous fluorescence is a stochastic process, thus this time measurement is repeated multiple times and the photon arrival times are sorted in a histogram. Provided adequate counts, the histogram reveals the exponential decay, which is analyzed to extract the fluorescence lifetime. (Lakowicz 2013)

(Lakowicz et al. 1992a) applied the fluorescence lifetime to microscopic imaging termed "Fluorescence Lifetime Imaging Microscopy" (FLIM). For FLIM the image contrast is obtained by the excited-state lifetime  $\tau$  of a fluorescent molecule (Fig. 5) instead of intensity and emission wavelength. When measured by TCSPC, each pixel contains an exponential photon arrival time histogram and after the analysis an individual fluorescence lifetime. In contrast to conventional microscopy techniques, FLIM identifies structures of similar emission spectra, but different lifetimes. Since the fluorescence lifetime of a molecule is exquisitely sensitive to its local chemical environment, FLIM opens new perspectives to study cellular functions. Thus FLIM offers an additional imaging dimension in addition to the spatial and temporal resolution (xyzt) and the identification of different cell types or cell organelles through different emission wavelengths (staining) compared to conventional microscope techniques.

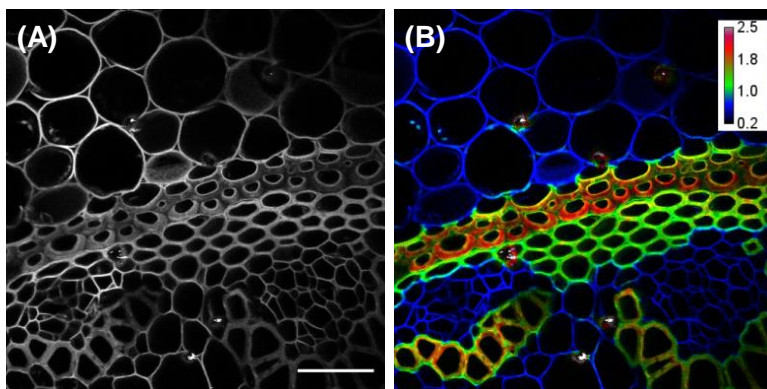


**Fig. 5:** *Slice of rhizome of Convallaria majalis. Stained with acridin-orange-staining for fluorescence (DAPI, FITC/GFP, TEX RED, Cy5 and DIC) by MEDICAL & SCIENCE MEDIA, excited at 800 nm, detected without wavelength discrimination. (A) Intensity image, (B) intensity-weighted FLIM of the same field of view. Calibration bar is given in nanoseconds. Scale bar indicates 50  $\mu\text{m}$ .*

### 1.3. Cellular autofluorescence by NAD(P)H

The ubiquitous co-enzymes NAD<sup>+</sup>/NADH and their phosphorized variants NADP<sup>+</sup>/NADPH form the basis of the cellular energy metabolism including glycolysis and OxPhos as well as of pathogen-defense provided by NADPH oxidases (NOX). Since the oxidized forms are autofluorescent, they can serve as markers to monitor these life-sustaining mechanisms label-free and *in vivo*.

The coenzyme NAD<sup>+</sup> was discovered by (Harden and Young 1906). As depicted in Fig. 6 (A), NAD<sup>+</sup>/NADP<sup>+</sup> reduce to NADH/NADPH by adding a hydrogen nucleus H<sup>+</sup> and two electrons to provide electron carrier functions in cellular energy production (Blacker and Duchen 2016). (Warburg and Christian 1936) discovered the fluorescence of the reduced molecule under blue-violet light and described its absorption properties. (Chance and Baltscheffsky 1958; Chance et al. 1962; Chance et al. 1979) as well as (Boyer and Theorell 1956) monitored changes in the NAD<sup>+</sup>/NADP<sup>+</sup> and NADH/NADPH pools and associated them to the redox states of cells and tissues via changes in the excitation properties and fluorescence intensity of mitochondrial NADH and NADPH (Mayevsky and Rogatsky 2007). The nicotinamide ring of the reduced form was identified to be the fluorescent part of NADH and NADPH (Kierdaszuk et al. 1996), unaffected by the phosphate at the most distant part of the molecule (Fig. 6 (A) green X). Consequently, spectral properties of NADH and NADPH are identical in the visible/ infrared light and the molecules are often labelled as NAD(P)H in context of fluorescence (Blacker and Duchen 2016).

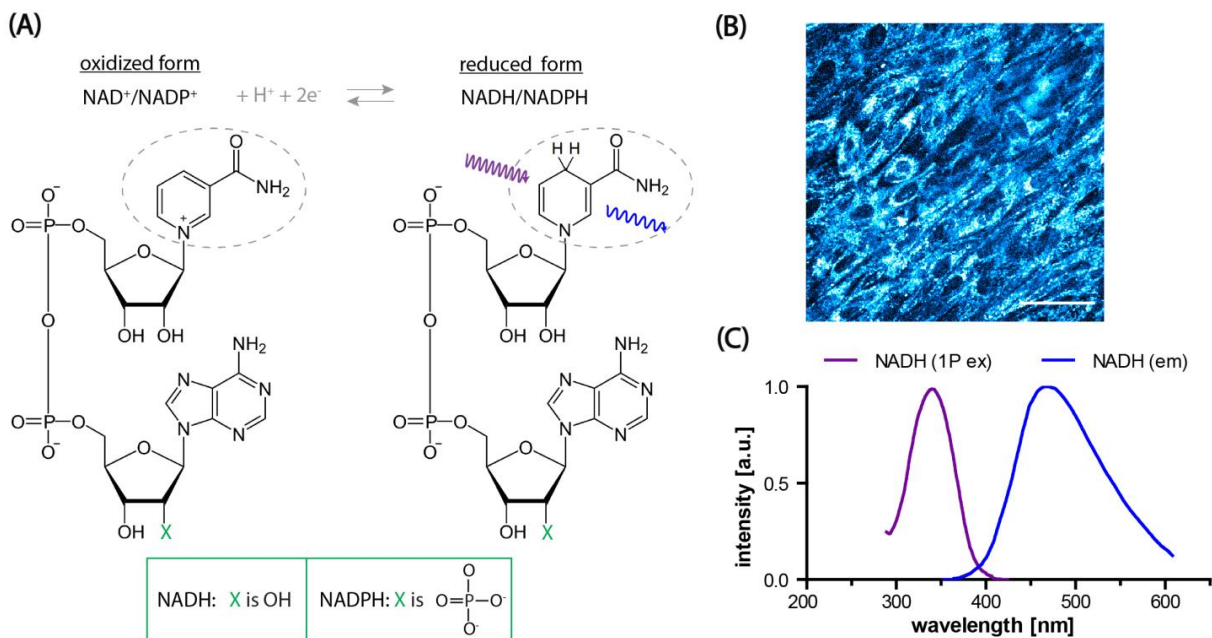


**Fig. 6: NAD(P)H autofluorescence** (A) The molecular structures of the redox couples  $\text{NAD}^+/\text{NADH}$  and their phosphorylated forms  $\text{NADP}^+/\text{NADPH}$ , reduction and oxidation reaction is shown in gray; grey, dashed encirclings indicate changed parts. (B) NAD(P)H fluorescence of unlabeled MC3T3 cells at day 10 of differentiation (unpublished data). Ex 760 nm (2PE), Em 466/40 nm. Scale bar indicates 50  $\mu\text{m}$ . (C) Normalized one-photon excitation (violet) and emission (blue) spectra of NADH (data taken from Arizona Spectra Database “NADH(AB)” and “NADH(EM)” (Utzinger 2011)).

The one-photon absorption spectrum peak is at 340 nm (FWHM=60 nm) and its emission spectrum at 460 nm (FWHM=100 nm) (Fig. 6 (C)). Experiments in UV-spectrum showed that the other aromatic rings  $\text{NAD}^+/\text{NADP}^+$  and  $\text{NADH}/\text{NADPH}$  have absorption peaks as well: at approx. 220 nm for the nicotinamide ring in  $\text{NAD}^+/\text{NADP}^+$  and at approx. 260 nm for the adenine part (De Ruyck et al. 2007). Since the molecule does not fluoresce, when it was excited by this wavelength (Berezin and Achilefu 2010) and the irradiation with UV-light is known to cause massive photodamage and phototoxicity, these peaks are impractical for biological applications anyway (Blacker and Duchon 2016).

In the 1970s and 1980s several groups showed the elongated fluorescence lifetime of NAD(P)H when the coenzyme is bound to an enzyme, such as lactate dehydrogenase (Scott et al. 1970), liver alcohol dehydrogenase (Gafni and Brand 1976) or malate dehydrogenase (Jameson et al. 1989). The fluorescence lifetime of NAD(P)H spreads over 1.5-3.0 ns when bound to an enzyme

and 0.4-0.5 ns in its free, unbound form (Scott et al. 1970; Gafni and Brand 1976; Jameson et al. 1989). When the coenzyme NAD(P)H binds to another enzyme, for example to catalyze the oxidation of alcohols to aldehydes, the molecular structure of the whole construct changes and limits small scale motions that are responsible to the majority of deexcitation events (Blacker et al. 2019). A change in the depopulation rate results in the molecule to remain for a longer time in the excited energy state. Furthermore, other mechanisms based on dynamic quenching by the adenine part of the molecule have been suggested to contribute to the observed lifetime differences (Berezin and Achilefu 2010; Maeda-Yorita and Aki 1984).

The fluorescence intensity as well as the fluorescence lifetime of NAD(P)H was initially investigated mainly spectroscopically in solutions or in isolated mitochondria until the first microscopic images of NAD(P)H fluorescence intensity in cells were taken in the 1980s (Eng et al. 1989). (Lakowicz et al. 1992b) suggested to apply FLIM to a microscope to investigate unlabeled living cells using fluorescence lifetime of NADH but he showed only macroscopic lifetime images of soved NADH and NADH bound to malate dehydrogenase in cuvettes. Interestingly, in the same year similar techniques were published by different groups, for instance (Clegg et al. 1992), who initially named it “time-resolved imaging fluorescence microscopy” (TRIM) and (Schneckenburger and Koenig 1992), who delivered the first NAD(P)H-FLIM images of yeast cells. Later, the NAD(P)H-FLIM was applied to two-photon microscopy (Piston et al. 1995), as described in more detail in the next section.

Since then, the time-resolved measurement of NAD(P)H fluorescence has been widely used in living biological samples to image the NAD(P)H-dependent cellular energy metabolism. Especially in cancer research, it has been used to delineate tumorous from normal tissue based on the Warburg effect (Berezin and Achilefu 2010; Skala et al. 2007b; Bird et al. 2005). Even its potential as clinical diagnostic tool to identify cancer tissue has been shown (McGinty et al. 2010). Furthermore NAD(P)H-FLIM is the method of choice to investigate NOX activation and the resulting neuronal dysfunctions in chronic neuroinflammation (Mossakowski et al. 2015; Radbruch et al. 2016) or the cellular defense against invading pathogens in polymorphonuclear cells (PMN) (Niesner et al. 2008a).

Whether the fluorescence lifetime of enzyme-bound NAD(P)H is individual to the respective enzyme or is the same for all NAD(P)H-dependant enzyme is controversially discussed in this field (Ranjit et al. 2019). If fluorescence lifetime is enzyme-specific, the excat values of many NAD(P)H-dependant enzyme are unknown.

## 1.4. Monitoring cell signaling by energy transfer

Förster resonance energy transfer (FRET) is the physical process of radiationless energy transfer from an energetically excited fluorescent molecule, the donor, to another fluorescent molecule, the acceptor (Fig. 7 (A)), which was named after T. Förster, who described this phenomenon in 1948 (Förster 1948).

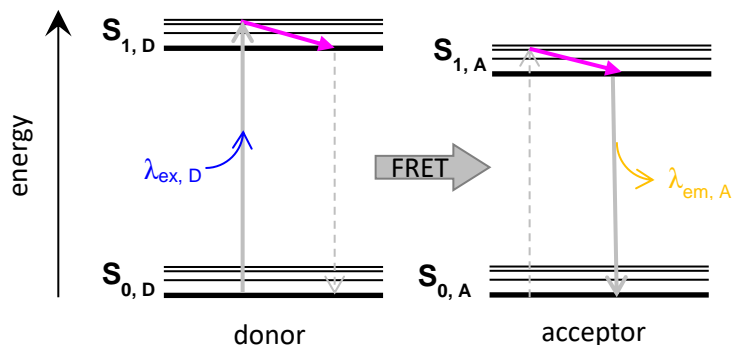


**Fig. 7:** *Simplified Jablonski diagram of the Förster resonance energy transfer. (Same declaration abbreviation as in Fig. 4).*

Using Fermis golden rule the transfer rate of the FRET process  $k_T(r)$  can be calculated (Fermi 1950):

$$k_T(r) = \frac{\Phi_D k^2 J(\lambda) K}{\tau_D n^4} \frac{1}{r^6} \quad (\text{Eq. 13})$$

$\Phi_D$	... fluorescence quantum field of donor
$k^2$	... factor of orientation
$J(\lambda)$	... orbital overlap integral
$\tau_D$	... fluorescence lifetime of donor
$r$	... distance between donor and acceptor
$n$	... refractive index of solvent medium
$K$	... constant ( $K = 9 (\ln 10) / 128 \pi^5 N_A$ ) with $N_A$ Avogadro constant

This equation (Eq. 13) shows that the transfer rate decreases with the 6<sup>th</sup> power of the distance  $r$  between the donor and acceptor molecules, which means that FRET is only efficient when the molecules are very close to each other. In common fluorophores, FRET is negligibly small, if the distance is larger than 10 nm. Furthermore, the equation (Eq. 13) shows that in addition to the distance  $r$ , the orbital overlap integral  $J(\lambda)$  and the orientation  $k^2$  of the molecules are important factors for an efficient energy transfer.

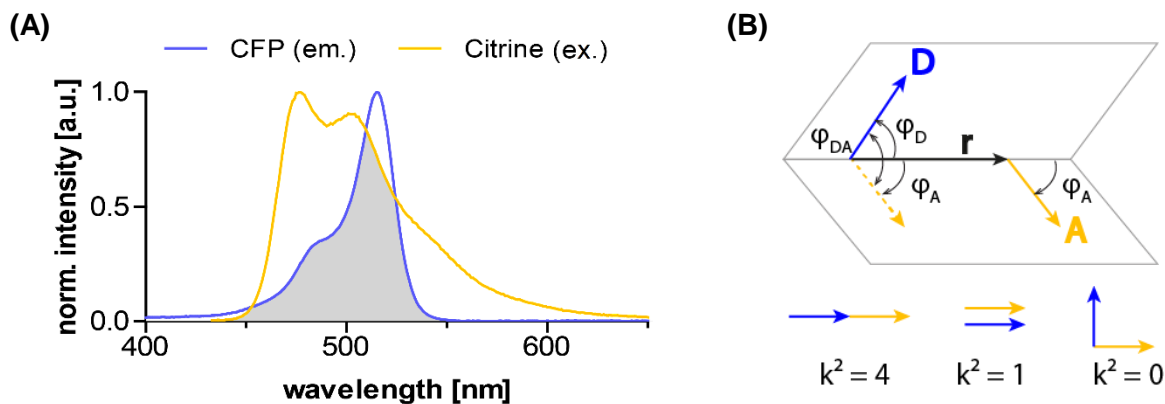


**Fig. 8: Conservation of energy and momentum in FRET.** (A) Overlap integral  $J(\lambda)$  (gray area) of the donor emission spectrum (eCFP) and the acceptor excitation spectrum (Citrine) (data taken from (Utzinger 2011)), (B) Angles of the transition dipoles and the resulting orientation factor  $k^2$ , nomenclature see (Eq. 14).

In any energy transfer, both the conservation of energy and the conservation of momentum must be fulfilled. To conserve the energy, the transition dipole moments of the fluorophores must be resonant with each other, meaning that the emission spectrum of the donor must overlap with the excitation spectrum of the acceptor Fig. 8 (A). The grade of this spectral overlap of the orbitals can be described by the overlap integral  $J(\lambda)$  (Lakowicz 2013):

$$J(\lambda) = \int_0^{\infty} F_D(\lambda) \epsilon_A(\lambda) \lambda^4 d\lambda \quad (\text{Eq. 14})$$

$\lambda$	... wavelength
$F_D(\lambda)$	... fluorescence intensity of donor
$\epsilon_A(\lambda)$	... extinction coefficient of acceptor

The orientation factor  $k^2$  provides the geometric orientation of the molecules Fig. 8 (B). The value results from the relative position of the dipole moments and can be expressed as (Lakowicz 2013):

$$k^2 = (\cos\varphi_{DA} - 3\cos\varphi_D \cos\varphi_A)^2 \quad (\text{Eq. 15})$$

$\varphi_{DA}$	... angle between the emission transition dipole of donor and the absorption transition dipole acceptor
$\varphi_D$	... angle between the transition emission dipole of donor and vector containing the two transition dipoles
$\varphi_A$	... angle between the absorption transition dipole of acceptor and vector containing the two transition dipoles

In order to conserve the momentum, the transition dipoles of donor and acceptor need to be as parallel as possible. The value of the orientation factor  $k^2$  reaches values between 0 and 4. If transition dipoles of donor and acceptor are “head-to-tail parallel” the orientation factor  $k^2$  is 4, thus the most efficient orientation. For parallel dipoles  $k^2$  is 1. And if transition dipoles are rectangular to each other,  $k^2$  is 0, thus the most inefficient orientation. (Lakowicz 2013)

If the three criteria (distance, spectral overlap and parallel orientation) are met and the energy transfer takes place, the acceptor emits its fluorescence instead of the donor. This is detectable by the increase in intensity in the spectral range of the acceptor fluorescence, so that the ratio of donor and acceptor intensities can be used to determine the FRET efficiency  $E$  (Wallrabe and Periasamy 2005).

$$E = 1 - \frac{I_{DA}}{I_D} \quad (\text{Eq. 16})$$

$I_D$  ... intensity of donor fluorescence  
 $I_{DA}$  ... intensity of donor and acceptor fluorescence

This may be used to measure distances in the nanometer region, but more widely it is used to detect the binding of a substance to a ligand to prove its presence and measure its amount, as in this thesis.

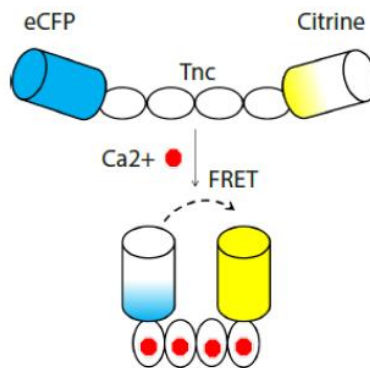


**Fig. 9:** *Scheme of the Troponin-C (TnC)-based FRET in presence of calcium ( $\text{Ca}^{2+}$ , red). The FRET-pair is eCFP (donor) and citrine (acceptor). (Scheme taken from (Ulbricht et al. 2021)).*

The calcium-sensitive FRET-construct TN-XXL (Geiger et al. 2012) is genetically encoded in  $\text{CD19}^+$  B-cells (Yellow CaB mouse) (Ulbricht et al. 2021). In this construct the protein troponin C

(TnC) connects the fluorophores eCFP (donor) and Citrine (acceptor) (Geiger et al. 2012). In absence of calcium the distance between the partners is too large so the proximity criterion of FRET is not fulfilled and the construct fluoresces with the emission of the donor (Fig. 9 top). In the presence of calcium, the connecting troponin C folds and shortens the distance between the partners, thus the energy is transferred and the fluorescence of the acceptor predominates (Fig. 9 bottom).

FLIM is an adequate measuring method, since the fluorescence lifetime of the donor fluorophore is affected by FRET (Eq. 13). When FRET takes place the donor lifetime is quenched, thus the retention time of the donor molecule in the excited state is shortened. Compared to the ratiometric method, the intensity ratio of donor and acceptor, in donor-FLIM only the donor fluorescence is taken into account. This prevents the measurement results to be impacted by differences in scattering properties of the emission photons in tissue, different bleaching behavior of the fluorophore or wavelength-dependent sensitivity of the detectors. Based on calibration curves it is possible to measure the absolute calcium concentration *in vivo* (Geiger et al. 2012) using the following equation.

$$\log[Ca^{2+}] = \log K_d + 0.2 \cdot \ln \left[ \frac{\tau_{unquen} - \tau_{quen}}{\tau - \tau_{quen}} - 1 \right] \quad (\text{Eq. 17})$$

$K_d$	... molecular dissociation constant,	$K_d(\text{TN-XXL}) = 453 \text{ nM}$ (Geiger et al. 2012)
$\tau$	... measured fluorescence lifetime [ns] in the pixel	
$\tau_{unquen}$	... fluorescence lifetime of unquenched donor,	$\tau_{unquen}(\text{TN-XXL}) = 2.3 \text{ ns}$
$\tau_{quen}$	... fluorescence lifetime of quenched donor,	$\tau_{quen}(\text{TN-XXL}) = 0.7 \text{ ns}$

Troponin C consists of an N-terminal regulatory lobe with two sites that bind calcium specifically with lower affinity and a C-terminal structural lobe with another two sites that bind calcium with high affinity (Geiger et al. 2012). Due to the two  $Ca^{2+}$ -binding sites, troponin C theoretically has two molecular dissociation constants  $K_d$  (Geiger et al. 2012). Resulting from the two real  $K_d$  values, an effective  $K_d$  is used to calculate the  $Ca^{2+}$  concentration (Geiger et al. 2012). Magnesium ions ( $Mg^{2+}$ ) can also bind to the binding sites mentioned, but only in much higher concentrations. These  $Mg^{2+}$  concentrations are in the mM range in contrast to calcium, which is in the nM- $\mu$ M range (Mank and Griesbeck 2008), thus an order of magnitude less.

### 1.5. A view inside - deep tissue microscopy

To study dynamic processes at a cellular level in living, intact organs in areas of biomedical interest, a long-wavelength excitation is required that can penetrate tissue (Benninger and Piston 2013). The far-red and near-infrared region of the electro-magnetic spectrum is known as the “optical window” of biological samples that offers high tissue transparency and relatively low scattering, due to minima in the absorption spectrum of oxidized and non-oxidized hemoglobin as well as water from approx. 650 nm to 900 nm (Fig. 10) (Xu et al. 1996).

The penetration depth depends on the observed tissue, such as in brain it is possible to imaged up into 1000  $\mu\text{m}$  (Theer et al. 2003) in contrast to  $\sim 100\text{-}200$   $\mu\text{m}$  in more scattering tissue like the spleen or lymph nodes, since SNR is depth-dependent and decreases with increasing depth (Herz et al. 2010; Niesner et al. 2007). Furthermore, the low-energy, i.e. long-wavelength photons cause less damage in biological samples, such as chemical bond breaks and photo ablation or photo bleaching of fluorophores (Zipfel et al. 2003).

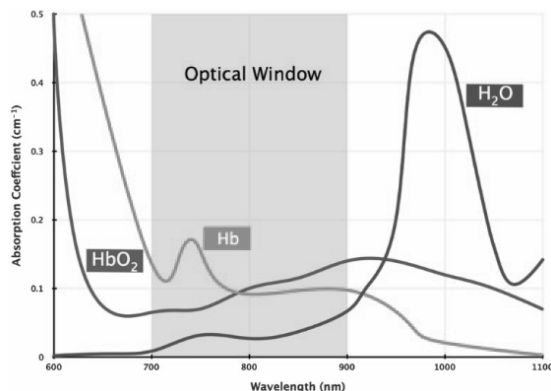


**Fig. 10: Biological optical window.** Absorption coefficient of hemoglobin (Hb), its oxidized form (HbO<sub>2</sub>) and water (H<sub>2</sub>O). (Figure taken from (Phan and Bullen 2010) with permission from John Wiley and Sons (Oct, 12, 2020)).

This wavelength region is predestinated for deep tissue *in vivo* imaging, but not many fluorophores can be excited in the classical way here. During the course of the quantum mechanical revolution (Göppert-Mayer 1931) described the principle of multiphoton excitation, which was experimentally proven by (Kaiser and Garrett 1961). Here two (or more) photons are absorbed instantaneously (within  $\sim 10^{-16}$  s). Due to the energy conservation the sum energy of the photons must be equal to the energy of single-photon excitation, thus far-red or infrared excitation wavelength are used (Fig. 11 (A)).

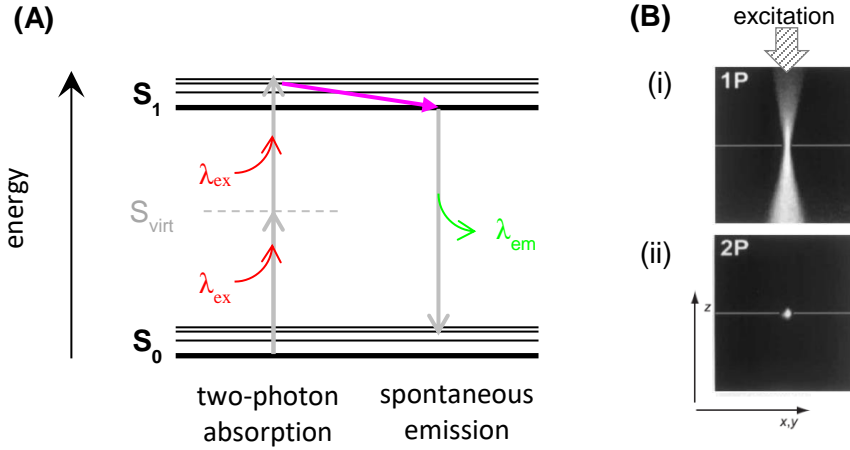


**Fig. 11: Two-photon excitation. (A)** Extension of the simplified Jablonski diagram in Fig. 4, **(B)** excitation volume and focal plane (horizontal line) in one-photon (i) and two-photon (ii) excitation. ((B) taken from Fig 2 in (Soeller and Cannell 1999) with permission from John Wiley and Sons (Oct, 12, 2020)).

(Denk et al. 1990) applied multiphoton excitation in microscopy. In a sense, a multiphoton microscope is a modification of the confocal laser scanning microscope. In a confocal microscope two mirrors, the Galvano scanners, scan the focused laser beam over the sample and the fluorophores contained in it are excited to emit fluorescence. The fluorescence light is separated from the excitation light by a dichroic mirror and detected in photomultiplier tubes (PMT). Using a PC the overall image is created by reconstructing the pixel mosaic based on the xy-position of the scanner mirrors. An aperture in the beam path blocks the light from planes outside the excitation volume and produces images with high contrast. Due to the punctual excitation and self-illuminating objects the optical resolution of such a confocal laser scanning microscope is increased compared to a wide field microscope as developed by K. Zeiss in at the end of the 19th century, which was constructed based on Abbes principles on only diffraction-limited microscope (Abbe 1873):

lateral: 
$$d_{x,y} = \frac{1,22 \cdot \lambda}{2 \cdot \sqrt{2} \cdot N.A.} \approx \frac{0,431 \cdot \lambda}{N.A.} \quad (\text{Eq. 18})$$

axial: 
$$d_z = \frac{1,4 \cdot \lambda \cdot n}{N.A.^2} \quad (\text{Eq. 19})$$

d ... distance between two points that can just be perceived separately  
 $\lambda$  ... excitation wavelength  $\rightarrow$

N.A.                   ... numerical aperture of the objective  
where  $N.A. = n \cdot \sin\alpha$   
    n                   ... refractive index of the medium between objective and sample  
     $\alpha$                ... aperture angle of the lens

The probability of the instantaneous absorption of multiple low-energy photons does not increase linearly with the number of the irradiated photons, but in polynomial manner, meaning in square, when two photons and in cubic when three photons are absorbed. Only in the focus of a pulsed laser sufficiently high photon flux densities are achieved for this purpose and fluorophores outside this range are not excited at all and thus cannot lead to a deterioration of the resolution (Fig. 11 (B)). The aperture, like in a confocal microscope used, is obsolete.

In multiphoton microscopy, the higher depths are reached compared to conventional confocal laser scanning microscopy, while image resolution is almost the same. Only the absence of an aperture and the associated diffraction phenomena are eliminated, but there are still a punctual excitation and self-illuminating objects, just like in a confocal microscope.

## 1.6. Research aims of this thesis

In immunology the metabolic state of a cell is a parameter for its function. A dysfunction of the immune system may end as autoimmunity, an undesired immune responses against the body's own healthy cells and tissue that causes a variety of different diseases, like rheumatoid arthritis, diabetes mellitus type 1 or multiple sclerosis. After cardiovascular diseases and cancer, autoimmune diseases are the third most common group of diseases (IMD 2020). The cause of these chronic inflammatory processes and the basics of immunity are the subject of current, interdisciplinary research. Intravital imaging techniques improve our understanding, by providing spatial information in the tissue context of living organisms. It allows insights into the highly dynamic interactions of the cell populations involved. Multiphoton microscopy is the method of choice, due to its ability to penetrate deep into intact tissue and thus reach areas of biomedical interest. FLIM offers an additional dimension in imaging to resolve cellular function.

The molecules, NADH and NADPH are the main electron donors in cell metabolism. Since they are fluorescent, when excited properly, they serve as powerful non-invasive indicators to investigate metabolic states. Spectrally these molecules are undistinguishable, but their fluorescence lifetime  $\tau$  changes when they bind to an enzyme. NAD(P)H-FLIM has been widely used to investigate the

Warburg effect in cancerous cells (Skala et al. 2007b; Bird et al. 2005; Provenzano et al. 2009). The Warburg effect describes the switch from oxidative phosphorylation (OxPhos) in normal cells to an increased rate of glycolysis in cancerous cells, something that normally happens in hypoxia. In the literature, a lower (but not as low as free) NAD(P)H fluorescence lifetime in cells is correlated with metabolism based on glycolysis rather than OxPhos (Chacko and Eliceiri 2019). Cancerous cells are distinguishable from healthy cells by NAD(P)H-FLIM, even its potential as clinical diagnostic tool has been shown (Munro et al. 2005; McGinty et al. 2010). However, it is known that the Warburg effect is not unique to cancerous cells. All cells with a sudden increased energy demand, for example proliferating cells (Vander Heiden et al. 2009) or activated immune cells (Gaber et al. 2017), adapt their energy metabolism to the faster glycolysis. Thus, the central hypothesis of this work is that activated immune cells can be identified by NAD(P)H-FLIM.

Furthermore, NADPH is involved in innate immune response. During phagocytosis it activates NADPH oxidase to generate ROS to defuse pathogen fragments in the phagosomes. The potential of NAD(P)H-FLIM to identify oxidative burst or even oxidative stress, the excessive production of free oxygen radicals, has been shown in neurons of multiple sclerosis (MS) patients during neuroinflammation (Mossakowski et al. 2015).

Multicellular actions, for instance an acute immune response or the development of an immunological memory, are coordinated through cell signaling. Such intercellular signals occur in form of direct cell-to-cell contact or the indirect exchange of factors such as cytokines. Calcium ( $\text{Ca}^{2+}$ ), as a second messenger, transmits intercellular signals within the cell to process the exchanged information and to stimulate a suitable reaction. FRET-constructs, like TN-XXL, are genetically encoded  $\text{Ca}^{2+}$ -indicators. In presence of  $\text{Ca}^{2+}$ , the FRET donor is quenched and its fluorescence lifetime shortens significantly, thus FLIM is a suitable tool to monitor  $\text{Ca}^{2+}$ -based cell communication.

Two-photon excited FLIM is a valuable method to investigate life-sustaining mechanisms label-free and *in vivo*. However, measuring, analyzing and interpreting FLIM data are challenging and controversially discussed in this field (Niesner et al. 2008a; Ranjit et al. 2019; Chacko and Eliceiri 2019). In order to investigate and quantify these mentioned processes, it is necessary to develop a systematizing, generally applicable approach. This requires interdisciplinary cooperation involving biology, physics and medicine.

The aims of this thesis in brief:

- Establishment of the time-domain FLIM measurement as well as development of a Python-based routine to translate these data to a normalized, virtual phase domain (phasor approach)
- *In vitro* application of FLIM and phasor analysis to the autofluorescent molecules NAD(P)H in isolated human leukocytes and investigation of the temporal NOX activation in resting vs. stimulated cells
- Determination of the fluorescence lifetime of most abundant NAD(P)H-dependent enzymes in solution to mark the enzyme-specific positions in the phasor plot
- Development of a vector-analyzing algorithm based on the enzyme-specific positions, which will support the interpretation of NAD(P)H-FLIM results regarding the involved enzyme and their activity
- *In vivo* application of FLIM, phasor approach and vector analysis to the donor of a FRET-construct genetically-coded in CD19<sup>+</sup> B-cells in a lymph node to map the cellular Ca<sup>2+</sup> concentrations in the tissue.

The present work was carried out at the DRFZ (Deutsche Rheuma-Forschungszentrum) in close cooperation between the research groups "Biophysical Analysis" of Prof. Dr. rer. nat. Raluca Niesner and "Immune Dynamics" of Prof. Dr. vet. med. Anja Hauser.

## 1.7. Selected publications and author contributions

The present cumulative dissertation is primarily based on these first and second author publications, which are revered in the following as shown in square brackets. A complete list of all publications in which I was involved can be found in Appendix B.

**(Leben et al. 2018)**

### ***Phasor-Based Endogenous NAD(PH) Fluorescence Lifetime Imaging Unravels Specific Enzymatic Activity of Neutrophil Granulocytes Preceding NETosis.***

**Leben R**, Ostendorf L, van Koppen S, Rakhymzhan A, Hauser AE, Radbruch H, Niesner RA.

Int J Mol Sci. 2018 Mar 29;19(4). pii: E1018.  
doi: [10.3390/ijms19041018](https://doi.org/10.3390/ijms19041018).

#### *Author Contributions:*

R.A.N. is corresponding author.  
R.L., L.O., A.E.H, A.R, R.A.N designed experiments and performed research.  
R.L. programmed the phasor analysis algorithm and performed data analysis.  
S.v.K. and L.O. prepared samples.  
R.L. and S.v.K performed experiments.  
R.L., L.O. and R.A.N wrote the manuscript.  
R.L. designed figures.  
All authors edited and confirmed the manuscript

**(Leben et al. 2019)**

### **Systematic enzyme mapping of cellular metabolism by phasor-analyzed label-free NAD(P)H fluorescence lifetime imaging**

**Leben R\***, Köhler M\*, Radbruch H, Hauser AE, Niesner RA

Int J Mol Sci. 2019 Nov 7;20(22). pii: E5565.  
doi: [10.3390/ijms20225565](https://doi.org/10.3390/ijms20225565).

#### *Author Contributions:*

R.L. and M.K. contributed equally to this work.  
R.L. and R.A.N. are corresponding authors.  
R.L. and R.A.N. conceived the algorithm on which the analysis framework of NAD(P)H-FLIM data is based.

R.L. programmed the analysis algorithm and performed data analysis.  
R.L., M.K., and R.A.N. conceived the experimental project.  
M.K. prepared samples.  
R.L. and M.K. performed experiments.  
A.E.H. and H.R. provided expertise regarding the cellular metabolism of immune and stromal cells.  
R.L, M.K., A.E.H., and R.A.N. wrote the manuscript.  
R.L. designed figures.  
All authors edited and confirmed the manuscript.

**(Ulbricht et al. 2021)**

**Intravital quantification reveals dynamic calcium concentration changes across B cell differentiation stages**

Ulbricht C, **Leben R**, Rakhymzhan A, Kirchhoff F, Nitschke L, Radbruch H, Nienser RA, Hauser AE

Elife. 2021 Mar 22;10:e56020.  
doi: [10.7554/eLife.56020](https://doi.org/10.7554/eLife.56020).

*Author Contributions:*

A.E.H. is corresponding author.  
R.A.N. and A.E.H. contributed equally to this work.  
C.U.: Conceptualization, Data curation, Formal analysis, Validation, Visualization, Methodology, Writing - original draft.  
R.L.: Data curation, Software, Formal analysis, Validation, Investigation, Visualization, Methodology, Writing - review and editing.  
A.R.: Data curation, Software, Formal analysis, Investigation, Methodology;  
F.K.: Resources;  
L.N.: Resources, Methodology; Helena Radbruch, Supervision, Funding acquisition, Writing -original draft.  
R.A.N.: Conceptualization, Resources, Data curation, Software, Formal analysis, Supervision, Funding acquisition, Validation, Investigation, Visualization, Methodology, Projectadministration, Writing - review and editing.  
A.E.H.: Conceptualization, Resources, Formal analysis, Supervision, Funding acquisition, Validation, Investigation, Methodology, Project administration, Writing - review and editing.

## 2. Methods

### 2.1. Two-photon microscope setup for FLIM

The fluorescence lifetime images were acquired using a specialized laser-scanning two-photon upright microscope (TriMScope II, LaVision BioTec GmbH, Germany) as schematically illustrated in Fig. 12. The excitation beam was generated by a 80 MHz pulsed and tunable titanium sapphire laser Ti:Sa (Chameleon Ultra II, Coherent INC., USA) with a pulse width of 140 fs. The beam was modified by a beam shaper, which includes a telescope, a pulse compressor and a  $\lambda/2$  plate-based power attenuator. The beam was scanned over the sample by two galvanometric mirrors and focused by a water-immersion objective lens (20x, NA 1.05, Apochromat, Zeiss GmbH, Germany).

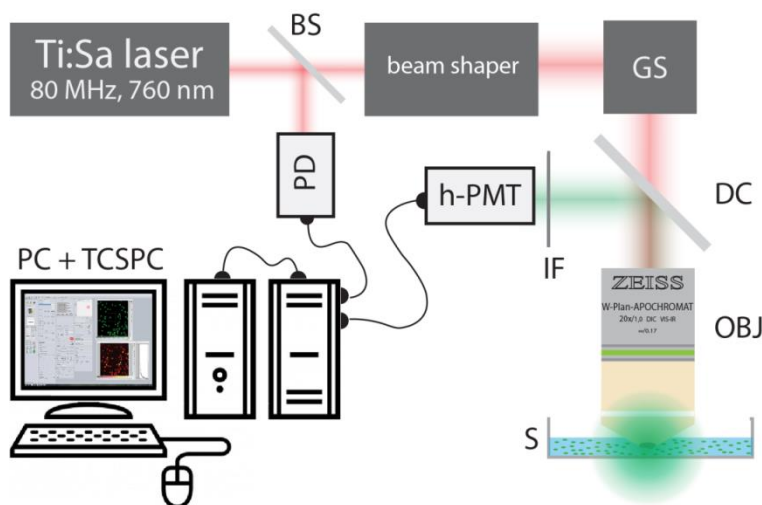


**Fig. 12:** *Schematic two-photon microscope setup to perform time-domain FLIM.* BS (beam splitter), GS (galvo scanner), DC (dichroic mirror), OBJ (objective), S (sample), IF interference filter, h-PMT (hybrid-PMT), PD (photon diode), PC (personal computer), TCSPC (time-correlated single photon counter). (Scheme taken from (Leben et al. 2018)).

A certain percentage of the excitation beam was reflected by a beam splitter (BS) into an ultrafast photodiode (DET08CL InGaAs, Thorlabs, Germany) to time-synchronize the time-correlated single photon counter (TCSPC, LaVision BioTec GmbH, Germany).

The fluorescence light was collected in backward direction using a hybrid photomultiplier tube (GaAsP, Hamamatsu K.K., Japan) separated for the excitation light by a 775 nm dichroic mirror (DC) and after it passed the interference filter (IF) 466/40 nm (both Chroma, USA). The FLIM raw data were acquired in 27 ps (binning 1) or 55 ps (binning 2) time steps within a measurement

window of 12.5 ns to cover at least 9 ns of the decay curve. The electronic components of a TCSPC device do not operate infinitely fast, the distribution of lag times between arrival of an emission photon in the detector and its registration in the control PC were taken into consideration. This distribution of lag time was characterized by the instrument response function (IRF) and measured by second harmonic generation (SHG) in potassium dihydrogen phosphate (KDP) powder ( $\lambda_{\text{ex}} = 940$  nm,  $\lambda_{\text{em}} = 470$  nm (in Ch 466/40),  $t_{\text{bin}} = 55$  ps). The TCSPC had a Gaussian-shaped IRF of 251 ps FWHM and its smallest resolvable fluorescence lifetime was  $(0.084 \pm 0.015)$  ns, (Fig. 13).

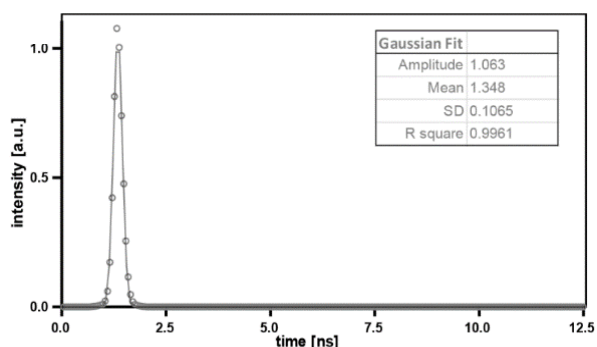


**Fig. 13:** *Normalized instrument response function of TCSPC. Measured by SHG of KDP crystals. Red circles: data points, blue line: Gaussian fit (Suppl. Fig. S6 B in [Leben et al., 2018]).*

The raw data were acquired using the Inspector Pro software (version 2.0.8; La Vision BioTec GmbH).

## 2.2. Data analysis: the phasor approach

In time-domain fluorescence lifetime experiments the determination of the lifetime  $\tau$  is based on an exponential fit of the photon arrival time histogram with the decay constant  $\tau$  (Bremer et al. 2017). Under the assumption that only a single species of fluorophores populates the observation volume, the temporal decay is mono-exponentially fitted. In most biological samples the observation volume contains two or more fluorescent molecule populations, which results in a multi-exponential temporal decay. Multi-exponential decays challenge the analysis, if the number of exponents is unknown. In contrast, the phasor approach is independent of the number of fluorophore species in heterogeneous samples. As schematically depicted in Fig. 14 the time-

domain lifetime data are transferred to a virtual phase domain by calculating the discrete Fourier transformation (DFT) (Eq. 20) numerically (Leben et al. 2018; Digman et al. 2008). The calculation resulted in a complex number, composed of a real part (Eq. 21) and an imaginary part (Eq. 22). Normalization of the real and imaginary part from the transformation provide the coordinates in the plot. The phase vector pointing from the origin to these coordinates is referred to as the "phasor" and is shown in the following as a single dot.

$$DFT(\omega) = \sum_{k=0}^{N-1} f[k] \exp(-i\omega kT) \quad (\text{Eq. 20})$$

results in:

$$Re = \frac{\sum_{k=0}^{N-1} f[k] \cos(\omega kT)}{\sum_{k=0}^{N-1} f[k]} \quad (\text{Eq. 21})$$

$$Im = \frac{\sum_{k=0}^{N-1} f[k] \sin(\omega kT)}{\sum_{k=0}^{N-1} f[k]} \quad (\text{Eq. 22})$$

- f[k] ... single data points of exponential decay in the time domain
- i ... imaginary number;  $i^2+1 = 0$
- $\omega = 2\pi f$  ... modulation frequency
- T ... time bin (time between two pulses divided by the number of timesteps)
- Re ... normalized real part of the complex number
- Im ... normalized imaginary part of the complex number

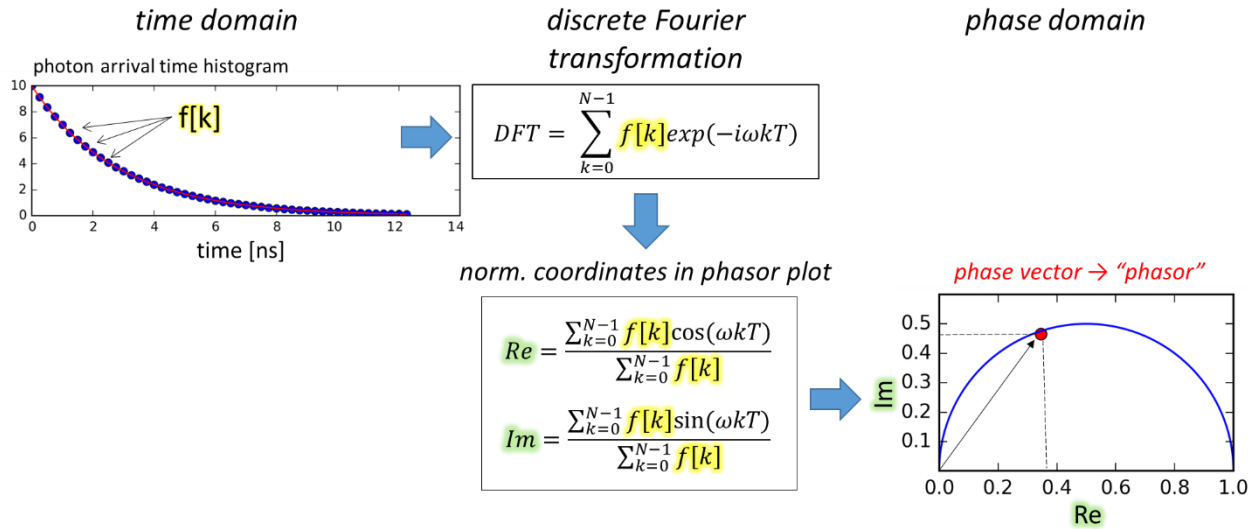


**Fig. 14:** Coordinate transformation of FLIM data from time domain to phase domain via a discrete Fourier transformation.

Coordinates that lie on the semi-circle (radius = 0.5, center at (0.5|0)) represent all possible phasor positions of mono-exponential lifetimes. Phasors are distributed on a logarithmic scale counterclockwise along the semi-circle as shown in Fig. 15, i.e. lifetimes that go towards zero can be the point (1|0), the very long ones (>20 ns) in the direction of the origin (0|0). According to vector algebra, the phasor will lay on the segment connecting the lifetimes of the pure components, if the phasor originates from a bi-exponential temporal decay (orange in Fig. 15). If the temporal decay is tri-exponential, the phasor lays within the triangle, formed by the segments connecting the pure components (green in Fig. 15) and so forth. Depending on the ratio of the involved fluorophores the phasor is shifted in the direction of the one with the higher fraction.

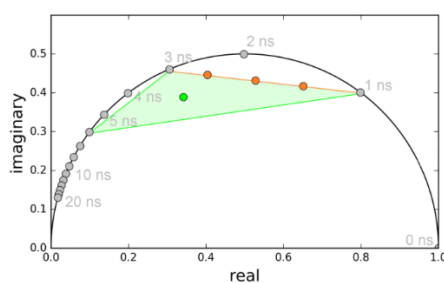


**Fig. 15:** *Phasor approach to graphically represent exponential decays.* Gray: phase vectors origin from mono-exponential temporal decays, orange: bi-exponential, green: tri-exponential. Modulations frequency is 80 MHz.

The Fourier transformation requires a modulation frequency  $f$  ( $\omega = 2\pi f$ ), which shifts the position of the phase vector along the semi-circle. A modulation frequency of 80 MHz was chosen to visualize lifetimes in the range of  $0 \text{ ns} \leq \tau \leq 6 \text{ ns}$ , which is limited by the observable time window given by the repetitions rate of the excitation laser. Since fluorescence ( $\tau$  is some ns) is investigated not phosphorescence (seconds, minutes, even hours), no higher lifetime are expected.

In FLIM every pixel of the image carries the temporal decay and will give a position in the phasor plot. The distribution of fluorescence lifetimes is represented as a 3D heatmap histogram in a violet (low frequency) to orange-yellow (increasing frequency) false color and referred to as “phasor cloud”. In order to obtain a spatial-resolved fluorescence lifetime image the pixels are transferred from the phase domain back into the time domain by a continuous Fourier transformation (Eq. 23)-(Eq. 27) and are arranged in their original position in the image.

$$FT(\omega) = \frac{1}{\sqrt{2\pi}} \int_0^{+\infty} f(t) \cdot e^{-i\omega t} dt \quad (\text{Eq. 23})$$

with:  $f(t) = e^{-\frac{t}{\tau}}$  (Eq. 24)

results in:  $Re = \frac{1}{1+(\omega\tau)^2}$  and  $Im = \frac{\omega\tau}{1+(\omega\tau)^2}$  (Eq. 25)

rearranged to  $\tau = \frac{1}{\omega} \frac{Im}{Re}$  (Eq. 26)

$$= \frac{1}{\omega} \frac{f[k]\sin(\omega kT)}{f[k]\cos(\omega kT)} = \frac{\tan(\omega kT)}{\omega} \quad (\text{Eq. 27})$$

The FLIM raw data were spatially Gaussian blurred (e.g.  $\sigma = 2$ ), in order to concentrate the decay curves of several neighboring pixels. In this calculation, improved temporal resolution comes at the cost of spatial information. The fluorescence lifetime images resulting from a phasor analysis show similar lifetime information as a monoexponential fitting, with the advantage of the additional phasor plot containing all multiexponential information of the data set.

This phasor plot can be used to further analyse the data as demonstrated in the results part of this thesis (section 5.3 and 6.3). All analyses were executed by an algorithm scripted in python programming language (see Appendix B).

### 2.3. NAD(P)H-FLIM and donor FRET-FLIM

The spectral excitation and emission properties and the selected wavelength to perform NAD(P)H FLIM and donor-FRET FLIM are shown in Fig. 16, respectively.

The two-photon excitation peak of NAD(P)H was at approx. 700 nm, but the laser power of the Ti:Sa laser was low at this wavelength and especially the pulse properties were insufficient to perform two-photon excitation or to trigger the TCSPC for FLIM. The power peak of the Ti:Sa laser was at approx. 800 nm. To excite NAD(P)H as effectively as possible in this setup a wavelength of 760/770 nm was chosen. The emission peak of NAD(P)H was at approx. 460 nm, which lies within the spectral range of the interference filter 466/40 nm.

The donor in the FRET-construct TN-XXL eCFP has a two-photon excitation peak at approx. 852 nm and thus 850 nm was chosen for excitation. The emission peak of CFP is at approx. 474 nm, as well covered by the interference filter 466/40 nm.

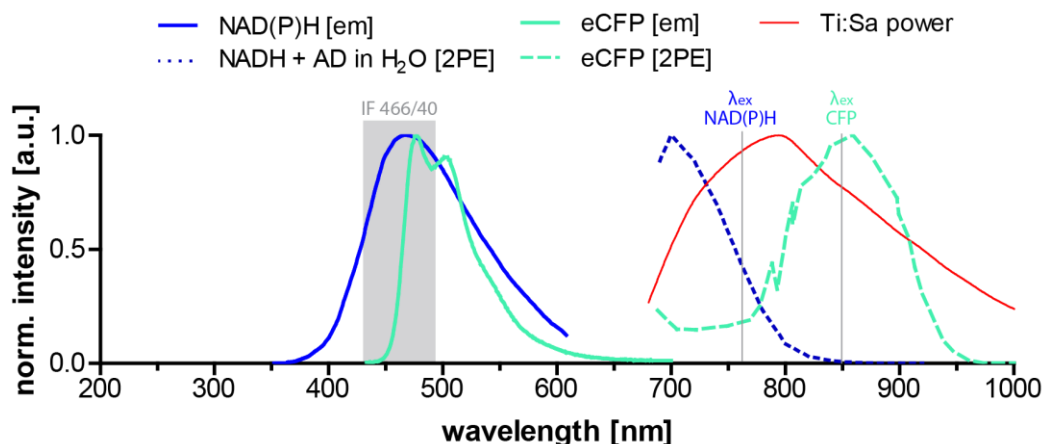


**Fig. 16:** *Spectral excitation and emission properties and the selected wavelength to perform NAD(P)H FLIM and donor-FRET FLIM. (Data taken from Arizona Spectra Database “NADH(EM)”, “NADH+AD in H<sub>2</sub>O – DRBIO-2P”, “CFP (Tsien) (EM)”, “ECFP-Drobizehev-2P (2P)”, “Ti:Saph” (Utzinger 2011)).*

## 2.4. Samples

The samples investigated in this thesis are outlined in detail (including cited protocols, concentrations used or manufacturers of the substances) in the methodological part of the corresponding publications, which can be found in Appendix B "Print versions of selected publications". To improve readability they are listed in brief:

- *Neutrophil granulocytes and CD11b+ monocytes— isolation from human peripheral blood*
  - In monocytes phorbol-myristate-acetate (PMA) mediated the stimulation of the NADPH oxidase family
  - Neutrophil phagocytosis was triggered by pHrodo™ beads conjugated with Staphylococcus aureus
  - DNA of neutrophil granulocytes was stained by Vybrant DyeCycle Green™ nuclear stain

- *Enzyme and NAD(P)H solutions*
  - NADH/ NADPH and all enzymes were solved in 100 mM MOPS buffer (pH 7.8)
  - The enzymes PDH, CTBP1, IDH, GAPDH, G6PDH, LDH, HADH and MDH were incubated in varying concentrations with NADH or NADPH, respectively.
  
- *Mesenchymal stromal-like 3T3-L1 cell culture*
  - Unstained to reveal subcellular heterogeneity of enzyme activity
  
- *Lymphocytes of YellowCaB mice in lymph node of WT C57/Bl6 mice (in vivo) after cell transfers and immunization*
  - FDCs were labeled with Fab-Fragment of CD21/35-Atto590 or CD21/35-Alexa647
  
- *Lymphocytes in the lymph node of a (Fucci-red)/Blimp-1:GFP double reporter mouse (in vivo)*

### 3. Results – Validation of the FLIM-system and data analysis

To validate the FLIM measurement setup and the performance of the data analysis, several samples of well-known fluorescence lifetimes were investigated. Besides eGFP transfected in the cytoplasm of HEK 293T cells, with an actual fluorescence lifetime, SHG in KDP powder and background noise in non-fluorescent medium were examined (Fig. 17). The resulting fluorescence lifetimes were determined by Gaussian-fitting the lifetime histogram of the FLIM-image.

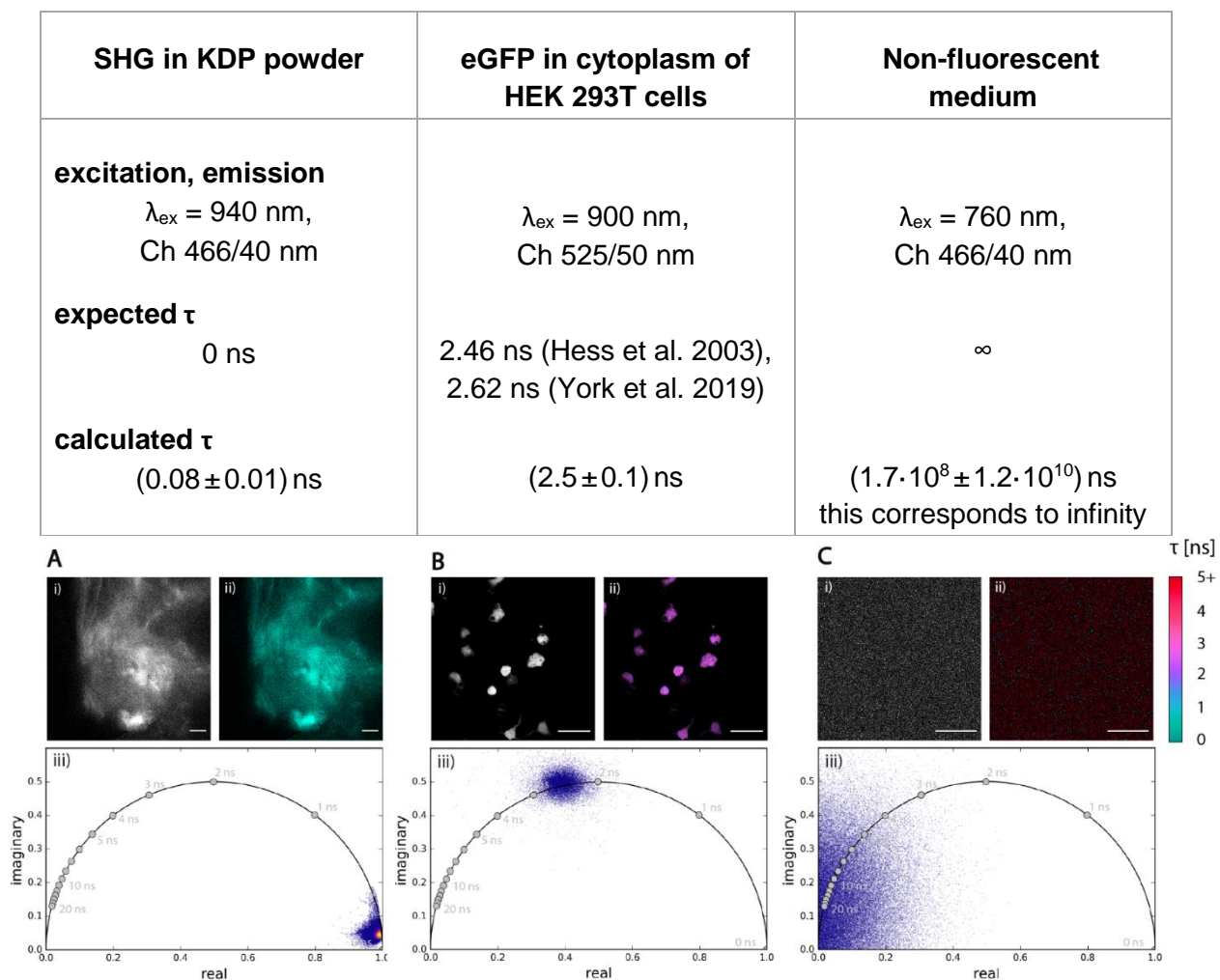


**Fig. 17:** Validation of the FLIM measurement setup and data analysis. (A) SHG in KDP (Suppl. Fig. S6 A in [Leben et al., 2018]), (B) eGFP in HEK 293T cells (C) background noise in non-fluorescent medium. All (i) are the normalized intensity images, all (ii) the intensity-weighted FLIM images and all (iii) the corresponding phasor plots. Scale bars indicate 50  $\mu\text{m}$ . (Ulbricht et al. 2021).

## 4. Results – Leben, R. *et al.*, (2018)

This paragraph reviews the results published in the article Leben, R., *et al.*, *Phasor-Based Endogenous NAD(P)H Fluorescence Lifetime Imaging Unravels Specific Enzymatic Activity of Neutrophil Granulocytes Preceding NETosis*, *Int J Mol Sci*, 2018. 19(4).

The complete article can be found in Appendix A. Some passages could be identical in wording.

### 4.1. Endogenous NAD(P)H-FLIM identifies oxidative burst in innate immune cells via NOX2

The well-studied NADPH oxidase 2 (NOX2) is the main catalyzer of the oxidative burst in monocytes, macrophages and neutrophils. In this study it was used to validate if the measurement system and analysis procedure are suitable to study NAD(P)H-dependent metabolism in living cells and organisms. The metabolic activity of innate immune cells, i.e. isolated polymorphonuclear cells and CD 11b<sup>+</sup> monocytes, was measured by NAD(P)H-FLIM and analyzed using the phasor approach. The NAD(P)H fluorescence lifetime of metabolic active cells ranges between approx. 1.5 ns and 2.5 ns and are shown in green in the FLIM image Fig. 18 (iii). The stimulation of the monocytes by phorbol-myristate-acetate (PMA) entails the stimulation of the NADPH oxidase family, which leads to a significant elongation of the NADPH fluorescence lifetime to 3.65 ns, which is also visible in a shift of the phasor cloud (Fig. 18 (B iv)). If brightness and contrast is set to 0–4 ns the long lifetimes are represented in red in the FLIM images, revealing the stimulated cells.

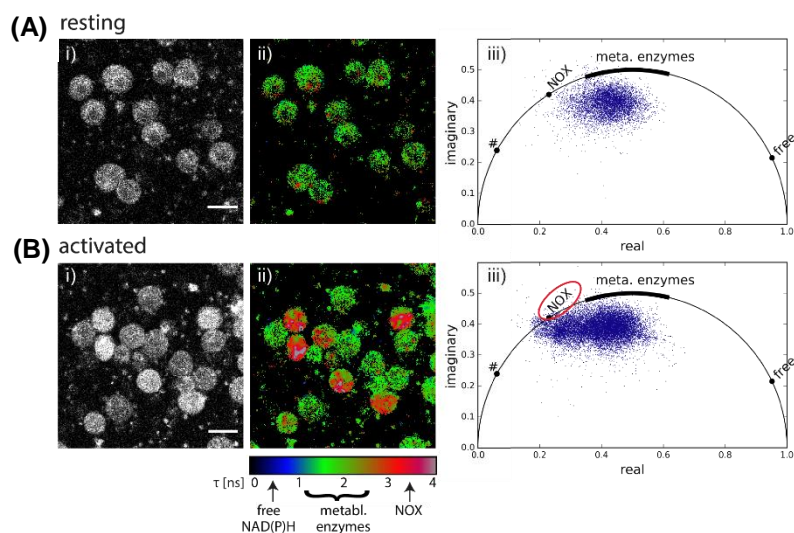


**Fig. 18:** NAD(P)H metabolism of (A) resting and (B) PMA-stimulated (activated) monocytes. Each i) intensity image, ii) fluorescence lifetime image, iii) pixel- →

based phasor plot; Scale bar indicates  $20\mu\text{m}$ . “#” marks the fluorescence lifetime of oxidized lipids as defined by e.g. (Datta et al. 2015). (Space-saving and RGB redesign of Fig 2 in (Leben et al. 2018).

#### 4.2. NADPH oxidase activation is localized in the phagosomes

Polymorpho-nuclear cells (PMNs) isolated from human peripheral blood were co-cultured with *S. aureus*-coated beads (pHrodo) and NAD(P)H-FLIM was recorded over 80 min. These beads are recognized and engulfed by the PMNs and the ROS production within the cells is activated. Since those beads are pH-sensitive, they become fluorescent (magenta in Fig. 19 (i)), when they are engulfed and indicate the location of the actual NOX2 activation.

PMNs freshly mixed with pHrodo beads show the basic enzymatic activity, whereas the fluorescence lifetime of NAD(P)H ranges mainly between approx. 1.5 ns and 2.5 ns (green in Fig. 19 (ii)), but during the time course the enzymatic activity shifts first toward higher fluorescence lifetimes as a result of the NOX2 activation and then towards very short lifetime of 0.45 ns (blue in Fig. 19 (ii)) indicating free NAD(P)H, which implicates with cell death. Whether the cell death after NOX2 activation is associated with NETosis (Brinkmann et al. 2004; Brinkmann and Zychlinsky 2012) or a general mechanism preceding pathways leading to cell death is unclear.

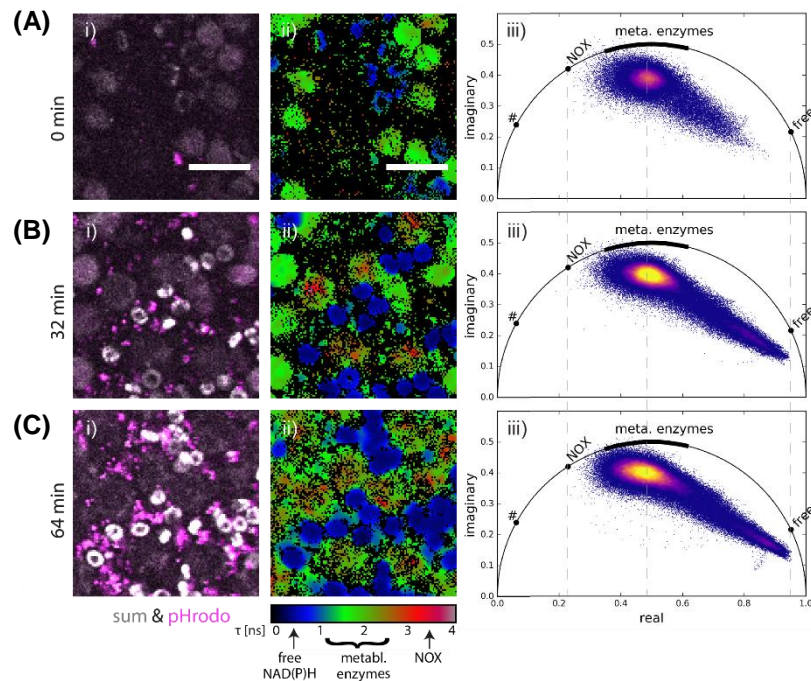


**Fig. 19: NAD(P)H-metabolism during phagocytosis.** Selected frames of time-lapse NAD(P)H-FLIM data of healthy human PMN phagocytosing *S. aureus* pHrodo™ beads. (A) 0 min, (B) 32 min, (C) 64 min after co-culturing. i) merged intensity images of NAD(P)H and pHrodo fluorescence, ii) FLIM images, iii) pixel-based phasor plots. Scale bar indicates  $20\mu\text{m}$ . “#” in all (iii) mark the fluorescence lifetime of oxidized →

---

lipids as defined by e.g. (Datta et al. 2015). (Space-saving and RGB redesign of Fig 3 in (Leben et al. 2018).

### 4.3. NADPH oxidase activation precedes NETosis

NETosis is distinguishable from other pathways of cellular death by the shape of the nucleus. During NETosis, in contrast to the other pathways the nucleus rounds up and almost fills the cell while the nuclear membrane disintegrates and ejects the DNA and granular contents into the surrounding area forming a NET. In order to identify the cellular death the DNA was stained by Vybrant DyeCycle Green™ which works in living cells due to its low cell toxicity. PMNs were co-cultured with (Fig. 20 A) and without (Fig. 20 B) *S. aureus* coated beads. The upper row of Fig. 20 A and B shows the cells immediately after co-culturing with the beads and the lower row 80 min or 60 min after. Both, Fig. 20 A and B have three columns. Each column (i) presents the intensity of the DNA-staining (green) and of NAD(P)H (gray), column (ii) the NAD(P)H-FLIM images and column (iii) the corresponding phasor plots. The intensity images of the cells 80 min after co-culturing with the bead shows the typical exploded nuclei indicating NETosis, which is co-localized with activated NOX2 in the FLIM images. The extent of activated NOX2, the red areas in the FLIM image, is much higher compared to the healthy, intact cells shortly after adding the beads (Fig. 20 AB a (ii)) or the dying cells with a large deformed nucleus (Fig. 20 B b (ii)). This is also evident in the phasor plots. 80 min after co-culturing with the bead, the plot shows a clear tendency toward the NOX position in contrast to the other. Under shear forces, the typical fibrous network of NETs are formed in co-cultured PMN and *S. aureus* coated beads, which become visible in the higher-contrast image of the DNA-stain (Fig. 20 C (ii)).

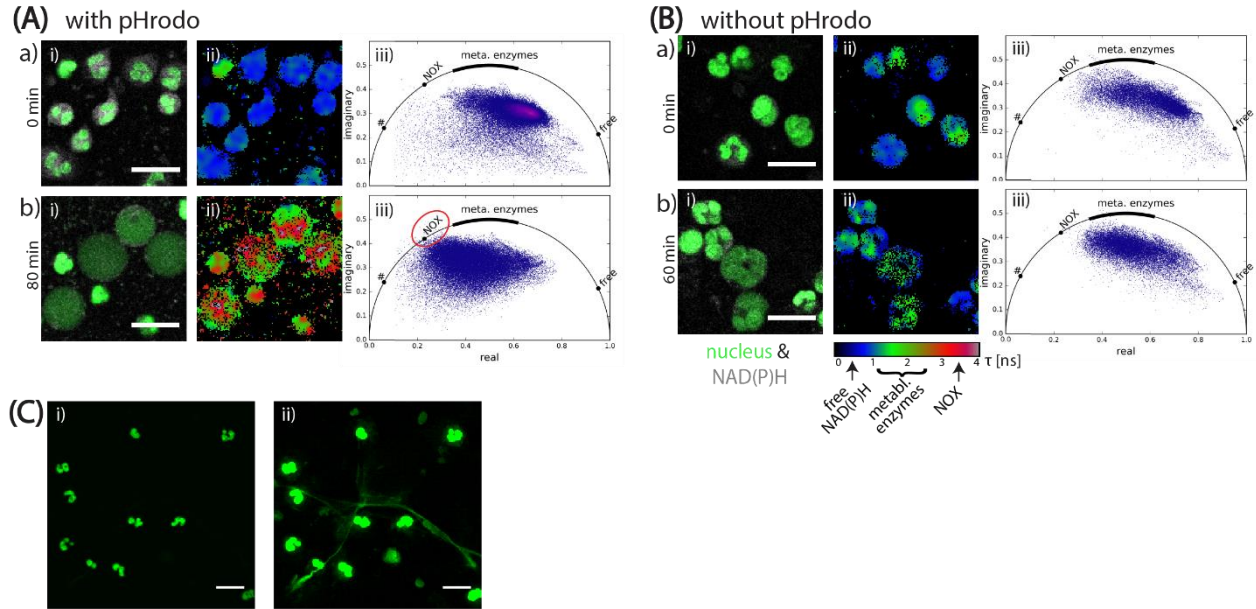


**Fig. 20: NET formation and cellular death.** Comparison of neutrophil metabolism in presence (A) and absence (B) of *S. aureus* pHrodo™ beads. Each a) cells immediately after and b) 80 min/60 min after co-culturing with beads. The columns (i) merged intensities of DNA stain (green) and NAD(P)H (gray), (ii) NAD(P)H FLIM, (iii) phasor plots, “#” mark the fluorescence lifetime of oxidized lipids as defined by (Datta et al. 2015). (C) Intensities of DNA stain after applying shear forces. (i) and (ii) is the same image, (ii) has a high-contrast adjustment. All scale bars indicate 20  $\mu\text{m}$ . (Space-saving and RGB redesign of Fig 5 in (Leben et al. 2018)).

#### 4.4. Unpublished data – “long-lifetime species” found in 3T3-L1 cell line

Phasor-analyzed NAD(P)H-FLIM was applied to 3T3-L1 cell line at day 5 of differentiation. 3T3-L1 is a mouse embryo cell line, which exhibits mesenchymal stromal cell-like properties and differentiate in adipocytes upon stimulation.

Here, pixels with long-lifetime species (LLS,  $\tau_{\text{LLS}} = 7.8 \text{ ns}$ ), as for instance shown by (Datta et al. 2015), were found in the lipid droplets of some cells in Fig. 21 i. They are represented as red spots in the FLIM image. The position of the LLS was marked as “#” on the semi-circle and the phasor cloud in the corresponding phasor plot points toward this position. This indicates that LLS are different from the NOX position. In addition, LLS in this amount was found in only one of three fields of view in the same cell culture Fig. 21.

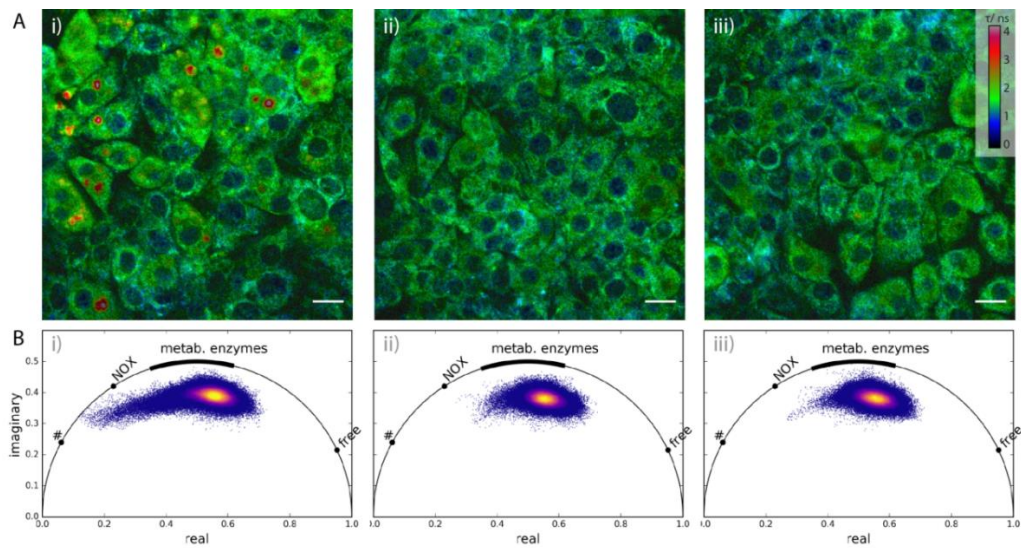


**Fig. 21:** *Phasor-analyzed NAD(P)H-FLIM of mouse embryo 3T3-L1 preadipocytes at day 5. (i) – (iii) Three fields of view in the same culture. (A) Thresholded and intensity-weighted FLIM images, 512 x 512 pixels covering 200 x 200  $\mu\text{m}^2$ , (B) corresponding phasor plots. Color bar in Aiii) applies to all 3 FLIM images (0-4 ns); scale bars in A indicate 20  $\mu\text{m}$ , “#” in B marks the fluorescence lifetime of oxidized lipids as defined by (Datta et al. 2015). (Unpublished data).*

## 5. Results – Leben, R., *et al.*, (2019)

This paragraph reviews the results published in the article Leben, R., Köhler, M., et al., *Systematic enzyme mapping of cellular metabolism by phasor-analyzed label-free NAD(P)H fluorescence lifetime imaging*, Int. J. Mol. Sci. 2019, 20(22), 5565.

The complete article can be found in Appendix A. Some passages could be identical in wording.

### 5.1. NAD(P)H-FLIM adequately determines fluorescence lifetimes using the phasor approach

FLIM data are convolved with shot noise, which is transferred to the phase domain and influences the position of the phasor. To improve interpretation of NAD(P)H-FLIM data the image and signal properties were defined by solutions of unbound NADH in different concentrations measured at fixed excitations power. The quality of the fluorescence signal was sufficient for FLIM with an SNR value above five. For varying the excitation power at fixed NADH concentration, the same result was found.

NADH-FLIM was used to measure the metabolic enzymes malate dehydrogenase (MDH) and lactate dehydrogenase (LDH) in different concentrations. Since the NADH:enzyme mixtures were homogenous solutions, their temporal decay curves were average over all pixels to smooth it and fitted bi-exponentially in time domain. The fit results in two fluorescence lifetimes:  $\tau_1$ , the unbound, free NADH has a lifetime of 450 ns and  $\tau_2$ , which is specific to the enzyme.  $\tau_2$  was transferred to the frequency domain to mark the semi-circle.

The lifetimes of MDH and LDH were double-checked using phasor-analyzed FLIM data. As the theory predicts, the phasor cloud migrates depending on the concentrations along the segment connecting the phasors of the lifetimes of the individual molecules. FX11 is a LDH inhibitor, its addition to the NADH:LDH solution results in a shift of the phasor cloud back to free NADH (Fig. 22).

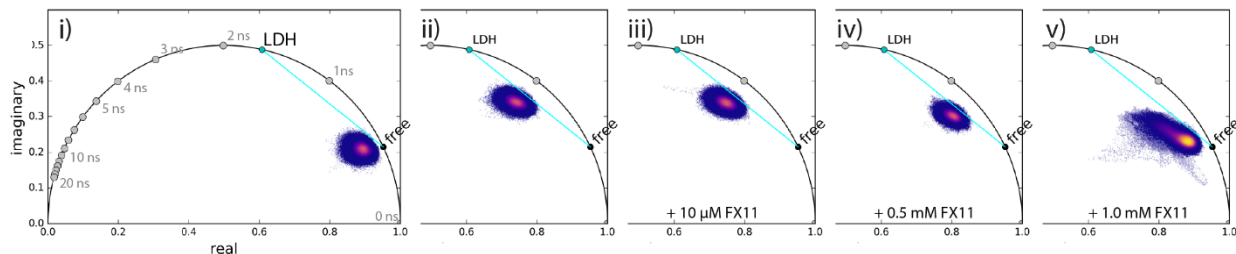


**Fig. 22:** *NADH, LDH, and FX11 solved in MOPS solution. (i) Only 50  $\mu\text{M}$  NADH; (ii) 50  $\mu\text{M}$  NADH and 10  $\mu\text{M}$  LDH; (iii) 50  $\mu\text{M}$  NADH, 10  $\mu\text{M}$  LDH, and 10  $\mu\text{M}$  FX11; (iv) 50  $\mu\text{M}$  NADH, 10  $\mu\text{M}$  LDH, and 0.5 mM FX11; (v) 50  $\mu\text{M}$  NADH, 10  $\mu\text{M}$  LDH, and 1.0 mM FX11. (Fig 1D in (Leben et al. 2019).*

## 5.2. The phasor approach enables an enzymes-based reference system

In order to allow interpretation of NAD(P)H-FLIM measurements a reference system was established. The metabolism of living cells and tissues is composed of approximately 350 NADH- and 300 NADPH-dependent enzymes. Using RNA-sequencing of mesenchymal stromal cells, the enzymes with the highest abundance were identified (unpublished data from colleagues). We measured their fluorescence lifetime when fully bound, as described in the previous paragraph.

In addition to MDH and LDH, glyceraldehyde-3-phosphate dehydrogenase (GAPDH) glucose-6-phosphate dehydrogenase (G6PDH), pyruvate dehydrogenase (PDH), alcohol dehydrogenase (ADH), C-terminal binding protein 1 (CTBP1), isocitrate dehydrogenase (IDH), hydroxyacyl-coenzyme-A dehydrogenase (HADH), sorbitol dehydrogenase (SDH) and inducible nitric oxide synthase (iNOS) were measured in solution as outlined in the previous paragraph. The only exception is the NADPH oxidase family (here NOX) whose fluorescence lifetime was determined intracellularly using chemical inhibition, activation and knock-out strategies (Leben et al. 2018; Niesner et al. 2008b). Complex I was excluded because its functionality could not be maintained in solution. All findings were listed (Fig. 23 B) and transferred into phase domain to benchmark the semi-circle (Fig. 23 A). This reference system was completed by previously published data (Fig. 23 C) (Mossakowski et al. 2015). The results for MDH and LDH were in agreement with result from other groups (Sharick et al. 2018). The fluorescence lifetime of free NADH  $\tau = (462 \pm 23)$  ps and NADPH  $\tau = (393 \pm 11)$  ps slightly differ, but are nevertheless mentioned below as "free NAD(P)H" to simplify the frame. For NADH bound to PDH and bound to CTBP1 a similar fluorescence lifetime of  $\tau_{\text{PDH}} = (2474 \pm 43)$  ps and  $\tau_{\text{CTBP1}} = (2472 \pm 49)$  ps was found. Their position in the phasor plot is marked as "NADH bound to PDH/CTBP1".

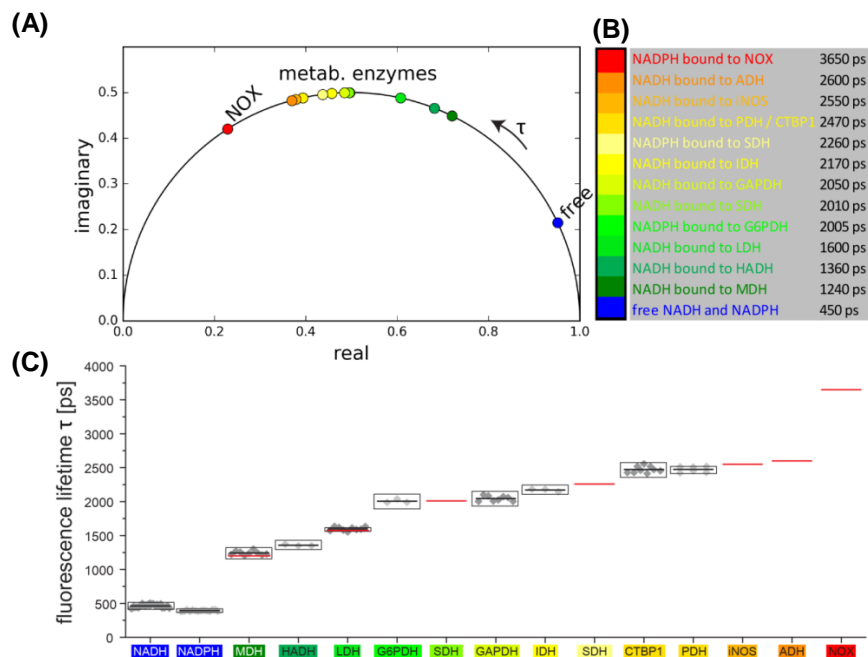


**Fig. 23:** Reference system of NAD(P)H fluorescence lifetimes and phase vectors in the free and enzyme-bound state. (A) Phasor plot with marked positions of the enzymes, (B) List of measured fluorescence lifetimes  $\tau_2$  of NADH or NADPH fully bound to enzymes. (C) Fluorescence lifetimes calculated from single images represented as gray dots, average values as black lines, standard error of the mean (s.e.m.) values over all pixels in all measured images per coenzyme/enzyme mixture as black boxes. The list was completed by our previously measured fluorescence lifetimes (Mossakowski et al. 2015). The color coding in (A) – (C) is consistent. (Fig 2 in (Leben et al. 2019)).

### 5.3. Assigning NAD(P)H-FLIM data to the metabolic enzymes: A systematic analysis framework

Based on the findings of the previous paragraph a systematic framework to analyze and interpret NAD(P)H-FLIM data was created. A time-domain data point was transferred to the phase domain when imaging criteria found in section 5.1 were met. The phasor was only considered when it falls within the semi-circle. Based on the phasor-analyzed FLIM-data of pure NADH in MOPS-solution, a radius around this phasor cloud was defined as metabolically inactive “free NAD(P)H” (suppl. Fig. 4 in (Leben et al. 2019)).

For data points outside that radius (violet dot, Fig. 24) the angles between the vector connecting the mean of measured free NADH and the data point  $\alpha_{data}$  (violet dash line in Fig. 24 B ii) and the vector connecting the mean of measured free NADH and every enzyme in the reference

system  $\alpha_i$  (dark green solid line in Fig. 24 ii)) were calculated and their similarities  $q_i$  were determined by (Eq. 28) :

$$q_i = \left| \frac{\alpha_{data}}{\alpha_i} - 1 \right| \quad (\text{Eq. 28})$$

The angle similarities  $q_i$  were normalized for all enzymes in each pixel to obtain the weights  $w_i$  of the angle similarities  $q_i$  as follows:

$$w_i = \frac{1}{q_i \sum \frac{1}{q_i}} \quad (\text{Eq. 29})$$

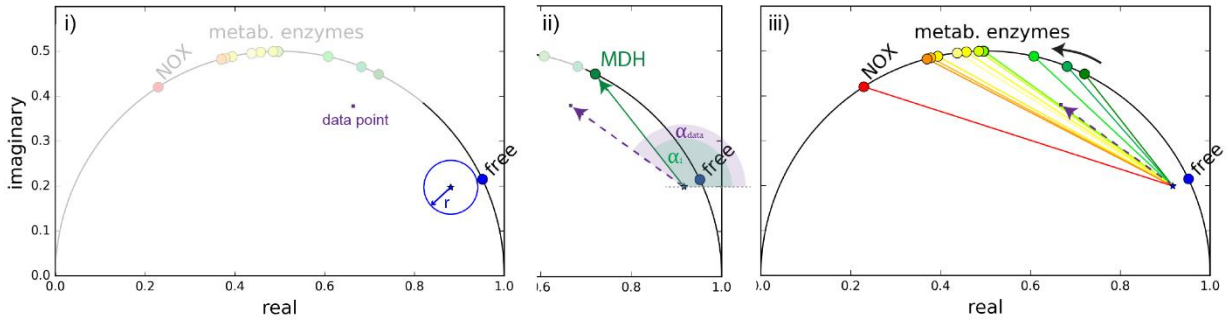


**Fig. 24:** *Systematic analysis framework of NAD(P)H-FLIM data. (i) Radius surrounding the pixels that are assumed to represent free NAD(P)H, (ii) Angle similarity of the vectors free NAD(P)H to data point (violet dashed) and free NAD(P)H to NADH bound to MDH, (iii) Applied to all measured enzyme-bound NAD(P)H lifetimes. (Fig 3A in (Leben et al. 2019)).*

The equation (Eq. 29) is a quality measure of enzyme assignment. A data point was assigned to that enzyme for which the result of (Eq. 29) reaches its maximum, i.e. the angle between the vectors is minimal. In the case of the data point shown in Fig. 24 the assigned enzyme was SDH (light green solid line, Fig. 24 iii)).

#### 5.4. Validation on homogeneous NAD(P)H-enzyme mixtures

To validate the analysis framework FLIM data from homogenous solutions of free NADH, NADH:MDH and NADH:PDH used. Of all pixels 99.9% were correctly assigned in the free NADH solution and 97.7% were correctly assigned in the MDH mixture. In these two images the SNR

was very good. In contrast 37.4% of the data points are assigned to ADH, 35.1% to iNOS and only 17.4% to PDH/CTBP1 in a PDH mixture. First, the SNR was in that case lower than in the previous examples (approx. only the half), which also becomes evident from the board phasor cloud of the PDH mixture. Second, the weak enzyme assignment is due to the high similarity of those lifetimes. In such a case the expression level of these enzymes and their subcellular distribution need to be taken into account.

Additionally to the angle between the above mentioned vectors to assign the data points to enzymes, the ratio of vectors length was used to map the activity of the enzymes in cells, which indicates the cellular vitality. Data points which are rather in the direction of free NAD(P)H, but are not inside the “free”-radius, reveal a low enzyme activity.

The data can be found in Figure 3 in of the original publication.

### **5.5. Systematic analysis is suitable in stromal-like 3T3-L1 cells**

In order to use the analysis framework to cellular metabolism, it was applied to NAD(P)H-FLIM data of 3T3-L1 cells. 3T3-L1 is a cell line, which exhibits mesenchymal stromal cell-like properties and can be differentiated in adipocytes upon stimulation.

Considering the above mentioned imaging criteria the SNR in these images were in a reliable range. The SNR ranged between  $28 \pm 6$  (mean  $\pm$  SD) in nuclei and  $48 \pm 16$  in cytoplasm, however it should be mentioned that these values could only be reached by adding up five sequentially acquired TCSPC raw image stacks, because the NAD(P)H fluorescence is weak in cells and excitation intensity is limited by photodamage. Similar metabolic activity was observed in the activity map Fig. 25 (B ii), meaning that the majority of NAD(P)H molecules were bound to metabolic enzymes. This indicates that the overall cellular vitality was roughly equal and cell death or damage can be excluded. In the activity map, no significant difference between nuclei and cytoplasm was observed. In contrast, the enzyme assignment maps (Fig. 25 (B iii)) show major differences between those subcellular structures. In the cytoplasm, a high predominance of PDH, iNOS and ADH was found, i.g. metabolic enzymes with rather long fluorescence lifetimes. In the nuclei, mainly G6PDH was identified, but the probabilities of enzyme assignment to LDH, SDH and GAPDH were at a similar level (Fig. 4 D ii) in (Leben et al. 2019)).



The cells 3 to 5 are examples of cells with a basic metabolism. All of them show the same enzyme assignment and activity. They do not have activated NOX, like cell 1, nor show an altered enzyme composition, like cell 2.

The NAD(P)H-FLIM images show a second cell population whose fluorescence lifetime is very short and which was therefore assumed to be metabolically rather inactive or even dead. However, among the cells showing an inactive metabolic state in the FLIM images are single cells, whose enzyme assignment differs from this. For example, all pixels of cell 6 in the enzyme map are assigned to activated NOX (red), rather than to free NAD(P)H as expected from the FLIM image, while its enzymatic activity is very low, less than 25%.

In contrast to that, the pixels of most of the cells with a very short fluorescence lifetime are assigned to free NAD(P)H as expected from the FLIM image, like cell 7. Interestingly all of these cells show a ring, whose pixels are assigned to active NOX.

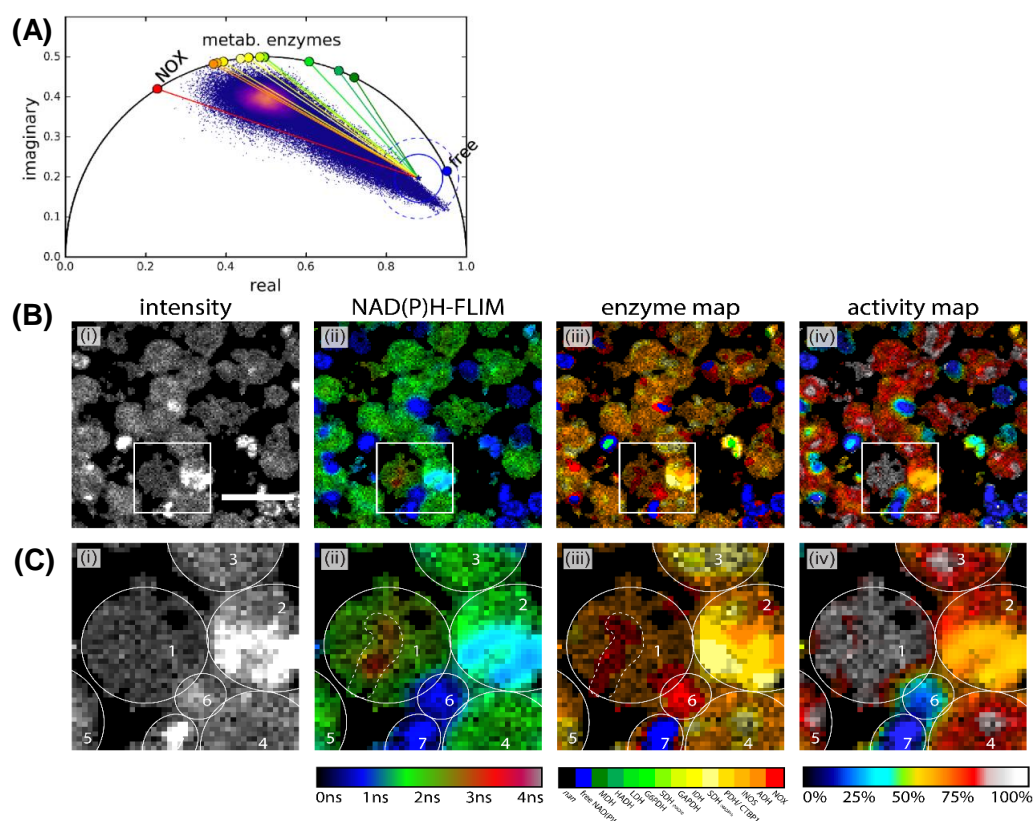


**Fig. 26:** *NAD(P)H-metabolism of healthy human neutrophils during phagocytosing S. aureus pHrodo™ after 20 min of co-culturing. (A) Phasor plot with free-to-enzyme vectors, (B) 125x125 μm<sup>2</sup> ROI, (i) NAD(P)H intensity, (ii) NAD(P)H-FLIM, (iii) enzyme map, (iv) activity map. All images/maps are intensity-weighted and background-thresholded (pixels with SNR<15 were excluded). (C) 21x21 μm<sup>2</sup> magnified ROI marked in (B). Scale bar indicates 20 μm. (Unpublished data)*

## 6. Results – Ulbricht, C. *et al.*, (2021)

This paragraph reviews the results I have been involved in and which will be published in the article Ulbricht, C., et al., *Intravital quantification reveals dynamic calcium concentration changes across B cell differentiation stages*, *Elife* 10 (2021): e56020.

The complete article can be found in Appendix A. Some passages could be identical in wording.

In close collaboration with Dr. Carolin Ulbricht and Prof. Dr. Anja Hauser, I further developed the donor FRET-FLIM method for intravital use to monitor calcium signaling in B cells during germinal center reactions.

### 6.1. Fluctuating calcium levels are observed *in vivo*

After the first *in vitro* experiments on functionality, gene expression and BCR stimulability of isolated B cells of YellowCaB mice, these cells were imaged *in vivo* in the germinal center of the popliteal lymph node to study the ability of the B cells to collect calcium signals and to identify the spatial distribution of possible BCR initiation.

Ratiometric analyzing the FRET signal showed time-dependent fluctuations of the signal, indicating fluctuating calcium concentrations in the B cells and, in particular cases, a sustained increase after prolonged contacts between two YellowCaB cells (Fig. 3b and movie S1 of (Ulbricht et al. 2021)). This might coincide with cell-to-cell contacts between follicular dendritic cells (FDC) and B cells during antigen-dependent BCR stimulation, and could be confirmed by colocalization and cell tracking analysis of the FRET signal and the staining signal of FDC.

In order to investigate whether the performed BCR signaling is dependent on BCR affinity, stained polyclonal, non-AG-specific YellowCaB cell were transferred to the mouse one day prior to intravital imaging. It turned out, that the non-AG-specific YellowCaB cells show a rather homogenous distribution of calcium concentration with low intensity fluctuations in the FRET signal. In contrast to that the AG-specific Yellow CaB cell showed heterogeneous signaling pattern with higher FRET intensities, presumably related to the diverse BCR activation levels in germinal centers.

## 6.2. Phasor-analyzed donor FRET-FLIM to calculate absolute cellular $\text{Ca}^{2+}$ concentration

The ratiometric FRET analysis is based on the comparison of normalized donor and acceptor intensities. Varying imaging depth permits only relative information about calcium concentrations due to depth-depending noise levels in the tissue. But universal statements on the calcium levels among different B cell populations demand absolute quantifications.

To avoid the obstacles of an intensity-based FRET measurement, the imaging setup was adapted to the measurement of the fluorescence lifetime of the FRET donor eCFP. The method of donor FRET-FLIM does not require taking into account the wavelength-dependent sensitivity of the detectors or different photobleaching or scattering properties of the two fluorophores in the tissue, since only one of the two FRET fluorophores is observed.

In presents of calcium the eCFP of the TN-XXL construct transfers its energy non-radiatively to the acceptor citrine and the eCFP fluorescence lifetime is quenched ( $\tau_{\text{quen}} = 0.7$  ns), much shorter than of the unquenched eCFP ( $\tau_{\text{unquen}} = 2.3$  ns). In the phasor approach, these two extremes are located on the semi-circle (Fig. 27) and all intermediate states are on the segment connecting them. The exact position on this segment (magenta dot in Fig. 27) depends on the ratio of quenched and unquenched eCFP molecules in the excitation volume, thus on the calcium concentration.

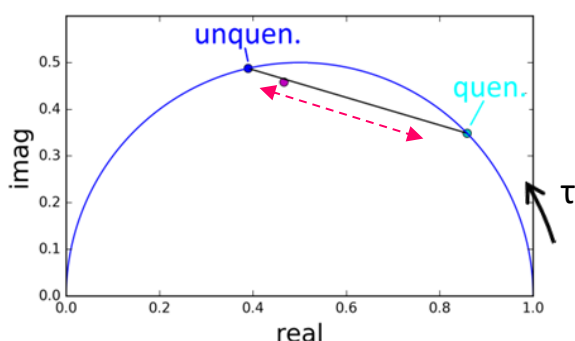


**Fig. 27:** *Phasor approach to analyze donor FRET-FLIM of the TN-XXL construct.* “Unquen.” marks the position of the fluorescence lifetime of unquenched eCFP, “quen.” marks the position of the fluorescence lifetime of quenched eCFP.

This position on the connecting segment was converted into an absolute  $\text{Ca}^{2+}$  concentration (Geiger et al. 2012) using (Eq. 17) in section 1.4. The linear range of the TN-XXL titration curve was determined to be 265 nM – 857 nM (Geiger et al. 2012). All values below or above these margins are subject to uncertainty and therefore simply referred to as  $\leq 265$  nM or  $\geq 875$  nM,

respectively. By calculating the concentration for each pixel in a FRET-donor FLIM image, a  $\text{Ca}^{2+}$  concentration map can be created.

### 6.3. *In vivo* donor FRET-FLIM of cytoplasmic TN-XXL construct in YellowCaB cells

In order to observe cell-to-cell contact between naïve and antigen specific YellowCaB cells and their  $\text{Ca}^{2+}$  signaling during BCR activation germinal center of the lymph node were imaged. In this experiment, the cell-cell communication was focused and five different cell populations were identified based on their location and their fluorescence appearance:

- Naïve B cells (red staining) found
  - inside (“naïve in”) and
  - outside (“naïve out”) the B cell follicle
- Antigen-specific B cells (green staining)
  - clustered in the germinal center close to the FDCs (“AG-speci in”) and
  - outside the GC boundaries (“AG-speci out”)
- Bigger, ellipsoid-shaped ones in the extra-follicular medullary cords (MC), probably comprising plasma blasts (“PB”)

The cells of these five populations were segmented using the software Imaris (Bitplane, Zurich, Switzerland) to generate a cell-based phasor plot instead of a pixel-based one. The phasor positions are averages of pixels within a segmented cell, excluding “black” pixels that do not contain a FLIM-signal and were set to “NaN” (“not a number”) a non-numerical place holder in the matrix of the image.

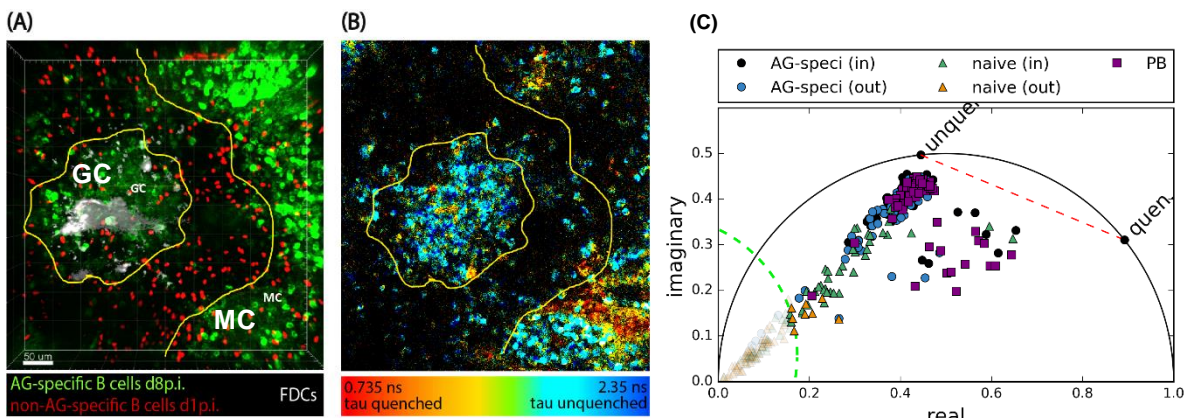


**Fig. 28:** Still frame of a 60-minute 3D *in vivo* imaging of YellowCaB cells in the lymph node, including the germinal center (GC) and the medullary cords (MC) (A) →

Merged intensity images of the stained naïve (red), AG-specific B cells (green) and FDC (white), **(B)** donor FRET-FLIM (intensity weighted), (Fig 5 in (Ulbricht et al. 2021)) **(C)** cell-based phasor plot with noise exclusion radius (green dashed), labeling as outlines in main text (unpublished). Scale bar indicates 50  $\mu\text{m}$ .

Due to scattering in the tissue, the FLIM-signal of the donor is shifted towards the origin in the phasor plot, indicating a high contribution of noise in *in vivo* FRET-FLIM measurements. The phase vectors are shortened and end within a triangle between the origin, 2.3 ns and 0.7 ns. The noise was therefore considered as a contribution of a third exponential component and the FRET-FLIM data were further processed to take this into account. In a non-fluorescent medium, a noisy FLIM-signal was measured under similar experimental conditions as those used in the intravital experiments. In the phase domain the histograms of real and imaginary part were Gaussian fitted, giving a mean, which indicates the center of the noise distribution. This is slightly shifted from origin due to the logarithmic nature of the universal circle. The Gaussian fit also gives the width of the noise distribution ( $FWHM = 2\sqrt{2\ln 2}\sigma$ ), which was the same for both real and imaginary parts and gives the radius  $\frac{1}{2}FWHM = 0.2$  (green, solid arc in Fig. 29) within which only noise is expected, meaning the signal-to-noise-ratio is unreliable small. In order to increase accuracy, the radius was enlarged to  $\frac{3}{4}FWHM = 0.3$  (green, dashed arc in Fig. 29) and all data points within that radius were excluded from further analysis.

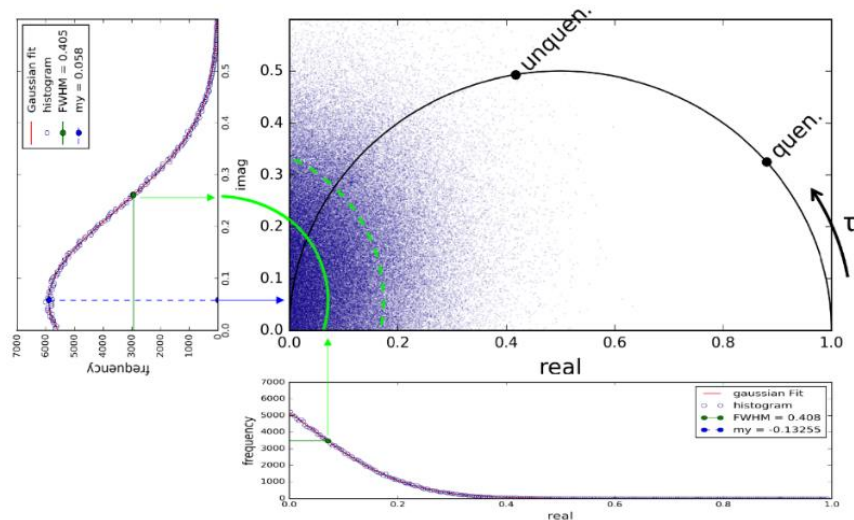


**Fig. 29: Determination of the noise exclusion radius (green) for phasor analysis. (Unpublished).**

In order to account for background, a second filtering was applied by determining the signal-to-noise ratio (SNR) from the summed TCSPC signal for all segmented cells. In Imaris, a sphere of radius = 20  $\mu\text{m}$  was determined around each cell to establish a reference value for background noise. The SNR was then calculated as follows:

$$\frac{I_{sig} - I_{BG}}{std_{BG}} \quad (\text{Eq. 30})$$

$I_{sig}$  ... intensity of TCSPC signal  
 $I_{BG}$  ... intensity of background noise  
 $std_{BG}$  ... standard deviation of background noise

AG specific signals with  $\text{SNR} < 2$  and non-Ag specific signals with  $\text{SNR} < 1$  were excluded from the analysis. All other phasor data points were projected on the segment connecting FRET-quenched and unquenched eCFP fluorescence lifetimes (Fig. 30 (A)) to calculate the absolute  $\text{Ca}^{2+}$  concentration by (Eq. 17) and thus gives a temporal time track of the  $\text{Ca}^{2+}$  concentration in single cells.

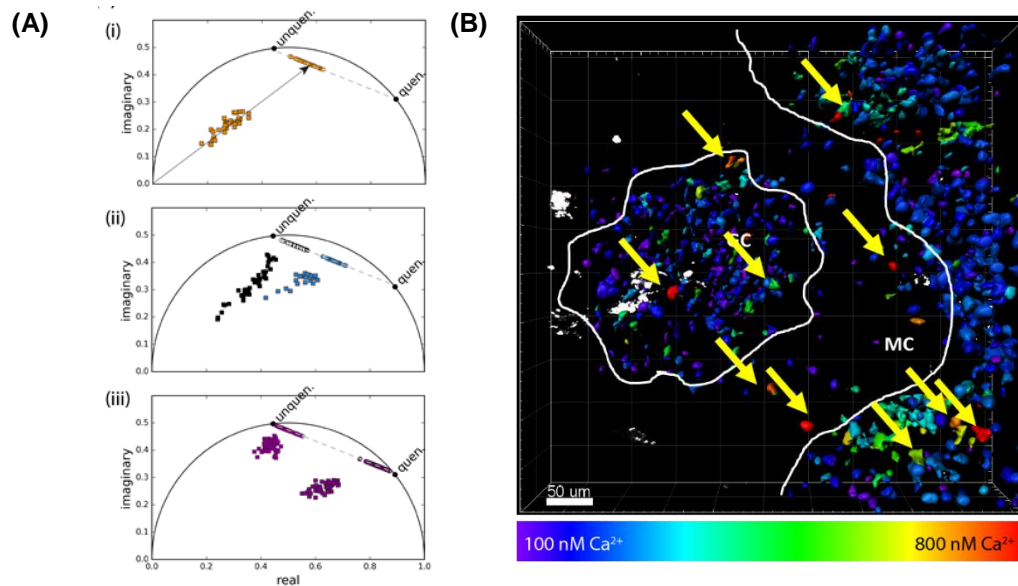


**Fig. 30: Determination of the absolute  $\text{Ca}^{2+}$  concentration.** (A) Phase vector projections of single B cells over time onto FRET segment under consideration of background noise (i) naïve B cell, (ii) two AG-specific B cells, (iii) two plasma blasts (unpublished). (B) 3D representation of  $\text{Ca}^{2+}$  concentration map, scale bar indicates 50  $\mu\text{m}$ . Arrows indicate cells with high  $\text{Ca}^{2+}$  concentration (Fig 5 in (Ulbricht et al. 2021)).

#### 6.4. Absolute quantification of cytoplasmic $\text{Ca}^{2+}$ reveals activation-dependent calcium heterogeneity in B cells

The color-coded 3D representation of the data over time (snapshot is shown in Fig. 30 (B)) reveal that the  $\text{Ca}^{2+}$  concentration is fluctuating within all B cell populations. Most B cells maintain a relatively low  $\text{Ca}^{2+}$  concentration (blue), with the exceptions of individual cells (red, Fig. 30 (B), arrows). The comparison between the different B cell populations suggests that the distribution of  $\text{Ca}^{2+}$  concentration depends on the BCR specificity and not on their location in the field of view, meaning in- or outside the germinal center or in the medullary cords, despite higher fluctuation are seen among AG-specific populations.

#### 6.5. Unpublished data – High dynamics of $\text{Ca}^{2+}$ signaling between B cells

Fig. 31 A shows a  $35 \times 35 \mu\text{m}^2$  detail of an about 30 minute FRET-FLIM sequence that illustrates the high dynamics of  $\text{Ca}^{2+}$  signaling between B cells. It was found between three AG-specific cells, evident by the green staining (Fig. 31 B (ii)), in the medullary cords. The nomenclatures “cell 1”, “cell 2” and “cell 3” refer to the circular markings in Fig. 31 B (i). The plot in Fig. 31 C shows the  $\text{Ca}^{2+}$  concentration in [nM] versus the time in [min] of the sequence, the period of assumed cell contact was marked in gray. The  $\text{Ca}^{2+}$  concentration of these three cell is very different. It ranges between the very low  $< 300$  nM (cell 3) to very high  $> 700$  nM, (cell 2) and changes during direct cell contact.

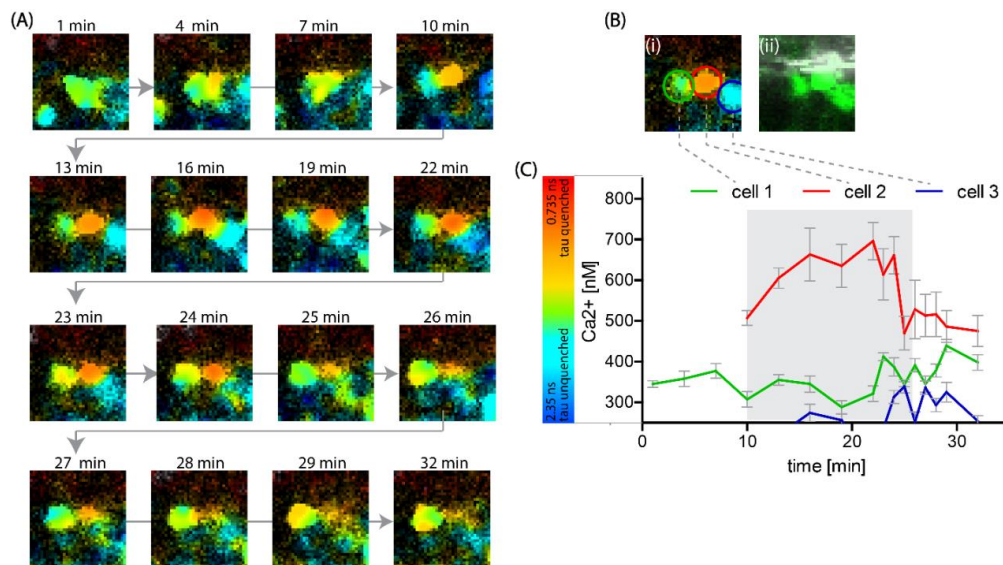


**Fig. 31:** *In vivo  $\text{Ca}^{2+}$ -dependent B cell signaling in the lymph node of YellowCaB mice (here in the medullary cord). (A)  $35 \times 35 \mu\text{m}^2$  stills of a 32 min sequence of the →*

donor FRET-FLIM shown in supplementary video 3 in (Ulbricht et al. 2021). **(B)** Still at 13 min (i) FLIM image marking the cell 1 (green), cell 2 (red) and cell 3 (blue), (ii) corresponding antigen staining indicating the AG-specific B cell (green), collagen is shown in white. **(C)**  $\text{Ca}^{2+}$  concentration in [nM] versus the time in [min] of the sequence, the period of direct cell contact was marked in gray. Color bar on the y-axis gives the color coding of donor FRET-FLIM data in (A) and (B) (unpublished).

## 7. Discussion

The fluorescence lifetime is exquisitely sensitive to the local chemical environment of the fluorescent molecule. Besides spatial and temporal resolution (xyzt) and identification of cell types or cell organelles by staining, FLIM provides an additional dimension to fluorescence images and therefore opens new perspectives for the analysis of pathophysiological processes both *in vitro* and *in vivo*. NAD(P)H is a powerful endogenous probe to study the energy metabolism of cells and tissues and give insights in the underlying functions of cells and tissues. NAD(P)H-FLIM is used to investigate metabolic changes for instance in cancer cells. While the technical environment was highly improved during the last years, its application in the broad field of biomedical researches was hindered by the lack of numerically robust analysis methods. Reliable exponential fitting methods were missing when the number of exponents in a biological sample is unknown. E. Gratton and his coworkers were able to circumvent this by translating time-domain FLIM data to a normalized, virtual phase domain, the so-called phasor analysis, a graphical representation of the FLIM data (Digman et al. 2008). Nevertheless, the phasor representation only transferred the problem of unknown exponents to the interpretation. More than 370 NAD(P)H dependent enzymes are known to be involved in the cellular metabolism, which complicates a valid data interpretation. This was the starting point of the present thesis.

### 7.1. Performance of the measurement system and steady-state analysis

First of all, TCSPC-based FLIM and state of the art mono-exponential FLIM data analysis was established (Bremer et al. 2017) and the phasor analysis to time-domain TCSPC-acquired FLIM data was coded in python programming language (see Appendix B). Both the time-domain measurement setup as well as the phasor analysis were validated by fluorophores with well-known fluorescence lifetimes. For instance, the lifetime of the green fluorescent protein (eGFP) expressed in the cytosol of human embryonic kidney cell line (HEK-293T) was studied (Fig. 17 (B)). The resulting fluorescence lifetime  $\tau_{\text{measured}} = (2.5 \pm 0.1) \text{ ns}$  was in good agreement with values found in the literature  $\tau_{\text{lit}} = 2.46 \text{ ns}$  (Hess et al. 2003) or  $2.62 \text{ ns}$  (York et al. 2019). Since eGFP was by far the brightest fluorophore species in the sample, its photon arrival histogram was mono-exponential and its phasor cloud laid, as expected, directly on the semi-circle, which represents all possible values of mono-exponential lifetimes. Furthermore, the SHG in KDP powder (Fig. 17 (A)) and electronic noise in a non-fluorescent medium (Fig. 17 (C)), respectively, were

measured to explore the extreme phasor positions. The underlying photonic process of SHG is no spontaneous emission of light but optically non-linear transformation (frequency-doubling) of the impinging laser radiation, thus its emission lifetime is infinitely short and the position of its phasor cloud is theoretically at (1|0). The experimental data cloud is slightly elevated from that position due to delay effects in the detection electronics, which spread the instrument response function to a narrow Gaussian-like shape (FWHM=250.8 ps). Back-transferring those IRF data into time domain results into an average lifetime of  $(0.084 \pm 0.015)$  ns, which is therefore the shortest resolvable lifetime of our system, and represents mainly the effect of electronic jitter. In contrast to that, the pure Poisson-distributed electronic noise (the noise of background), is the sum of undamped oscillations of various frequencies and has therefore an infinitely long lifetime. Its phasor position is at the very opposite side of the semi-circle at the origin of coordinates. The experimental data clouds in the phasor plot of SHG and electronic noise as well as of eGFP were at the exact expected positions, making additional position corrections, as suggested by (Ranjit et al. 2018), obsolete.

## 7.2. NAD(P)H as fluorescent endogenous bio-marker

The probability of a two-photon absorption process of a fluorescent molecule is given by the two-photon action cross-section  $\Phi_F \sigma_{2PE}$ , the product of the fluorescence quantum yield  $\Phi_F$  and the absolute two-photon absorption cross-section  $\sigma_{2PE}$  (Zipfel et al. 2003). In contrast to synthetic dyes or gene-encoded fluorescent proteins, the two-photon action cross-section of the intrinsic co-enzymes NAD(P)H is with  $\Phi_F \sigma_{2PE}(760 \text{ nm}) \leq 0.01 \text{ GM}$  (Huang et al. 2002) comparatively low in contrast to such as eGFP with  $\Phi_F \sigma_{eGFP}(760 \text{ nm}) \approx 15 \text{ GM}$  (Zipfel et al. 2003),  $1 \text{ GM} = 10^{-50} \text{ cm}^4 \text{ s}$ . Therefore, it is more difficult to measure NAD(P)H-FLIM, because it is much more sensitive to interfering effects, like electronic noise, background photons from the sample itself or even bleed-through photons of neighboring emission channels, if cell organelles were stained. It is known from former investigations of several groups, that the fluorescence lifetime NAD(P)H bound to a metabolic enzyme reaches from approx. 1.5 ns to 2.5 ns (Blacker et al. 2014; Niesner et al. 2008b; Niesner et al. 2004; Sharick et al. 2018; Skala et al. 2007b; Skala et al. 2007a; Bird et al. 2005; Schneckenburger and Koenig 1992; Lakowicz et al. 1992b). This is represented by the bold segment in the phasor plots in (Leben et al. 2018). In order to establish NAD(P)H-FLIM to biomedical applications to study NAD(P)H-dependent cellular metabolism, first the well-characterized NOX2 was investigated as discussed in (Leben et al. 2018). NOX2 is the main

catalyzer of the oxidative burst in monocytes/macrophages as well as neutrophils, responsible for defending the organism against invasive pathogens (Bedard and Krause 2007). The phagocyte NADPH oxidase (NOX2) is the first identified member of the NOX family and the best studied one (Bedard and Krause 2007). Isolated healthy human monocytes were stimulated by PMA and showed in contrast to unstimulated ones an increase in the fluorescence lifetime from  $\tau_{\text{enzyme}} \approx 2.0 \text{ ns}$ , the normal metabolic state, to  $\tau_{\text{NOX}} = 3.65 \text{ ns}$ , indicating the activation of NOX2. This is evident in the color change from green to red in some of the cells as well as by the second, separated “pixel population” of the phasor cloud in the corresponding phasor plot. The fluorescence lifetime of NADPH bound to activate NOX enzymes has been published in previous articles (Niesner et al. 2008b; Mossakowski et al. 2015) and was hereby confirmed. In addition, this showed that NAD(P)H-FLIM can be adequately acquired by the imaging setup and analysis program used.

### **7.3. NAD(P)H-FLIM in phagocytosing neutrophils**

The time-lapsed acquisition of NAD(P)H-FLIM in neutrophils phagocytosing pH-sensitive *Staphylococcus aureus* pHrodo™ beads reveals the spatiotemporal correlation of NADPH oxidase activation and NET formation. The corresponding phasor plots show that, over time, the phasor cloud reaches from the basic metabolic state in the beginning towards the expected NOX-activation position and then to the position of free (unbound) NAD(P)H. Free NAD(P)H is associated with metabolic inactivity and thus cellular death (Niesner et al. 2008b). The corresponding FLIM images support the observations in the phasor plots. There false colors change over time from green (basic metabolic state) towards red (NOX activation) and finally dark blue (free NAD(P)H) while the intensity of the pH sensitive beads increases in the red detection channel (593/40 nm). The pHrodo beads become fluorescent when their environment becomes more acid, i.e. the beads were taken up by the neutrophils. They start their “first order” cellular defense program, meaning they activate NOX in order to generate reactive oxygen species (ROS) within the phagosomes containing pathogens (Bedard and Krause 2007).

If the pathogens outnumber the PMNs, this “first order” defense program is followed by a “second order” defense, the programmed cell death pathway NETosis (Brinkmann et al. 2004; Brinkmann and Zychlinsky 2012). By forming neutrophil extracellular traps from their DNA and the contents of their granules, neutrophils are able to capture and even kill pathogens extracellularly until more phagocytic cells e.g. macrophages can immigrate from other regions of the tissue or from other

organs and destroy the trapped pathogens (Bratton and Henson 2011). The formation of the NET after NOX activation was confirmed by staining the DNA of the neutrophils with Vybrant DyeCycle Green™, a live cell nuclear staining, to monitor the shape of the nucleus. It is known that in contrast to other cellular death pathways, in NETosis the nuclei expand and lose their characteristic multilobar shape before NETs are formed (Brinkmann and Zychlinsky 2007). After 80 min of co-culturing the DNA-stained PNMs with pHrodo™ beads, both the color map of FLIM and the phasor plots show activation of NADPH oxidase while the Vybrant DyeCycle images show evidence of NET formation. In contrast, in absence of pHrodo beads the neutrophils show after 60 min neither hints of NOX activation the FLIM images and phasor plots respectively nor NET formation in the Vybrant DyeCycle images, although the cell viability was altered as evident from the irregular nuclear shapes. The smear of the phasor cloud of DNA-stained resting neutrophils in both experiments may result from either the green photons of the DNA-stain leaking into the NAD(P)H channel or the DNA-stain as a unnatural intervention influencing the cellular metabolism. This phenomenon was not further investigate due to the still prominent change of NAD(P)H fluorescence lifetime in activated cells in presents of the beads compared to the resting ones.

#### **7.4. NAD(P)H bound to NOX and “long-lifetime species” as indicators of oxidative burst/ stress**

However, when interpreting FLIM data, it is important not only to look at the fluorescence lifetime images alone, but always in connection with the corresponding phasor plots. The phasor-analyzed FLIM images show only the mean lifetime in each pixel, but the complexity of the composition of several lifetimes involved is only reflected by the phasor plots. The FLIM image of mouse embryo 3T3-L1 preadipocytes at day 5 of differentiation shows areas represented in red. This may erroneously be interpreted as activated NOX, because all pixels with a fluorescence lifetime less than 3 ns are shown in red when the color scale is set to 0–4.0 ns. The shoulder of the data cloud in the corresponding phasor plot points towards higher fluorescence lifetimes than 3.6 ns of activated NOX and reveals that these pixels are not related to NOX activation. Furthermore 3T3-L1 preadipocytes at day 5 are not known to highly express any member of the NOX family, thus an over-activation of these enzymes is not expected.

The fluorescence lifetime of the “long-lifetime species” (LLS) is  $\tau_{LLS} = 7.8$  ns and was introduced by the Gratton Lab as biomarkers of oxidative stress (Stringari et al. 2012; Datta et al. 2015; Datta et

al. 2016). LLS do not origin from NAD(P)H but are emitted by oxidized lipids, although they are observed by the same imaging setting as NAD(P)H-FLIM ( $\lambda_{\text{ex}} = 460 \text{ nm}$ , Ch466/40). The oxidation of poly-unsaturated fatty acids in lipids (lipid peroxidation) is one among several harmful effects that free radicals, what ROS are part of, may have on lipids. Stringari *et al.* presumed an increased energy metabolism in the mitochondria as the source of ROS leading to the appearance of LLS, but did not prove it. Datta *et al.* showed that the lipids in the cells are the source of LLS. As shown in Fig. 21 (Ai), the LLS are also observable in mouse embryo 3T3-L1 preadipocytes at day 5 of differentiation, when these cells start to form small lipid droplets. Here LLS appeared in areas associated with these lipid droplets, but LLS was detected only once out of three fields of view (FOV) in the same cell culture. We assume that the cells in this FOV were exposed to laser excitation for too long and their lipids were oxidized by photothermal effects that were not further clarified. There is no physiological reason why cells in one FOV are exposed to oxidative stress while they are not in other FOVs.

The oxidation of lipids is an effect of free radicals and not its production, thus the ROS origin and its underlying functional benefit is to our opinion not clarified by LLS. Here it was shown that LLS formation is not exclusively associated by a metabolic shift causing oxidative stress but may as well be induced by other factors, such as overheat. If the radicals that oxidize lipids are actually generated by ROS, LLS and NOX fluorescence lifetimes indicate the same phenomenon but on different molecular scales. In case of LLS fluorescence lifetimes, it detects the pathologic presents of ROS resulting in oxidative stress which starts in the chain reaction of lipid peroxidation. In contrast the NOX fluorescence lifetimes evidences the oxidative burst, meaning the physiological production of ROS as controlled cellular defense. Since the LLS was never detected in stimulated, ROS producing monocytes or neutrophils and can be generated by other effects, we decided to not follow this reasoning.

### **7.5. Individual lifetimes of enzyme-bound NAD(P)H**

Besides the activation of NOX, NAD(P)H is involved in a series of other pathways such as glycolysis or oxidative phosphorylation (OxPhos). When NAD(P)H binds to a metabolic enzyme, the molecular structure of the assembled enzyme compartment changes and with it the energetic levels, thus their fluorescence lifetimes. The composition of the complex distribution of NAD(P)H-dependent enzymes in cells continuously changes over time, making a thorough interpretation of NAD(P)H-FLIM results difficult (Leben et al. 2019). Especially, since the exact fluorescence

---

lifetime of NAD(P)H bound to metabolic enzymes is controversially discussed in the field (Ranjit et al. 2019). By RNA-Seq data of mesenchymal stromal cells (unpublished data of colleges) and confirmed by RNA-Seq and proteomics data of other cells (cancer cells) (Madhukar et al. 2015), the eleven most abundant NAD(P)H-dependent enzymes were identified. These enzymes are: malate dehydrogenase (MDH), hydroxyacyl-Coenzyme A dehydrogenase (HADH), lactate dehydrogenase (LDH), glyceraldehyde-3-phosphate dehydrogenase (GAPDH), glucose-6-phosphate dehydrogenase (G6PDH), pyruvate dehydrogenase (PDH), alcohol dehydrogenase (ADH), C-terminal binding protein 1 (CTBP1), isocitrate dehydrogenase (IDH), hydroxyacyl-coenzyme-A dehydrogenase (HADH), sorbitol dehydrogenase (SDH), inducible nitric oxide synthase (iNOS). From the highly expressed metabolic enzymes only complex I was excluded, due to difficulties in maintaining the functionality in solution (Leben et al. 2019). These enzymes were mixed with NADH or NADPH, respectively, and solved in MOPS medium, to ensure a cell-like environment (pH value, electrolyte concentration, refractive index) to maintain the necessary enzymatic folding and function. The homogeneous solutions contained only one fluorescent species in two different chemical states and the time domain decay curves were averaged over all pixels in order to smoothen it for proper bi-exponential fitting. The found fluorescence lifetime of enzyme-bound NAD(P)H were transferred to the phase domain in order to benchmark the semi-circle in the phasor representation.

The fluorescence lifetimes of NAD(P)H bound to the mentioned enzymes were in most cases, except of NAD(P)H bound to CTBP1 and PDH, specific to the respective enzymes. The statement in (Ranjit et al. 2019) that all enzyme-bound NAD(P)H lifetimes are identical and sufficiently represented by NADH bound to LDH is thus refuted.

## **7.6. Signal-to-noise ratio in NAD(P)H-FLIM**

The widely held opinion about FLIM is that it is independent of signal intensity, since the time is the imaging criterion and not the intensity. This holds true for bright samples, e.g. synthetic dyes, however, NAD(P)H is, as mentioned before, a rather dim fluorophore. Since we analyze the photon arrival histogram, which is subject of artifacts caused by the background noise, the photon count as such is not negligible. If the signal is too low to be completely separated from the noise, whose fluorescence lifetime is infinite, the measured total lifetime is erroneously extended and would lead to misinterpretations. In order to record reliable NAD(P)H-FLIM data, the minimum signal-to-noise ratio (SNR) required was determined by imaging unbound NADH solved in MOPS

solution at varying signal intensities. Independent how the signal intensity was modified, the curves in the Fig.1 (Aiii) and Suppl. Fig S1 in (Leben et al. 2019) show the same behavior. At first, the length of the vector connecting the origin and the phasor position “free NAD(P)H” increases with increasing signal intensity, up to a certain point where the curve changes to a plateau. This inflection point was defined as the minimum SNR required and is five for NAD(P)H-FLIM.

### **7.7. Systematic framework to analyze and interpret NAD(P)H-FLIM data**

Based on the specific NAD(P)H-bound-to-enzyme fluorescence lifetimes and under consideration of the SNR criterion, a systematic framework to analyze and especially to interpret NAD(P)H-FLIM data was developed. Here the data points in the phasor plot were allocated to one of the mentioned enzymes by vector analysis and transferred to the spatial domain to create a discrete enzyme map of cells. In addition, the relative length of these vectors implies the enzymatic activity reaching from 0% (no metabolic activity) to 100% (fully bound to the respective enzyme). Mapping these relative vector lengths over the entire image gives a spatial map of NAD(P)H-dependent enzymatic activity.

The performance of the systematic analysis framework was validated by homogenous solutions of NADH bound to enzymes and exemplary applied to a high-SNR NAD(P)H-FLIM of stromal-like cell line (preadipocytes, 3T3-L1). As a result, a different group of enzymes were active in the cytoplasm as compared to the cell nuclei, while the overall enzymatic activity did not differ between the various cellular compartments. In the nuclei, we identified the activation of “low-lifetime”-enzymes such as MDH, HADH or LDH, whereas in the cytoplasm, “higher-lifetime”-enzymes, such as SDH, PDH or iNOS, were preferentially activated. Since CTBP1 rather than MDH, HADH or LDH was expected to be active in the nuclei (Zhang et al. 2002), the underlying biological mechanism is not clear and would need further investigations. Interestingly, (Blacker et al. 2014) also observed significantly shorter NAD(P)H fluorescence lifetimes in the nuclei of HEK293 cells ( $\tau_2=2.3\pm 0.2$  ns) in contrast to the cytoplasm ( $\tau_2=2.7\pm 0.2$  ns).

### **7.8. Deeper insights in neutrophil metabolism by systematic enzyme mapping**

When the systematic analyzing framework is applied to the NAD(P)H-FLIM data of phagocytizing neutrophils published in (Leben et al. 2018), it reveals insights into their NAD(P)H-dependent

metabolism, which go beyond the NOX activation leading to the oxidative burst. The enzyme composition and enzymatic activity is more complex, but feasible, than the FLIM images suggest, while the previous findings on NOX activation still apply.

In some cells, that show a basic metabolism in the FLIM images, a different group of enzymes was found to be activated than in most others. The pixels of these cells were mainly assigned to shorter-lifetime enzymes. In literature a lower (but not as low as free) NAD(P)H fluorescence lifetime is correlated with metabolism based on glycolysis rather than OxPhos (Chacko and Eliceiri 2019). Thus, the activity of low lifetime enzymes could be a sign of activation, since most activated immune cells switch their metabolism to Warburg metabolism, to face an infection (Gaber et al. 2017). During glycolysis, the pyruvate is not transferred to the mitochondria but rather stays in the cytosol and is transformed in lactate, catalyzed by NADH bound to lactate dehydrogenase (LDH). The studies on the lifetime of NAD(P)H-dependent enzymes in solutions have shown that NADH bound to LDH is relatively short ( $\tau = 1.6$  ns), which explains the shortened fluorescence lifetime in glycolytic cells. Since OxPhos is not completely hindered in aerobic glycolysis but only downregulated (Gaber et al. 2017), the metabolism of these cells still consists of the NAD(P)H-dependent enzyme, which contribute to both glycolysis and OxPhos, but with changed ratio. Therefore, the pixels of these cells are not directly assigned to LDH by the systematic analysing framework. In addition, their metabolic activity is 15-20% less active compared to the other cells, while their intensity is surprisingly bright, indicating a high NAD(P)H concentration in these cells.

Surprisingly, almost all of the cells, which have a very short fluorescence lifetime indicating unbound NAD(P)H, show a ring, whose pixels are assigned to active NOX. Whether these are dead cells as assumed or phagosomes that were ejected shortly before NETosis together with the phagosome membrane to which the NOX is still bound, remains unclear. The pHrodo™ beads are made of indigestible polystyrene coated with opsonized *S. aureus* bioparticles. It is known that non-organic substances that cannot be broken down by the body are encapsulated in the connective tissue of the respective tissue. The enzymatic activity of these capsule should be very low, which explains the very short fluorescence lifetime in the FLIM image.

Analyzing NAD(P)H-FLIM data by the systematic framework holds the potential to identify activated immune cells by their altered metabolism and to distinguish them from inactive ones.

### 7.9. Donor FRET-FLIM reveals the dynamics of Ca<sup>2+</sup> concentration in B cells

In addition to the NAD(P)H-dependent cell metabolism, the calcium ion concentration is another factor of interest for the biosciences and biomedicine fields, since Ca<sup>2+</sup> plays an important role in cellular signal transduction pathways. Calcium ion channels on the cell membrane or on the membrane of cell organelles e.g. the endoplasmic reticulum, open as a reaction on intercellular signals, so that an increased Ca<sup>2+</sup> concentration can indicate cell-to-cell communication. Since the fluorescence lifetime of the donor in a FRET construct is significantly shortened in the quenched state, meaning in the presence of calcium ions, FLIM is an adequate method to monitor the Ca<sup>2+</sup>-dependent signaling. Like NAD(P)H-FLIM data donor-FRET FLIM can be analyzed by the phasor approach and it is in addition easier to interpret, since the donor has only two states: unquenched, in the absence of Ca<sup>2+</sup>, and quenched, in the presence of Ca<sup>2+</sup>.

The CD19<sup>+</sup> cells of the YellowCaB mice carry the genetically encoded Calcium-sensor TN-XXL, a FRET-construct (Mank and Griesbeck 2008). This way we were able to investigate the cell-to-cell communication, between naïve, antigen specific B cells and plasma blast in various regions of the lymph node. The absolute Ca<sup>2+</sup> concentrations were calculated from the fluorescence lifetime data, since they are directly linked (Geiger et al. 2012). The expression of the TN-XXL construct is very weak in naïve B cells, thus only by the amount of expressed Ca<sup>2+</sup> sensors, the FLIM signal can be very noisy. Since the communication between naïve B cells, AG specific B cells and plasma blast should be considered for the investigation of B cell differentiation, the data of naïve B cells are of great interest. Due to the noise exclusion radius and the following vector analysis in the phasor plot, these noisy data points could be used as well to calculate the absolute Ca<sup>2+</sup> concentration so that a Ca<sup>2+</sup> map of all relevant cells could be generated. However, it should be noted that the data resulting from such projections are more uncertain, because the greater the projection distance, the more the data points are scattered.

In this way we showed *in vivo* that calcium concentrations in B cells are highly dynamic during different stages of affinity maturation. The heterogeneity in temporal Ca<sup>2+</sup> concentration is the smallest among naïve B cells, increases with activation in AG-specific GC B cells and is most prominent among plasma blasts. In conclusion, the cells of high Ca<sup>2+</sup> concentration are communicating by transferring signals and will probably develop to plasma blasts later.

This technique has the potential to answer long standing questions of B cell selection and maturation and how plasma cells can maintain longevity in combination with high qualitative and quantitative output of antibodies (Ulbricht et al. 2021).

## 8. Conclusion and future prospects

FLIM offers valuable insights into the life-sustaining functions of living cells and tissues. This includes the cellular defence by NOX activation, the NAD(P)H-dependant cellular metabolism or the calcium-ion-dependant cellular response to cell-to-cell-communication.

With this thesis NAD(P)H- and donor FRET-FLIM were established and a vector-based method for the analysis of FLIM data was developed, which is applicable to both. In the field of NAD(P)H-FLIM it is based on the specific fluorescence lifetimes of enzyme-bound NAD(P)H, which were determined here for the most frequent NAD(P)H-dependent enzymes. In this way, discrete enzyme maps as well as maps of general enzymatic activity were generated, systematizing the interpretation of these data. In donor FRET-FLIM, the vector analysis method was used to calculate maps of absolute  $\text{Ca}^{2+}$  concentration in cells even of noisy signals. Using the general applicable SNR criterion that was established here, pixels with too low SNR are systematically decomposed.

This method allows a quantitative observation of the energy metabolism of different cell types as well as the  $\text{Ca}^{2+}$  signaling in cells carrying a gene encoded FRET construct. It meets the increasing demand to interpret *in vitro* and *in vivo* FLIM data in a reliable, systematic way in order to understand and reveal the underlying metabolic mechanism, e.g. in cells of the activated immune system (Gaber et al. 2017), during mesenchymal stem cell differentiation (Evers et al. 2018; Meleshina et al. 2016; Meleshina et al. 2017), during the B-cell development, maturation and communication (Jellusova 2018; Jellusova et al. 2017; Jellusova and Rickert 2017) or the development of malignant tissue changes (Skala et al. 2007a; Provenzano et al. 2009).

A challenge for the future is the *in vivo* combination of NAD(P)H- and FRET-FLIM, for example in lymph nodes of YellowCaB mice. Metabolism is directly or indirectly linked to every cellular process (Vander Heiden et al. 2009). However detailed information about metabolism in B cells is rare (Gaber et al. 2017), especially how it directs the fate of healthy B cells during differentiation in the secondary lymphoid tissue. B cell maturation is a multicellular process coordinated signaling pathways, so there should be a close cross-talk between signaling pathways and metabolic control.

In a *in vivo* experiment the already weak signal of NAD(P)H has to be taken into account, since it is strongly scattered in the tissue due to its blue emission. A first pilot measurement has already

shown that it is possible to image through the intact capsule of a lymph node and to obtain an adequate NAD(P)H-FLIM signal based on the SNR criterion.

Furthermore, cross-talk effects from other detection channels need to be taken into account. A large number of reporter mouse lines express GFP or its enhanced version eGFP in specific cells, such as Blimp:GFP mouse line in the antibody secreting cells or CX3CR1<sup>+/-</sup> eGFP mouse line in monocytes and microglia. It would be interesting to clarify the influence of the green fluorescent protein GFP on NAD(P)H-FLIM data. It is known that a small percentage of the emission spectrum GFP leaks into the blue (NAD(P)H) channel (Rakhymzhan et al. 2017), so it could interfere with the NAD(P)H signal. Recently, (York et al. 2019) observed that GFP-positive cells show in the NAD(P)H-FLIM imaging setup ( $\lambda_{\text{ex}} = 460 \text{ nm}$ , Ch 466/50) a fluorescence lifetime that is very similar to that of free NAD(P)H and thus can lead to fatal misinterpretations. Whether this could be a second excitation peak of GFP, where the S<sub>2</sub> level is excited with the higher energy wavelength, remains speculation and requires further investigation. However, this phenomenon should be clarified.

## 9. References

- Abbe E (1873) Beiträge zur Theorie des Mikroskops und der mikroskopischen Wahrnehmung. *Archiv für mikroskopische Anatomie* 9 (1):413-418
- Bastiaens PI, Squire A (1999) Fluorescence lifetime imaging microscopy: spatial resolution of biochemical processes in the cell. *Trends in cell biology* 9 (2):48-52
- Bedard K, Krause K-H (2007) The NOX family of ROS-generating NADPH oxidases: physiology and pathophysiology. *Physiological reviews* 87 (1):245-313
- Benninger RK, Piston DW (2013) Two-photon excitation microscopy for the study of living cells and tissues. *Current protocols in cell biology* 59 (1):4.11. 11-14.11. 24
- Berezin MY, Achilefu S (2010) Fluorescence lifetime measurements and biological imaging. *Chemical reviews* 110 (5):2641-2684
- Bird DK, Yan L, Vrotsos KM, Eliceiri KW, Vaughan EM, Keely PJ, White JG, Ramanujam N (2005) Metabolic mapping of MCF10A human breast cells via multiphoton fluorescence lifetime imaging of the coenzyme NADH. *Cancer research* 65 (19):8766-8773
- Blacker TS, Duchen MR (2016) Investigating mitochondrial redox state using NADH and NADPH autofluorescence. *Free Radical Biology and Medicine* 100:53-65
- Blacker TS, Mann ZF, Gale JE, Ziegler M, Bain AJ, Szabadkai G, Duchen MR (2014) Separating NADH and NADPH fluorescence in live cells and tissues using FLIM. *Nature communications* 5:3936
- Blacker TS, Sewell MD, Szabadkai G, Duchen MR (2019) Metabolic profiling of live cancer tissues using NAD (P) H fluorescence lifetime imaging. In: *Cancer Metabolism*. Springer, pp 365-387
- Boyer P, Theorell H (1956) Alcohol D 'ehydrogenase (ADH). *ACTA CHEMICA SCANDINAVICA* 10 (3):447-450
- Bratton DL, Henson PM (2011) Neutrophil clearance: when the party is over, clean-up begins. *Trends in immunology* 32 (8):350-357
- Bremer D, Leben R, Mothes R, Radbruch H, Niesner R (2017) Method to Detect the Cellular Source of Over-Activated NADPH Oxidases Using NAD(P)H Fluorescence Lifetime Imaging. *Curr Protoc Cytom* 80:9 52 51-59 52 14. doi:10.1002/cpcy.20
- Brinkmann V, Reichard U, Goosmann C, Fauler B, Uhlemann Y, Weiss DS, Weinrauch Y, Zychlinsky A (2004) Neutrophil extracellular traps kill bacteria. *science* 303 (5663):1532-1535
- Brinkmann V, Zychlinsky A (2007) Beneficial suicide: why neutrophils die to make NETs. *Nature Reviews Microbiology* 5 (8):577

- Brinkmann V, Zychlinsky A (2012) Neutrophil extracellular traps: is immunity the second function of chromatin? *J Cell Biol* 198 (5):773-783
- Brynjolfsson SF, Persson Berg L, Olsen Ekerhult T, Rimkute I, Wick M-J, Mårtensson I-L, Grimsholm O (2018) Long-Lived Plasma Cells in Mice and Men. *Frontiers in Immunology* 9 (2673). doi:10.3389/fimmu.2018.02673
- Celli A, Sanchez S, Behne M, Hazlett T, Gratton E, Mauro T (2010) The epidermal Ca<sup>2+</sup> gradient: measurement using the phasor representation of fluorescent lifetime imaging. *Biophysical journal* 98 (5):911-921
- Chacko JV, Eliceiri KW (2019) Autofluorescence lifetime imaging of cellular metabolism: Sensitivity toward cell density, pH, intracellular, and intercellular heterogeneity. *Cytometry Part A* 95 (1):56-69
- Chance B, Baltscheffsky H (1958) Respiratory enzymes in oxidative phosphorylation VII. Binding of intramitochondrial reduced pyridine nucleotide. *Journal of Biological Chemistry* 233 (3):736-739
- Chance B, Cohen P, Jobsis F, Schoener B (1962) Intracellular Oxidation-Reduction States in Vivo: The microfluorometry of pyridine nucleotide gives a continuous measurement of the oxidation state. *Science* 137 (3529):499-508
- Chance B, Schoener B, Oshino R, Itshak F, Nakase Y (1979) Oxidation-reduction ratio studies of mitochondria in freeze-trapped samples. NADH and flavoprotein fluorescence signals. *Journal of Biological Chemistry* 254 (11):4764-4771
- Christen P, Jaussi R (2006) *Biochemie: Eine Einführung mit 40 Lerneinheiten*. Springer-Verlag,
- Clegg RM, Feddersen BA, Gratton E, Jovin TM Time-resolved imaging fluorescence microscopy. In: *Time-Resolved Laser Spectroscopy in Biochemistry III*, 1992. International Society for Optics and Photonics, pp 448-460
- Datta R, Alfonso-García A, Cinco R, Gratton E (2015) Fluorescence lifetime imaging of endogenous biomarker of oxidative stress. *Scientific reports* 5:9848
- Datta R, Heylman C, George SC, Gratton E (2016) Label-free imaging of metabolism and oxidative stress in human induced pluripotent stem cell-derived cardiomyocytes. *Biomedical optics express* 7 (5):1690-1701
- De Ruyck J, Famerée M, Wouters J, Perpète EA, Preat J, Jacquemin D (2007) Towards the understanding of the absorption spectra of NAD (P) H/NAD (P)<sup>+</sup> as a common indicator of dehydrogenase enzymatic activity. *Chemical Physics Letters* 450 (1-3):119-122
- Denk W, Strickler J, Webb W (1990) Two-photon laser scanning fluorescence microscopy. *Science* 248 (4951):73-76. doi:10.1126/science.2321027
- Digman MA, Caiolfa VR, Zamai M, Gratton E (2008) The phasor approach to fluorescence lifetime imaging analysis. *Biophys J* 94 (2):L14-16. doi:10.1529/biophysj.107.120154

- Einstein A (1917) Zur quantentheorie der strahlung. *Phys Z* 18:121-128
- Eng J, Lynch RM, Balaban RS (1989) Nicotinamide adenine dinucleotide fluorescence spectroscopy and imaging of isolated cardiac myocytes. *Biophysical journal* 55 (4):621-630
- Engelke M, Engels N, Dittmann K, Stork B, Wienands J (2007) Ca<sup>2+</sup> signaling in antigen receptor-activated B lymphocytes. *Immunological reviews* 218 (1):235-246
- Evers M, Salma N, Osseiran S, Casper M, Birngruber R, Evans CL, Manstein D (2018) Enhanced quantification of metabolic activity for individual adipocytes by label-free FLIM. *Scientific reports* 8 (1):8757
- Fenninger F, Jefferies WA (2019) What's bred in the bone: calcium channels in lymphocytes. *The Journal of Immunology* 202 (4):1021-1030
- Fermi E (1950) *Nuclear physics: a course given by Enrico Fermi at the University of Chicago*. University of Chicago Press,
- Förster T (1948) Zwischenmolekulare energiewanderung und fluoreszenz. *Annalen der physik* 437 (1-2):55-75
- Frauwirth KA, Riley JL, Harris MH, Parry RV, Rathmell JC, Plas DR, Elstrom RL, June CH, Thompson CB (2002) The CD28 signaling pathway regulates glucose metabolism. *Immunity* 16 (6):769-777
- Gaber T, Strehl C, Buttgerit F (2017) Metabolic regulation of inflammation. *Nature Reviews Rheumatology* 13 (5):267
- Gafni A, Brand L (1976) Fluorescence decay studies of reduced nicotinamide adenine dinucleotide in solution and bound to liver alcohol dehydrogenase. *Biochemistry* 15 (15):3165-3171
- Geiger A, Russo L, Gensch T, Thestrup T, Becker S, Hopfner KP, Griesinger C, Witte G, Griesbeck O (2012) Correlating calcium binding, Förster resonance energy transfer, and conformational change in the biosensor TN-XXL. *Biophys J* 102 (10):2401-2410. doi:10.1016/j.bpj.2012.03.065
- Göppert-Mayer M (1931) Über Elementarakte mit zwei Quantensprüngen. *Annalen der Physik* 401 (3):273-294. doi:10.1002/andp.19314010303
- Harden A, Young WJ (1906) The alcoholic ferment of yeast-juice. Part II.—The coferment of yeast-juice. *Proceedings of the Royal Society of London Series B, Containing Papers of a Biological Character* 78 (526):369-375
- Herz J, Siffrin V, Hauser AE, Brandt AU, Leuenberger T, Radbruch H, Zipp F, Niesner RA (2010) Expanding two-photon intravital microscopy to the infrared by means of optical parametric oscillator. *Biophysical journal* 98 (4):715-723

- Hess ST, Sheets ED, Wagenknecht-Wiesner A, Heikal AA (2003) Quantitative analysis of the fluorescence properties of intrinsically fluorescent proteins in living cells. *Biophysical journal* 85 (4):2566-2580
- Hoek KL, Antony P, Lowe J, Shinnars N, Sarmah B, Wente SR, Wang D, Gerstein RM, Khan WN (2006) Transitional B cell fate is associated with developmental stage-specific regulation of diacylglycerol and calcium signaling upon B cell receptor engagement. *The Journal of Immunology* 177 (8):5405-5413
- Huang S, Heikal AA, Webb WW (2002) Two-photon fluorescence spectroscopy and microscopy of NAD (P) H and flavoprotein. *Biophysical journal* 82 (5):2811-2825
- IMD IfMD (2020) IMD Labor Berlin - Autoimmunerkrankungen. <https://www.imd-berlin.de/spezielle-kompetenzen/autoimmunerkrankungen.html>. Accessed 20.04.2020
- Jabłoński A (1935) Über den mechanismus der Photolumineszenz von Farbstoffphosphoren. *Zeitschrift für Physik* 94 (1-2):38-46
- Jameson DM, Thomas V, Zhou D (1989) Time-resolved fluorescence studies on NADH bound to mitochondrial malate dehydrogenase. *Biochimica et Biophysica Acta (BBA)-Protein Structure and Molecular Enzymology* 994 (2):187-190
- Janeway Jr C, Travers P, Walport M (2012) *Immunobiology*. 8th Editio. New York: Garland Science
- Jellusova J (2018) Cross-talk between signal transduction and metabolism in B cells. *Immunology letters*
- Jellusova J, Cato MH, Apgar JR, Ramezani-Rad P, Leung CR, Chen C, Richardson AD, Conner EM, Benschop RJ, Woodgett JR (2017) Gsk3 is a metabolic checkpoint regulator in B cells. *Nature immunology* 18 (3):303
- Jellusova J, Rickert RC (2017) A Brake for B Cell Proliferation: Appropriate responses to metabolic stress are crucial to maintain B cell viability and prevent malignant outgrowth. *Bioessays* 39 (11). doi:10.1002/bies.201700079
- Kaiser W, Garrett C (1961) Two-photon excitation in Ca F 2: Eu 2+. *Physical review letters* 7 (6):229
- Kasha M (1950) Characterization of electronic transitions in complex molecules. *Discussions of the Faraday society* 9:14-19
- Kierdaszuk B, Malak H, Gryczynski I, Callis P, Lakowicz JR (1996) Fluorescence of reduced nicotinamides using one-and two-photon excitation. *Biophysical chemistry* 62 (1-3):1-13
- Krantz S (2007) *Biochemie-GK 1*. Springer Medizin Verlag Heidelberg,
- Kurosaki T, Kometani K, Ise W (2015) Memory B cells. *Nature Reviews Immunology* 15 (3):149-159
-

- Lakowicz JR (2013) Principles of fluorescence spectroscopy. Springer Science & Business Media,
- Lakowicz JR, Szmacinski H, Nowaczyk K, Berndt KW, Johnson M (1992a) Fluorescence lifetime imaging. *Anal Biochem* 202 (2):316-330. doi:10.1016/0003-2697(92)90112-k
- Lakowicz JR, Szmacinski H, Nowaczyk K, Johnson ML (1992b) Fluorescence lifetime imaging of free and protein-bound NADH. *Proceedings of the National Academy of Sciences* 89 (4):1271-1275
- Leben R, Köhler M, Radbruch H, Hauser AE, Niesner RA (2019) Systematic Enzyme Mapping of Cellular Metabolism by Phasor-Analyzed Label-Free NAD (P) H Fluorescence Lifetime Imaging. *International journal of molecular sciences* 20 (22):5565
- Leben R, Ostendorf L, van Koppen S, Rakhymzhan A, Hauser AE, Radbruch H, Niesner RA (2018) Phasor-Based Endogenous NAD(P)H Fluorescence Lifetime Imaging Unravels Specific Enzymatic Activity of Neutrophil Granulocytes Preceding NETosis. *Int J Mol Sci* 19 (4). doi:10.3390/ijms19041018
- Löffler G, Petrides PE (2019) Biochemie und pathobiochemie. Springer-Verlag,
- Madhukar NS, Warmoes MO, Locasale JW (2015) Organization of enzyme concentration across the metabolic network in cancer cells. *PLoS one* 10 (1):e0117131
- Maeda-Yorita K, Aki K (1984) Effect of nicotinamide adenine dinucleotide on the oxidation-reduction potentials of lipoamide dehydrogenase from pig heart. *The Journal of Biochemistry* 96 (3):683-690
- Mank M, Griesbeck O (2008) Genetically encoded calcium indicators. *Chemical reviews* 108 (5):1550-1564
- Mayevsky A, Rogatsky GG (2007) Mitochondrial function in vivo evaluated by NADH fluorescence: from animal models to human studies. *American journal of physiology-Cell physiology* 292 (2):C615-C640
- McGinty J, Galletly NP, Dunsby C, Munro I, Elson DS, Requejo-Isidro J, Cohen P, Ahmad R, Forsyth A, Thillainayagam AV (2010) Wide-field fluorescence lifetime imaging of cancer. *Biomedical optics express* 1 (2):627-640
- Medzhitov R (2015) Bringing Warburg to lymphocytes. *Nature Reviews Immunology* 15 (10):598-598
- Meleshina AV, Dudenkova VV, Bystrova AS, Kuznetsova DS, Shirmanova MV, Zagaynova EV (2017) Two-photon FLIM of NAD (P) H and FAD in mesenchymal stem cells undergoing either osteogenic or chondrogenic differentiation. *Stem cell research & therapy* 8 (1):15
- Meleshina AV, Dudenkova VV, Shirmanova MV, Shcheslavskiy VI, Becker W, Bystrova AS, Cherkasova EI, Zagaynova EV (2016) Probing metabolic states of differentiating stem cells using two-photon FLIM. *Scientific reports* 6:21853
-

- Mossakowski AA, Pohlan J, Bremer D, Lindquist R, Millward JM, Bock M, Pollok K, Mothes R, Viohl L, Radbruch M, Gerhard J, Bellmann-Strobl J, Behrens J, Infante-Duarte C, Mahler A, Boschmann M, Rinnenthal JL, Fuchtemeier M, Herz J, Pache FC, Bardua M, Priller J, Hauser AE, Paul F, Niesner R, Radbruch H (2015) Tracking CNS and systemic sources of oxidative stress during the course of chronic neuroinflammation. *Acta Neuropathol* 130 (6):799-814. doi:10.1007/s00401-015-1497-x
- Munro IH, McGinty JA, Galletly NP, Requejo-Isidro J, Lanigan PM, Elson DS, Dunsby CW, Neil MA, Lever MJ, Stamp GW (2005) Toward the clinical application of time-domain fluorescence lifetime imaging. *Journal of Biomedical Optics* 10 (5):051403
- Niesner R, Andresen V, Neumann J, Spiecker H, Gunzer M (2007) The power of single and multibeam two-photon microscopy for high-resolution and high-speed deep tissue and intravital imaging. *Biophysical journal* 93 (7):2519-2529
- Niesner R, Narang P, Spiecker H, Andresen V, Gericke K-H, Gunzer M (2008a) Selective detection of NADPH oxidase in polymorphonuclear cells by means of NAD (P) H-based fluorescence lifetime imaging. *Journal of Biophysics* 2008
- Niesner R, Narang P, Spiecker H, Andresen V, Gericke KH, Gunzer M (2008b) Selective detection of NADPH oxidase in polymorphonuclear cells by means of NAD(P)H-based fluorescence lifetime imaging. *J Biophys* 2008:602639. doi:10.1155/2008/602639
- Niesner R, Peker B, Schlüsche P, Gericke K-H, Hoffmann C, Hahne D, Müller-Goymann C (2005) 3D-resolved investigation of the pH gradient in artificial skin constructs by means of fluorescence lifetime imaging. *Pharmaceutical research* 22 (7):1079-1087
- Niesner R, Peker B, Schlüsche P, Gericke KH (2004) Noniterative biexponential fluorescence lifetime imaging in the investigation of cellular metabolism by means of NAD (P) H autofluorescence. *ChemPhysChem* 5 (8):1141-1149
- Pearce EL, Pearce EJ (2013) Metabolic pathways in immune cell activation and quiescence. *Immunity* 38 (4):633-643
- Phan TG, Bullen A (2010) Practical intravital two-photon microscopy for immunological research: faster, brighter, deeper. *Immunology and cell biology* 88 (4):438-444
- Piston D, Masters B, Webb W (1995) Three-dimensionally resolved NAD (P) H cellular metabolic redox imaging of the in situ cornea with two-photon excitation laser scanning microscopy. *Journal of microscopy* 178 (1):20-27
- Provenzano PP, Eliceiri KW, Keely PJ (2009) Multiphoton microscopy and fluorescence lifetime imaging microscopy (FLIM) to monitor metastasis and the tumor microenvironment. *Clinical & experimental metastasis* 26 (4):357-370
- Radbruch H, Bremer D, Guenther R, Cseresnyes Z, Lindquist R, Hauser AE, Niesner R (2016) Ongoing oxidative stress causes subclinical neuronal dysfunction in the recovery phase of EAE. *Frontiers in immunology* 7:92

- Rakhymzhan A, Leben R, Zimmermann H, Günther R, Mex P, Reismann D, Ulbricht C, Acs A, Brandt AU, Lindquist RL (2017) Synergistic strategy for multicolor two-photon microscopy: application to the analysis of germinal center reactions in vivo. *Scientific reports* 7 (1):1-16
- Ranjit S, Malacrida L, Jameson DM, Gratton E (2018) Fit-free analysis of fluorescence lifetime imaging data using the phasor approach. *Nature protocols* 13 (9):1979
- Ranjit S, Malacrida L, Stakic M, Gratton E (2019) Determination of the metabolic index using the fluorescence lifetime of free and bound NADH in the phasor approach. *Journal of biophotonics*:e201900156
- Remmele W (1955) Atmung und glykolyse der Leukocyten. *Acta Haematologica* 13 (2):103-123
- Schneckenburger H, Koenig K (1992) Fluorescence decay kinetics and imaging of NAD (P) H and flavins as metabolic indicators. *Optical Engineering* 31 (7):1447-1452
- Schütt C, Bröker B (2011) *Grundwissen Immunologie*. Springer-Verlag,
- Scott TG, Spencer RD, Leonard NJ, Weber G (1970) Synthetic spectroscopic models related to coenzymes and base pairs. V. Emission properties of NADH. Studies of fluorescence lifetimes and quantum efficiencies of NADH, AcPyADH,[reduced acetylpyridineadenine dinucleotide] and simplified synthetic models. *Journal of the American Chemical Society* 92 (3):687-695
- Seelich F, Letnansky K, Frisch W, Schneck O (1957) Zur Frage des Stoffwechsels normaler und pathologischer menschlicher Leukocyten. *Zeitschrift für Krebsforschung* 62 (1):1-8
- Sharick JT, Favreau PF, Gillette AA, Sdao SM, Merrins MJ, Skala MC (2018) Protein-bound NAD(P)H Lifetime is Sensitive to Multiple Fates of Glucose Carbon. *Sci Rep* 8 (1):5456. doi:10.1038/s41598-018-23691-x
- Skala MC, Ricking KM, Bird DK, Gendron-Fitzpatrick A, Eickhoff J, Eliceiri KW, Keely PJ, Ramanujam N (2007a) In vivo multiphoton fluorescence lifetime imaging of protein-bound and free nicotinamide adenine dinucleotide in normal and precancerous epithelia. *Journal of biomedical optics* 12 (2):024014
- Skala MC, Ricking KM, Gendron-Fitzpatrick A, Eickhoff J, Eliceiri KW, White JG, Ramanujam N (2007b) In vivo multiphoton microscopy of NADH and FAD redox states, fluorescence lifetimes, and cellular morphology in precancerous epithelia. *Proceedings of the National Academy of Sciences* 104 (49):19494-19499
- Soeller C, Cannell M (1999) Two-photon microscopy: Imaging in scattering samples and three-dimensionally resolved flash photolysis. *Microscopy research and technique* 47 (3):182-195
- Strickler S, Berg RA (1962) Relationship between absorption intensity and fluorescence lifetime of molecules. *The Journal of chemical physics* 37 (4):814-822

- Stringari C, Sierra R, Donovan PJ, Gratton E (2012) Label-free separation of human embryonic stem cells and their differentiating progenies by phasor fluorescence lifetime microscopy. *Journal of biomedical optics* 17 (4):046012
- Theer P, Hasan MT, Denk W (2003) Two-photon imaging to a depth of 1000  $\mu\text{m}$  in living brains by use of a Ti: Al<sub>2</sub>O<sub>3</sub> regenerative amplifier. *Optics letters* 28 (12):1022-1024
- Ulbricht C (2018) In vivo-Analyse der B-Zell-Rezeptor-Signaltransduktion im Keimzentrum.
- Ulbricht C, Leben R, Rakhymzhan A, Kirchhoff F, Nitschke L, Radbruch H, Niesner RA, Hauser AE (2021) Intravital quantification reveals dynamic calcium concentration changes across B cell differentiation stages. *Elife* 10:e56020
- Utzinger U (2011) Spectra Database hosted at the University of Arizona. <http://www.spectra.arizona.edu/>. Accessed 24.01.2020
- Vander Heiden MG, Cantley LC, Thompson CB (2009) Understanding the Warburg effect: the metabolic requirements of cell proliferation. *science* 324 (5930):1029-1033
- Wallrabe H, Periasamy A (2005) Imaging protein molecules using FRET and FLIM microscopy. *Current opinion in biotechnology* 16 (1):19-27
- Warburg O, Christian W (1936) Pyridin, der wasserstoffübertragende Bestandteil von Gärungsfermenten. *Helvetica Chimica Acta* 19 (1):E79-E88
- Warburg O, Gawehn K, Geissler A-W (1958) Stoffwechsel der weissen Blutzellen. *Zeitschrift Für Naturforschung B* 13 (8):515-516
- Xu C, Zipfel W, Shear JB, Williams RM, Webb WW (1996) Multiphoton fluorescence excitation: new spectral windows for biological nonlinear microscopy. *Proceedings of the National Academy of Sciences* 93 (20):10763-10768
- York EM, Weilinger NL, LeDue JM, MacVicar BA (2019) Green fluorescent protein emission obscures metabolic fluorescent lifetime imaging of NAD (P) H. *Biomedical optics express* 10 (9):4381-4394
- Zhang Q, Piston DW, Goodman RH (2002) Regulation of corepressor function by nuclear NADH. *Science* 295 (5561):1895-1897
- Zipfel WR, Williams RM, Webb WW (2003) Nonlinear magic: multiphoton microscopy in the biosciences. *Nat Biotechnol* 21 (11):1369-1377. doi:10.1038/nbt899



## Acknowledgment

At the very beginning of my doctoral thesis, when something (I even can't remember what!) didn't quite work out, another doctoral researcher who was about to graduate told me: "Don't worry, a master's thesis is a sprint, but a doctoral thesis is a marathon! So you have plenty of time to figure it out." And she was right! The last four and a half years have been a challenging, nerve-wracking and exciting time, but I have learned so much more than I ever imagined. I had the luck to work in a friendly, warm-hearted, almost family environment and I owe this luck to the people I would like to thank at this point.

First and foremost, of course, I would like to thank my supervisors Prof. Dr. Raluca A. Niesner (Biophysical Analytics) and Prof. Dr. Anja E. Hauser (Immune Dynamics), for their enthusiasm and unchanged trust that everything will turn out well in the end. You have challenged me, supported me and defended me, always had an open ear and advice for me and left me the freedom I needed for this work. Miraculously, you have always found a pot from which I could to be financed. I really enjoyed the working with you and in your teams.

My special thanks go to Dr. Asylkhan Rakhymzhan, who introduced me to the microscope. We all know how sensitive it is to newcomers. Also for our fruitful discussions and for being a member of my advisory committee. I would also like to thank Peggy Mex, Ralf Uecker and Robert Günther for preparing cells and tissue samples for me as well as Dr. Helena Radbruch who kindly provided some these samples and put me in contact with people who were interested in my approach.

The excellent exchange, the open teamwork and the solidarity, which created the friendly working atmosphere, is due to all members of the working groups. I cannot call them all by name, but you know who you are. It was a pleasure to be a part of your crew. Here I would like to thank my past and present doctoral siblings for all the exhilarating bright moments, especially those with whom I shared our micro-small office. If you were not as you are, I would have had a much harder time.

I do not know how appropriate it is to mention a deadly virus here. But I certainly owe the week-lasting lock-down that came with it, the time and leisure to fully concentrate on this dissertation, otherwise I would probably still be chasing another idea that could be considered.

Zu guter Letzt möchte ich meiner Familie und meinen Freunden danken. Ihr habt Euch immer wieder wirre Geschichten über Mikroskope wie Raumschiffe, Moleküle in anderen Ebenen und wundersame Halbkreise angehört und trotzdem nicht aufgehört Euch nach dem Fortgang meiner Arbeit zu erkundigen.

- I thank you all!! -

## Appendix A

### A.1. Conference contributions

R. Leben, A. Rakhymzhan, R.A. Niesner, “Two-photon spectra of chromophores”, FOM - Focus on Microscopy 2015, Göttingen, Germany, **poster**

R. Leben, L. Ostendorf, A.E. Hauser, H. Radbruch, R.A. Niesner, “Phasor analyzed fluorescence lifetime imaging to investigate changes in neutrophil metabolism preceding NETosis”, CYTO 2018 - The 33<sup>rd</sup> Congress of the International Society for Advancement of Cytometry, Prague, Czech Republic, **poster**

R. Leben, C. Ulbricht, A.E. Hauser, R.A. Niesner, “Determining the dynamics of local absolute calcium concentrations in germinal center B cells in vivo by donor FRET-FLIM”, FOM - Focus on Microscopy 2019, London, United Kingdom, **talk**

“Biology III: Nanoparticles for Optical Imaging”, FOM - Focus on Microscopy 2019, London, United Kingdom, **chair**

R. Leben, M. Köhler, H. Radbruch, A.E. Hauser, R.A. Niesner, “Systematic enzyme mapping of cellular metabolism by phasor-analyzed label-free NAD(PH) fluorescence lifetime imaging”, DGfZ 2019 – 29<sup>th</sup> Annual Conference of the German Society for Cytometry, Berlin, Germany, **poster**

R. Leben, M. Köhler, H. Radbruch, A.E. Hauser, R.A. Niesner, “Systematic enzyme mapping of cellular metabolism by phasor-analyzed label-free NAD(PH) fluorescence lifetime imaging”, NEUBIAS 2020 – 4<sup>th</sup> conference of european bioimage analysts, Bordeaux, France, **poster**

R. Leben, M. Köhler, H. Radbruch, A.E. Hauser, R.A. Niesner, “Systematic enzyme mapping based on by phasor-analyzed label-free NAD(P)H-FLIM reveals deeper insights in neutrophil metabolism”, CYTO virtual 2020 - The 35<sup>rd</sup> Congress of the International Society for Advancement of Cytometry, online, **poster**

R. Leben, M. Köhler, H. Radbruch, A.E. Hauser, R.A. Niesner, “Deeper insights in neutrophil metabolism by systematic enzyme mapping based on phasor-analyzed label-free NAD(P)H-FLIM”, DiGifZ 2020, Virtual 30th Anniversary conference of the German Society of Cytometry (DGfZ), online, **poster**

R. Leben, A. Rakhymzhan, R.A. Niesner, „Towards ultra-deep three-photon tissue oxygenation imaging in murine lymphoid organs“, DiGifZ 2021, Virtual 31th Anniversary conference of the German Society of Cytometry (DGfZ), online, **talk**

## A.2. Complete list of publications

- 2021 Method for Multiplexed Dynamic Intravital Multiphoton Imaging.  
Rakhymzhan A, Acs A, **Leben R**, Winkler TH, Hauser AE, Niesner RA.  
Methods Mol Biol. 2021;2350:145-156. doi: [10.1007/978-1-0716-1593-5\\_10](https://doi.org/10.1007/978-1-0716-1593-5_10). PMID: 34331284
- 2021# Intravital quantification reveals dynamic calcium concentration changes across B cell differentiation stages  
Ulbricht C, **Leben R**, Rakhymzhan A, Kirchhoff F, Radbruch H, Nitschke L, Niesner R A, Hauser A E,  
Elife. 2021 Mar 22;10:e56020. doi: [10.7554/eLife.56020](https://doi.org/10.7554/eLife.56020). PMID: 33749591
- 2020 Teriflunomide Does Not Change Dynamics of Nadph Oxidase Activation and Neuronal Dysfunction During Neuroinflammation.  
Mothes R, Ulbricht C, **Leben R**, Günther R, Hauser AE, Radbruch H, Niesner R.  
Front Mol Biosci. 2020 Apr 30;7:62. doi: [10.3389/fmolb.2020.00062](https://doi.org/10.3389/fmolb.2020.00062). eCollection 2020. PMID: 32426367
- 2020 Immunoglobulin expression in the endoplasmic reticulum shapes the metabolic fitness of B lymphocytes.  
Jumaa H, Caganova M, McAllister EJ, Hoenig L, He X, Saltukoglu D, Brenker K, Köhler M, **Leben R**, Hauser AE, Niesner R, Rajewsky K, Reth M, Jellusova J.  
Life Sci Alliance. 2020 Apr 27;3(6). pii: e202000700. doi: [10.26508/lsa.202000700](https://doi.org/10.26508/lsa.202000700). Print 2020 Jun. PMID:32341085
- 2020 Coregistered Spectral Optical Coherence Tomography and Two-Photon Microscopy for Multimodal Near-Instantaneous Deep-Tissue Imaging.  
Rakhymzhan A, Reuter L, Raspe R, Bremer D, Günther R, **Leben R**, Heidelin J, Andresen V, Cheremukhin S, Schulz-Hildebrandt H, Bixel MG, Adams RH, Radbruch H, Hüttmann G, Hauser AE, Niesner RA.  
Cytometry A. 2020 May;97(5):515-527. doi: [10.1002/cyto.a.24012](https://doi.org/10.1002/cyto.a.24012). Epub 2020 Apr 15. PMID: 32293804
- 2019# Systematic enzyme mapping of cellular metabolism by phasor-analyzed label-free NAD(P)H fluorescence lifetime imaging  
**Leben R\***, Köhler M\*, Radbruch H, Hauser AE, Niesner RA  
Int J Mol Sci. 2019 Nov 7;20(22). pii: E5565. doi: [10.3390/ijms20225565](https://doi.org/10.3390/ijms20225565).

- 2018 NAD(P)H Oxidase Activity in the Small Intestine Is Predominantly Found in Enterocytes, Not Professional Phagocytes.  
Lindquist RL, Bayat-Sarmadi J, **Leben R**, Niesner R, Hauser AE.  
Int J Mol Sci. 2018 May 4;19(5. pii: E1365. doi: [10.3390/ijms19051365](https://doi.org/10.3390/ijms19051365).
- 2018# Phasor-Based Endogenous NAD(PH) Fluorescence Lifetime Imaging Unravels Specific Enzymatic Activity of Neutrophil Granulocytes Preceding NETosis.  
**Leben R**, Ostendorf L, van Koppen S, Rakhymzhan A, Hauser AE, Radbruch H, Niesner RA.  
Int J Mol Sci. 2018 Mar 29;19(4. pii: E1018. doi: [10.3390/ijms19041018](https://doi.org/10.3390/ijms19041018).
- 2017 Analyzing Nicotinamide Adenine Dinucleotide Phosphate Oxidase Activation in Aging and Vascular Amyloid Pathology.  
Radbruch H, Mothes R, Bremer D, Seifert S, Köhler R, Pohlan J, Ostendorf L, Günther R, **Leben R**, Stenzel W, Niesner RA, Hauser AE.  
Front Immunol. 2017 Jul 31;8:844. doi: [10.3389/fimmu.2017.00844](https://doi.org/10.3389/fimmu.2017.00844). eCollection 2017
- 2017 Synergistic Strategy for Multicolor Two-photon Microscopy: Application to the Analysis of Germinal Center Reactions In Vivo.  
Rakhymzhan A, **Leben R**, Zimmermann H, Günther R, Mex P, Reismann D, Ulbricht C, Acs A, Brandt AU, Lindquist RL, Winkler TH, Hauser AE, Niesner RA.  
Sci Rep. 2017 Aug 2;7(1:7101. doi: [10.1038/s41598-017-07165-0](https://doi.org/10.1038/s41598-017-07165-0).
- 2017 Method to Detect the Cellular Source of Over-Activated NADPH Oxidases Using NAD(PH) Fluorescence Lifetime Imaging.  
Bremer D\*, **Leben R\***, Mothes R, Radbruch H, Niesner R.  
Curr Protoc Cytom. 2017 Apr 3;80:9.52.1-9.52.14. doi: [10.1002/cpcy.20](https://doi.org/10.1002/cpcy.20).
- 2016 Longitudinal Intravital Imaging of the Retina Reveals Long-term Dynamics of Immune Infiltration and Its Effects on the Glial Network in Experimental Autoimmune Uveoretinitis, without Evident Signs of Neuronal Dysfunction in the Ganglion Cell Layer.  
Bremer D, Pache F, Günther R, Hornow J, Andresen V, **Leben R**, Mothes R, Zimmermann H, Brandt AU, Paul F, Hauser AE, Radbruch H, Niesner R.  
Front Immunol. 2016 Dec 23;7:642. doi: [10.3389/fimmu.2016.00642](https://doi.org/10.3389/fimmu.2016.00642). eCollection 2016.

\* equally contributing authors

# selected publications printed in A.3

**A.3. Printed versions of selected publications**



Article

# Phasor-Based Endogenous NAD(P)H Fluorescence Lifetime Imaging Unravels Specific Enzymatic Activity of Neutrophil Granulocytes Preceding NETosis

Ruth Leben <sup>1</sup>, Lennard Ostendorf <sup>2</sup>, Sofie van Koppen <sup>1,2</sup>, Asylkhan Rakhymzhan <sup>1</sup>, Anja E. Hauser <sup>3,4</sup>, Helena Radbruch <sup>2</sup> and Raluca A. Niesner <sup>1,\*</sup>

<sup>1</sup> Biophysical Analytics, German Rheumatism Research Center, 10117 Berlin, Germany; ruth.leben@drfz.de (R.L.); vakoppen.s@gmail.com (S.v.K.); asylkhan.rakhymzhan@drfz.de (A.R.)

<sup>2</sup> Neuropathology, Charité—Universitätsmedizin, 10117 Berlin, Germany; lennard.ostendorf@charite.de (L.O.); helena.radbruch@charite.de (H.R.)

<sup>3</sup> Intravital Microscopy and Immune Dynamics, Charité—Universitätsmedizin, 10117 Berlin, Germany; hauser@drfz.de

<sup>4</sup> Immune Dynamics, German Rheumatism Research Center, 10117 Berlin, Germany

\* Correspondence: niesner@drfz.de; Tel.: +49-30-2846-0708; Fax: +49-30-2846-0604

Received: 30 January 2018; Accepted: 17 March 2018; Published: 29 March 2018



**Abstract:** Time-correlated single-photon counting combined with multi-photon laser scanning microscopy has proven to be a versatile tool to perform fluorescence lifetime imaging in biological samples and, thus, shed light on cellular functions, both in vitro and in vivo. Here, by means of phasor-analyzed endogenous NAD(P)H (nicotinamide adenine dinucleotide (phosphate)) fluorescence lifetime imaging, we visualize the shift in the cellular metabolism of healthy human neutrophil granulocytes during phagocytosis of *Staphylococcus aureus* pHrodo™ beads. We correlate this with the process of NETosis, i.e., trapping of pathogens by DNA networks. Hence, we are able to directly show the dynamics of NADPH oxidase activation and its requirement in triggering NETosis in contrast to other pathways of cell death and to decipher the dedicated spatio-temporal sequence between NADPH oxidase activation, nuclear membrane disintegration and DNA network formation. The endogenous FLIM approach presented here uniquely meets the increasing need in the field of immunology to monitor cellular metabolism as a basic mechanism of cellular and tissue functions.

**Keywords:** NAD(P)H (nicotinamide adenine dinucleotide (phosphate)); fluorescence lifetime imaging; neutrophil granulocytes; NADPH oxidase; NETosis

## 1. Introduction

Since 1990, when Winfried Denk et al. first introduced the concept of two-photon laser-scanning microscopy and showed the unique benefits of ultra-short pulsed, near-infrared excitation for imaging highly-scattering biological tissue [1], this laser-based technology tremendously expanded its field of application, especially in neurosciences [2–4] and immunology [5] but also in other disciplines such as nephrology [6] or developmental biology. Over almost three decades of multi-photon microscopy research, we have gained unprecedented insights into cellular dynamics and communication in living organisms [7–12]. In the past years, the further development in multi-photon microscopy heads towards a better understanding of function in living cells, tissue or even organisms. In this sense, fluorescence lifetime imaging microscopy (FLIM) is a promising technology, which probes the immediate microenvironment of molecules, as the basis of cellular function [13–19]. FLIM generates

images in which contrast is obtained by the excited-state lifetime  $\tau$  of fluorescent molecules instead of their intensity, thus, having negligible experimental bias. Fluorescence lifetimes are typically in the range of a few nanoseconds, and are sensitive to ion concentrations, pH, viscosity and other cellular or extracellular parameters [20–23]. Various technologies have been developed to perform FLIM, both in frequency-domain and in time-domain. The time-correlated single-photon counting (TCSPC), which requires pulsed excitation as delivered by multi-photon microscopy, proved to be a highly versatile (but rather slow, i.e., typically 1–10 s/frame) technology to comprehensively acquire the molecular complexity within biological samples. TCSPC directly measures the fluorescence decay of all contained fluorophores, however, its thorough analysis remains a challenge [24,25].

A special application of FLIM is based on probing the endogenous fluorescence of the ubiquitous co-enzymes nicotinamide adenine dinucleotide (NADH) and nicotinamide adenine dinucleotide phosphate (NADPH), hereafter NAD(P)H. The fluorescence lifetime of the free NAD(P)H is much shorter than that of enzyme-bound NAD(P)H [22]. This allows us to distinguish between metabolically inactive, e.g., dormant or dying cells on the one hand and highly vital cells on the other. The fluorescence lifetime of the enzyme-bound NAD(P)H is strongly dependent on the NAD(P)H binding-site on the enzyme as measured under extra-cellular conditions in mixtures of NAD(P)H, various enzymes and corresponding substrates [26–28]. These differences are related both to the enzymes as well as to the coenzyme itself, as reported by Blacker et al. [29].

The members of the NADPH oxidase (NOX) family, i.e., NOX1 through 4 and DUOX1 and 2, are membrane-bound enzymes specifically expressed in different cell subsets [30]. They fulfill in the first line a pathogen-clearing function based on oxidative burst generation, next to signaling functions triggered by intracellular reactive oxygen species (ROS). Using NAD(P)H-FLIM, we have shown that a preferential activation of NOX enzymes against basic, survival enzymes leads to a specific increase in the fluorescence lifetime of enzyme-bound NAD(P)H, independent of cell type or NOX isotype [4,26,31].

Polymorphonuclear cells (PMNs) are cells of the innate immune system mainly engaged in clearing fungi and bacteria. After pathogen engulfment, the cells activate NADPH oxidases (mainly NOX2) to catalyze massive ROS production and, thus, to specifically degrade the pathogens, either within phagosomes or outside of the cells. If the pathogens are too large [32] or too numerous [33], neutrophils are able to enter a specific cell death program called NETosis [34]. In ROS are an essential part of the canonical NETosis pathway. Consequently, neutrophils of chronic granulomatous disease (CGD) patients, carrying mutations in the NOX system, are severely compromised in their ability to produce NETs [35]. In recent years, rapid/early NET generation without NETosis (sometimes named *vital NETosis*) has been demonstrated, that is under certain circumstances supposed to be ROS-independent [36]. However, different studies with various stimuli leading to NETosis show contradictory results in response to the same stimuli regarding this process. Therefore, we aimed to develop a reproducible unbiased and effective approach for quantitative analysis of NOX-dependent NETosis.

Here, we employ dynamic NAD(P)H-FLIM to study changes in the metabolic activity of human polymorphonuclear cells during pathogen-induced phagocytosis and found typical enzymatic finger-prints, which distinguish suicidal NETosis from other pathways of cell death. Our multi-photon TCSPC-based fluorescence lifetime imaging method in combination with the phasor-approach for data evaluation represents a generally valid, highly reliable technology, allowing the investigation of cellular metabolism as an underlying mechanism of life. Our approach takes advantage of the newest hardware developments allowing for optimal photon yield combined with self-written, model-free algorithms. Hence, with our approach we meet the increasing demand to monitor cellular metabolism at subcellular resolution, which gains attention especially in the field of immunology.

## 2. Results

### 2.1. Endogenous NAD(P)H Fluorescence Lifetime Imaging Unravels the Metabolism of Innate Immune Cells on an Enzymatic Basis

The ubiquitous coenzymes NADH and NADPH, hereafter NAD(P)H, are key players of the basic metabolism as well as of various other functions in cells. At the same time, they are endogenous fluorescence probes, since they can be selectively detected by two-photon microscopy when they are excited at 760 nm and their fluorescence is detected at 460 nm (Figure 1b). The fluorescence decay of the coenzymes contains a short-lived component, i.e., the fluorescence decay of free NAD(P)H ( $\tau_1 \sim 450$  ps) and a longer-lived component, i.e., the fluorescence decay of enzyme-bound NAD(P)H ( $\tau_2$ ). Enzyme-bound NAD(P)H is involved in various biochemical reactions within the cell, catalyzed by the enzymes to which these co-enzymes are bound (Figure 1b). The short fluorescence lifetime is the average over all conformational structures of NAD(P)H, spanning between approx. 200 and 700 ps.

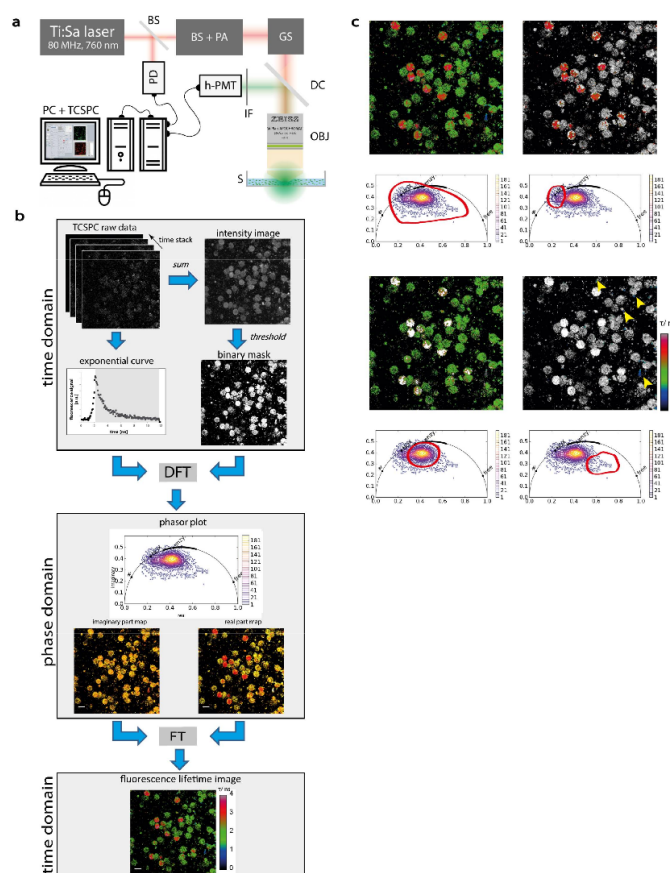


**Figure 1.** Acquisition and evaluation of NAD(P)H fluorescence lifetime imaging data in cells (a) Experimental setup. The beam of a 80MHz pulsed titanium sapphire laser (Ti:Sa) at 760 nm passes a beam shaper (BS), including a telescope and pulse compressor, and a  $\lambda/2$  plate-based power attenuator (PA). A galvoscan (GS) scans the beam over the sample (S). The laser beam is focused by a  $20\times$  water immersion NA 1.05 objective (OBJ). Excitation and emission light are separated by a dichroic

mirror (DC, 695 nm), the emission light passes an interference filter (IF 466/40) and is time-resolved detected by a time-correlated single photon counter (TCSPC) equipped with a Hybrid-PMT (h-PMT). A beam splitter (BS) reflects 5-10% of the laser light onto a photodiode (PD) to time-synchronize the TCSPC. (b) Data acquisition and evaluation. The TCSPC raw data containing 227 single images form in a time-domain plot the typical exponential curve. A binary mask to exclude background pixels is created by thresholding the sum image of the single 227 images of the decay curve. Each pixel in the raw data set is converted by discrete Fourier Transformation to the phase domain (with 80MHz modulation frequency); each pixel has now a real and an imaginary part, which can be shown as real and imaginary part maps and give the coordinates of the phasor plot respectively. The phasors of free NAD(P)H, NAD(P)H bound to metabolic, survival enzymes and NADPH bound to NADPH oxidase are marked on the normalized half circle from shorter (right) to longer (left) lifetimes. In order to re-calculate a fluorescence lifetime image, the phasor data need to be back-transformed to time domain by continuous Fourier transform. (c) Back grating of data points in phasor plot to image pixels. In the phasor plot freehand selected data points (red line) are colored represented in the lifetime image in contrast to the unselected pixel shown in grayscale, to visualize the correspondence between populations in the phasor plot to those in the lifetime images. The data points reaching toward “free NAD(P)” are blue in the lifetime image and are marked by arrow, due to bad contrast from blue to black. Scale bar is 20  $\mu\text{m}$ . In the phasor plots in b and c “free” encodes free NAD(P)H, “enzym.” NAD(P)H bound to metabolic enzymes, “NOX” NADPH bound to NADPH oxidases and “#” oxidized lipids as defined by Datta et al. [37].

By transferring the fluorescence decay of cellular NAD(P)H to the frequency domain using the phasor approach to FLIM, we characterized the enzymatic activity of innate immune cells, i.e., polymorphonuclear cells and CD11b<sup>+</sup> monocytes (Figure 1b). Cells with generally low metabolic activity display a high concentration of free NAD(P)H and are located within the half-circle near to values between 400 and 450 ps, characteristic for free NAD(P)H. We previously found that cells treated with KCN or NaCN, i.e., dying cells mainly containing free NAD(P)H [38], display short fluorescence lifetimes of approx. 450 ps [26,31]. Moreover, cells kept on ice, at 4 °C showed a similar fluorescence lifetime behavior [13]. Metabolically active cells, are located next to values between 1500 and 2500 ps in the phasor plot. If the cells are stimulated to activate specific enzymes, such as phorbol-myristate-acetate (PMA) mediated stimulation of the NADPH oxidase family in monocytes (Figure 2b), the signal in the phasor plot shifts towards 3600 ps.

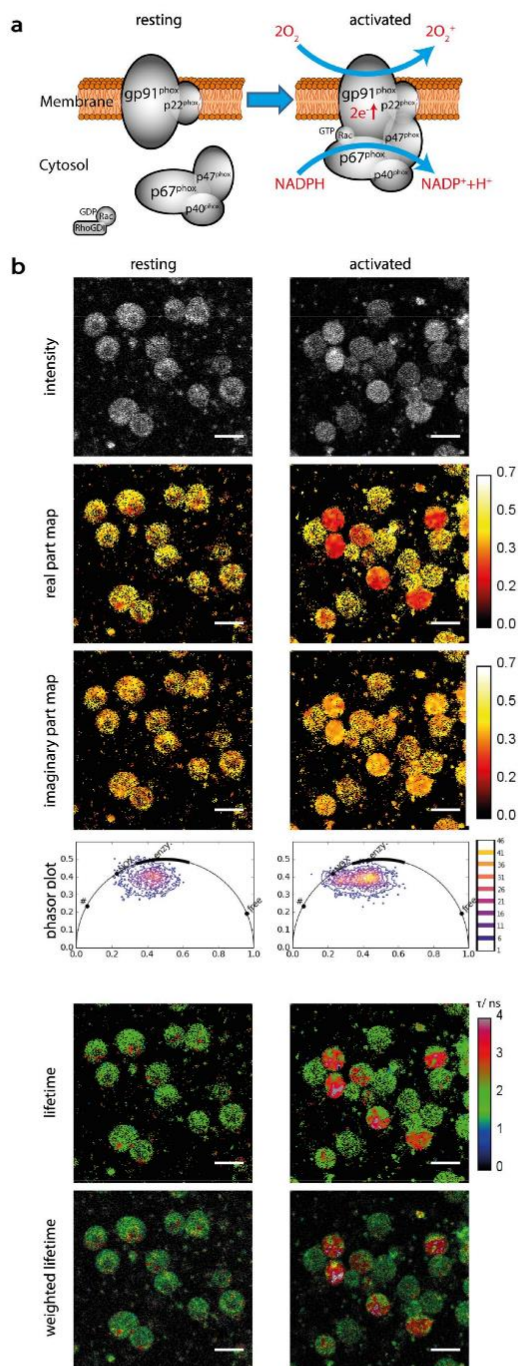


**Figure 2.** Selective detection of NAD(P)H-dependent enzymatic activity (a) Resting and active NADPH oxidase 2 (NOX2). The subunits gp91<sup>phox</sup> and p22<sup>phox</sup> form the membrane-associated component of the enzyme, whereas p67<sup>phox</sup>, p47<sup>phox</sup> and p40<sup>phox</sup> the cytosolic cyclic hetero-trimer. If stimuli, e.g., pathogens, are present, the cytosolic part translocates to the membrane-associated part under phosphorylation of p67 and the activable enzyme assembles. The assembled NOX2 is now able to bind

NADPH and to catalyze the oxidation of  $O_2$  to the highly reactive  $O_2^-$ . This is rapidly transformed in chain reaction to various reactive oxygen species (ROS). (b) Validation of the FLIM approach on resting and PMA-stimulated monocytes, respectively. The pixel values in the real and imaginary part maps reach due to normalization from 0 to 1 and from 0 to 0.5, respectively. The calibration bar was set to 0 to 0.7 for better visibility. The images in the sixth row show fluorescence lifetime images weighted by the intensity (sum) image. Green color in the lifetime images indicates the resting status; red activated cells, in which NADPH binds to NOX2. These two populations can also be identified in the phasor plots, since the activated cells are displayed at the position marked as NADPH oxidase, not present in resting cells. Scale bar = 20  $\mu$ m. In the phasor plots in b and c "free" encodes free NAD(P)H, "enzym." NAD(P)H bound to metabolic enzymes, "NOX" NADPH bound to NADPH oxidases and "#" oxidized lipids as defined by Datta et al.

Since the NADPH oxidase NOX2—the main catalyzer of oxidative burst and highly expressed in PMNs—plays a central role in the process of phagocytosis, we focus on the detection of its activation during phagocytosis of *S. aureus* coated beads by means of NAD(P)H-FLIM.

## 2.2. NADPH Oxidase Activation Co-Localizes with Phagocytosed *Staphylococcus aureus* Beads

Co-cultures of PMNs isolated from human blood with *S. aureus*-coated *pHrodo* beads were imaged over up to 80 min by conventional two-photon fluorescence microscopy and NAD(P)H-FLIM. Thereby, engulfment of the beads, the corresponding change in pH value and the activation of NOX2 catalyzing the oxidative burst were correlatively monitored (*Movie 1*).

Using a feed-back loop between the fluorescence lifetime images and the phasor plot, we show that PMNs freshly mixed with *pHrodo* beads and kept at 37 °C have a high basic enzymatic activity, typical for their survival function. After the beads are engulfed by PMNs, the pH value in their microenvironment decreases a process concurrent with the appearance of red fluorescence of the beads. The *pHrodo* beads alone are non-fluorescent in medium (Figure S1). At the sites where acidic *pHrodo* beads are present, the NAD(P)H fluorescence lifetime in PMNs shifts towards longer values, i.e., 3600 ps. Hence, the basic enzymatic activity at these sites shifts towards a preferential enzymatic activity of catalyzers of oxidative burst—mainly NOX2 in PMNs (Figure 3). In blood-derived PMNs from two healthy individuals ( $n = 150$  cells per individual), we measured a significant increase of the real component in the phasor plots in the range 0.1–0.5 at the initial time point and 80 min after adding *S. aureus* *pHrodo* beads, respectively, i.e.,  $p = 0.02$  using Student *t*-test. Interestingly, *pHrodo E. coli* beads have been used only recently to correlate NETosis and phagocytosis [39].

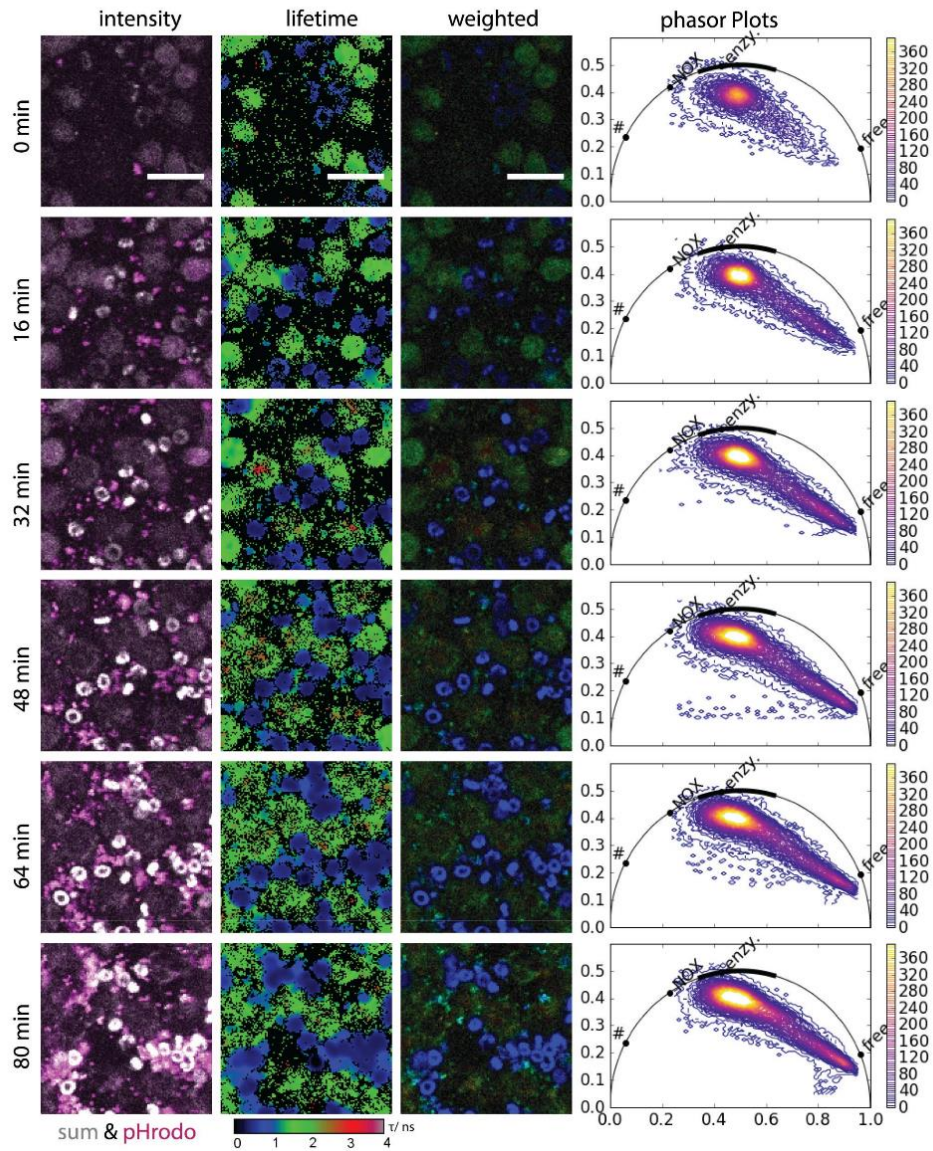


**Figure 3.** NAD(P)H-metabolism during phagocytosis. Selected frames of time-lapse NAD(P)H-FLIM data of healthy human neutrophil granulocytes phagocytosing *Staphylococcus aureus* pHrodo™ beads (representative for  $n = 150$  cells per individual, two healthy individuals). The first row shows the merged images of NAD(P)H fluorescence (grey) and acidic pHrodo™ beads (magenta). The second and third rows show corresponding original and intensity-weighted fluorescence lifetime images. During the imaging time, the beads are taken up by the neutrophils and became fluorescent due to the pH shift within the phagosomes. Both the color map of FLIM images and the phasor plots show over time a shift to activated NADPH oxidase 2 followed by a shift towards free NAD(P)H, which indicates cellular death. For a better visibility, only a  $124 \times 124$  pixel area is shown from the original data (Movie 1). The phasor plots rely on the total area of  $512 \times 512$  pixels, the movie is shown in original dimensions. In the movie, the ROI showed in the figure is marked. Scale bar =  $20 \mu\text{m}$ . In the phasor plots in b and c “free” encodes free NAD(P)H, “enzy.” NAD(P)H bound to metabolic enzymes, “NOX” NADPH bound to NADPH oxidases and “#” oxidized lipids as defined by Datta et al.

After approx. 40 min, the NAD(P)H fluorescence lifetime in several PMNs significantly shifts towards 450 ps, towards low enzymatic activity, i.e., a decrease in the real component of the phasor plot in the range 0.6 to 1.0,  $p = 0.01$  by Student  $t$ -test. Since this behavior is similar to that of PMNs as well as other cells after treatment with NaCN, we attributed it to cell death (Figure 3). In this context, we question whether the cell death following NOX2 activation is associated with NETosis, as a PMN-typical clearing mechanism, or whether it is a general mechanism preceding any pathway leading to cell death (Figure 4).

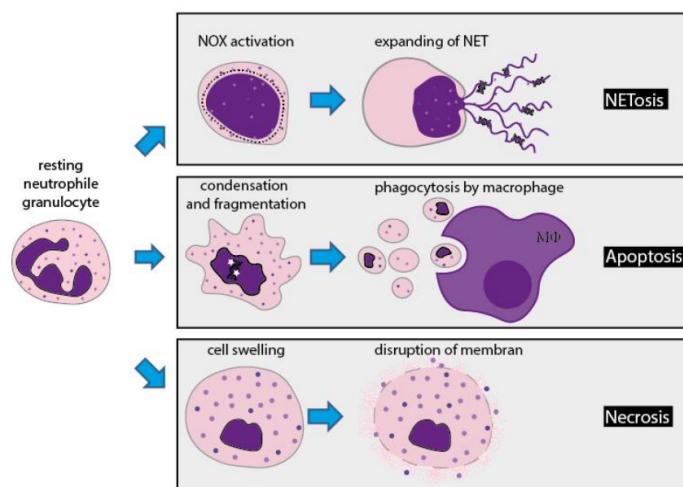


**Figure 4.** NETosis vs. apoptosis/necrosis. Three different pathways of cellular death of neutrophil granulocytes. (a) NETosis is the beneficial suicide. If the cells are outnumbered by pathogens, the cell nuclei round up and almost fill the cell while the nuclear membrane disintegrates and the nuclear content merges with the content of the granules. The cell contracts, DNA and granular content leak out the cells and forms NET. NET immobilizes pathogens extracellularly, making them an easy target for other immune cells. (b) Apoptosis is the programmed (natural) cell death. The cell shrinks, the chromatin condenses and the cell membrane blebs. The cell disintegrates to fragments, which are subsequently phagocytosed e.g., by macrophages (MΦ). (c) Necrosis is the traumatic cell death. The cell swells up due to acute cellular injury, until the cell membrane disrupts and releases all cellular contents uncontrolled into the extracellular space. Both NETosis and necrosis leads, in contrast to apoptosis, to tissue inflammation.

### 2.3. NADPH Oxidase Activation Precedes NETosis but Not Other Pathways of Cell Death

We added Vybrant DyeCycle Green™ to the co-cultures of human PMNs and *S. aureus* pHrodo beads in order to in vivo label the cell nuclei and monitored the process of phagocytosis as previously described. Synchronously acquired fluorescence images of the cell nuclei, of pHrodo beads and NAD(P)H-FLIM maps of PMNs reveal that exploded, misshaped nuclei co-localize with NOX2 over-activation and with phagocytosed beads of low pH, (Figure 5a). The extent of activated NOX (red regions in the NAD(P)H fluorescence lifetime maps) in cells with multi-lobar nuclei, i.e., healthy, intact PMNs, is much lower when compared to dying cells with a large, misshaped nucleus. We could detect phagocytosis but not the early NETosis observed using several vital pathogens, including *S. aureus* [40–42].

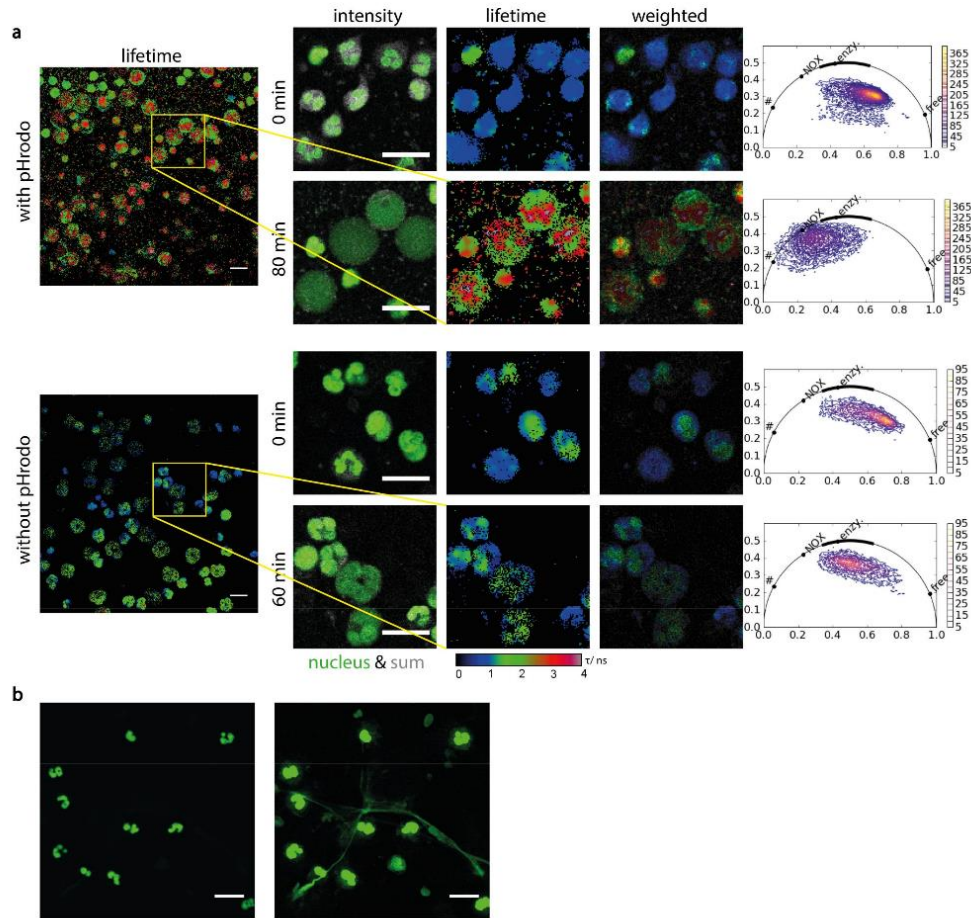


**Figure 5.** Orchestration of NADPH oxidase activation, cellular death and NET formation (a) Comparison of neutrophil metabolism in presence (first two rows) and absence (last two rows) of *Staphylococcus aureus* pHrodo™ beads ( $n = 120$  cells per individual and condition, two healthy individuals). The images were picked up at the beginning of the measurement, shortly after the pHrodo™ were added to the cells, and 80 or 60 min later. First column show the sum image (grey) merged with Vybrant DyeCycle Green™ stained DNA. The second and third column show original and intensity-weighted fluorescence lifetime images. Both the color map of FLIM images and phasor plots show the activation of NADPH oxidase in the neutrophils in presence of pHrodo™ beads after 80 min, whereas NETosis can be seen in the Vybrant DyeCycle images. The FLIM images and phasor plots of the other rows remain almost the same, even the nucleus of neutrophils in absence of the beads are slightly swollen. For better visibility, a  $124 \times 124$  pixel area is displayed from the original  $512 \times 512$  pixel images. The phasor plots rely on the total area of  $512 \times 512$  pixels. (b) NETs after applying shear forces. DNA was stained by Vybrant DyeCycle Green™, showing in the higher-contrast image the formation of fibrous NETs. Scale bar =  $20 \mu\text{m}$ . In the phasor plots in a “free” encodes free NAD(P)H, “enzym.” NAD(P)H bound to metabolic enzymes, “NOX” NADPH bound to NADPH oxidases and “#” oxidized lipids as defined by Datta et al.

In contrast, PMNs imaged in the same way after 4 h, when they are naturally dying and without undergoing phagocytosis, do not show a shift in enzymatic activity towards NOX2 activation. In the phasor plot, their signal shifts from the high basic enzymatic activity to the typical signal of free

coenzymes, indicating cell death. Also, the nuclei of these cells change from a multi-lobar appearance to a diffuse, round shape in the process of cell death (Figure 5b). The shift in the real component of the phasor plot at the initial time point in PMNs with and without pHrodo and after 60 min, without pHrodo is statistically not significant. In contrast, after 80 min of treatment with pHrodo beads led to a significant increase of the real component in the phasor plot ( $p = 0.002$  Student  $t$ -test) as compared to untreated, dying PMNs (without pHrodo). If shear forces, e.g., through shaking, were applied to the co-cultures of PMNs and *S. aureus* beads, a fibrillary network typical for the process of NETosis was observed (Figure 5b). Hence, the observed misshaped PMN nuclei concretely lead in this situation to NET formation and to immobilization of pathogens.

### 3. Discussion

The use of ultra-short pulsed near-infrared or infrared lasers in intravital multi-photon microscopy boosted our general understanding of highly developed mammalian organisms on a cellular basis in health and disease. Nevertheless, the benefits of the pulsed radiation sources are not only related to the observation of cellular motility and communication but opens new perspectives for the study of cellular and tissue functions, at a molecular level. A prominent example of how cellular and tissue function can be quantified is given by fluorescence lifetime imaging (FLIM). Time-domain FLIM, in general, and time-correlated single photon counting, in particular, require ultra-short pulsed excitation of chromophore molecules followed by a radiation-free time-period during which the fluorescence decay is acquired. The fluorescence decay contains detailed information on the molecular environment exclusively deciding cellular functions and, thus, on the general state of tissues, of organs and of the entire organism. Despite its high potential, up to now FLIM has not reached broad application in biosciences and biomedicine due to technical drawbacks of the complex electronics leading to a poor photon management, especially when endogenous chromophores such as the ubiquitous metabolic co-enzymes NADH and NADPH are monitored. The difficult data interpretation caused by slow, less robust numerical approaches for data evaluation further impeded FLIM application in these research fields. First, latest technological developments allowing the acquisition of high fluorescence signals within the shortest time and model-free evaluation algorithms, as we present in this work, are able to change this paradigm and may enable a broader application for FLIM in life sciences. In order to demonstrate the high potential of our FLIM approach for answering biologically relevant questions, we focused on the phenomenon of phagocytosis in polymorphonuclear cells (neutrophil granulocytes) and monitored it by endogenous NAD(P)H-FLIM over time.

Polymorphonuclear cells (PMNs) are fulfilling their main function, i.e., the clearing of pathogens, especially fungi and bacteria, using various mechanisms. Among these, phagocytosis encompasses pathogen engulfment, followed by activation of NADPH oxidase 2 (NOX2), catalyzing the oxidative burst, and causing complete degradation of the pathogens. In addition, PMNs can undergo NETosis as a pathogen killing process. The molecular mechanisms and dynamics in vivo are not fully understood. Variation in study designs and readout parameters are confusing our understanding of NET formation, for example.

If pathogens outnumber the granulocytes, in order to still ensure their clearing, the cells proceed to programmed cellular death: their nuclear membrane disintegrates, and the leaking DNA forms networks, which can trap the pathogens. This process is known as NETosis. The process of NETosis and its relevance for the clearing of various pathogens have been extensively investigated and discussed. Moreover, a link between NADPH oxidase, phagocytosis and NETosis has been demonstrated by several research groups [43,44].

We present NAD(P)H-FLIM on PMNs isolated from human blood as a unique approach to analyze the association between phagocytically induced NETosis and NOX activation. Furthermore, the NAD(P)H-dependent enzymatic fingerprint spans cellular functions between mere survival and catalysis of massive reactive oxygen species production, aiming to destroy pathogens. Several recent studies showed a direct link between the phenomenon of oxidative burst or oxidative stress and long

fluorescence lifetimes detected in cells and tissues. Like Blaker et al., we detected the activation of NADPH-dependent enzymes, i.e., in this context the NADPH oxidases family, to lead to NADPH fluorescence lifetimes of approx. 3600 ps [26,29]. Datta et al. demonstrated that oxidized lipids, as the product of oxidative stress, display an even longer fluorescence lifetime reaching over 7000 ps [37,45]. In contrast to previous studies, which used NOX inhibitors, ROS scavengers or genetic models to address the role of NOX for NETosis induction indirectly, we present here an approach to monitor the enzymatic activity in real time. We found that over-activation of NADPH oxidase, co-localizing with pathogen-containing phagosomes, precedes cell death indicated by high concentrations of free NAD(P)H. Even before cell death, we observed in cells with over-activated NADPH oxidases nuclear membrane disintegration and DNA network formation under the influence of shear forces. Thus, we provided direct evidence that NADPH oxidase activation correlates in time and space with the process of NETosis in PMNs phagocytosing *S. aureus* beads. In contrast, nuclear membrane disintegration and cell death indicated by low or no NAD(P)H-dependent enzymatic activity are not necessarily taking place in a sequential manner but rather arbitrary, following rules that need further investigations. The correlation between NADPH oxidase activation, membrane disintegration and NETosis-related cell death does not hold true for other cell death pathways, since PMNs imaged at late time points after their isolation show high concentration of free NAD(P)H, misshaped cell nuclei, generally indicative for cell death, but no sign of NADPH oxidase activation at any time.

Besides the quite diverse imaging approaches of NETosis in vitro such as imaging flow cytometry or fluorescence microscopy [39,46–48], NADPH-FLIM phasor analysis has the advantage not to depend on external labeling as NAD(P)H auto-fluorescence signal is used. Therefore, we believe that this approach has the unique potential to investigate the role of NOX-dependent NETosis also in vivo as we have shown the feasibility of intravital NAD(P)H FLIM in several inflammatory mouse models [3,4,26–28].

The protocol presented in this study opens new perspectives for monitoring immune cell metabolism, both in vitro and in vivo. Moreover, we expect that it will facilitate screening molecules having impact on the signaling cascades which trigger NOX-dependent NET formation and, thus, will become a useful tool for designing new therapeutic strategies.

#### 4. Materials and Methods

##### 4.1. Two-Photon Microscopy Setup for Fluorescence Lifetime Imaging

Experiments were performed using a specialized multi-photon laser-scanning microscope for fluorescence lifetime imaging (FLIM) as displayed in Figure 1a [49]. In brief, the beam of a tuneable fs-pulsed Ti:Sa laser (wavelength range 700–1080 nm, 140 fs, 80 MHz, Cameleon Ultra II, Coherent, Dieburg, Germany) is scanned by two galvanometric mirrors and focused into the sample by an objective lens for deep-tissue imaging (20× dipping lens, NA 1.05, WD 1 mm—Zeiss, Jena, Germany). The resulting fluorescence signal is detected and analyzed either by a TCSPC point detector (FLIM, LaVision Biotech GmbH, Bielefeld, Germany) or photomultiplier tubes (H7422-40, Hamamatsu, Japan). Spectral discrimination of the fluorescence signal was achieved by appropriate dichroic mirrors and interference filters. NADH and NADPH (NAD(P)H) were excited at 760 nm and detected through an interference filter at  $460 \pm 30$  nm. The time step (bin) was 27 ps and the time window for measuring the fluorescence decay was 12 ns. Both pHrodo and Vybrant DyeCycle Green™ (for nuclear staining of live cells) were excited at 760 nm as well and detected at  $593 \pm 20$  nm (pHrodo) and  $525 \pm 25$  nm (Vybrant DyeCycle Green™) respectively simultaneous to NAD(P)H detection.

##### 4.2. Neutrophil Granulocytes and CD11b<sup>+</sup> Monocytes—Isolation from Human Blood

Neutrophil granulocytes (polymorphonuclear cells) were isolated according to published protocols [50]. In summary, granulocytes were isolated from 10 mL of heparin-anticoagulated whole blood with two separate density-gradients under sterile conditions, guarantying minimal pre-activation

of the cells of interest by *no touch isolation*. Monocytes were isolated from whole blood as previously described by us [27].

#### 4.3. The Phasor Approach to FLIM

In time-domain FLIM, the determination of a fluorescence lifetime is based on fitting the histogram of the photon delay exponentially, while the decay constant is the fluorophore lifetime. Ideally, only a single species of fluorophores populates the observed excitation volume and the temporal decay is mono-exponential. However, most biological samples are highly heterogeneous, which means that their fluorescence decay contains two or even more lifetime components and complicates the analysis, especially if the number of lifetime components is unknown. In that case, the phasor approach [51] is a promising analysis method, since it is model-free. Here the lifetime data are measured in time domain and transferred to a virtual phase domain by numerically calculating the discrete Fourier transform. The sum of all fluorescence lifetimes contained in a pixel is calculated from the normalized real and imaginary result. In case of a mono-exponential decay, plotting those results will give a position on a half-circle termed the phasor ( $r = 0.5$ , center at  $(0.5/0)$ ). If the excitation volume contains two fluorescent species, this position in the plot will lie along the straight line connecting the phasors of the pure components. If there are three species, this position would lie within the triangle formed by the line connecting the phasors of the pure components. The phasor analysis was performed using our own routines written in Python and it is available as executable files upon request. Our data analysis was verified by resting and PMA stimulated healthy human monocytes (Figure 2b).

#### 4.4. Preparation of the Phagocytosis Assay

After isolation, the PMN cell count was adjusted to  $1 \times 10^6$  per mL and suspended in RPMI medium without phenol red (Thermo Fisher Scientific, Berlin, Germany) in 12 well plates. Vybrant DyeCycle Green™ nuclear stain (Thermo Fisher Scientific, Berlin, Germany) was added. Directly prior to imaging, pHrodo™ beads conjugated with *Staphylococcus aureus* (Thermo Fisher Scientific, Berlin, Germany) were suspended in 1 mL RPMI medium and introduced drop by drop into the cell suspension, while controlling for a suitable ratio of bacteria to PMNs in bright-field microscopy (typically between 10:1 and 20:1). During the entire imaging experiment, the cell suspension was kept at 37 °C.

**Supplementary Materials:** Supplementary materials can be found at <http://www.mdpi.com/1422-0067/19/4/1018/s1>.

**Acknowledgments:** We thank Nikolaus Deigendesch for very helpful discussions during the experiments as well as Robert Günther, Peggy Mex and Ralf Uecker for excellent technical assistance. We acknowledge the Deutsche Forschungsgemeinschaft under grant FOR2165 (NI1167/4-2), TRR130 (C01) to Raluca A. Niesner, FOR2165 (HA5354/6-2), SPP1937 (HA5354/8-1) and TRR130 (P17, C01) to Anja E. Hauser, TRR130 (P17) to Helena Radbruch and SFB650 training group to Lennard Ostendorf for financial support.

**Author Contributions:** Ruth Leben, Lennard Ostendorf, Anja E. Hauser, Helena Radbruch and Raluca A. Niesner designed and performed research and analyzed data. Sofie van Koppen and Asylkhan Rakhymzhan performed research and analyzed data. Ruth Leben, Lennard Ostendorf and Raluca A. Niesner wrote the manuscript.

**Conflicts of Interest:** The authors declare no conflict of interest.

#### References

1. Denk, W.; Strickler, J.H.; Webb, W.W. Two-photon laser scanning fluorescence microscopy. *Science* **1990**, *248*, 73–76. [[CrossRef](#)] [[PubMed](#)]
2. Nimmerjahn, F.; Lux, A.; Albert, H.; Woigk, M.; Lehmann, C.; Dudziak, D.; Smith, P.; Ravetch, J.V. FcγR4 deletion reveals its central role for IgG2a and IgG2b activity in vivo. *Proc. Natl. Acad. Sci. USA* **2010**, *107*, 19396–19401. [[CrossRef](#)] [[PubMed](#)]

3. Bayerl, S.H.; Niesner, R.; Cseresnyes, Z.; Radbruch, H.; Pohlan, J.; Brandenburg, S.; Czabanka, M.A.; Vajkoczy, P. Time lapse in vivo microscopy reveals distinct dynamics of microglia-tumor environment interactions—a new role for the tumor perivascular space as highway for trafficking microglia. *Glia* **2016**, *64*, 1210–1226. [[CrossRef](#)] [[PubMed](#)]
4. Radbruch, H.; Bremer, D.; Guenther, R.; Cseresnyes, Z.; Lindquist, R.; Hauser, A.E.; Niesner, R. Ongoing Oxidative Stress Causes Subclinical Neuronal Dysfunction in the Recovery Phase of EAE. *Front. Immunol.* **2016**, *7*, 92. [[CrossRef](#)] [[PubMed](#)]
5. Hauser, A.E.; Junt, T.; Mempel, T.R.; Sneddon, M.W.; Kleinstein, S.H.; Henrickson, S.E.; von Andrian, U.H.; Shlomchik, M.J.; Haberman, A.M. Definition of germinal-center B cell migration in vivo reveals predominant intrazonal circulation patterns. *Immunity* **2007**, *26*, 655–667. [[CrossRef](#)] [[PubMed](#)]
6. Dunn, K.W.; Sandoval, R.M.; Molitoris, B.A. Intravital imaging of the kidney using multiparameter multiphoton microscopy. *Nephron Exp. Nephrol.* **2003**, *94*, e7–e11. [[CrossRef](#)] [[PubMed](#)]
7. Reismann, D.; Stefanowski, J.; Gunther, R.; Rakhymzhan, A.; Matthys, R.; Nutzi, R.; Zehentmeier, S.; Schmidt-Bleek, K.; Petkau, G.; Chang, H.D.; et al. Longitudinal intravital imaging of the femoral bone marrow reveals plasticity within marrow vasculature. *Nat. Commun.* **2017**, *8*, 2153. [[CrossRef](#)] [[PubMed](#)]
8. Roth, K.; Oehme, L.; Zehentmeier, S.; Zhang, Y.; Niesner, R.; Hauser, A.E. Tracking plasma cell differentiation and survival. *Cytometry A* **2014**, *85*, 15–24. [[CrossRef](#)] [[PubMed](#)]
9. Zehentmeier, S.; Roth, K.; Cseresnyes, Z.; Sercan, O.; Horn, K.; Niesner, R.A.; Chang, H.D.; Radbruch, A.; Hauser, A.E. Static and dynamic components synergize to form a stable survival niche for bone marrow plasma cells. *Eur. J. Immunol.* **2014**, *44*, 2306–2317. [[CrossRef](#)] [[PubMed](#)]
10. Rakhymzhan, A.; Leben, R.; Zimmermann, H.; Gunther, R.; Mex, P.; Reismann, D.; Ulbricht, C.; Acs, A.; Brandt, A.U.; Lindquist, R.L.; et al. Synergistic Strategy for Multicolor Two-photon Microscopy: Application to the Analysis of Germinal Center Reactions In Vivo. *Sci. Rep.* **2017**, *7*, 7101. [[CrossRef](#)] [[PubMed](#)]
11. Tas, J.M.; Mesin, L.; Pasqual, G.; Targ, S.; Jacobsen, J.T.; Mano, Y.M.; Chen, C.S.; Weill, J.C.; Reynaud, C.A.; Browne, E.P.; et al. Visualizing antibody affinity maturation in germinal centers. *Science* **2016**, *351*, 1048–1054. [[CrossRef](#)] [[PubMed](#)]
12. Victora, G.D.; Nussenzweig, M.C. Germinal centers. *Annu. Rev. Immunol.* **2012**, *30*, 429–457. [[CrossRef](#)] [[PubMed](#)]
13. Radbruch, H.; Bremer, D.; Mothes, R.; Gunther, R.; Rinnenthal, J.L.; Pohlan, J.; Ulbricht, C.; Hauser, A.E.; Niesner, R. Intravital FRET: Probing Cellular and Tissue Function in Vivo. *Int. J. Mol. Sci.* **2015**, *16*, 11713–11727. [[CrossRef](#)] [[PubMed](#)]
14. Rinnenthal, J.L.; Bornchen, C.; Radbruch, H.; Andresen, V.; Mossakowski, A.; Siffrin, V.; Seelemann, T.; Spiecker, H.; Moll, I.; Herz, J.; et al. Parallelized TCSPC for dynamic intravital fluorescence lifetime imaging: Quantifying neuronal dysfunction in neuroinflammation. *PLoS ONE* **2013**, *8*, e60100. [[CrossRef](#)] [[PubMed](#)]
15. Kumar, S.; Dunsby, C.; De Beule, P.A.; Owen, D.M.; Anand, U.; Lanigan, P.M.; Benninger, R.K.; Davis, D.M.; Neil, M.A.; Anand, P.; et al. Multifocal multiphoton excitation and time correlated single photon counting detection for 3-D fluorescence lifetime imaging. *Opt. Express* **2007**, *15*, 12548–12561. [[CrossRef](#)] [[PubMed](#)]
16. Lee, K.C.; Siegel, J.; Webb, S.E.; Leveque-Fort, S.; Cole, M.J.; Jones, R.; Dowling, K.; Lever, M.J.; French, P.M. Application of the stretched exponential function to fluorescence lifetime imaging. *Biophys. J.* **2001**, *81*, 1265–1274. [[CrossRef](#)]
17. Suhling, K.; French, P.M.; Phillips, D. Time-resolved fluorescence microscopy. *Photochem. Photobiol. Sci.* **2005**, *4*, 13–22. [[CrossRef](#)] [[PubMed](#)]
18. Krstajic, N.; Levitt, J.; Poland, S.; Ameer-Beg, S.; Henderson, R. 256 × 2 SPAD line sensor for time resolved fluorescence spectroscopy. *Opt. Express* **2015**, *23*, 5653–5669. [[CrossRef](#)] [[PubMed](#)]
19. Krstajic, N.; Poland, S.; Levitt, J.; Walker, R.; Erdogan, A.; Ameer-Beg, S.; Henderson, R.K. 0.5 billion events per second time correlated single photon counting using CMOS SPAD arrays. *Opt. Lett.* **2015**, *40*, 4305–4308. [[CrossRef](#)] [[PubMed](#)]
20. Chowdhury, M.H.; Lakowicz, J.R.; Ray, K. Ensemble and Single Molecule Studies on the Use of Metallic Nanostructures to Enhance the Intrinsic Emission of Enzyme Cofactors. *J. Phys. Chem. C Nanomater. Interfaces* **2011**, *115*, 7298–7308. [[CrossRef](#)] [[PubMed](#)]
21. Kierdaszuk, B.; Malak, H.; Gryczynski, I.; Callis, P.; Lakowicz, J.R. Fluorescence of reduced nicotinamides using one- and two-photon excitation. *Biophys. Chem.* **1996**, *62*, 1–13. [[CrossRef](#)]

22. Lakowicz, J.R.; Szmacinski, H.; Nowaczyk, K.; Johnson, M.L. Fluorescence lifetime imaging of free and protein-bound NADH. *Proc. Natl. Acad. Sci. USA* **1992**, *89*, 1271–1275. [[CrossRef](#)] [[PubMed](#)]
23. Agronskaia, A.V.; Tertoolen, L.; Gerritsen, H.C. Fast fluorescence lifetime imaging of calcium in living cells. *J. Biomed. Opt.* **2004**, *9*, 1230–1237. [[CrossRef](#)] [[PubMed](#)]
24. Elson, D.; Requejo-Isidro, J.; Munro, I.; Reavell, F.; Siegel, J.; Suhling, K.; Tadrous, P.; Benninger, R.; Lanigan, P.; McGinty, J.; et al. Time-domain fluorescence lifetime imaging applied to biological tissue. *Photochem. Photobiol. Sci.* **2004**, *3*, 795–801. [[CrossRef](#)] [[PubMed](#)]
25. Wahl, M.; Rahn, H.J.; Rohlicke, T.; Kell, G.; Nettels, D.; Hillger, F.; Schuler, B.; Erdmann, R. Scalable time-correlated photon counting system with multiple independent input channels. *Rev. Sci. Instrum.* **2008**, *79*, 123113. [[CrossRef](#)] [[PubMed](#)]
26. Mossakowski, A.A.; Pohlan, J.; Bremer, D.; Lindquist, R.; Millward, J.M.; Bock, M.; Pollok, K.; Mothes, R.; Viohl, L.; Radbruch, M.; et al. Tracking CNS and systemic sources of oxidative stress during the course of chronic neuroinflammation. *Acta Neuropathol.* **2015**, *130*, 799–814. [[CrossRef](#)] [[PubMed](#)]
27. Bremer, D.; Leben, R.; Mothes, R.; Radbruch, H.; Niesner, R. Method to Detect the Cellular Source of Over-Activated NADPH Oxidases Using NAD(P)H Fluorescence Lifetime Imaging. *Curr. Protoc. Cytom.* **2017**, *80*. [[CrossRef](#)]
28. Radbruch, H.; Mothes, R.; Bremer, D.; Seifert, S.; Kohler, R.; Pohlan, J.; Ostendorf, L.; Gunther, R.; Leben, R.; Stenzel, W.; et al. Analyzing Nicotinamide Adenine Dinucleotide Phosphate Oxidase Activation in Aging and Vascular Amyloid Pathology. *Front. Immunol.* **2017**, *8*, 844. [[CrossRef](#)] [[PubMed](#)]
29. Blacker, T.S.; Mann, Z.F.; Gale, J.E.; Ziegler, M.; Bain, A.J.; Szabadkai, G.; Duchon, M.R. Separating NADH and NADPH fluorescence in live cells and tissues using FLIM. *Nat. Commun.* **2014**, *5*, 3936. [[CrossRef](#)] [[PubMed](#)]
30. Babior, B.M. NADPH oxidase. *Curr. Opin. Immunol.* **2004**, *16*, 42–47. [[CrossRef](#)] [[PubMed](#)]
31. Niesner, R.; Narang, P.; Spiecker, H.; Andresen, V.; Gericke, K.H.; Gunzer, M. Selective detection of NADPH oxidase in polymorphonuclear cells by means of NAD(P)H-based fluorescence lifetime imaging. *J. Biophys.* **2008**, *2008*, 602639. [[CrossRef](#)] [[PubMed](#)]
32. Branzk, N.; Lubojemska, A.; Hardison, S.E.; Wang, Q.; Gutierrez, M.G.; Brown, G.D.; Papayannopoulos, V. Neutrophils sense microbe size and selectively release neutrophil extracellular traps in response to large pathogens. *Nat. Immunol.* **2014**, *15*, 1017–1025. [[CrossRef](#)] [[PubMed](#)]
33. Hoppenbrouwers, T.; Autar, A.S.A.; Sultan, A.R.; Abraham, T.E.; van Cappellen, W.A.; Houtsmuller, A.B.; van Wamel, W.J.B.; van Beusekom, H.M.M.; van Neck, J.W.; de Maat, M.P.M. In vitro induction of NETosis: Comprehensive live imaging comparison and systematic review. *PLoS ONE* **2017**, *12*, e0176472. [[CrossRef](#)] [[PubMed](#)]
34. Brinkmann, V.; Reichard, U.; Goosmann, C.; Fauler, B.; Uhlemann, Y.; Weiss, D.S.; Weinrauch, Y.; Zychlinsky, A. Neutrophil extracellular traps kill bacteria. *Science* **2004**, *303*, 1532–1535. [[CrossRef](#)]
35. Fuchs, T.A.; Abed, U.; Goosmann, C.; Hurwitz, R.; Schulze, I.; Wahn, V.; Weinrauch, Y.; Brinkmann, V.; Zychlinsky, A. Novel cell death program leads to neutrophil extracellular traps. *J. Cell Biol.* **2007**, *176*, 231–241. [[CrossRef](#)] [[PubMed](#)]
36. Yipp, B.G.; Kubes, P. NETosis: How vital is it? *Blood* **2013**, *122*, 2784–2794. [[CrossRef](#)] [[PubMed](#)]
37. Datta, R.; Alfonso-Garcia, A.; Cinco, R.; Gratton, E. Fluorescence lifetime imaging of endogenous biomarker of oxidative stress. *Sci. Rep.* **2015**, *5*, 9848. [[CrossRef](#)] [[PubMed](#)]
38. Chance, B. Mitochondrial NADH redox state, monitoring discovery and deployment in tissue. *Methods Enzymol.* **2004**, *385*, 361–370. [[PubMed](#)]
39. Pelletier, M.G.; Szymczak, K.; Barbeau, A.M.; Prata, G.N.; O'Fallon, K.S.; Gaines, P. Characterization of neutrophils and macrophages from ex vivo-cultured murine bone marrow for morphologic maturation and functional responses by imaging flow cytometry. *Methods* **2017**, *112*, 124–146. [[CrossRef](#)] [[PubMed](#)]
40. Byrd, A.S.; O'Brien, X.M.; Johnson, C.M.; Lavigne, L.M.; Reichner, J.S. An extracellular matrix-based mechanism of rapid neutrophil extracellular trap formation in response to *Candida albicans*. *J. Immunol.* **2013**, *190*, 4136–4148. [[CrossRef](#)] [[PubMed](#)]
41. Rochaël, N.C.; Guimaraes-Costa, A.B.; Nascimento, M.T.; DeSouza-Vieira, T.S.; Oliveira, M.P.; Garcia e Souza, L.F.; Oliveira, M.F.; Saraiva, E.M. Classical ROS-dependent and early/rapid ROS-independent release of Neutrophil Extracellular Traps triggered by *Leishmania* parasites. *Sci. Rep.* **2015**, *5*, 18302. [[CrossRef](#)] [[PubMed](#)]

42. Pilszczek, F.H.; Salina, D.; Poon, K.K.; Fahey, C.; Yipp, B.G.; Sibley, C.D.; Robbins, S.M.; Green, F.H.; Surette, M.G.; Sugai, M.; et al. A novel mechanism of rapid nuclear neutrophil extracellular trap formation in response to *Staphylococcus aureus*. *J. Immunol.* **2010**, *185*, 7413–7425. [[CrossRef](#)] [[PubMed](#)]
43. Bruns, S.; Kniemeyer, O.; Hasenberg, M.; Aimaniananda, V.; Nietzsche, S.; Thywissen, A.; Jeron, A.; Latge, J.P.; Brakhage, A.A.; Gunzer, M. Production of extracellular traps against *Aspergillus fumigatus* in vitro and in infected lung tissue is dependent on invading neutrophils and influenced by hydrophobin RodA. *PLoS Pathog.* **2010**, *6*, e1000873. [[CrossRef](#)] [[PubMed](#)]
44. Kenny, E.F.; Herzig, A.; Kruger, R.; Muth, A.; Mondal, S.; Thompson, P.R.; Brinkmann, V.; Bernuth, H.V.; Zychlinsky, A. Diverse stimuli engage different neutrophil extracellular trap pathways. *eLife* **2017**, *6*, e24437. [[CrossRef](#)] [[PubMed](#)]
45. Datta, R.; Heylman, C.; George, S.C.; Gratton, E. Label-free imaging of metabolism and oxidative stress in human induced pluripotent stem cell-derived cardiomyocytes. *Biomed. Opt. Express* **2016**, *7*, 1690–1701. [[CrossRef](#)] [[PubMed](#)]
46. Gupta, S.; Chan, D.W.; Zaal, K.J.; Kaplan, M.J. A High-Throughput Real-Time Imaging Technique To Quantify NETosis and Distinguish Mechanisms of Cell Death in Human Neutrophils. *J. Immunol.* **2018**, *200*, 869–879. [[CrossRef](#)] [[PubMed](#)]
47. Kraaij, T.; Tengstrom, F.C.; Kamerling, S.W.; Pusey, C.D.; Scherer, H.U.; Toes, R.E.; Rabelink, T.J.; van Kooten, C.; Teng, Y.K. A novel method for high-throughput detection and quantification of neutrophil extracellular traps reveals ROS-independent NET release with immune complexes. *Autoimmun. Rev.* **2016**, *15*, 577–584. [[CrossRef](#)] [[PubMed](#)]
48. Brinkmann, V.; Goosmann, C.; Kuhn, L.I.; Zychlinsky, A. Automatic quantification of in vitro NET formation. *Front. Immunol.* **2012**, *3*, 413. [[CrossRef](#)] [[PubMed](#)]
49. Rakymzhan, A.; Radbruch, H.; Niesner, R.A. Quantitative Imaging of Ca<sup>2+</sup> by 3D-FLIM in Live Tissues. *Adv. Exp. Med. Biol.* **2017**, *1035*, 135–141. [[PubMed](#)]
50. Brinkmann, V.; Laube, B.; Abu Abed, U.; Goosmann, C.; Zychlinsky, A. Neutrophil extracellular traps: How to generate and visualize them. *J. Vis. Exp.* **2010**. [[CrossRef](#)] [[PubMed](#)]
51. Digman, M.A.; Caiolfa, V.R.; Zamai, M.; Gratton, E. The phasor approach to fluorescence lifetime imaging analysis. *Biophys. J.* **2008**, *94*, L14–L16. [[CrossRef](#)] [[PubMed](#)]



© 2018 by the authors. Licensee MDPI, Basel, Switzerland. This article is an open access article distributed under the terms and conditions of the Creative Commons Attribution (CC BY) license (<http://creativecommons.org/licenses/by/4.0/>).

Article

# Systematic Enzyme Mapping of Cellular Metabolism by Phasor-Analyzed Label-Free NAD(P)H Fluorescence Lifetime Imaging

Ruth Leben <sup>1,2,\*,†</sup> , Markus Köhler <sup>1,2,†</sup>, Helena Radbruch <sup>3</sup>, Anja E. Hauser <sup>4,5</sup> and Raluca A. Niesner <sup>1,2,\*</sup>

<sup>1</sup> Biophysical Analytics, Deutsches Rheuma-Forschungszentrum (DRFZ), 10117 Berlin, Germany; markus.koehler@drfz.de

<sup>2</sup> Dynamic and Functional in vivo Imaging, Freie Universität Berlin, 14163 Berlin, Germany

<sup>3</sup> Institute for Neuropathology, Charité–Universitätsmedizin Berlin, 10117 Berlin, Germany; helena.radbruch@charite.de

<sup>4</sup> Immune Dynamics, Deutsches Rheuma-Forschungszentrum (DRFZ), 10117 Berlin, Germany; hauser@drfz.de

<sup>5</sup> Immunodynamics and Intravital Microscopy, Charité–Universitätsmedizin Berlin, 10117 Berlin, Germany

\* Correspondence: ruth.leben@drfz.de (R.L.); niesner@drfz.de (R.A.N.);

Tel.: +49-30-2846-0674 (R.L.); +49-30-2846-0708 (R.A.N.)

† These authors contributed equally to this work.

Received: 17 October 2019; Accepted: 4 November 2019; Published: 7 November 2019



**Abstract:** In the past years, cellular metabolism of the immune system experienced a revival, as it has become clear that it is not merely responsible for the cellular energy supply, but also impacts on many signaling pathways and, thus, on diverse cellular functions. Label-free fluorescence lifetime imaging of the ubiquitous coenzymes NADH and NADPH (NAD(P)H-FLIM) makes it possible to monitor cellular metabolism in living cells and tissues and has already been applied to study metabolic changes both under physiologic and pathologic conditions. However, due to the complex distribution of NAD(P)H-dependent enzymes in cells, whose distribution continuously changes over time, a thorough interpretation of NAD(P)H-FLIM results, in particular, resolving the contribution of various enzymes to the overall metabolic activity, remains challenging. We developed a systematic framework based on angle similarities of the phase vectors and their length to analyze NAD(P)H-FLIM data of cells and tissues based on a generally valid reference system of highly abundant NAD(P)H-dependent enzymes in cells. By using our analysis framework, we retrieve information not only about the overall metabolic activity, i.e., the fraction of free to enzyme-bound NAD(P)H, but also identified the enzymes predominantly active within the sample at a certain time point with subcellular resolution. We verified the performance of the approach by applying NAD(P)H-FLIM on a stromal-like cell line and identified a different group of enzymes that were active in the cell nuclei as compared to the cytoplasm. As the systematic phasor-based analysis framework of label-free NAD(P)H-FLIM can be applied both *in vitro* and *in vivo*, it retains the unique power to enable dynamic enzyme-based metabolic investigations, at subcellular resolution, in genuine environments.

**Keywords:** NADH and NADPH fluorescence lifetime imaging; enzyme activity; 3T3-L1 cell line; phasor approach; cellular metabolism

## 1. Introduction

The importance of cellular metabolism in immunology has become increasingly recognized in the last years. Although, in the last decades, molecular immunology mainly focused on signaling pathways within various immune cell subtypes and their supporting cells, such as stroma cells, it has become evident that cellular metabolism does not merely provide energy necessary for transcription and biosynthesis in immune cells, but is tightly interconnected with their function [1,2]. For instance, the process of selection and further differentiation of germinal B cells was shown to be directly linked to cellular metabolism [3]. These correlations between metabolism and immune cell function and dysfunction still require extensive investigations, as oxygen consumption measurements related to enzymatic activity are mainly performed *ex vivo* and not at the single-cell level. Only by using synthetic probes, such as dichlorotris(1,10-phenanthroline) ruthenium(II) hydrate (Ru(Phen)) [4], the oxygen concentration in cells and tissues can be measured at the level of single cells [5]. However, these approaches allow only an indirect link to enzymatic (metabolic) activity.

Fluorescence lifetime imaging (FLIM) was developed three decades ago, and since then it has been applied to study cellular function in a quantitative manner [6]. FLIM generates images in which contrast is obtained by the excited-state lifetime  $\tau$  of fluorophores instead of their intensity, therefore, having negligible experimental bias. The combination of FLIM with two-photon microscopy—the technology of choice when performing dynamic deep tissue imaging in living mammals [7]—allowed it to reach its full potential under genuine conditions and to study tissue and cellular function and dysfunction *in vivo*. In this way, using FLIM, molecular mechanisms underlying neuronal damage and oxidative stress have been understood in chronic neuroinflammation [8–12], neurodegeneration [13], and glioblastoma [14,15]. Furthermore, the shift from differentiation towards uncontrolled proliferation in cancer cells has been elucidated in several primary and metastatic tumor cells [16], and the physiologic process of differentiation has been unraveled in cells and organs [17–21].

A multitude of approaches have been developed over the years to measure fluorescence lifetimes in bulk solution, without spatial resolution. Later on, they have been applied to microscopy to perform FLIM. Both frequency-domain and time-domain methods have been developed to meet different needs in biosciences, biomedicine and medicine [22–28]. Frequency-domain technologies are particularly adequate for fast, high-throughput measurements [22,29,30], as well as for retrieving multiple differing fluorescence lifetimes from complex samples using several modulation frequencies, ranging from kHz to MHz [31,32]. Among the time-domain technologies, time-correlated single-photon counting (TCSPC), which requires pulsed excitation as delivered by two-photon microscopy, is the method of choice to comprehensively acquire the molecular complexity within living cells in deep tissue, despite its rather slow speed (1–10 s/frame) [11,33]. TCSPC directly measures the fluorescence decay of all contained fluorophores; however, its thorough analysis remains a challenge especially in complex microenvironments as found in cells.

The fluorophores first imaged by FLIM were the coenzymes nicotinamide adenine dinucleotide—NADH and nicotinamide adenine dinucleotide phosphate—NADPH [6] (hereafter NAD(P)H), i.e., ubiquitous coenzymes governing energy production in all cells across species, as well as being responsible for various biosynthetic processes and influencing diverse signaling pathways [34]. NAD(P)H-FLIM [35] has been extensively employed in cancer research, revealing shorter NAD(P)H fluorescence lifetimes in tumor cells as compared to controls, presumably due to a shift from oxidative phosphorylation (OxPhos) towards glycolysis [16,36–41]. By enabling the differentiation between the two major cellular metabolic pathways, namely, glycolysis and OxPhos, it has also revealed the tight link between metabolism and differentiation in other cell types, for example, in neuronal stem cells [18], in mesenchymal stromal cells during their differentiation towards various fates such as adipocytes, in chondrocytes, or osteoblasts [21,42–44], and in enterocytes in the small intestine [17]. Additionally, by dynamically monitoring the activation of NADPH oxidases, this technique has been applied to monitor the oxidative burst and massive oxidative stress production during infection in the small intestine [45], as well as apoptosis in cells [46].

Both fluorescence lifetime spectroscopy and FLIM are able to differentiate between the states of free and enzyme-bound coenzymes NADH and NADPH. In the free state (unbound to enzymes), the fluorescence of the adenine is intramolecularly quenched by nicotinamide, resulting in a short fluorescence lifetime of around 450 ps [29,47]. Upon enzymatic binding, this quenching is prevented due to steric hindrance caused by the specific binding site of the coenzyme, resulting in enzyme-specific prolongation of the fluorescence lifetime towards 2000 ps [48]. Additionally, the fluorescence lifetime of both free and enzyme-bound NAD(P)H, as with the lifetimes of the majority of fluorophores, is also influenced by other factors such as refractive index [49], solvent polarity [29], pH [50,51], ion concentration [52], or the degree of freedom for the diffusional rotation of the fluorescent molecules. Gregorio Weber in 1970, and then Joseph R. Lakowicz in 1992, showed that there are differences in the fluorescence lifetime of NADH and NADPH depending on the binding site of the enzyme [6,29]. This principle has been used for a number of isolated enzymes. However, in living cells, multiple pathways employing NAD(P)H-dependent enzymes are active at any given time, making it hard to interpret NAD(P)H-FLIM data derived from living cells with respect to the proportionate usage of certain enzymatic reactions. No framework allowing a systematic interpretation of the NAD(P)H-FLIM data with respect to both metabolic activity and specific, predominant enzymatic activity is available yet. As such, there are apparently contradictory interpretations, indicating that the fluorescence lifetime of NAD(P)H bound to enzymes depends on the coenzyme alone [53] is caused by other molecular species, e.g., oxidized lipids [54], or has a fixed value of ~2000 ps [23,39,48,55,56] or ~3400 ps [54,57].

Here, we established a general framework retrieving two kinds of information from NAD(P)H-FLIM data: (i) the fraction of free vs. enzyme-bound NAD(P)H present in cells, i.e., a measure of immediate metabolic activity, and (ii) which enzymes are the major contributors to the NAD(P)H-dependent metabolic activity in a certain cellular compartment, at a particular time point. Our approach is based on the measurement of the fluorescence lifetime of NADH and NADPH free and bound to enzymes, which are highly and ubiquitously expressed by mammalian cells. We performed the measurements of homogeneous mixtures of NAD(P)H and single enzymes in buffered media resembling the pH, ion concentration, solvent polarity, and refractive index of cells to ensure that only the binding state of the coenzymes affected the fluorescence lifetime. Typical images acquired by NAD(P)H-FLIM on cells and tissues have a voxel size of 500 nm × 500 nm × 1500 nm. Considering the mean concentration of proteins in a cell [58], we calculated that a number in the range  $10^8$ – $10^9$  protein molecules are present within a voxel. Of these proteins, 18% are metabolic enzymes [58]. Even if the number of enzyme molecules may vary between different cell populations, a large number of enzymes are competing to bind NAD(P)H. Therefore, we expect that only the activity of highly abundant NAD(P)H-dependent enzymes will have a major impact on the NAD(P)H fluorescence lifetime. Unpublished RNA-Seq data from our colleagues showed that out of 191 NAD(P)H-dependent enzymes expressed by mesenchymal stromal cells, 16 ubiquitously expressed metabolic enzymes, their including isoforms are contained within the 50 most abundantly expressed genes. These findings are in line with other studies, i.e., cancer cells [58], and presumably hold true for many other cell types. From these highly expressed metabolic enzymes we only excluded complex I, due to difficulties in maintaining the activity of its flavin mononucleotide-binding domain in solution. The NADH-binding unit of complex I is one of the less abundant among these 16 enzymes. We focused on these highly abundant NAD(P)H-dependent metabolic enzymes (covering the metabolic enzymes but excluding their isoforms), i.e., malate dehydrogenase (MDH), lactate dehydrogenase (LDH), glyceraldehyde-3-phosphate dehydrogenase (GAPDH), glucose-6-phosphate dehydrogenase (G6PDH), pyruvate dehydrogenase (PDH), alcohol dehydrogenase (ADH), C-terminal binding protein 1 (CTBP1) [57], and isocitrate dehydrogenase (IDH); complemented by the still abundant enzymes, i.e., hydroxyacyl-coenzyme-A dehydrogenase (HADH) and sorbitol dehydrogenase (SDH); and enzymes playing distinct roles in the cells, i.e., inducible nitric oxide synthase (iNOS) and the NADPH oxidases family (NOX1-4 and DUOX1,2) [59], which play a major role in the catalysis of oxidative burst. As the quaternary structure of the NAD(P)H binding site and the related catalytic function in these

NAD(P)H-dependent enzymes is highly conserved across species and in various cellular organelles, it was sufficient to investigate only one variant for each enzyme.

Our framework to evaluate NAD(P)H-FLIM data by the phasor approach, i.e., a model-free analysis tool of FLIM data [59,60], additionally uses for normalization the signal-to-noise ratio of the NAD(P)H intensity image for signal quality control. It decouples the metabolic activity level, i.e., the fraction of free to enzyme-bound NAD(P)H, from the type of predominant enzymatic activity, as indicated by the angle similarity to the phase vector of NAD(P)H bound to pure enzymes. We validated the performance of our analysis framework on homogeneous mixtures of NADH and enzymes as well as on a stromal-like 3T3-L1 cell line. Our systematic framework meets the increasing demand to interpret in a reliable manner, the metabolism of immune and stromal cells, at subcellular resolution, by NAD(P)H-FLIM, both in cell culture [61] and in living tissues and organisms [8,9,13].

## 2. Results

### 2.1. Benchmarking of NAD(P)H-FLIM Data Evaluated Using the Phasor Approach

To define the image and signal properties to ensure reliable data interpretation, we performed NADH-FLIM measurements in standardized NADH solutions of various concentrations, as well as in NADH mixtures with metabolic enzymes, i.e., malate dehydrogenase (MDH) or lactate dehydrogenase (LDH).

We evaluated the FLIM data acquired in time-domain by time-correlated single-photon counting in a two-photon microscope using the phasor approach. The raw data consist of a fluorescence decay curve of the fluorophore, in our case NADH, in each pixel of the image. The decay curve is monoexponential if all fluorophore molecules in the volume corresponding to a pixel in the image have the same molecular environment. If the molecules have various molecular environments, the decay curve became multiexponential. The characterizing parameter of the fluorescence decay curve is the fluorescence lifetime, i.e., the time period the fluorescence intensity decreases to  $1/e$  (where  $e$  is Euler's number) of its maximum value immediately after the excitation pulse. In the phasor plot, the lifetimes follow a naturally logarithmic distribution on the half-circle (Figure 1(Ai)).

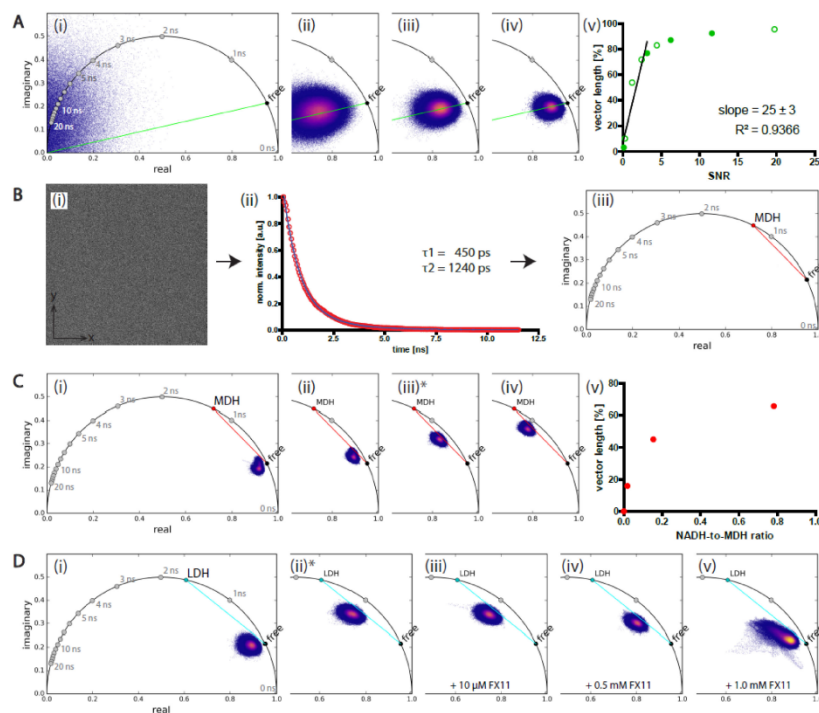


**Figure 1.** Benchmarking of NAD(P)H-FLIM data evaluated by the phasor approach. Phasor plots of mixtures of NADH and various enzymes solved. Gray dots onto half circle show the positions of  $0 \text{ ns} \leq \tau \leq 20 \text{ ns}$  in 1 ns-steps in phase domain. Phasor cloud: violet to orange–yellow false color representation of 3D histogram of phasor distribution; violet: low frequency; orange to yellow: increasing frequency, each dot in phasor plot has a counterpart in the xy fluorescence lifetime image. ( $n = 3$  measurements in the same sample). **(A)** NADH solved in MOPS medium: **(Ai)** only nonfluorescent MOPS medium (background BG), **(Aii)** 5  $\mu\text{M}$ , **(Aiii)** 10  $\mu\text{M}$ , and **(Aiv)** 20  $\mu\text{M}$  NADH. Green line indicates the phase vector pointing towards the position of free NADH onto the half circle. **(Av)** Graph displays signal–noise ratio (SNR) versus vector length in percent (as described in Results). The increase in SNR is caused by an increasing NADH concentration at constant excitation power. Filled circles indicates the data shown in panels **(Ai–iv)**, blank circles represent results of the same experiments with other NADH solution concentrations. The line describes the linear regression of the displayed data points. **(B)** Strategy to determine the position of the phase vector of NAD(P)H bound to pure enzymes onto the half circle; here, 50  $\mu\text{M}$  NADH and 39.1  $\mu\text{M}$  MDH solved in MOPS medium: **(Bi)** homogeneous intensity image  $512 \times 512$  pixel covering  $200 \mu\text{m} \times 200 \mu\text{m}$ , **(Bii)** averaged time domain decay curve over all pixel with biexponential fit, as line and data points (red circles), **(Biii)**  $\tau_2$  was transferred to phase domain to mark MDH's position onto the half circle (red dot), red vector connects position of free NADH and MDH bound to NADH. **(C)** Mixtures of NADH and MDH solved in MOPS medium: **(Ci)** only 200  $\mu\text{M}$  NADH, **(Cii)** 132  $\mu\text{M}$  NADH and 2.6  $\mu\text{M}$  MDH [ratio MDH:NADH 0.019], **(Ciii)** 50  $\mu\text{M}$  NADH and 7.7  $\mu\text{M}$  MDH [0.154], and **(Civ)** 50  $\mu\text{M}$  NADH and 39.1  $\mu\text{M}$  MDH [0.782]. The position of NADH bound to MDH fluorescence lifetime was determinate as described in **(B)**. **(Cv)** Graph displays MDH:NADH ratio vs. vector length [%]. Red dots indicate the data shown in **(Ci–iv)**. **(D)** NADH, LDH, and FX11 solved in MOPS solution: **(Di)** only 50  $\mu\text{M}$  NADH; **(Dii)** 50  $\mu\text{M}$  NADH and 10  $\mu\text{M}$  LDH; **(Diii)** 50  $\mu\text{M}$  NADH, 10  $\mu\text{M}$  LDH, and 10  $\mu\text{M}$  FX11; **(Div)** 50  $\mu\text{M}$  NADH, 10  $\mu\text{M}$  LDH, and 0.5 mM FX11; and **(Dv)** 50  $\mu\text{M}$  NADH, 10  $\mu\text{M}$  LDH, and 1.0 mM FX11. The position of LDH lifetime was determined as described in **(B)** ( $\tau_2 = 1600 \text{ ps}$ ). After adding the LDH inhibitor, FX11, the experimental data cloud migrates back to free NADH with increasing FX11 concentration. The asterisks indicate the data sets used to calculate the SNR (Figure S3) as well as calculate  $\tau_2$  to mark the half circle. The cyan lines represent the trajectories on which the data cloud migrates if the enzyme activity increases.

### 2.1.1. Low Signal-to-Noise Ratio of the Image Affects the NAD(P)H-FLIM Data

Both mono- and multiexponential decays are convolved with shut noise, i.e., an undamped multifrequency oscillation, which is also transformed to the phase domain and lies within the area defined by the half circle. To quantify the role of shut noise, we first investigated the impact of the signal-to-noise ratio of the image on the results of the phasor-evaluated NAD(P)H-FLIM data by varying either the concentration of NADH while the laser power stayed the same at 100 mW (Figure 1A) or by varying the excitation laser power while the NADH concentration was fixed at 50  $\mu$ M (Video S1 and Figure S1).

The signal-to-noise ratio (SNR) is defined as the ratio of the mean background-free fluorescence signal ( $\mu_{\text{signal}} - \mu_{\text{BG}}$ ) and the noise of the background (shut noise), i.e., the standard deviation of the background intensity distribution ( $\sigma_{\text{BG}}$ ):

$$\text{SNR} = \frac{\mu_{\text{signal}} - \mu_{\text{BG}}}{\sigma_{\text{BG}}} \quad (1)$$

An increasing NADH concentration results in increasing signal-to-noise-ratio (SNR), identifiable by decreasing width of the phasor cloud, i.e., the distribution of the phase vectors measured in each pixel of the image, in the phasor plots. Figure 1(Av) shows the SNR vs. the vector length, which is the ratio of the vector “(0|0) to free NAD(P)H position onto the half circle” (green line in Figure 1(Aii–v)) and the vector connecting (0|0) with the center of the phasor cloud, in percent. Increasing the laser power while the NADH concentration is fixed shows the same effect.

Independently of the way we modified the SNR in the image, we found that for SNR values above 5, the quality of the fluorescence signal delivered results very similar to those predicted by the theory of the phasor approach. No experimental data are able to reach the accuracy of theoretically calculated values due to the shut noise contained therein. In the range of SNR values less than 5, the vector length, i.e.,  $Re^2 + Im^2$  (where  $Re$  is the real part and  $Im$  the imaginary part of the complex number), decreases linearly with decreasing SNR, whereas the direction of the vector given by the angle to the abscise remains constant.

### 2.1.2. Validation of Phasor-Evaluated FLIM Data on Mixtures of NADH and MDH or LDH

The theory of the phasor approach predicts that, for a mixture of fluorophore molecules experiencing two different molecular environments, the vector will point onto the segment connecting the positions on the half circle corresponding to fluorophore molecules experiencing only one of these molecular environments. Therefore, the phase vectors of a FLIM measurement of a mixture of NADH and malate dehydrogenase (MDH) point onto the segment connecting the position of free NADH onto the half circle and that of NADH completely bound to MDH.

As the NADH:MDH mixture was a homogeneous solution containing only two fluorescent species, the time domain decay curve was averaged over all pixels in order to smooth it for proper biexponential fitting (least-square sum method). This fit results in  $\tau_1 = 450$  ps and  $\tau_2 = 1240$  ps ( $R^2 = 0.99956$ ).  $\tau_1$  is the lifetime of free NADH and is in good agreement to known data [47].  $\tau_2$  indicates the lifetime of NADH bound to MDH and was transferred to the phase domain to mark the position of MDH onto the half circle (Figure 1(Bi–iii)).

In Figure 1(Ci–iv), we investigated mixtures of NADH and MDH with various relative concentrations of coenzyme and enzyme given by the ratio MDH:NADH. We performed the FLIM experiments in such a way that the SNR remained the same for all measurements. SNR was calculated for panel (iii) (marked by asterisk) and was 39.6 (Figure S3). As expected, the position of the phasor cloud migrates from the free NADH position, towards the position of NADH fully bound to MDH with increasing MDH:NADH ratio, along the connecting vector. FLIM, especially when transformed to phase domain, is very sensitive to noise. Noise has an infinite fluorescence lifetime, which is positioned around the origin (0|0) in the phasor plot. Although our SNR is very high, in the case of MDH and

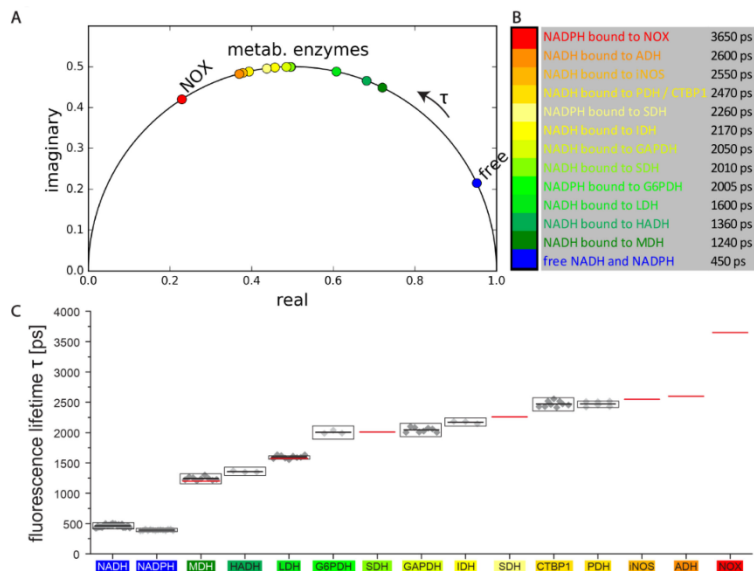
LDH, respectively, noise still represents a third “lifetime component”. For this reason, the phasor cloud does not lie exactly on the connecting line, but migrates slightly parallel to it. In the following analysis (especially later in the enzyme assignment), this circumstance was taken into account by the fact that the vector free-enzyme starts at the center of the measured phasor cloud and does not start from the marked position on the half circle (Figure 3A).

Figure 1(Cv) shows the MDH:NADH ratio vs. the vector length, which is the ratio of the vector “free NADH to the center of the center of the phasor cloud” to “free NADH to NADH fully bound to MDH position on the half circle” (red line), in percent.

NADH-FLIM experiments on mixtures of NADH and lactate dehydrogenase (LDH) performed at a SNR far above 5 generally revealed the same valid behavior. Due to the low LDH concentration (10  $\mu$ M, LDH:NADH ratio = 0.2), the phasor cloud did not reach the position corresponding to NADH fully bound to LDH. By adding the LDH inhibitor FX11 at various concentrations, we could reverse the binding of NADH to LDH, which resulted into a shift back to free NADH in the phasor plot (Figure 1D and Figure S2). The smearing of the experimental data at high FX11 concentrations in panel (Figure 1(Dv)) results from enzyme denaturation since the intensity image becomes in this case heterogeneous. The SNR remains constant at 22.3 (Figure S3).

## 2.2. Enzyme-Based Reference System to Interpret Label-Free NAD(P)H-FLIM Data in Cells

The basic concept of our approach for interpreting NAD(P)H-FLIM data takes into account the most likely states in which NADH and NADPH can be found in cells and tissues. Except for the free state, we find the coenzymes bound to diverse enzymes, in a mixture containing ~350 NADH- and 300 NADPH-dependent enzymes. However, many of these enzymes are so rare that they have a negligible effect on the overall fluorescence decay of the coenzymes. We identified from RNA-Seq data the most abundant and, thus, relevant NADH and NADPH-dependent enzymes and completed the list with NADPH oxidases, i.e., enzymes responsible for oxidative burst generation in certain cell types. The phasors of free NAD(P)H and fully bound NAD(P)H to these enzymes, respectively, are depicted in Figure 2A. The corresponding fluorescence lifetimes are listed in Figure 2B. Using FLIM, we measured mixtures of NADH or NADPH and several of these pure enzymes (Figure 2C) and evaluated the data using the phasor approach as described in Figure 1B for the NADH/MDH mixtures. The list is completed by our previously published data on other relevant enzymes measured extracellularly in solution [8]. The only exception represents the NADPH Oxidases family (here NOX), which has a fluorescence lifetime and position in the phasor plot and was determined intracellularly using chemical inhibition, activation, and knockout strategies [33,55]. We paid particular attention to perform all FLIM measurements on NAD(P)H solutions and NAD(P)H-enzyme mixtures in buffered media resembling similar pH, ion concentrations, and refractive index as the cellular environment to avoid lifetime artifacts caused by these parameters. As shown by the good agreement of our results of NADH/MDH and NADH/LDH mixtures with the findings of other groups [47] (red lines in Figure 2C), our reference system is a generally valid system that can be applied to any cell or tissue type. The fact that we were not able to measure NADH bound to functional complex I, neither extracellularly nor intracellularly, is a limitation of our reference system.



**Figure 2.** Reference system of NADH and NADPH fluorescence lifetimes and phase vectors in the free and enzyme-bound state. **(A)** Phasor plot with the positions of the coenzymes NADH and NADPH fully bound to the identified relevant, abundant NAD(P)H-dependent enzymes, as chosen by from RNA sequencing data. The positions on the plot have been either determined as described for NADH and MDH in Figure 1B from our experimental FLIM data on mixtures of coenzyme and pure enzyme or calculated from our previously published data on such mixtures. The arrow outside the half-circle shows the direction in which the fluorescence lifetime  $\tau$  increases. **(B)** List of measured fluorescence lifetimes  $\tau_2$  of NADH or NADPH fully bound to enzymes. **(C)** The fluorescence lifetimes in panel (B) were determined as described in Figure 1B, fluorescence lifetimes calculated from single images represented as gray dots, average values as black lines, standard error of the mean (s.e.m.) values over all pixels in all measured images per coenzyme/enzyme mixture as black boxes. The list was completed by our previously measured fluorescence lifetimes [6] measured for NADH and NADPH bound to SDH, NADH bound to iNOS, NADH bound to ADH, and NADPH bound to enzymes of the NOX family (red lines). For LDH and MDH the literature data of other groups are indicated as red lines. The color coding in panels (A–C) is consistent.

### 2.3. Analysis Framework of NAD(P)H-FLIM Data: Validation on Homogeneous NAD(P)H-Enzyme Mixtures

Based on the previously generated reference system of coenzymes bound to pure enzymes, we created a systematic analysis framework of NAD(P)H-FLIM data. First, we determined the SNR of the NAD(P)H fluorescence intensity image, which is a quality criterion of the time-domain signal. After calculating the phasor in each pixel of the image, we selected the data points that were located within the circular area in the phasor plot identified as “free NAD(P)H” area (Figure 3(Ai)). The radius  $r$  and position of this circular area was determined from the measured distribution of free NADH (Figure S4). We attribute those data points to “free NAD(P)H” and consider that a cell would not show any metabolic activity in those image areas where these data points originate from. To assign the data point to enzymes of our reference system, we calculated the angles  $\alpha_i$  and  $\alpha_{\text{data}}$  (Figure 3(Aii)) in the remaining pixels.  $\alpha_i$  is the angle of the vector connecting the position of measured free NAD(P)H and the positions of NAD(P)H fully bound to the pure enzyme of our reference system with the index  $i$  (e.g.,  $i = 2$  for MDH, represented as dark green, solid line), and  $\alpha_{\text{data}}$  is the angle of the vector connecting the position measured free NAD(P)H and each experimental data point (violet, dashed line) (Figure 3(Aii,Aiii)). Furthermore, we calculated the absolute value (expressed by |...|) of angle similarity  $q_i$  to each enzyme of the reference system as follows,

$$q_i = \left| \frac{\alpha_{\text{data}}}{\alpha_i} - 1 \right|$$

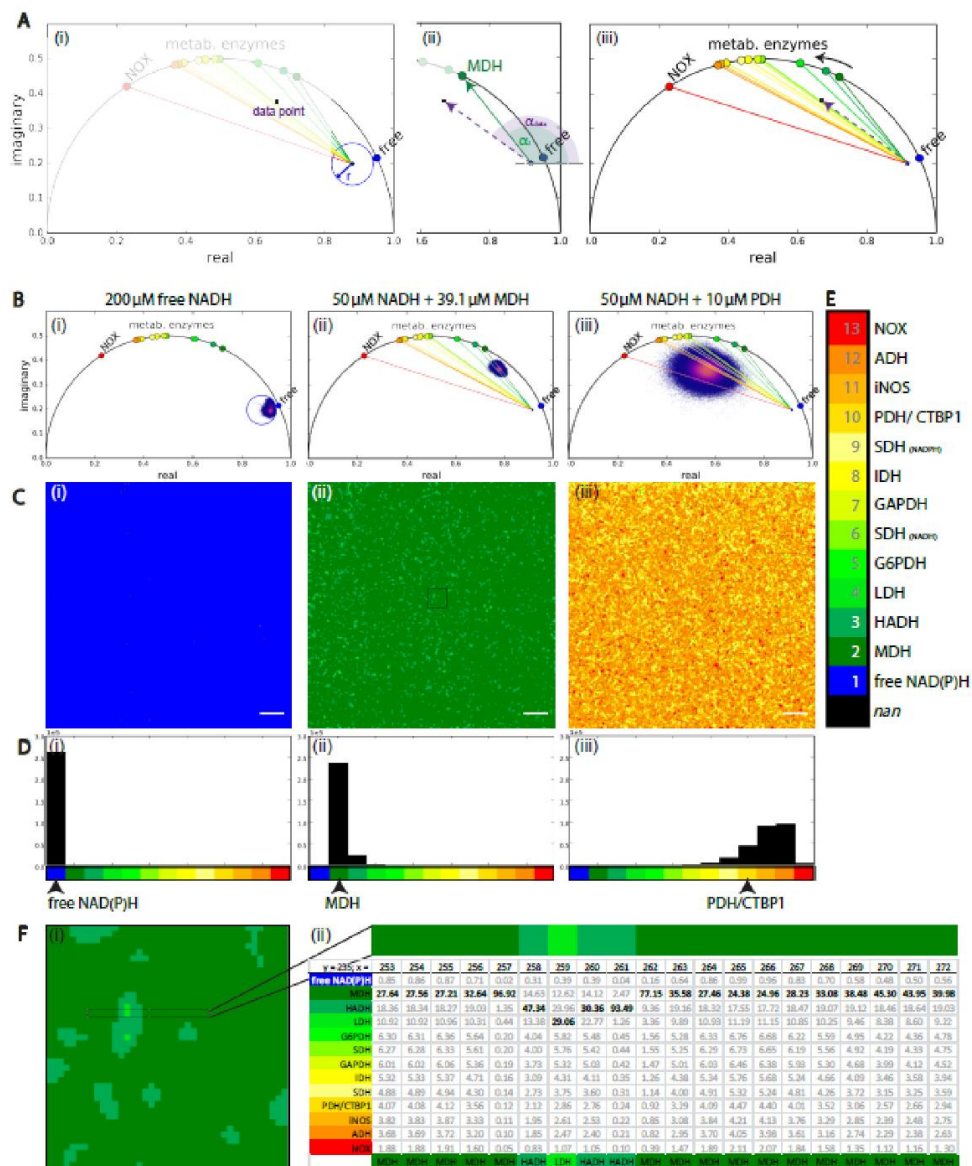


**Figure 3.** Validating the systematic framework of NAD(P)H-FLIM data analysis. **(A)** Strategy for assigning a data point (violet) to free or enzyme-bound NAD(P)H. **(Ai)** Inspection whether the data point is within the radius  $r$ , which indicates the measured phasor position of free NAD(P)H. The blue circle describes the experimental area of only free (unbound) NAD(P)H. **(Aii)** If **(Ai)** does not apply, the angles  $\alpha_{\text{data}}$  and  $\alpha_i$  ( $i$  = enzyme index) are calculated and compared for every single NAD(P)H-dependent enzyme by equations (Equations (2) and (5)). The data point is assigned to the enzyme for which (Equation (5)) it becomes maximal. The purple dotted arrow describes an experimental trajectory vector of a pixel, whereas the solid green arrow stands for the expected trajectory vector of NADH bound only to MDH (enzyme index 2). The green sector describes the angle  $\alpha_2$  between the x-axis (Re-axis) and the green trajectory vector whereas the purple sector describes the same angle  $\alpha_{\text{data}}$  calculated from the experimental data (purple trajectory vector). **(Aiii)** Phasor plot

containing all enzymes used for benchmarking and an experimental trajectory vector of a pixel (purple dotted arrow). The enzymes are indexed from 2 to 13. 1 corresponds to free NAD(P)H. These numbers are associated with specific colors as displayed in (E). The colors of the dots in the phasor plot (Aiii) correspond to expected phasor points of NADH or NADPH entirely bound to the enzymes indexed from 2 through 13. The colored lines correspond to the trajectory vectors of the same enzymes, color-encoded as displayed in (E). (B) Phasor plots of NADH mixed with different enzymes solved in MOPS medium. (Bi) 200  $\mu$ M free NADH, blue circle indicates free NAD(P)H (Bii) 50  $\mu$ M NADH and 39.1  $\mu$ M MDH (same data as shown in Figure 1(Civ)), (Biii) 50  $\mu$ M NADH and 10  $\mu$ M PDH. (Ci–iii) to (Bi–iii) corresponding enzyme maps, the enzymes were assigned as described in (A). (Di–iii) to (Ci–iii) corresponding histograms. Scale bar corresponds to 20  $\mu$ m. (E) Color legend of enzyme assignment. The gray numbers represent the enzyme indices used throughout this work. *nan* = “not a number”: a non-numerical place holder in the enzyme matrix (e.g., after thresholding) used to represent the enzyme map spatially correct. All other abbreviations refer to the enzymes mentioned in the introduction. (F) (Fi) Magnified region of interest from (C) (Fii) representing the enzyme assignment. ROI is marked in (Cii) by a black square. (Fii) 20  $\times$  1 pixel line (ROI marked in (Fi)), in (Cii) pixel line  $y = 235, 253 \leq x \leq 272$ . The table in (Fii) displays the normalized angle similarities  $w_i$  (Equation (5)) for all enzymes of the reference system in each pixel of the selected ROI. Maximum values are displayed bold. The lowest line of the table shows the enzyme assignment based on the maximum  $w_i$  value. The pixel line in (Fii) is 7.8  $\mu$ m long.

Further, we normalized the angle similarities  $q_i$  for all enzymes in each pixel and obtained the weights  $w_i$  of the angle similarities  $q_i$  as follows,

$$w_i q_i = \text{const} \quad (3)$$

$$\sum w_i = 1 \quad (4)$$

$$w_i = \frac{1}{q_i \sum \frac{1}{q_i}} \quad (5)$$

Equation (5) gives the assignment probability for each enzyme of our reference system. After multiplying by 100, it may reach from 0 to 100 and the data point is assigned to the enzyme for which this value reaches its maximum. Repeating this procedure for each pixel of an image generated an enzyme map as shown in (Figure 3(Ci–iii)). At the same time, all weights  $w_i$  may be retrieved as a 3D matrix (2D  $\times$  13), as depicted in Figure 3(Fii), for an exemplary 20  $\times$  1 pixel line. In the case that the maximum weight  $w_i$ , on the basis of which the enzyme assignment is performed, is similar to the neighboring enzymes, the comparison of the weights in the 3D matrix becomes relevant for data interpretation.

In Figure 3B–D, we validated our analysis framework on homogeneous mixtures of free NADH (i), NADH and MDH (ii), and of NADH and PDH (iii), respectively. The enzyme maps (Figure 3C) of free NADH, as well as NADH mixed with MDH, show a high accuracy of the analysis framework, substantiated by the histograms shown in Figure 3D. The histograms show that 99.9% of the pixels are correctly assigned to free NADH (Figure 3(B,Ci)) and 97.7% of the pixels in Figure 3(B,Cii) are correctly assigned to MDH (enzyme index = 2). The SNR of free NADH image was 39.6 and for MDH:NADH mixture image 22.3. In contrast, the histograms of the enzyme map of NADH mixed with PDH showed that 37.4% of the data points were assigned to ADH, 35.1% to iNOS and only 17.4% to PDH/CTBP1. This is partially due to the high similarity of the lifetimes of NADH if bound to PDH/CTBP1, iNOS, and ADH (see Figure 2C), which makes an accurate assignment difficult. In such a case, the expression level of these enzymes and their subcellular distribution need to be taken into account. Furthermore, the SNR in the PDH:NADH mixture image was with a value of 9.99 lower than that for free NADH and MDH:NADH mixture. As becoming evident from the broad phasor cloud in the corresponding phasor plot (Figure 3(Biii)), in a pixel-based evaluation the SNR criterion needs to be set higher for a sufficient accuracy.

The island-shaped structures in the enzyme maps, especially in the case of the mixture NADH and PDH, do not result from a badly solved enzyme solution, but rather originates from the Gaussian blurring of the time-resolved fluorescence data; one of the very first steps of the analysis. By spatially blurring the time domain raw data, the time resolution is improved at the cost of spatial information. The Gaussian blur with a radius of two pixel ( $\sigma = 2$ ) is a good compromise between time and space accuracy (Figure S5). In the case of homogeneous solutions, the spatial resolution is irrelevant, but this becomes important when performing label-free NAD(P)H-FLIM of cells and tissues (Figure 4). In this case, we additionally mapped the ratio length of the vectors we used to calculate angle  $\alpha_1$  and  $\alpha_{data}$  as defined above. This ratio represents the fraction of free NAD(P)H vs. bound NAD(P)H to the assigned enzyme in each pixel of the image, and thus is a hint for the metabolic activity in this area of the cell.

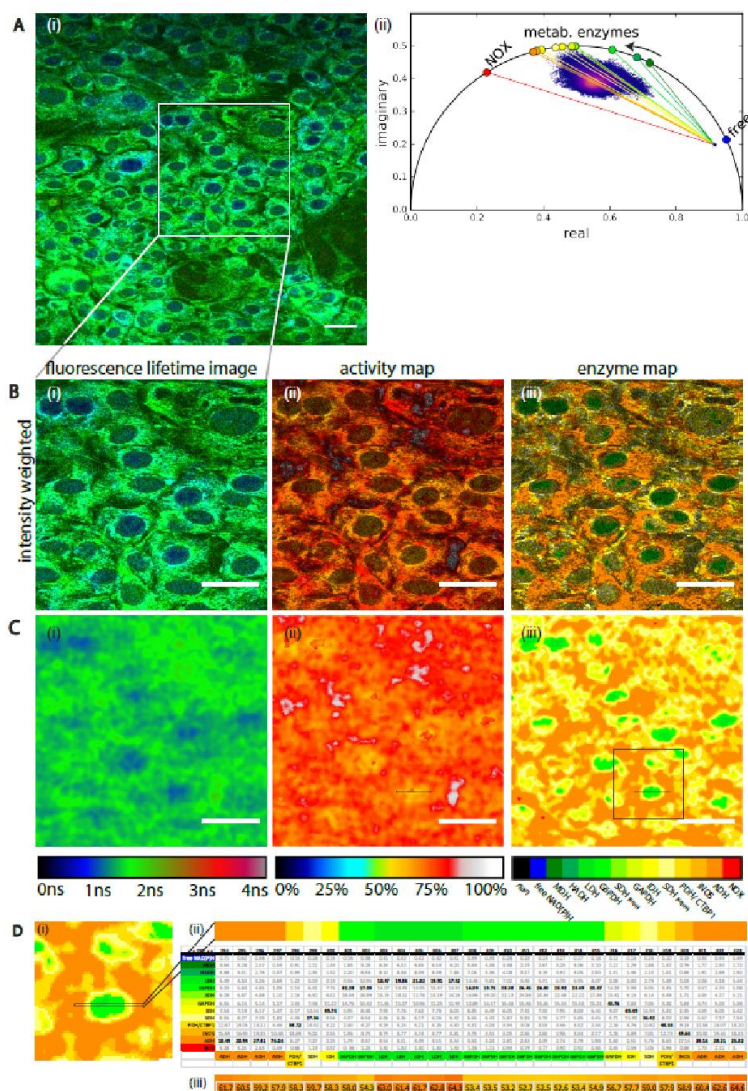


**Figure 4.** Label-free NAD(P)H-FLIM reveals subcellular heterogeneity of enzyme activity but homogeneous metabolic activity in stromal-like 3T3-L1 cells. (A) Spatial-resolved fluorescence lifetime

image of living 3T3-L1 cells. (Ai) Intensity-weighted fluorescence lifetime image  $505 \times 505$  pixel covering  $500 \mu\text{m} \times 500 \mu\text{m}$  and (Aii) corresponding phasor plot. (B,C)  $198 \mu\text{m} \times 198 \mu\text{m}$  region of interest, (B) intensity weighted, (C) unweighted images of (Ci) fluorescence lifetime image, (Cii) distance map, and (Ciii) enzyme map; white bar indicates  $50 \mu\text{m}$ . The “distance map” maps the ratio in percent of the vector “free NADH to data point” to “free NADH to assigned enzyme position on the half circle”. The mean vector length is  $(68 \pm 6) \%$ . (D) Magnified region of interest from (Ciii), the ROI is marked by black square and asterisk, (Dii)  $30 \times 1$  pixel line (ROI marked in (Di) in the original image it is the pixel line  $y = 290, 294 \leq x \leq 323$ ) and table with corresponding  $w_i$  of Equation (5) for each shown pixel and each enzyme. Maximum values are highlighted in black. The lowest line of the table shows the enzyme assignment by finding the maximum, (Diii) the corresponding vector length in that pixel line and is also marked in (Dii). The pixel line in (Dii) and (Diii) is the magnified picture of the small rectangle displayed in (Ci) and in (Ciii). The dimension of the pixel line is  $30 \mu\text{m}$ .

#### 2.4. Validation of the NAD(P)H-FLIM Analysis Framework on Stromal-Like 3T3-L1 Cells

We applied our systematic analysis framework on NAD(P)H-FLIM data acquired in 3T3-L1 cells (Figure 4A)—a cell line which has mesenchymal stromal cell-like properties and can differentiate into adipocytes when appropriately stimulated. In the bone marrow, stromal cells, the heterogeneity of which is still poorly understood, are known to fulfill various functions. Particularly, in the deep marrow cavity of long bones, they, together with the vasculature, form crucial components of the survival niche for various immune cell populations such as long-lived plasma cells [61], as well as for hematopoietic stem cells [62]. Both in homeostasis and during bone regeneration, stromal cells may differentiate towards osteoblasts, chondrocytes or adipocytes. In different phases of life, the balance between these differentiation pathways and the nondifferentiated state is expected to shift, e.g., in aged individuals, or due to metabolic syndrome, differentiation towards adipocytes is more dominant [63]. The various differentiation pathways have been previously linked to differences in the NAD(P)H metabolism as measured by FLIM [20,42,47].

In particular, differences between the mean NAD(P)H fluorescence lifetime in the nucleus vs. cytoplasm have been reported. However, it is not yet clear which metabolic mechanisms underline these observations.

The SNR in the image ranged between  $28 \pm 6$  in nuclei and  $48 \pm 16$  in cytoplasm, thus our measurements lies within a reliable range. Note that these SNR values could be only reached by summing up subsequently acquired five time-domain images of the cells. The NAD(P)H fluorescence signal is dim in cells and an increase in excitation power would entail the risk of photodamage [64]. Our systematic framework for NAD(P)H-FLIM in 3T3-L1 cells revealed similar metabolic activity as substantiated by the distance maps in Figure 4(B,Cii), i.e., similar fraction of free NAD(P)H. Although there was a certain degree of heterogeneity among the metabolic activity, we observed no significant differences between cytoplasm and nucleus in this respect. In contrast, we found, in the enzyme map, predominant activity of different NAD(P)H-dependent enzymes in nuclei as compared to the surrounding cytoplasm (Figure 4(B,Ciii)). These data are also supported by the corresponding weights in the table in Figure 4(Dii). They reveal that different enzymes from a group of enzymes with presumably similar NAD(P)H binding sites are active in nuclei as compared to cytoplasm. G6PDH was identified as the mainly predominant active enzyme in the nuclei, the probabilities of enzymatic activity of LDH, SHD if bound to NADH and of GAPDH are at similar levels, due to the high similarity of the phasors of the enzymes. We expected to find CTBP1 as a NAD(P)H-dependent enzyme in the nucleus [57], but only found evidence for the presence of LDH, G6PDH, GAPDH, and SDH in there. As these are cytosolic enzymes, we expect the yet uncharacterized nuclear enzymes to have a similar fluorescence lifetime. In the cytoplasm, we found a high predominance of PDH, but also of iNOS and ADH. The contribution of CTBP1 (having a phasor identical to that of PDH) is rather improbable, as this is to the best of our knowledge mainly located in the cellular nucleus [57].

### 3. Discussion

Cellular metabolism has a strong impact on cell functions—this holds true for the majority of cell types, across species. In immunology, the need for appropriate methods for the analysis of metabolism has increased since it became evident that there is a strong cross-link between signaling pathways and the cellular metabolism, beyond the mere supply of energy. For example, the activation of B and T lymphocytes coincides with metabolic reprogramming towards a preferential usage of glycolysis [1,65,66], whereas their transition into memory cells goes along with an increase in oxidative phosphorylation. In the bone marrow, the birth place of immune cells and the site of immunological memory, various immune subsets find special microenvironments, which secure their survival and support their function. These special microenvironments are denoted as survival niches. The stable components of these niches are built by mesenchymal stromal cells (MSC), supported by the dense marrow vasculature [67,68]. Except for providing nutrients to diverse immune cell subsets, MSC may differentiate under certain conditions, e.g., during bone growth or bone regeneration after injury, into osteoblasts or chondrocytes. Under other conditions, e.g., in aged individuals or due to metabolic syndrome, they may differentiate into adipocytes [63]. Although these differentiation pathways are possible, the microenvironmental constraints which favor one or the other pathway are not yet fully understood. By using NAD(P)H-FLIM, others have provided evidence that cellular metabolism and differentiation stage of MSC are closely linked [21,42,47]. The interpretation of the NAD(P)H-FLIM data in these studies is hampered by either strongly simplified or too complex models of NAD(P)H fluorescence lifetime. If a monoexponential model is assumed, the decision whether a shorter mean fluorescence lifetime is caused by a lower NAD(P)H consumption (more free NAD(P)H) or by a higher activity of MDH or LDH cannot be made. Biexponential and multiexponential models, which facilitate this decision, are numerically instable and do not take into account the enzymatic landscape within the cell. The phasor approach proposed by Enrico Gratton and coworkers is a model-free analysis approach that circumvents the majority of numerical artifacts [69]. Nevertheless, data interpretation without a reference system of pure, relevant enzymes is also in this case not reliable.

To establish the systematic framework for a generally valid label-free NAD(P)H-FLIM data analysis, we first identified the most relevant, i.e., abundant NADH- and NADPH-dependent enzymes. These are responsible as catalyzers of biochemical reactions within the cell engine for energy supply, reductive biosynthesis, and other vital cell functions such as oxidative burst during phagocytosis. We measured the fluorescence decay of the coenzymes specifically bound to the respective enzymes, completing and validating published data from our and other laboratories. Although our reference NAD(P)H-dependent enzyme system for NAD(P)H-FLIM data is generally valid, an extension with other NAD(P)H-dependent enzymes relevant to specific cell populations or in certain tissue, organs, or pathologies is easily possible and desirable. Our systematic analysis framework of NAD(P)H-FLIM data relies on the following steps. (i) Calculating the SNR of the fluorescence intensity image; (ii) performing the phasor analysis of the time-domain NAD(P)H-FLIM data and identifying the pixel containing only free NAD(P)H; (iii) based on our reference enzyme system, calculating the enzymatic activity probability for all considered enzymes and assigning the predominantly activated enzyme to each pixel; and (iv) calculating the fraction of free to enzyme-bound NAD(P)H, as an index of metabolic activity.

We first validated our systematic analysis framework of NAD(P)H-FLIM data on homogeneous mixtures of NAD(P)H and pure enzymes. These data revealed the fact that the SNR value has a strong impact on the quality of the phasor data and their interpretation. If focusing only on the accuracy of the phase vector averaged over an image representing the central position of the phasor cloud, our results indicate that up to SNR 5, a linear correction of its modulation length, i.e., vector length, is necessary while the phasor angle does not need any correction. Above a SNR value of 5, both length and angle of the phase vector averaged over the whole image are numerically reliable and the effects on the position of the phasor cloud are caused by biologically relevant phenomena. Therefore, although it is often mentioned that FLIM is independent of intensity—time and not intensity is the

imaging criterion—this holds true only for higher SNR values (above 5) for which the decay curve properties remain unchanged. Additionally, the SNR value in an image also strongly influences the width of the phasor cloud. The width of the phasor cloud has an immediate impact on the pixel-based calculation of enzymatic activity probabilities, enzyme activity assignment, and on the fraction free to enzyme-bound NAD(P)H. Our FLIM data on pure NADH solution and on NADH:MDH mixtures revealed that for high accuracy above 97%, SNR values above 20 are necessary. These results are in line with our finding concerning the interdependency of GFP fluorescence lifetimes on the SNR values [9]. Our data on the NADH:PDH mixture revealed that lower SNR values and high similarity of the phase vectors of several enzymes, in this case of PDH as compared to CTBP1, iNOS, and ADH, lead to a lower accuracy of enzyme assignment. Although the reference enzyme system cannot be changed, the SNR values in an image can be increased by increasing fluorophore concentration or the excitation power, smoothing the raw data in time or in space, or increasing the image acquisition time; whereas, in cells, a concentration increase is not possible, as this would change the cell physiology, all the other strategies to improve the SNR are linked to experimental drawbacks. An increase of excitation power may lead to photodamage [64], spatial smoothing of the data leads to loss of subcellular information, whereas temporal smoothing of the time-domain data decreases the accuracy of fluorescence decay curves and, thus, the accuracy of the phasor analysis. Increasing the acquisition time per image lowers the repetition rate of time-lapse imaging. In living cells and tissues, fast changes may be overseen in this way. Therefore, a combination of these procedures to improve SNR is required if FLIM is to be performed in living cells or tissues.

Taking this into account, we applied our systematic analysis framework to NAD(P)H-FLIM data on stromal-like 3T3-L1 cells, which develop into adipocytes upon stimulation. We decided to increase the SNR to highly reliable values by increasing the acquisition time of the imaged cells, because these cells do not migrate. In this way, we found shorter mean NAD(P)H fluorescence lifetimes in the nuclei as compared to the cytoplasm, in line with previous results in differentiating myoblast cells [19]. However, we found no differences in metabolism at the subcellular level, but a different predominant enzymatic activity in nuclei as compared to the surrounding cytoplasm, leading to this change in the NAD(P)H fluorescence lifetime. Although G6PDH was identified as the predominant active enzyme in the nuclei, the probabilities of enzymatic activity of LDH, SHD if bound to NADH, and GAPDH are at similar levels, due to the high similarity of the phase vectors of the enzymes. We expected to find CTBP1 as a NAD(P)H-dependent enzyme in the nucleus [57], but did not find any hints for the presence of LDH, G6PDH, GAPDH, and SDH there. In the cytoplasm, we found a high predominance of PDH, but also of iNOS and ADH. The contribution of CTBP1 (having a phase vector identical to that of PDH) is rather improbable, as this is mainly located in the cellular nucleus.

Our unexpected results regarding the metabolic activity in the nuclei of stromal-like cells led us to the conviction that our systematic analysis framework of NAD(P)H-FLIM retains the potential of detecting yet unknown enzymatic mechanisms related to cellular metabolism. This will have a tremendous impact on the way we will interpret the impact of cellular metabolism of immune and stromal cell populations, at a subcellular level and under *in vivo* conditions [61].

## 4. Material and Methods

### 4.1. Two-Photon Microscope Setup Adequate for FLIM

Two-photon fluorescence imaging experiments were performed as previously described [33], using a specialized laser-scanning microscope based on a commercial scan head (TriMScope II, LaVision BioTec, Bielefeld, Germany). A near-infrared laser (Ti:Sa, Chameleon Ultra II, Coherent, Duisburg, Germany) tuned at 760 nm, repetition rate 80 MHz, and pulse width 140 fs was used as excitation source. The linearly polarized Ti:Sa beam was scanned over the sample by two galvanometric mirrors. A water-immersion objective lens (20×, NA 1.05, Achromat, Olympus, Hamburg Germany) was used to focus the laser beam into the sample. The laser power was controlled by combinations of

$\lambda/2$  wave-plates and polarizers. The ultrashort pulses of the laser were compressed using external compressor. NADH and NADPH fluorescence was collected in the backward direction using a dichroic mirror (775, Chroma, Marlborough, MA, USA), passed through an interference filter ( $466 \pm 30$  nm) and was detected by a GaAsP PMT (Hamamatsu, Herrsching, Germany) connected to previously described TCSPC electronics (LaVision BioTec). The TCSPC data were collected at a time resolution of 55 ps, over at least 9 ns and with a Gaussian-shaped instrument response function of 250 ps FWHM (Figure S6). In all imaging experiments, we used an average maximum laser power of 10 mW to avoid photodamage. The acquisition time for an image with a field-of-view of  $200 \mu\text{m} \times 200 \mu\text{m}$  and a digital resolution of  $512 \times 512$  pixel was 472 ms.

#### 4.2. Phasor Analysis of Time-Domain NAD(P)H-FLIM Data

Fluorescence lifetime data were measured and analyzed as previously described [33,60,69]. The phasor approach transforms the time-domain data (the fluorescence decay curve), to a virtual, normalized phase domain by calculating the discrete Fourier transformation numerically (modulations frequency = 80 MHz). The transformation leads to a complex number the real and imaginary parts of which give the coordinates of the vector in the phase domain ("phasor"). That vector originated in (0|0) and points towards the half circle (centrum at (0.5|0), radius = 0.5), due to the exponential nature of the original time domain data. Because of the value normalization, the real part of the phasor reaches from 0 to 1, and those of the imaginary part from 0 to 0.5. In this way, short fluorescence lifetimes of homogeneous fluorophores (monoexponential decay) are located on the half circle at large real values, whereas with increasing lifetime, the real value decreases.

#### 4.3. Enzyme and NAD(P)H Solutions

NADH (10107735001, Roche, Basel, Switzerland), NADPH (N7505, Sigma, Darmstadt, Germany), and all enzymes were solved in 100 mM MOPS buffer (pH 7.8) (6979.4, Carl Roth, Karlsruhe, Germany). The enzymes PDH (8646-DH-050, R&D Systems, Minneapolis, MN, USA), CTBP1 (PRO-796, ProSpec, Rehovot, Israel), IDH (I5036, Sigma), GAPDH (G2267, Sigma), G6PDH (10127655001, Roche), LDH (LLDH-RO, Roche), HADH (ENZ-499, ProSpec), and MDH (LMDH-RO, Roche) were incubated in varying concentrations with NADH or NADPH, respectively. For the inhibition of LDH, the small molecule FX11 (427218, Sigma) was solved in DMSO and used in varying concentrations (10  $\mu\text{M}$ , 0.5 mM, and 1 mM). All measurements were performed at room temperature.

#### 4.4. T3-L1 Cell Culture and Preparation for Imaging

The culture of 3T3-L1 cells was performed in T75 cell culture flasks (658 175, Greiner, Frickenhausen, Germany) in growth medium (90% DMEM, high glucose (61965-026, Fisher Scientific GmbH, Darmstadt, Germany), 10% fetal calf serum (FCS) (S1810-500, Biowest, Nuaille, France), 1% penicillin-streptomycin (15140-122, Life Technologies GmbH, Darmstadt, Germany), and 1 mM sodium pyruvate (11360-070, Fisher Scientific GmbH)). Cells were split in a 1:10 ratio every 2 to 3 days. The utilized cultured cells were in passages 14–18.

For NAD(P)H-FLIM measurements, 240,000 cells per well were seeded into 6-well plates (657160, Greiner) in regular growth medium. The growth medium was exchanged daily. After 3 days, the medium was aspirated and replenished with imaging medium (90% DMEM, high glucose, HEPES, no phenol red (21063-029, Fisher Scientific GmbH), 10% FCS (S1810-500, Biowest)). During imaging cells were kept on 37 °C.

**Supplementary Materials:** The following are available online at <http://www.mdpi.com/1422-0067/20/22/5565/s1>.

**Author Contributions:** R.L. and R.A.N. conceived the algorithm on which the analysis framework of NAD(P)H-FLIM data is based. R.L., M.K., and R.A.N. conceived the experimental project. R.L. and M.K. performed experiments and analyzed data. A.E.H. and H.R. provided expertise regarding the cellular metabolism of immune and stromal cells. R.L., M.K., A.E.H., and R.A.N. wrote the manuscript. All authors edited and confirmed the manuscript.

**Funding:** This research was funded by the German Research Council (DFG) under grants TRR130 (C01 to R.A.N. and A.E.H.; P17 to A.E.H. and H.R.), FOR2165/2 (Ni1167/4-2 to R.A.N. and Ha5354/6-2 to A.E.H.), and Ha5354/8-2 to A.E.H.

**Acknowledgments:** We thank Robert Günther and Peggy Mex for excellent technical support. Ruth Leben is a member of the Dahlem Research School (DRS), Freie Universität, Berlin. Additionally, we would like to thank Mairi McGrath for language and style proofreading.

**Conflicts of Interest:** The authors declare no conflict of interest. The funders had no role in the design of the study; in the collection, analyses, or interpretation of data; in the writing of the manuscript, or in the decision to publish the results.

## References

1. Jellusova, J.; Rickert, R.C. A Brake for B Cell Proliferation: Appropriate responses to metabolic stress are crucial to maintain B cell viability and prevent malignant outgrowth. *Bioessays* **2017**, *39*. [[CrossRef](#)]
2. Caputa, G.; Castoldi, A.; Pearce, E.J. Metabolic adaptations of tissue-resident immune cells. *Nat. Immunol.* **2019**, *20*, 793–801. [[CrossRef](#)]
3. Jellusova, J.; Cato, M.H.; Apgar, J.R.; Ramezani-Rad, P.; Leung, C.R.; Chen, C.; Richardson, A.D.; Conner, E.M.; Benschop, R.J.; Woodgett, J.R.; et al. Gsk3 is a metabolic checkpoint regulator in B cells. *Nat. Immunol.* **2017**, *18*, 303–312. [[CrossRef](#)]
4. Huntosova, V.; Gay, S.; Nowak-Sliwinska, P.M.; Rajendran, S.K.; Zellweger, M.; Van Den Bergh, H.; Wagnières, G. In vivo measurement of tissue oxygenation by time-resolved luminescence spectroscopy: Advantageous properties of dichlorotris (1, 10-phenanthroline)-ruthenium (II) hydrate. *J. Biomed. Opt.* **2014**, *19*, 077004. [[CrossRef](#)] [[PubMed](#)]
5. Papkovsky, D.B.; Dmitriev, R.I. Biological detection by optical oxygen sensing. *Chem. Soc. Rev.* **2013**, *42*, 8700–8732. [[CrossRef](#)] [[PubMed](#)]
6. Lakowicz, J.R.; Szmacinski, H.; Nowaczyk, K.; Johnson, M.L. Fluorescence lifetime imaging of free and protein-bound NADH. *Proc. Natl. Acad. Sci. USA* **1992**, *89*, 1271–1275. [[CrossRef](#)] [[PubMed](#)]
7. Denk, W.; Strickler, J.H.; Webb, W.W. Two-photon laser scanning fluorescence microscopy. *Science* **1990**, *248*, 73–76. [[CrossRef](#)]
8. Mossakowski, A.A.; Pohlan, J.; Bremer, D.; Lindquist, R.; Millward, J.M.; Bock, M.; Pollok, K.; Mothes, R.; Viohl, L.; Radbruch, H.; et al. Tracking CNS and systemic sources of oxidative stress during the course of chronic neuroinflammation. *Acta Neuropathol.* **2015**, *130*, 799–814. [[CrossRef](#)]
9. Radbruch, H.; Guenther, R.; Cseresnyes, Z.; Lindquist, R.; Hauser, A.E.; Niesner, R. Ongoing Oxidative Stress Causes Subclinical Neuronal Dysfunction in the Recovery Phase of EAE. *Front. Immunol.* **2016**, *7*, 92. [[CrossRef](#)]
10. Radbruch, H.; Bremer, D.; Mothes, R.; Gunther, R.; Rinnenthal, J.L.; Pohlan, J.; Ulbricht, C.; Hauser, A.E.; Niesner, R. Intravital FRET: Probing Cellular and Tissue Function in Vivo. *Int. J. Mol. Sci.* **2015**, *16*, 11713–11727. [[CrossRef](#)]
11. Rinnenthal, J.L.; Bornchen, C.; Radbruch, H.; Andresen, V.; Mossakowski, A.; Siffrin, V.; Seelemann, T.; Spiecker, H.; Moll, I.; Herz, J.; et al. Parallelized TCSPC for dynamic intravital fluorescence lifetime imaging: Quantifying neuronal dysfunction in neuroinflammation. *PLoS ONE* **2013**, *8*, e60100. [[CrossRef](#)] [[PubMed](#)]
12. Rakymzhan, A.; Radbruch, H.; Niesner, R.A. Quantitative Imaging of Ca(2+) by 3D-FLIM in Live Tissues. *Adv. Exp. Med. Biol.* **2017**, *1035*, 135–141. [[CrossRef](#)] [[PubMed](#)]
13. Radbruch, H.; Mothes, R.; Bremer, D.; Seifert, S.; Kohler, R.; Pohlan, J.; Ostendorf, L.; Gunther, R.; Leben, R.; Stenzel, W.; et al. Analyzing Nicotinamide Adenine Dinucleotide Phosphate Oxidase Activation in Aging and Vascular Amyloid Pathology. *Front. Immunol.* **2017**, *8*, 844. [[CrossRef](#)] [[PubMed](#)]
14. Bayerl, S.H.; Niesner, R.; Cseresnyes, Z.; Radbruch, H.; Pohlan, J.; Brandenburg, S.; Czabanka, M.A.; Vajkoczy, P. Time lapse in vivo microscopy reveals distinct dynamics of microglia-tumor environment interactions—a new role for the tumor perivascular space as highway for trafficking microglia. *Glia* **2016**, *64*, 1210–1226. [[CrossRef](#)]
15. Tomkova, S.; Misuth, M.; Lenkavska, L.; Miskovsky, P.; Huntosova, V. In vitro identification of mitochondrial oxidative stress production by time-resolved fluorescence imaging of glioma cells. *Biochim. Biophys. Acta* **2018**, *1865*, 616–628. [[CrossRef](#)]

16. Kumar, S.; Dunsby, C.; De Beule, P.A.; Owen, D.M.; Anand, U.; Lanigan, P.M.; Benninger, R.K.; Davis, D.M.; Neil, M.A.; Anand, P.; et al. Multifocal multiphoton excitation and time correlated single photon counting detection for 3-D fluorescence lifetime imaging. *Opt. Express* **2007**, *15*, 12548–12561. [[CrossRef](#)]
17. Stringari, C.; Cinquin, A.; Cinquin, O.; Digman, M.A.; Donovan, P.J.; Gratton, E. Phasor approach to fluorescence lifetime microscopy distinguishes different metabolic states of germ cells in a live tissue. *Proc. Natl. Acad. Sci. USA* **2011**, *108*, 13582–13587. [[CrossRef](#)]
18. Stringari, C.; Nourse, J.L.; Flanagan, L.A.; Gratton, E. Phasor fluorescence lifetime microscopy of free and protein-bound NADH reveals neural stem cell differentiation potential. *PLoS ONE* **2012**, *7*, e48014. [[CrossRef](#)]
19. Wright, B.K.; Andrews, L.M.; Jones, M.R.; Stringari, C.; Digman, M.A.; Gratton, E. Phasor-FLIM analysis of NADH distribution and localization in the nucleus of live progenitor myoblast cells. *Microsc. Res. Tech.* **2012**, *75*, 1717–1722. [[CrossRef](#)]
20. Wright, B.K.; Andrews, L.M.; Markham, J.; Jones, M.R.; Stringari, C.; Digman, M.A.; Gratton, E. NADH distribution in live progenitor stem cells by phasor-fluorescence lifetime image microscopy. *Biophys. J.* **2012**, *103*, L7–L9. [[CrossRef](#)]
21. Guo, H.W.; Chen, C.T.; Wei, Y.H.; Lee, O.K.; Gukassyan, V.; Kao, F.J.; Wang, H.W. Reduced nicotinamide adenine dinucleotide fluorescence lifetime separates human mesenchymal stem cells from differentiated progenies. *J. Biomed. Opt.* **2008**, *13*, 050505. [[CrossRef](#)] [[PubMed](#)]
22. Gratton, E.; Breusegem, S.; Sutin, J.; Ruan, Q.; Barry, N. Fluorescence lifetime imaging for the two-photon microscope: Time-domain and frequency-domain methods. *J. Biomed. Opt.* **2003**, *8*, 381–390. [[CrossRef](#)] [[PubMed](#)]
23. Elson, D.; Requejo-Isidro, J.; Munro, I.; Reavell, F.; Siegel, J.; Suhling, K.; Tadrous, P.; Benninger, R.; Lanigan, P.; McGinty, J.; et al. Time-domain fluorescence lifetime imaging applied to biological tissue. *Photochem. Photobiol. Sci.* **2004**, *3*, 795–801. [[CrossRef](#)] [[PubMed](#)]
24. Soloviev, V.Y.; Tahir, K.B.; McGinty, J.; Elson, D.S.; Neil, M.A.; French, P.M.; Arridge, S.R. Fluorescence lifetime imaging by using time-gated data acquisition. *Appl. Opt.* **2007**, *46*, 7384–7391. [[CrossRef](#)] [[PubMed](#)]
25. Suhling, K.; French, P.M.; Phillips, D. Time-resolved fluorescence microscopy. *Photochem. Photobiol. Sci.* **2005**, *4*, 13–22. [[CrossRef](#)] [[PubMed](#)]
26. Poland, S.P.; Krstajic, N.; Monypenny, J.; Coelho, S.; Tyndall, D.; Walker, R.J.; Devauges, V.; Richardson, J.; Dutton, N.; Barber, P.; et al. A high speed multifocal multiphoton fluorescence lifetime imaging microscope for live-cell FRET imaging. *Biomed. Opt. Express* **2015**, *6*, 277–296. [[CrossRef](#)] [[PubMed](#)]
27. Agronskaia, A.V.; Tertoolen, L.; Gerritsen, H.C. Fast fluorescence lifetime imaging of calcium in living cells. *J. Biomed. Opt.* **2004**, *9*, 1230–1237. [[CrossRef](#)] [[PubMed](#)]
28. Gerritsen, H.C.; Asselbergs, M.A.; Agronskaia, A.V.; Van Sark, W.G. Fluorescence lifetime imaging in scanning microscopes: Acquisition speed, photon economy and lifetime resolution. *J. Microsc.* **2002**, *206*, 218–224. [[CrossRef](#)]
29. Scott, T.G.; Spencer, R.D.; Leonard, N.J.; Weber, G. Synthetic spectroscopic models related to coenzymes and base pairs. V. Emission properties of NADH. Studies of fluorescence lifetimes and quantum efficiencies of NADH, AcPyADH, [reduced acetylpyridineadenine dinucleotide] and simplified synthetic models. *J. Am. Chem. Soc.* **1970**, *92*, 687–695. [[CrossRef](#)]
30. Lakowicz, J.R.; Szmajcinski, H.; Nowaczyk, K.; Berndt, K.W.; Johnson, M. Fluorescence lifetime imaging. *Anal. Biochem.* **1992**, *202*, 316–330. [[CrossRef](#)]
31. Squire, A.; Verveer, P.J.; Bastiaens, P.I. Multiple frequency fluorescence lifetime imaging microscopy. *J. Microsc.* **2000**, *197*, 136–149. [[CrossRef](#)] [[PubMed](#)]
32. Verveer, P.J.; Rocks, O.; Harpur, A.G.; Bastiaens, P.I. FLIM measurements and frequency domain FLIM data analysis. *CSH Protoc.* **2006**, *2006*. [[CrossRef](#)] [[PubMed](#)]
33. Leben, R.; Ostendorf, L.; van Koppen, S.; Rakhymzhan, A.; Hauser, A.E.; Radbruch, H.; Niesner, R.A. Phasor-Based Endogenous NAD(P)H Fluorescence Lifetime Imaging Unravels Specific Enzymatic Activity of Neutrophil Granulocytes Preceding NETosis. *Int. J. Mol. Sci.* **2018**, *19*, 1018. [[CrossRef](#)] [[PubMed](#)]
34. Chance, B. Mitochondrial NADH redox state, monitoring discovery and deployment in tissue. *Methods Enzymol* **2004**, *385*, 361–370. [[CrossRef](#)] [[PubMed](#)]
35. Chacko, J.V.; Eliceiri, K.W. Autofluorescence lifetime imaging of cellular metabolism: Sensitivity toward cell density, pH, intracellular, and intercellular heterogeneity. *Cytometry A* **2019**, *95*, 56–69. [[CrossRef](#)]

36. Xu, H.N.; Tchou, J.; Chance, B.; Li, L.Z. Imaging the redox states of human breast cancer core biopsies. *Adv. Exp. Med. Biol.* **2013**, *765*, 343–349. [[CrossRef](#)]
37. Bird, D.K.; Yan, L.; Vrotsos, K.M.; Eliceiri, K.W.; Vaughan, E.M.; Keely, P.J.; White, J.G.; Ramanujam, N. Metabolic mapping of MCF10A human breast cells via multiphoton fluorescence lifetime imaging of the coenzyme NADH. *Cancer Res.* **2005**, *65*, 8766–8773. [[CrossRef](#)]
38. Skala, M.C.; Riching, K.M.; Bird, D.K.; Gendron-Fitzpatrick, A.; Eickhoff, J.; Eliceiri, K.W.; Keely, P.J.; Ramanujam, N. In vivo multiphoton fluorescence lifetime imaging of protein-bound and free nicotinamide adenine dinucleotide in normal and precancerous epithelia. *J. Biomed. Opt.* **2007**, *12*, 024014. [[CrossRef](#)]
39. Skala, M.C.; Riching, K.M.; Gendron-Fitzpatrick, A.; Eickhoff, J.; Eliceiri, K.W.; White, J.G.; Ramanujam, N. In vivo multiphoton microscopy of NADH and FAD redox states, fluorescence lifetimes, and cellular morphology in precancerous epithelia. *Proc. Natl. Acad. Sci. USA* **2007**, *104*, 19494–19499. [[CrossRef](#)]
40. Provenzano, P.P.; Eliceiri, K.W.; Keely, P.J. Multiphoton microscopy and fluorescence lifetime imaging microscopy (FLIM) to monitor metastasis and the tumor microenvironment. *Clin. Exp. Metastasis* **2009**, *26*, 357–370. [[CrossRef](#)]
41. Meleshina, A.V.; Cherkasova, E.I.; Shirmanova, M.V.; Klementieva, N.V.; Kiseleva, E.V.; Snopova, L.; Ve, C.; Prodanets, N.N.; Zagaynova, E.V. Influence of mesenchymal stem cells on metastasis development in mice in vivo. *Stem Cell Res. Ther.* **2015**, *6*, 15. [[CrossRef](#)] [[PubMed](#)]
42. Meleshina, A.V.; Dudenkova, V.V.; Bystrova, A.S.; Kuznetsova, D.S.; Shirmanova, M.V.; Zagaynova, E.V. Two-photon FLIM of NAD(P)H and FAD in mesenchymal stem cells undergoing either osteogenic or chondrogenic differentiation. *Stem Cell Res. Ther.* **2017**, *8*, 15. [[CrossRef](#)] [[PubMed](#)]
43. Meleshina, A.V.; Dudenkova, V.V.; Shirmanova, M.V.; Shcheslavskiy, V.I.; Becker, W.; Bystrova, A.S.; Cherkasova, E.I.; Zagaynova, E.V. Probing metabolic states of differentiating stem cells using two-photon FLIM. *Sci. Rep.* **2016**, *6*, 21853. [[CrossRef](#)] [[PubMed](#)]
44. Evers, M.; Salma, N.; Osseiran, S.; Casper, M.; Birngruber, R.; Evans, C.L.; Manstein, D. Enhanced quantification of metabolic activity for individual adipocytes by label-free FLIM. *Sci. Rep.* **2018**, *8*, 8757. [[CrossRef](#)] [[PubMed](#)]
45. Lindquist, R.L.; Bayat-Sarmadi, J.; Leben, R.; Niesner, R.; Hauser, A.E. NAD(P)H Oxidase Activity in the Small Intestine Is Predominantly Found in Enterocytes, Not Professional Phagocytes. *Int. J. Mol. Sci.* **2018**, *19*, 1365. [[CrossRef](#)] [[PubMed](#)]
46. Alturkistany, F.; Nichani, K.; Houston, K.D.; Houston, J.P. Fluorescence lifetime shifts of NAD(P)H during apoptosis measured by time-resolved flow cytometry. *Cytometry A* **2019**, *95*, 70–79. [[CrossRef](#)] [[PubMed](#)]
47. Sharick, J.T.; Favreau, P.F.; Gillette, A.A.; Sdao, S.M.; Merrins, M.J.; Skala, M.C. Protein-bound NAD(P)H Lifetime is Sensitive to Multiple Fates of Glucose Carbon. *Sci. Rep.* **2018**, *8*, 5456. [[CrossRef](#)]
48. Niesner, R.; Peker, B.; Schlusche, P.; Gericke, K.H. Noniterative biexponential fluorescence lifetime imaging in the investigation of cellular metabolism by means of NAD(P)H autofluorescence. *Chemphyschem* **2004**, *5*, 1141–1149. [[CrossRef](#)]
49. Strickler, S.J.; Robert, A.B. Relationship between Absorption Intensity and Fluorescence Lifetime of Molecules. *J. Chem. Phys.* **1962**, *37*, 814–822. [[CrossRef](#)]
50. Behne, M.J.; Meyer, J.W.; Hanson, K.M.; Barry, N.P.; Murata, S.; Crumrine, D.; Clegg, R.W.; Gratton, E.; Holleran, W.M.; Elias, P.M.; et al. NHE1 regulates the stratum corneum permeability barrier homeostasis. Microenvironment acidification assessed with fluorescence lifetime imaging. *J. Biol. Chem.* **2002**, *277*, 47399–47406. [[CrossRef](#)]
51. Niesner, R.; Peker, B.; Schlusche, P.; Gericke, K.H.; Hoffmann, C.; Hahne, D.; Müller-Goymann, C. 3D-resolved investigation of the pH gradient in artificial skin constructs by means of fluorescence lifetime imaging. *Pharm. Res.* **2005**, *22*, 1079–1087. [[CrossRef](#)] [[PubMed](#)]
52. Celli, A.; Sanchez, S.; Behne, M.; Hazlett, T.; Gratton, E.; Mauro, T. The epidermal Ca(2+) gradient: Measurement using the phasor representation of fluorescent lifetime imaging. *Biophys. J.* **2010**, *98*, 911–921. [[CrossRef](#)]
53. Blacker, T.S.; Mann, Z.F.; Gale, J.E.; Ziegler, M.; Bain, A.J.; Szabadkai, G.; Duchen, M.R. Separating NADH and NADPH fluorescence in live cells and tissues using FLIM. *Nat. Commun.* **2014**, *5*, 3936. [[CrossRef](#)] [[PubMed](#)]
54. Datta, R.; Alfonso-Garcia, A.; Cinco, R.; Gratton, E. Fluorescence lifetime imaging of endogenous biomarker of oxidative stress. *Sci. Rep.* **2015**, *5*, 9848. [[CrossRef](#)] [[PubMed](#)]

55. Niesner, R.; Narang, P.; Spiecker, H.; Andresen, V.; Gericke, K.H.; Gunzer, M. Selective detection of NADPH oxidase in polymorphonuclear cells by means of NAD(P)H-based fluorescence lifetime imaging. *J. Biophys.* **2008**, *2008*, 602639. [[CrossRef](#)] [[PubMed](#)]
56. Lee, K.C.; Siegel, J.; Webb, S.E.; Leveque-Fort, S.; Cole, M.J.; Jones, R.; Dowling, K.; Lever, M.J.; French, P.M. Application of the stretched exponential function to fluorescence lifetime imaging. *Biophys. J.* **2001**, *81*, 1265–1274. [[CrossRef](#)]
57. Zhang, Q.; Piston, D.W.; Goodman, R.H. Regulation of corepressor function by nuclear NADH. *Science* **2002**, *295*, 1895–1897. [[CrossRef](#)]
58. Madhukar, N.S.; Warmoes, M.O.; Locasale, J.W. Organization of enzyme concentration across the metabolic network in cancer cells. *PLoS ONE* **2015**, *10*, e0117131. [[CrossRef](#)]
59. Babior, B.M. NADPH oxidase. *Curr. Opin. Immunol.* **2004**, *16*, 42–47. [[CrossRef](#)]
60. Ranjit, S.; Malacrida, L.; Jameson, D.M.; Gratton, E. Fit-free analysis of fluorescence lifetime imaging data using the phasor approach. *Nat. Protoc.* **2018**, *13*, 1979–2004. [[CrossRef](#)]
61. Lindquist, R.L.; Niesner, R.A.; Hauser, A.E. In the Right Place, at the Right Time: Spatiotemporal Conditions Determining Plasma Cell Survival and Function. *Front. Immunol.* **2019**, *10*, 788. [[CrossRef](#)] [[PubMed](#)]
62. Itkin, T.; Gur-Cohen, S.; Spencer, J.A.; Schajnovitz, A.; Ramasamy, S.K.; Kusumbe, A.P.; Ledergor, G.; Jung, Y.; Milo, I.; Poulos, M.G.; et al. Distinct bone marrow blood vessels differentially regulate haematopoiesis. *Nature* **2016**, *532*, 323–328. [[CrossRef](#)] [[PubMed](#)]
63. Ambrosi, T.H.; Scialdone, A.; Graja, A.; Gohlke, S.; Jank, A.M.; Bocian, C.; Woelk, L.; Fan, H.; Logan, D.W.; Schurmann, A.; et al. Adipocyte Accumulation in the Bone Marrow during Obesity and Aging Impairs Stem Cell-Based Hematopoietic and Bone Regeneration. *Cell Stem Cell* **2017**, *20*, 771–778. [[CrossRef](#)] [[PubMed](#)]
64. Czechowska, K.; Lannigan, J.; Wang, L.; Arcidiacono, J.; Ashhurst, T.M.; Barnard, R.M.; Bauer, S.; Bispo, C.; Bonilla, D.L.; Brinkman, R.R.; et al. Cyt-Geist: Current and Future Challenges in Cytometry: Reports of the CYTO 2018 Conference Workshops. *Cytometry A* **2019**, *95*, 598–644. [[CrossRef](#)] [[PubMed](#)]
65. Jellusova, J. Cross-talk between signal transduction and metabolism in B cells. *Immunol. Lett.* **2018**, *201*, 1–13. [[CrossRef](#)]
66. O'Neill, L.A.; Kishton, R.J.; Rathmell, J. A guide to immunometabolism for immunologists. *Nat. Rev. Immunol.* **2016**, *16*, 553–565. [[CrossRef](#)]
67. Holzwarth, K.; Kohler, R.; Philipsen, L.; Tokoyoda, K.; Ladyhina, V.; Wahlby, C.; Niesner, R.A.; Hauser, A.E. Multiplexed fluorescence microscopy reveals heterogeneity among stromal cells in mouse bone marrow sections. *Cytometry A* **2018**, *93*, 876–888. [[CrossRef](#)]
68. Zehentmeier, S.; Roth, K.; Cseresnyes, Z.; Sercan, O.; Horn, K.; Niesner, R.A.; Chang, H.D.; Radbruch, A.; Hauser, A.E. Static and dynamic components synergize to form a stable survival niche for bone marrow plasma cells. *Eur J. Immunol.* **2014**, *44*, 2306–2317. [[CrossRef](#)]
69. Digman, M.A.; Caiolfa, V.R.; Zamai, M.; Gratton, E. The phasor approach to fluorescence lifetime imaging analysis. *Biophys. J.* **2008**, *94*, L14–L16. [[CrossRef](#)]



© 2019 by the authors. Licensee MDPI, Basel, Switzerland. This article is an open access article distributed under the terms and conditions of the Creative Commons Attribution (CC BY) license (<http://creativecommons.org/licenses/by/4.0/>).

## Supplementary Materials

**Supplement video 1.** To supplement figure 1 corresponding phasor plots.

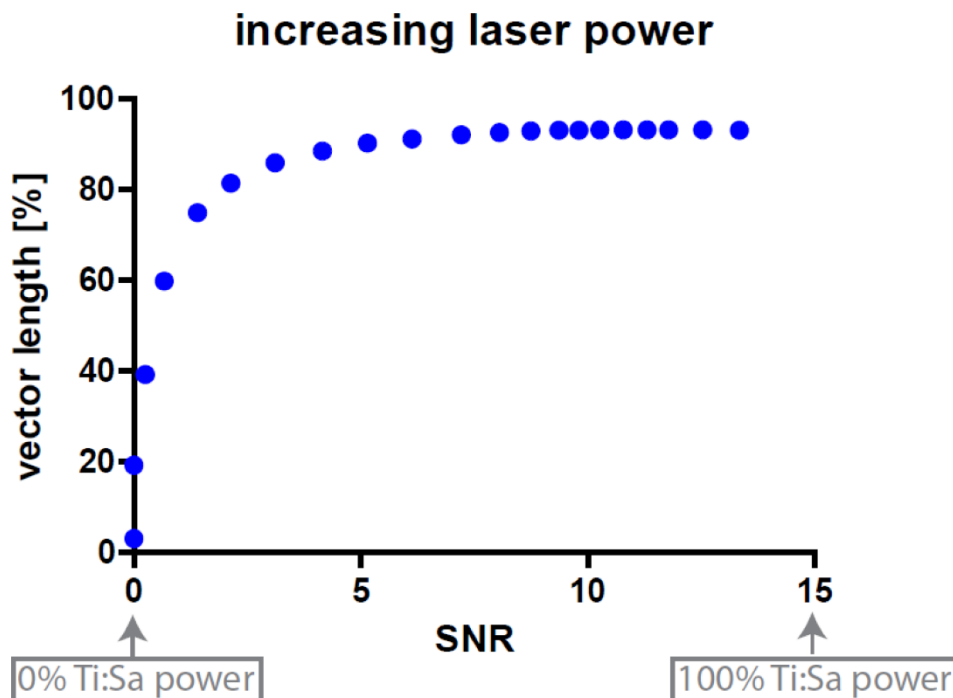


**Figure S1.** Free NADH solved in MOPS buffer excited with increasing laser power. Graph depicts SNR vs. vector length in percent (as described in *Results*). By increasing the excitation power, the SNR increased at a constant NADH concentration (50  $\mu$ M NADH). The power at “0% Ti:Sa” is 0mW and at “100% Ti:Sa” approx. 150 mW, it was altered in 5% steps by rotating a lambda-half plate. The SNR shows the same behavior as the increase of NADH concentration at fixed laser power (Fig. 1 Av)). In order to avoid photo bleaching and photo damage we used approx. 100mW excitation power in the following.

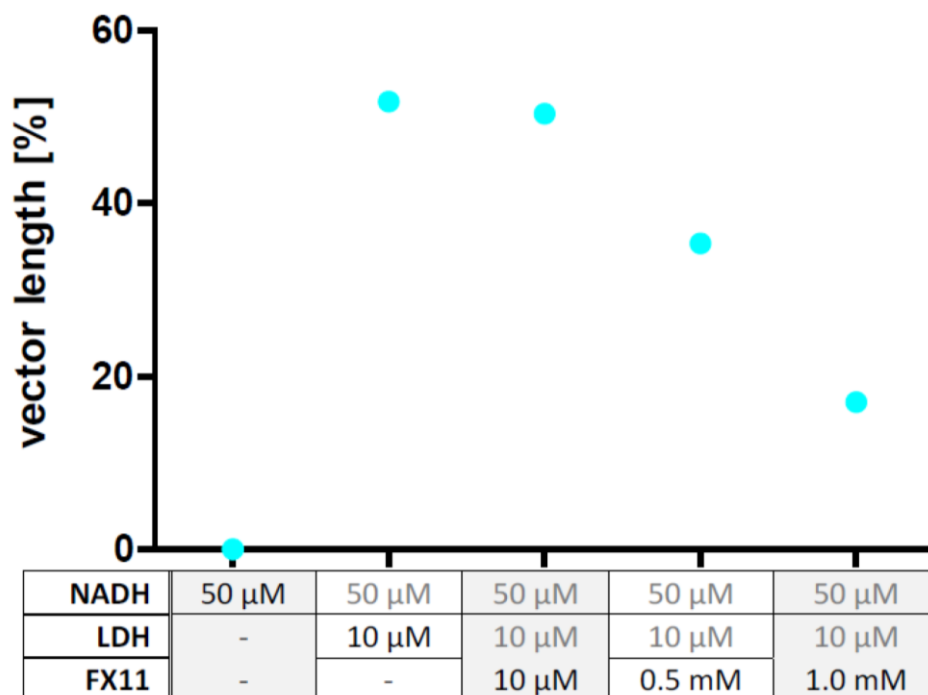


**Figure S2.** Tabled concentrations of NADH, LDH and FX11 vs. vector length. Vector length means the ratio of the vector “free NADH to the center of the center of the phasor cloud” to “free NADH to NADH fully bound to LDH position on the half circle” (cyan line in Fig. 1C), in percent. The addition of 10  $\mu$ M LDH to 50  $\mu$ M NADH results in an increase of the vector length ratio. The addition of FX11 to that mixture in different concentrations results in a decrease of the vector length ratio. FX11 is a LDH inhibitor, thus the phasor cloud migrates back towards free NAD(P)H with increasing FX11 concentration. (Same data as shown in Fig. 1C).

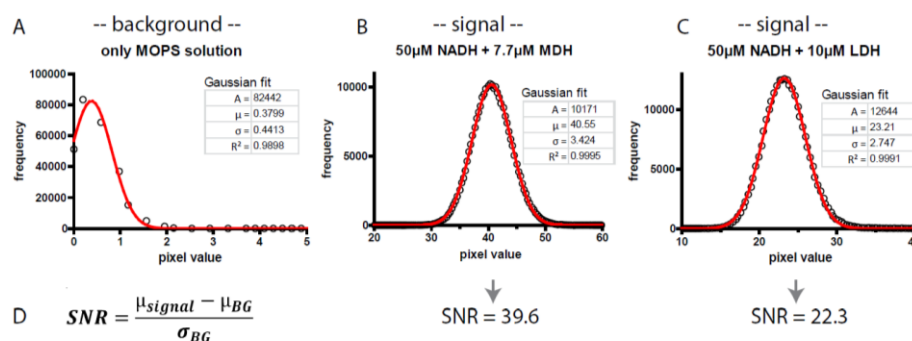


**Figure 3.** Calculation of signal-to-noise-ratio (SNR). **(A-C)** Gaussian fitted intensity histogram of **(A)** background measured in non-fluorescent MOPS solution (same data as shown in Fig. 1A i)), **(B)** 50  $\mu$ M NADH and 7.7  $\mu$ M MDH solved in MOPS solution (same data as shown in Fig. 1C iii)) and **(C)** 50  $\mu$ M NADH and 10  $\mu$ M LDH (same data as shown in Fig. 1C iii)). **(D)** formula to calculate SNR.  $\mu_{signal}$  mean intensity signal,  $\mu_{BG}$  mean intensity background,  $\sigma_{BG}$  standard deviation background. The SNR of **(B)** is 39.6 and **(C)** 22.3.

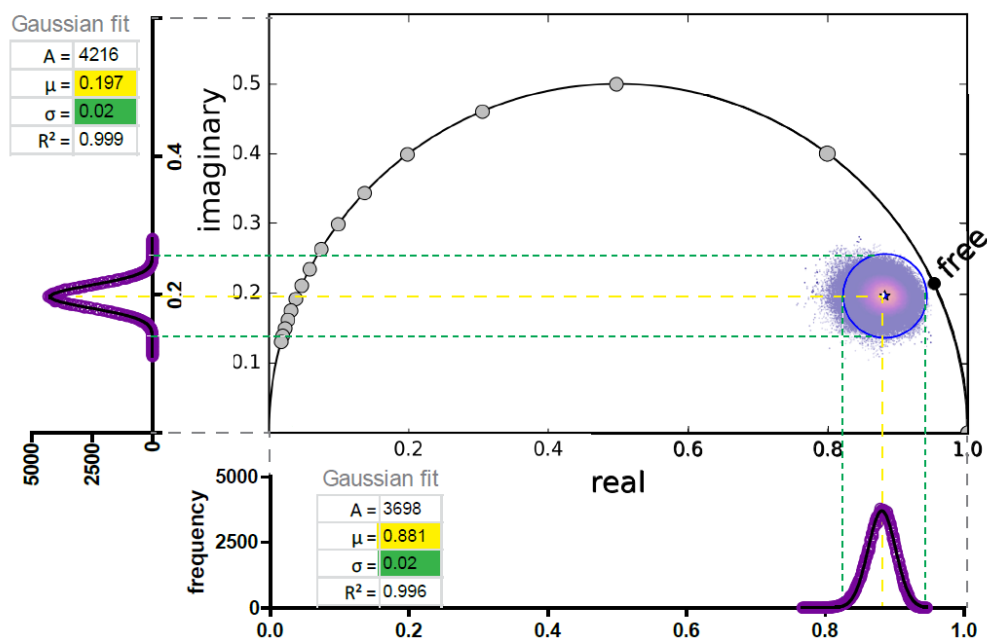


**Figure S4.** Determination of radius  $r$  to identify free NAD(P)H. The histograms of real and imaginary part of the dot cloud were Gaussian fitted. Used data are shown in Fig1 iv).  $\mu_{\text{real}}$  and  $\mu_{\text{imag}}$  give the coordinates of the center (0.881 | 0.197).  $\sigma_{\text{real}}$  and  $\sigma_{\text{imag}}$  are equal ( $\sigma = 0.02$ ).  $3\sigma (=0.06)$  gives the radius within which, by definition, 99.7% of the values are located. Gray dots onto half circle mark  $0 \leq \tau \leq 20$  ns in 1 ns steps.

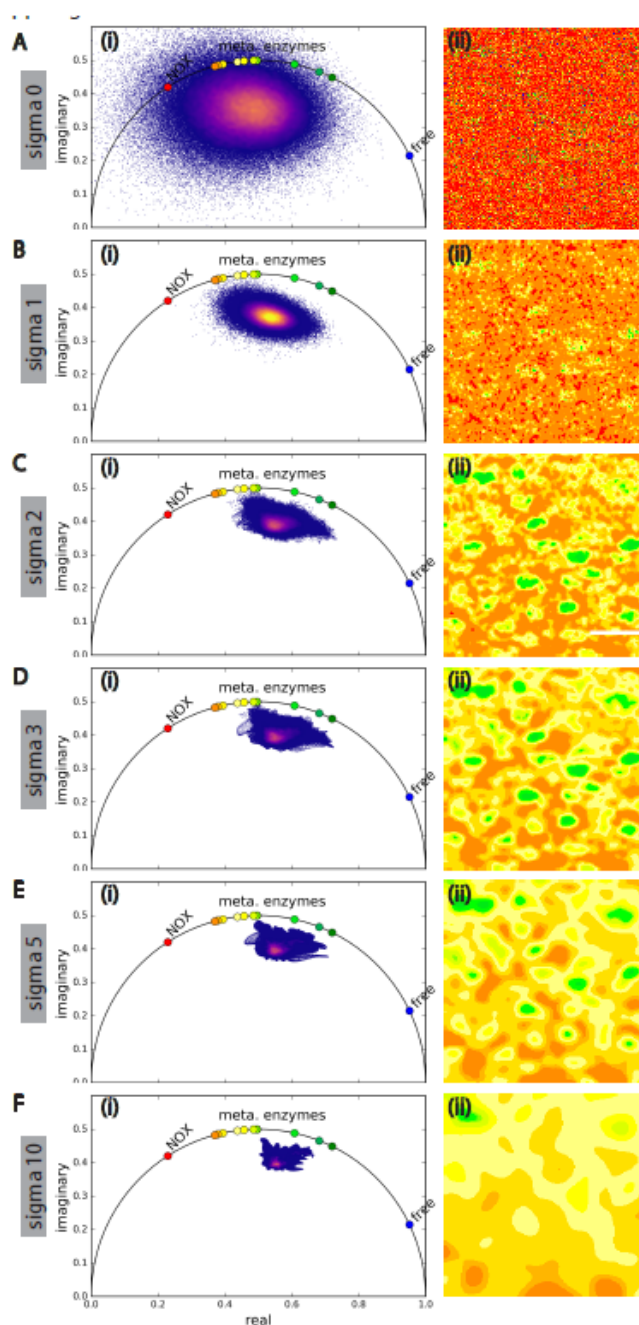


**Figure S5.** Influence of different sigma of Gaussian blur of time-domain raw data on phasor cloud (i) and enzyme map (ii). A-F same ROI as shown in Fig. 4C iii). The higher the sigma, the narrower the phasor cloud and the clearer the enzyme assignment, but at the cost of spatial resolution. If not stated otherwise, we always blurred our raw data with sigma 2 (C), which is (to our mind) a good compromise, between temporal and spatial resolution. White bar in D ii) indicates 50  $\mu\text{m}$  and is valid for all enzyme maps here.

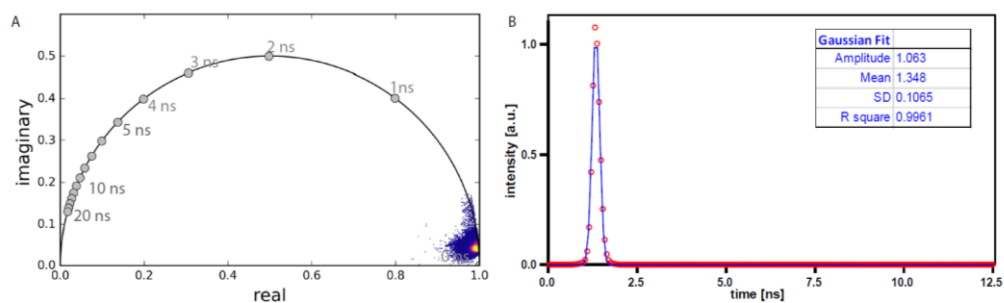


**Figure S6.** Instrument response function (IRF) of TCSPC measured by second harmonic generation (SHG) in potassium dihydrogen phosphate (KDP) powder ( $\lambda_{ex}=940$  nm,  $\lambda_{em}=470$  nm (in Ch 466/60),  $t_{bin}=55$  ps). **(A)** phasor plot. **(B)** Gaussian fitted IRF: the standard deviation is  $\sigma=0.1065$  ns, full width half maximum  $FWHM=2\sqrt{2\ln 2}\sigma=250.8$  ps. The retransfer of the phase domain data into the time domain results in an average lifetime of  $(0.084\pm 0.015)$  ns, which is the smallest resolvable time of our system. The phasor cloud of the IRF lies exactly where we expected it to be, so no position corrections were made in the following.

# Intravital quantification reveals dynamic calcium concentration changes across B cell differentiation stages

Carolyn Ulbricht<sup>1,2</sup>, Ruth Leben<sup>3</sup>, Asylkhan Rakhymzhan<sup>3</sup>, Frank Kirchhoff<sup>4</sup>, Lars Nitschke<sup>5</sup>, Helena Radbruch<sup>6</sup>, Raluca A Niesner<sup>3,7†</sup>, Anja E Hauser<sup>1,2†\*</sup>

<sup>1</sup>Charité – Universitätsmedizin Berlin, corporate member of Freie Universität Berlin and Humboldt-Universität zu Berlin, Department of Rheumatology and Clinical Immunology, Charitéplatz 1, Berlin, Germany; <sup>2</sup>Immune Dynamics, Deutsches Rheuma-Forschungszentrum Berlin, ein Institut der Leibniz-Gemeinschaft, Berlin, Germany; <sup>3</sup>Biophysical Analytics, Deutsches Rheuma-Forschungszentrum, ein Institut der Leibniz-Gemeinschaft, Berlin, Germany; <sup>4</sup>Universität des Saarlandes, Saarbrücken, Germany; <sup>5</sup>Friedrich-Alexander-Universität Erlangen-Nürnberg, Erlangen, Germany; <sup>6</sup>Charité – Universitätsmedizin Berlin, corporate member of Freie Universität Berlin and Humboldt-Universität zu Berlin, Department of Neuropathology, Charitéplatz 1, Berlin, Germany; <sup>7</sup>Veterinary Medicine, Freie Universität Berlin, Berlin, Germany

**Abstract** Calcium is a universal second messenger present in all eukaryotic cells. The mobilization and storage of Ca<sup>2+</sup> ions drives a number of signaling-related processes, stress-responses, or metabolic changes, all of which are relevant for the development of immune cells and their adaption to pathogens. Here, we introduce the Förster resonance energy transfer (FRET)-reporter mouse YellowCaB expressing the genetically encoded calcium indicator TN-XXL in B lymphocytes. Calcium-induced conformation change of TN-XXL results in FRET-donor quenching measurable by two-photon fluorescence lifetime imaging. For the first time, using our novel numerical analysis, we extract absolute cytoplasmic calcium concentrations in activated B cells during affinity maturation in vivo. We show that calcium in activated B cells is highly dynamic and that activation introduces a persistent calcium heterogeneity to the lineage. A characterization of absolute calcium concentrations present at any time within the cytosol is therefore of great value for the understanding of long-lived beneficial immune responses and detrimental autoimmunity.

\*For correspondence:  
hauser@drfz.de

†These authors contributed  
equally to this work

Competing interest: See  
page 21

Funding: See page 21

Received: 14 February 2020

Accepted: 19 March 2021

Published: 22 March 2021

Reviewing editor: Michael L  
Dustin, University of Oxford,  
United Kingdom

© Copyright Ulbricht et al. This  
article is distributed under the  
terms of the [Creative Commons  
Attribution License](#), which  
permits unrestricted use and  
redistribution provided that the  
original author and source are  
credited.

## Introduction

During generation of humoral immunity to pathogens, calcium-mobilizing events in lymphocytes can communicate such diverse outcomes as migration, survival, stress responses, or proliferation. An elevation of cytoplasmic calcium from external space is mostly mediated through ligand binding to surface receptors (Baba et al., 2014). Especially in the germinal center (GC), where B cells fine-tune their B cell receptor (BCR) in order to become positively selected by T cells, ligand density in the form of native antigen (AG), stimuli for toll-like receptors (TLR), or chemokine receptors, is high. Selected B cells that leave the GCs fuel the pool of memory B cells and long-lived plasma cells (LLPCs). These cells produce high-affinity antibodies granting up to lifelong protection against threats such as infectious diseases, but also can account for the persistence of an autoimmune phenotype, when selection within the GC is impaired (Berek et al., 1991; da Silva et al., 1998; Hiepe et al., 2011; Victora and Nussenzweig, 2012). B cell activation by AG uptake through the

BCR promotes calcium influx into B cells (Tolar et al., 2009). Calcium mobilization eventually switches on effector proteins and transcription factors like nuclear factor kappa B, nuclear factor of activated T cells, or myelocytomatosis oncogene cellular homolog, thereby inducing differentiation events and remodeling of metabolic requirements (Crabtree and Olson, 2002; Jellusova, 2018; Luo et al., 2018; Saijo et al., 2002; Su et al., 2002). Dependent on the amount of AG taken up and the quality of major histocompatibility complex II (MHCII)-mediated presentation to T follicular helper cells, B cells receive additional, costimulatory signals (Gitlin et al., 2015). Interestingly, recent studies propose that costimulatory signals have to occur within a limited period of time after initial BCR activation and that the limit is set by a calcium threshold, eventually leading to mitochondrial dysfunction (Akkaya et al., 2018). Thus, quantification of changes in absolute cytoplasmic calcium concentration tolerated by GC B cells would help to understand how B cell selection in the GC is accomplished.

In contrast to qualitative description, absolute calcium measurements in B cells have not yet been performed in vivo, partly because of the lack of internal concentration standards. Two-fluorophore genetically encoded calcium indicators (GECI) relying on Förster resonance energy transfer (FRET) can take on a calcium-saturated (quenched) and calcium-unsaturated (unquenched) condition, overcoming this issue. However, intravital application of quantitative FRET has been hampered by light distortion effects in deeper tissue. The differential scattering and photobleaching properties of the two fluorophores would lead to a false bias towards a higher quenching state. We here introduce a single-cell fluorescence lifetime imaging (FLIM) approach for absolute calcium quantification in living organisms that is tissue depth-independent. Both time-domain and frequency-domain FLIM technologies have been employed in the past 30 years to sense changes in pH, ionic strength, pO<sub>2</sub>, metabolism, and many other cellular parameters within living cells. Due to the impact of these parameters on the chemical structure, the fluorescence lifetime of the analyzed fluorophores can change (Elson et al., 2004; Lakowicz et al., 1992; Le Marois and Suhling, 2017). Particularly, the versatility of FLIM to quantify FRET quenching has been demonstrated and applied in various biological contexts (Chen et al., 2003; Levitt et al., 2020; Mossakowski et al., 2015). The enhanced cyan fluorescent protein (eCFP)/citrine-FRET pair-GECI TN-XXL is able to measure fluctuations in cytoplasmic calcium concentration through the calcium binding property of the muscle protein troponin C (TnC) (Mank et al., 2006). Calcium binding to the fluorophore-linker TnC quenches eCFP fluorescence through energy transfer to citrine (FRET), linking decreasing eCFP fluorescence lifetime to increasing calcium concentration. Whereas eCFP fluorescence lifetime changes with refractive index (Strickler and Berg, 1962) and may change upon large shifts in pH value, ionic strength, oxygenation, or temperature, these parameters hardly vary in the cytosol of living cells. Thus, we expect only changes in cytosolic calcium concentration to have an impact on the fluorescence lifetime of eCFP as donor in the TN-XXL construct. In addition, phasor analysis of FLIM data elegantly condenses multicomponent fluorescent decay curves into single vector-based information (the phasor) (Digman et al., 2008). For calcium concentration analysis in microscopic images, we first took advantage of the previously published titration curve of TN-XXL by Geiger et al., which we also confirmed in our experimental setup (Geiger et al., 2012). We further adapted the phasor-based calibration strategy to quantify calcium levels in vivo proposed by Celli and colleagues to the TN-XXL construct expressed in B lymphocytes (Celli et al., 2010). With this method, we are able to describe short- and long-term changes in absolute calcium concentrations within B cells during affinity maturation and differentiation into antibody-producing plasma cells.

We here describe the calcium reporter mouse strain 'YellowCaB' (termed after energy transfer to the yellow fluorescent protein citrine in case of calcium present in the cytosol of B cells). These mice express cytosolic TN-XXL in all CD19-positive cells. Intravital FLIM of adoptively transferred YellowCaB cells shows that calcium concentrations are highly dynamic in B cells involved in the GC reaction. We describe different patterns of calcium fluctuation regarding amplitude and baseline within non-activated and AG experienced cells and plasma blasts. We observe the emergence of Ca<sup>2+</sup>-high differentiated B cells and plasma blast populations, which might point to cells undergoing metabolic stress.

## Results

**YellowCaB: a system for FRET-based calcium analysis in B cells**

Mice expressing a loxP-flanked STOP sequence followed by the TN-XXL-construct inserted into the ROSA26 locus were crossed with the CD19-Cre strain (Rickert *et al.*, 1997). The offspring had exclusive expression of the GECI TN-XXL in CD19<sup>+</sup> B lymphocytes, as confirmed by visualization of eCFP and citrine fluorescence by confocal microscopy after magnetic B cell isolation (Figure 1a, b). These YellowCaB cells were excited with a 405 nm laser that is capable of exciting eCFP but not citrine. The detection of yellow emission thus can be attributed to baseline FRET representing steady-state calcium levels. Expression of TN-XXL in YellowCaB mice was further confirmed by flow cytometry after excitation with the 488 nm laser and detection in a CD19<sup>+</sup>GFP<sup>+</sup> (green fluorescent protein) gate that would also detect citrine fluorescence. Citrine was found to be present in a substantial part of CD19<sup>+</sup> B lymphocytes and was not detectable in the CD19<sup>-</sup> population (Figure 1c). *Cd19<sup>cre/+</sup>* mice heterozygous for TN-XXL and *Cd19<sup>cre/+</sup>* mice homozygous for TN-XXL did not differ in the

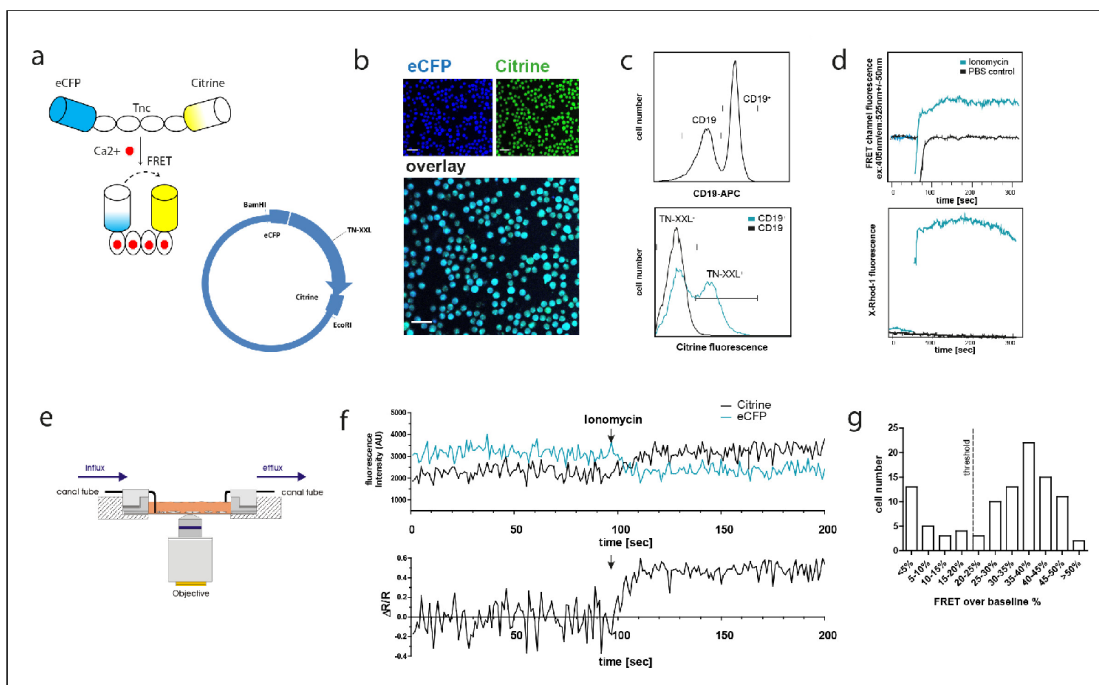


**Figure 1.** The genetically encoded calcium indicator (GECI) TN-XXL is functionally expressed in CD19<sup>+</sup> B cells of YellowCaB mice. (a) Schematic representation of the genetically encoded calcium indicator TN-XXL with the calcium-sensitive domain troponin C (TnC) fused to donor fluorophore eCFP and acceptor fluorophore citrine. Binding of Ca<sup>2+</sup> ions within (up to) four loops of TnC leads to quenching of eCFP and Förster resonance energy transfer (FRET) to citrine. (b) Confocal image of freshly isolated CD19<sup>+</sup> B cells. Overlapping blue and yellow-green fluorescence of eCFP and citrine, respectively, can be detected after Cre-loxP-mediated expression of the TN-XXL vector in YellowCaB mice. (c) Flow cytometric analysis of TN-XXL expression in lymphocytes from YellowCaB mice. (d) Flow cytometric measurement of calcium flux after addition of ionomycin and phosphate buffered saline control. (e) Continuous perfusion imaging chamber for live cell imaging. (f) Confocal measurement of mean fluorescence intensity and FRET signal change after addition of ionomycin to continuously perfused YellowCaB cells. Data representative for at least 100 cells out of three independent experiments. (g) Frequency histogram of > 100 YellowCaB single cells, FRET analyzed after ionomycin stimulation. Threshold chosen for positive FRET signal change = 20% over baseline intensity.

The online version of this article includes the following figure supplement(s) for figure 1:

**Figure supplement 1.** Genotyping of YellowCaB mice and cell numbers.

proportion of cells within the CD19<sup>+</sup>GFP<sup>+</sup> population, nor did male and female mice (*Figure 1—figure supplement 1*). In addition, no differences in total cell numbers and B cell numbers between *Cd19<sup>cre/+</sup>Tn-xxl<sup>+/+</sup>*, *Cd19<sup>cre/+</sup>Tn-xxl<sup>+/+</sup>*, and wild-type mice were detected (*Figure 1—figure supplement 1*). We next set out to test if we could induce a FRET signal change under calcium-saturating conditions in the cytoplasm. The ionophore ionomycin is commonly used as positive control in *in vitro* experiments measuring calcium concentrations as it uncouples the increase of calcium concentration from the physiological entry sites of Ca<sup>2+</sup> ions by forming holes in the cell membrane. When stimulated with ionomycin, a steep increase of the FRET level over baseline was recorded by flow cytometry in the GFP-channel after excitation with the 405 nm laser. Calcium-dependence of the signal increase was further independently confirmed by staining with the calcium sensitive dye X-Rhod-1, that shows a red fluorescence signal increase after calcium binding (*Figure 1d*; *Li et al., 2003*).

In preparation of our intravital imaging experiments, we first tested if the YellowCaB system is stable enough for time-resolved microscopic measurements and sensitive enough for subtle cytoplasmic calcium concentration changes as they occur after store-operated calcium entry (SOCE). In SOCE, stimulation of the BCR with AG leads to drainage of intracellular calcium stores in the endoplasmic reticulum (ER), which triggers calcium influx from the extracellular space into the cytosol through specialized channels (*Baba et al., 2014*). We established a customizable perfusion flow chamber system to monitor and manipulate YellowCaB cells over the duration of minutes to hours (*Figure 1e*). Division of the fluorescence intensity of electron acceptor citrine by that of donor eCFP yields the FRET ratio (R), which is then put into relationship to baseline FRET levels. As expected, we detected a decrease of the eCFP signal, concurrent with an increased citrine fluorescence after the addition of 4 μg/ml ionomycin to continuous flow of 6 mM Krebs-Ringer solution. Overall, this resulted in a maximal elevation of ΔR/R of 50–55% over baseline (*Figure 1f*). Analysis of >100 cells showed that approximately in three quarters of the cells we were able to detect FRET in response to ionomycin treatment, and that the majority of these cells showed 35–40% FRET signal change. According to the two populations visible in the histogram, we defined a change of 20% ΔR/R as a relevant threshold for the positive evaluation of responsiveness (*Figure 1g*). In conclusion, we achieved the functional and well-tolerated expression of TN-XXL exclusively in murine CD19<sup>+</sup> B cells for measurement of changes of cytoplasmic calcium concentrations.

### Repeated BCR stimulation results in fluctuating cytoplasmic calcium concentrations

SOCE in B cells can be provoked experimentally by stimulation of the BCR with multivalent AG, for example, anti-Ig heavy chain F(ab)<sub>2</sub> fragments. To test the functional performance of the GECI TN-XXL in YellowCaB cells, we stimulated isolated YellowCaB cells with 10 μg/ml anti-IgM F(ab)<sub>2</sub> fragments to activate the BCR. In an open culture imaging chamber, we induced an elevated FRET signal with a peak height of >30% that lasted over 3 min (*Figure 2a*). The signal declines after this time span, probably due to BCR internalization or the activity of ion pumps. We tested antibody concentrations at 2, 4, 10, and 20 μg/ml. An antibody concentration of 2 μg/ml was not enough to provoke calcium flux (data not shown), whereas at 4 μg/ml anti-IgM-F(ab)<sub>2</sub> we observed 20% an elevated ΔR/R over baseline (*Figure 2b*). At 20 μg/ml anti-IgM-F(ab)<sub>2</sub>, we detected no further FRET increase (*Figure 2—figure supplement 1a, b*). Thus, we conclude a concentration dependency of the GECI TN-XXL and saturating conditions at 10 μg/ml BCR heavy chain stimulation. Interestingly, the reaction is not completely cut off after the FRET signal has declined, but a residual FRET signal of about 7% compared to baseline values was measured for approximately 3.5 additional minutes (*Figure 2a*). Thus, B cells seem to be able to store extra calcium within the cytoplasm for some time. We therefore wondered if it is possible to stimulate YellowCaB cells more than once. For this purpose, we connected our imaging culture chamber to a peristaltic pump and took advantage of the fact that under continuous perfusion with Ringer solution the flow will dilute the antibody out of the chamber. This way, it is possible to stimulate B cells several times rapidly and subsequently, before BCRs are internalized, indicated by multiple peaks in ΔR/R (*Figure 2b*). In addition, stimulation of the BCR light chain using an anti-kappa antibody led to calcium increase within YellowCaB cells (*Figure 2—figure supplement 1a*). Of note, the resulting FRET peak is shaped differently, and concentrations > 150 μg/ml antibody were needed in order to generate a response.

Since T cell engagement and the binding of microbial targets to innate receptors like TLRs have also been described to raise cytoplasmic calcium in B cells (*Ojaniemi et al., 2003*; *Pone et al.,*

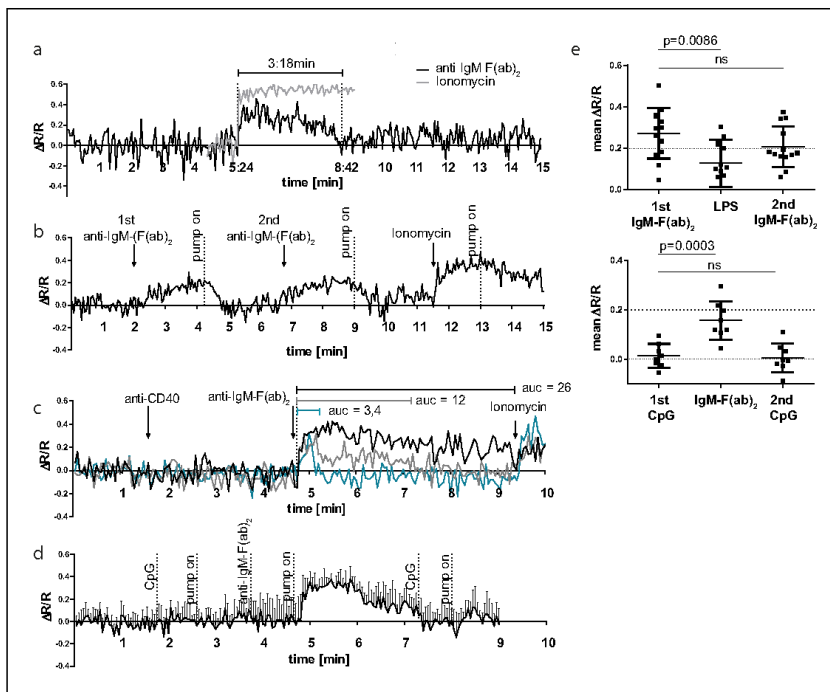


**Figure 2.** B cell receptor (BCR) stimulation specifically leads to calcium mobilization in YellowCaB cells *in vitro*. (a) Confocal measurement of Förster resonance energy transfer (FRET) duration ( $\Delta R/R > 0$ ) in non-perfused primary polyclonal YellowCaB cells after addition of 10  $\mu\text{g/ml}$  anti-IgM-F(ab)<sub>2</sub> (black) and ionomycin control (gray). Data representative for at least 35 single cells in four independent experiments. (b) Confocal measurement of FRET signal change after repeated addition of anti-IgM-F(ab)<sub>2</sub> to perfused primary polyclonal YellowCaB cells. Data representative for at least 50 cells out of five independent experiments. (c) Confocal measurement of FRET signal change after addition of anti-IgM-F(ab)<sub>2</sub> to perfused primary polyclonal YellowCaB cells following stimulation with anti-CD40 antibody and ionomycin as positive control. Examples of transient cytoplasmic (blue), intermediate (gray), and sustained calcium mobilization shown, area under the curve compared. Data representative for 26 cells out of two independent experiments. (d) Resulting FRET curve out for  $n = 7$  primary polyclonal YellowCaB cells perfused with toll-like receptor (TLR)9 stimulator cytosine phosphate guanine (CpG) in Ringer solution and subsequent addition of anti-IgM-F(ab)<sub>2</sub>. (e) Mean FRET signal change over time after addition of TLR4 or TLR9 stimulation in combination with BCR crosslinking by anti-IgM-F(ab)<sub>2</sub> in perfused polyclonal YellowCaB cells.  $n = 12$  (top) and  $n = 8$  (bottom), one-way ANOVA. Error bars: SD/mean.

The online version of this article includes the following figure supplement(s) for figure 2:

**Figure supplement 1.** Confocal measurement and plot of TN-XXL  $\Delta R/R$  over time.

2015; Ren *et al.*, 2014), we investigated the response of YellowCaB cells after incubation with anti-CD40 antibodies, as well as the TLR4 and TLR9 stimuli lipopolysaccharide (LPS) and cytosine-phosphate-guanine-rich regions of bacterial DNA (CpG), respectively. Within the same cells, we detected no reaction to anti-CD40 treatment alone, but observed three types of shapes in post-CD40 BCR-stimulated calcium responses, which differed from anti-CD40-untreated cells (Figure 2a). These calcium flux patterns were either sustained, transient, or of an intermediate shape (Figure 2c). Sustained calcium flux even saturated the sensor at a level comparable to that achieved by ionomycin treatment. Cells that showed only intermediate flux maintained their ability to respond to ionomycin treatment at high FRET levels, as demonstrated by the  $\Delta R/R$  reaching 0.4 again after stimulation (Figure 2c). Furthermore, integrated TLR and BCR stimulation affected the appearance of the calcium signal. The addition of TLR9 stimulus CpG alone had no effect on YellowCaB FRET levels; however, the subsequent FRET peak in response to anti-Ig-F(ab)<sub>2</sub> was delayed (Figure 2d, e).

TLR4 stimulation via LPS could elevate calcium concentration of B cells, but only to a minor extent (Figure 2e). When TLR4 stimulation by LPS was performed before BCR stimulation, decreased FRET levels in response to anti-IgM-F(ab)<sub>2</sub> were observed. We conclude that, in order to become fully activated, B cells are able to collect and integrate multiple BCR-induced calcium signals and that signaling patterns are further shaped by innate signals or T cell help. BCR inhibition abolishes a FRET signal change in response to anti-IgM-F(ab)<sub>2</sub> (Figure 2—figure supplement 1b). Of note, we excluded the possibility that measured signal changes were related to chemokine stimulation. In vitro, we detected no FRET peak after applying CXCL12, probably because of lacking GECl sensitivity to small cytoplasmic changes (Figure 2—figure supplement 1c, d). Thus, the YellowCaB system is well suited for the detection of BCR-induced cytosolic calcium concentration changes.

### Fluctuating calcium levels are observed as a result of sequential cell contacts in vivo

We next set out to investigate if the ability of B cells to collect calcium signals sequentially is also shared by GC B cells. For two-photon intravital imaging, nitrophenyl (NP)-specific B1-8<sup>hi</sup> B cells from YellowCaB mice were magnetically isolated and transferred into wild-type hosts, which were subsequently immunized with NP-chicken gamma globulin (CGG) into the right foot pad (Shih et al., 2002a). Mice were imaged at day 8 p.i. when GCs had been fully established. Activated TN-XXL<sup>+</sup> YellowCaB cells had migrated into the GC, as confirmed by positive PNA- and anti-FP-immunofluorescence histology (Figure 3a). At this time point, mice were surgically prepared for imaging as described before (Ulbricht et al., 2017). Briefly, the right popliteal lymph node was exposed, moisturized, and flattened under a cover slip sealed against liquid drainage by an insulating compound. The temperature of the lymph node was adjusted to 37°C and monitored during the measurement. Our experiments revealed that the movement of single YellowCaB cells is traceable in vivo. Calcium fluctuations can be made visible by intensity changes in an extra channel that depicts the FRET signal, as calculated from relative quenching of TN-XXL. Color coding of intensity changes in the FRET channel showed time-dependent fluctuations of the signal and, in some particular cases, a sustained increase after prolonged contacts between two YellowCaB cells (Figure 3b, Video 1). Interestingly, FRET intensity seemed to be mostly fluctuating around low levels in moving cells, whereas sustained increase required cell arrest, as reported previously (Negulescu et al., 1996; Shulman et al., 2014), (Figure 3—figure supplement 1). The observed calcium fluctuations might therefore coincide with cell-to-cell contacts between follicular dendritic cells (FDCs) and B cells, resulting in AG-dependent BCR stimulation. To test for this, we first measured the colocalization between signals within the FDC channel and the citrine channel. The intensity of colocalization  $I_{\text{coloc}}$  of all cells was plotted as a function of frequency and biexponentially fitted (Figure 3c). We set the threshold for a strong and sustained colocalization of FDCs and B cells to an intensity of 150 AU within the colocalization channel. At this value, the decay of the biexponential fit was below 10%. We thus decided to term all cells with a colocalization intensity = 0 (naturally the most abundant ones) not colocalized, cells with a colocalization intensity between 1 and 150 transiently colocalized to FDCs ('scanning' or shortly touching the FDCs), and all cells above this intensity threshold strongly or stably colocalized. We compared the relative FRET intensity changes  $\Delta R/R$  of two tracked cells (Figure 3b, cells 1 and 2), where baseline R is the lowest FRET intensity measured, and its contacts to FDCs. We detected several transient B-cell-FDC contacts in cell 1 that were followed by a gradual increase of  $\Delta R/R$ , indicating an increase of cytoplasmic calcium concentration (Figure 3d). Cell 2 kept strong FDC contact over the whole imaging time and maintained elevated, mostly stable values. These experiments confirmed that GC B cells are able to collect calcium as a consequence of repeated contact events, which are mediated by B cell-to-FDC contacts in vivo.

### Calibration of the TN-XXL construct for in vivo quantification of cytosolic calcium in B lymphocytes using the phasor approach to FRET-FLIM

The comparison of calcium responses in different B cell subsets of multiple GCs requires normalization of TN-XXL FRET. Since this is hardly achievable in tissue due to its inherent heterogeneity, we aimed for the determination of absolute cytosolic concentration values in YellowCaB cells by calibration of TN-XXL FRET intensities. However, ratiometric calibration would require equal conditions for

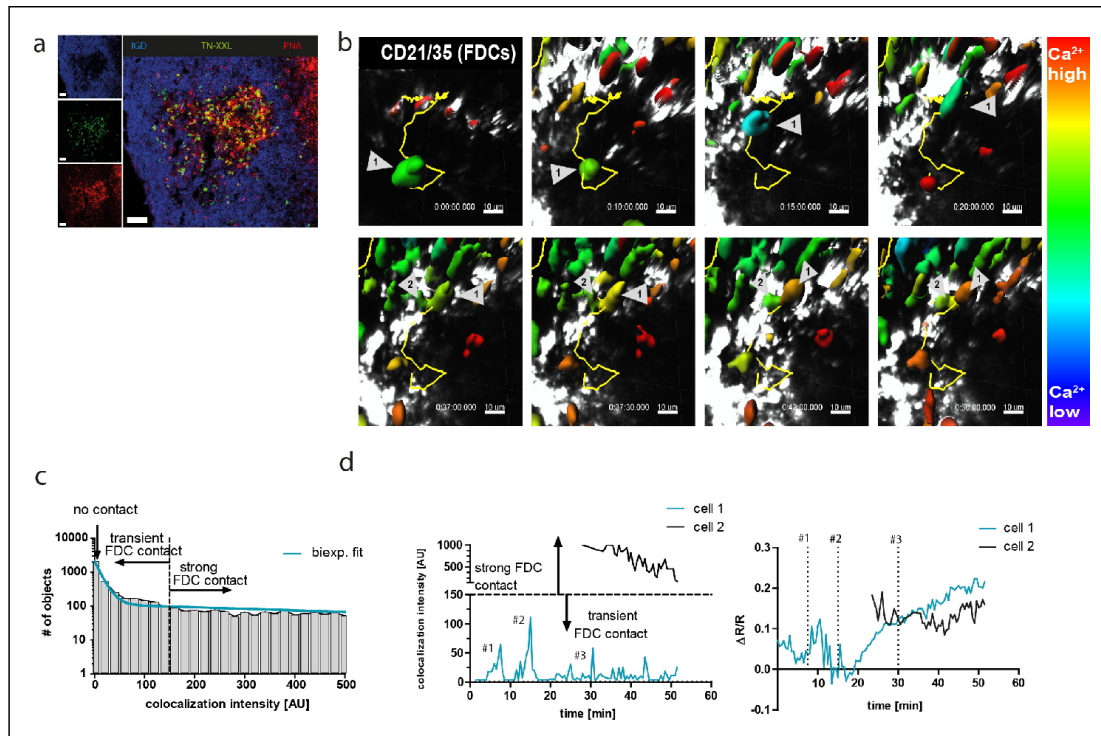
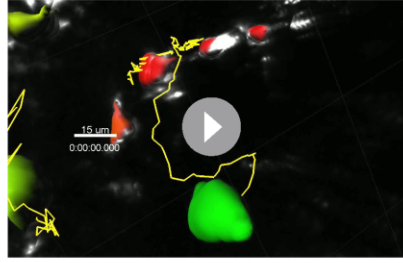


**Figure 3.** YellowCaB cells form productive germinal centers in vivo and show active B cell receptor signaling after cell-to-cell contacts. (a) Histological analysis of host mouse lymph nodes after adoptive transfer of YellowCaB cells. TN-XXL (green)-positive cells cluster in IgD (blue)-negative regions; a germinal center phenotype is confirmed by PNA staining (red). Scale bar 50  $\mu$ m. (b) Stills of ratiometric intravital imaging of adoptively transferred YellowCaB cells. 3D surface rendering and single-cell tracking (track line in yellow) with relative color coding ranging from blue = low  $\Delta R/R$  to red = high  $\Delta R/R$ . (c) Histogram showing segmented objects binned due to colocalization intensity within bin width of 20 AU and biexponential fit of data. Total number of objects = 6869. A curve decay of <10% was set as threshold, parting transient from strong B cell–FDC contact. All cells with colocalization intensity <1 were assigned negative. (d) Colocalization intensities of tracked cells 1 and 2 over time versus Förster resonance energy transfer signal change of cells 1 and 2 over time. Contact events to FDCs were assigned numbers #1, #2, and #3. The online version of this article includes the following figure supplement(s) for figure 3:

**Figure supplement 1.** Cell velocity versus calcium flux.

donor and acceptor fluorescence signals, especially in terms of scattering and photobleaching. Due to the aforementioned heterogeneous tissue composition, these requirements cannot be met in vivo (Radbruch *et al.*, 2015). Therefore, donor FLIM is the appropriate solution as it circumvents comparative evaluation of different fluorescence signals. Fluorescence lifetime is defined as the mean time a fluorescent molecule stays in an elevated energetic state after excitation, before photon emission and relaxation to the ground state take place. As a fully calcium-quenched eCFP in the GECl TN-XXL would transfer its energy mainly to citrine, its fluorescence lifetime would be measurably shorter than that of unquenched eCFP. Time-correlated single-photon counting (TCSPC) devices offer the possibility of simultaneous photon detection and recording of the respective fluorescent lifetimes within a nanosecond scale, yielding a fluorescence lifetime decay histogram of photons. Deriving fluorescent lifetimes  $\tau$  from the eCFP decay curve of photon histograms requires fitting. We decided to use the phasor analysis as it virtually transfers time-resolved fluorescence data into phase domain data by discrete Fourier transformation (Digman *et al.*, 2008). This approach overcomes the



**Video 1.** Detail of intravital ratiometric imaging (day 8 p.i.) within germinal center. YellowCaB cells had been adoptively transferred, and FDCs were in vivo-labeled with anti-CD21/35 antibody (white). 3D surface rendering and single-cell tracking (track line in yellow) with color coding ranging from blue = low  $\Delta R/R$  to red = high  $\Delta R/R$ . 103 frames, 7 frames per second (fps), scale bar 50  $\mu\text{m}$ .

<https://elifesciences.org/articles/56020#video1>

obstacles of multicomponent exponential analysis and yields model-free, readily comparable pixel- or cell-based plots that assign a position within a semicircle to each data point, dependent on the mixture of lifetime components present (Leben et al., 2018).

Typically, data correction based on reference dyes is needed for reliable phasor analysis (Ranjit et al., 2018). We verified the reliability of our TCSPC setup to acquire high-quality fluorescence decays in an image to be evaluated using the phasor approach by measuring the instrument response function given by the second harmonic generation signal (SHG) of potassium-dihydro-phosphate crystals (laser excitation wavelength 940 nm) and the fluorescence decays of eGFP, expressed in HEK cells (laser excitation wavelength 900 nm). As shown with the phasor plots of the raw data (Figure 4a), both the SHG signal and the eGFP fluorescence are located in expected positions on the semicircle (Murakoshi et al., 2008; Rinnenthal et al., 2013). Therefore, no further correction of the

data is necessary in our system.

As the TN-XXL construct is exclusively expressed in the cytosol of B lymphocytes from YellowCaB mice, the following equilibrium holds true for  $\text{Ca}^{2+}$  (free cytosolic calcium), TNXXL (the calcium-free FRET construct, i.e., the unfolded tertiary structure of TnC), and  $\text{Ca}^{2+}\text{TNXXL}$  (the FRET construct saturated by calcium, i.e., the completely folded tertiary structure of TnC):



characterized by the dissociation constant  $K_d$ :

$$K_d = \frac{[\text{Ca}^{2+}][\text{TNXXL}]}{[\text{Ca}^{2+}\text{TNXXL}]} \quad (2)$$

As measured in lysate of YellowCaB B cells expressing TN-XXL, the fluorescence lifetime  $\tau$  of the donor eCFP of the FRET Ca-sensitive construct TN-XXL depends on the free calcium concentration  $[\text{Ca}^{2+}]$  following a sigmoidal function (Eq. 3).

$$\tau = \tau_{\text{FRET}} + \frac{\tau_{\text{free}} - \tau_{\text{FRET}}}{1 + 10^{-(\log_{10}[\text{Ca}^{2+}] - \log_{10}K_d) \cdot \text{Hill.slope}}} \quad (3)$$

with  $\tau_{\text{free}}$  the fluorescence lifetime eCFP at 0 nM free calcium, and  $\tau_{\text{FRET}}$  the fluorescence lifetime of completely FRET-quenched eCFP in the TN-XXL-construct at 39  $\mu\text{M}$  free calcium. By fitting the fluorescence lifetime of eCFP in TN-XXL excited at 850 nm and detected at  $460 \pm 30$  nm acquired in time domain using our TCSPC system at various free calcium concentrations, we determined  $K_d = 475 \pm 46$  nM and Hill slope =  $-1.43 \pm 0.17$  (Figure 4b). Thus, we can calculate the free calcium concentration as

$$\log_{10}[\text{Ca}^{2+}] = \log_{10}K_d - \frac{\log_{10}\left(\frac{\tau_{\text{free}} - \tau_{\text{FRET}}}{\tau - \tau_{\text{FRET}}} - 1\right)}{\text{Hill.slope}} \quad (4)$$

Similar to the calculation in time domain, for the phase domain we can express each phasor vector  $\vec{p}$  based on the formalism proposed by Celli and colleagues (Celli et al., 2010) as

$$\vec{p} = \frac{[\text{Ca}^{2+}\text{TNXXL}] \varepsilon_{\text{FRET}} \vec{p}_{\text{FRET}} + [\text{TNXXL}] \varepsilon_{\text{free}} \vec{p}_{\text{free}}}{[\text{Ca}^{2+}\text{TNXXL}] \varepsilon_{\text{FRET}} + [\text{TNXXL}] \varepsilon_{\text{free}}} \quad (5)$$

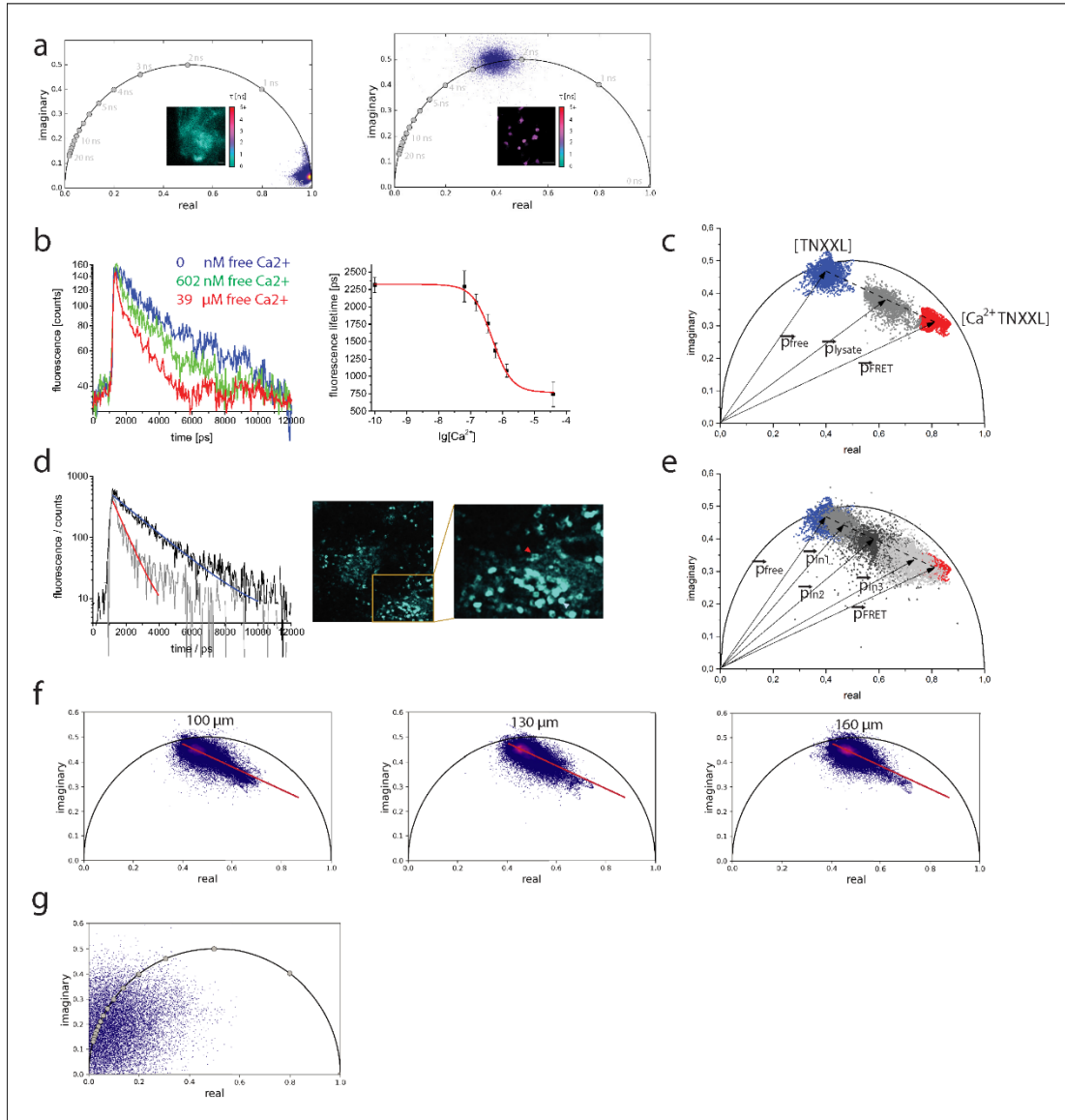


**Figure 4.** Calibration of the TN-XXL construct using fluorescence lifetime imaging of its Förster resonance energy transfer donor. (a) Left panel: phasor plot of second harmonic generation signal of potassium dihydrogen phosphate crystals and lifetime image (inset, scale in picoseconds) corresponding to the instrument response function ( $\tau = 80 \pm 10$  ps).  $\lambda_{\text{exc}} = 940$  nm,  $\lambda_{\text{detection}} = 466 \pm 20$  nm. Right panel: phasor plot of GFP fluorescence expressed in HEK cells and fluorescence lifetime image (inset, the same scale as in the left panel), corresponding to mono-exponential decay GFP fluorescence ( $\tau = 2500 \pm 100$  ps).  $\lambda_{\text{exc}} = 900$  nm,  $\lambda_{\text{detection}} = 525 \pm 25$  nm. (b) Left panel: fluorescence decays of CFP in TN-XXL construct from lysates of B lymphocytes at 0 nM, 602 nM, and 39  $\mu\text{M}$  free calcium. Right panel: titration curve of TN-XXL resulting from the time-domain evaluation of decay curves as shown in the left panel (three independent experiments).  $\lambda_{\text{exc}} = 850$  nm,  $\lambda_{\text{detection}} = 466 \pm 20$  nm. (c) Phasor plot of representative data shown in (b) – time-

Figure 4 continued on next page

Figure 4 continued

resolved fluorescence images  $422 \times 422$  pixels ( $200 \times 200 \mu\text{m}^2$ ); time-bin = 55 ps; time window = 12.4 ns. Blue phasor cloud (with central phase vector  $\vec{p}_{free}$ ) corresponds to 0 nM free calcium, gray cloud (with central phase vector  $\vec{p}_{lysate}$ ) to 602 nM free calcium, and red cloud (with central phase vector  $\vec{p}_{FRET}$ ) to 39  $\mu\text{M}$  free calcium. The dotted line connects the centers of the blue and red clouds, respectively, whereas the gray cloud is located on this line. The dotted line corresponds to the calibration segment as it results from measurements of TN-XXL in cell lysates. (d) Left panel: representative fluorescence decays of eCFP in two B lymphocytes (indicated by red and blue arrowheads in the inset image, right panel) expressing TN-XXL in the medullary cords of a popliteal lymph node of a YellowCaB mouse (right panel) and corresponding mono-exponential fitting curves (red fitting curve:  $\tau = 703 \pm 56$  ps; blue fitting curve:  $\tau = 1937 \pm 49$  ps). We measured  $\tau = 2303 \pm 53$  ps in splenocytes expressing only CFP. (e) Phasor plot showing time-resolved CFP fluorescence data from three lymph nodes, in three YellowCaB mice (light gray – with central phase vector  $\vec{p}_{ln3}$ , gray – with central phase vector  $\vec{p}_{ln1}$ , and dark gray – with central phase vector  $\vec{p}_{ln2}$ ) – time-resolved fluorescence images  $505 \times 505$  pixels ( $512 \times 512 \mu\text{m}^2$ ); time-bin = 55 ps; time window = 12.4 ns. Additionally, the calibration segment (dotted line) and the phasor clouds measured in lysates of B lymphocytes expressing TN-XXL at 0 nM and 39  $\mu\text{M}$  free calcium from (c) are displayed. (f) Phasor plots of the CFP fluorescence (time-resolved fluorescence images  $505 \times 505$  pixels /  $512 \times 512 \mu\text{m}^2$ ) acquired at three different depths (100, 130, and 160  $\mu\text{m}$  from the organ capsule surface) in the popliteal lymph node of a YellowCaB mouse. The red line in each phasor plot represents the calibration segment also displayed in (c) and (e). (g) Phasor plot of signal acquired in the lymph node of a non-fluorescent mouse.  $\lambda_{exc} = 850$  nm,  $\lambda_{detection} = 466 \pm 20$  nm.

The online version of this article includes the following figure supplement(s) for figure 4:

**Figure supplement 1.** Phasor plot showing time-resolved CFP fluorescence data of B lymphocytes from YellowCaB mice in culture (gray cloud – with central phase vector  $\vec{p}_{Bcell}$ ) – time-resolved fluorescence images  $471 \times 471$  pixels ( $250 \times 250 \mu\text{m}^2$ ); time-bin = 55 ps; time window = 12.4 ns.

with  $\epsilon_{free}$  and  $\epsilon_{FRET}$  the relative brightness (Chen et al., 1999; Müller et al., 2000) of eCFP in TNXXL at 0 nM and saturated (39  $\mu\text{M}$ ) free calcium, given by the following equations:

$$\epsilon_{free} = \delta_{CFP} \cdot \eta_{free} = \delta_{CFP} \cdot k_F \cdot \tau_{free} \quad (6)$$

$$\epsilon_{FRET} = \delta_{CFP} \cdot \eta_{FRET} = \delta_{CFP} \cdot k_F \cdot \tau_{FRET} \quad (7)$$

with  $\delta_{CFP}$  the effective two-photon absorption cross section of eCFP (independent of the pathways of relaxation from the excited state), and  $k_F$  the fluorescence rate of eCFP in vacuum, that is, no quenching due to surrounding molecules.

The phase vectors can be written also as complex numbers as given by the following equations:

$$\vec{p} = Re + i \cdot Im \quad (8)$$

$$\vec{p}_{free} = Re_{free} + i \cdot Im_{free} \quad (9)$$

$$\vec{p}_{FRET} = Re_{FRET} + i \cdot Im_{FRET} \quad (10)$$

We determined the averages and median real and imaginary values of the phasor distributions obtained by performing FRET-FLIM in lysates of YellowCaB B cells at 0 nM and 39  $\mu\text{M}$  free calcium to be  $Re_{free} = 0.4035$  (average), 0.40326 (median);  $Im_{free} = 0.45801$  (average), 0.45779 (median) and  $Re_{FRET} = 0.82377$  (average), 0.82203 (median);  $Im_{FRET} = 0.3225$  (average), 0.32093 (median), respectively, indicating that both distributions are symmetric, corresponding to normal distributions (Figure 4c).

From Eqs. (5–10) combined with Eq. (2), the free cytosolic calcium concentration is given by

$$[Ca^{2+}] = K_d \frac{\epsilon_{free}}{\epsilon_{FRET}} \frac{\vec{p} - \vec{p}_{free}}{\vec{p}_{FRET} - \vec{p}} = K_d \frac{\tau_{free}}{\tau_{FRET}} \frac{\sqrt{(Re - Re_{free})^2 + (Im - Im_{free})^2}}{\sqrt{(Re_{FRET} - Re)^2 + (Im_{FRET} - Im)^2}} \quad (11)$$

Thus, the free calcium concentration depends only on the  $K_d$ ,  $t_{free}$ ,  $t_{FRET}$  as determined from the calibration curve measured in lysate and the phase vectors, describing the extreme states of eCFP in the TN-XXL construct.

Since variations in refractive index, ion strength, pH value, or temperature in the cytosol of the B lymphocytes may additionally influence the fluorescence lifetime of eCFP, as well as the phase

vectors  $\vec{p}_{free}$  and  $\vec{p}_{FRET}$  (Jameson et al., 1984; Scott et al., 1970), we verified whether the FRET trajectory of the TN-XXL construct changes in the cytosol of B lymphocytes in cell culture (Figure 4—figure supplement 1) and under in vivo conditions, in lymph nodes (Figure 4d, e). We found that in all our measurements the phasor cloud lays on the trajectory determined in lysate solutions (Figure 4e). Measurements performed at different depths in lymph nodes led to the same result: there is no change in the slope of the trajectory at different tissue depths (Figure 4f).

To assess the impact of autofluorescence on the interpretation of the fluorescence signal in the phasor plot and, thus, on the cytosolic calcium levels, we also performed FLIM in B cell follicles of lymph nodes of non-fluorescent wild-type mice. While the acquired signal was extremely low, the phasor cloud in these measurements was located around position (0,0) in the plot, indicating that it mainly originates from detector noise (Figure 4g).

We compared the results of cytosolic free calcium concentration determined using the time-domain and the phase-domain approach and found deviations of max. 5% between the evaluation pathways using Eqs. (4) and (11) due to numerical uncertainty. We determined the calcium dynamic range of TN-XXL measured by phasor-analyzed FRET-FLIM to span between 100 nM and 4  $\mu$ M free calcium, with the linear range of the titration curve in the range between 265 and 857 nM free calcium.

### Comparative FLIM-FRET reveals heterogeneity of absolute calcium concentrations in B cells in vivo

Adoptively transferring AG-specific YellowCaB cells and non-AG-specific (polyclonal) YellowCaB cells (stained ex vivo) allowed us to divide GC B cells into five different populations based on their location in the imaging volume and their fluorescent appearance (Figure 5a, b). At day 8 p.i., polyclonal YellowCaB cells, identified by their red labeling, mostly lined up at the follicular mantle around the GC, with some of them having already entered into activated B cell follicles. AG-specific, citrine-positive B1-8<sup>hi</sup>:YellowCaB cells were found clustered in the GC, close to FDCs, outside of GC boundaries, or as bigger, ellipsoid cells in the extrafollicular medullary cords (MC), probably comprising plasma blasts (Figure 5b, left). Color-coded 2D- and 3D FLIM analysis of these populations confirmed that calcium concentrations were fluctuating within all of those B cell populations, and that most B cells were maintaining relatively high mean eCFP fluorescence lifetimes and therefore low calcium concentrations on average, with only few exceptions (Figure 5b, middle and right, Video 2).

Bulk analysis of cells revealed additional calcium-intermediate and calcium-high cell subsets present among AG-specific cells and plasma blasts (Figure 5c, Video 3). Especially for plasma blasts this was somehow unexpected, given that these are thought to downregulate their surface BCR during differentiation.

Comparison of AG-specific cells inside GCs with those outside GCs and non-AG-specific cells inside GCs as well with those outside GCs showed that the distribution of calcium concentrations of these B cells was dependent on BCR specificity and rather independent from their location within the imaging volume, despite higher fluctuation seen among AG-specific populations (Figure 5—figure supplement 1). These maxima were reached as transient fluctuation peaks, that is, periods shorter than 1 min, in which these concentrations seem to be tolerated. Calcium values exceeding the dynamic range of TN-XXL (>857 nM) were recorded for all measured subsets, but most cells >857 nM were found among intrafollicular AG-specific B cells and extrafollicular AG-specific B cells (Figure 5d). The heterogeneity in temporal calcium concentrations therefore is smallest among non-AG-specific B cells, increases with activation in AG-specific GC B cells, and is most prominent among MC-plasma blasts. The high cytoplasmic calcium levels observed in MC-plasma blasts were unlikely to be the result of chemokine-induced signaling since only a minor calcium increase was detected after CXCL12 stimulation in vitro (Figure 2—figure supplement 1d). Thus, a progressive heterogeneity of calcium signals within B cells can be seen alongside the process of activation and differentiation.

### Functional relevance of increased calcium concentration among extrafollicular YellowCaB cells

We next wondered if high cytoplasmic calcium levels within certain B cell subsets could be the result of AG-mediated signals. We therefore intravenously (i.v.) injected NP-bovine serum albumine (BSA)

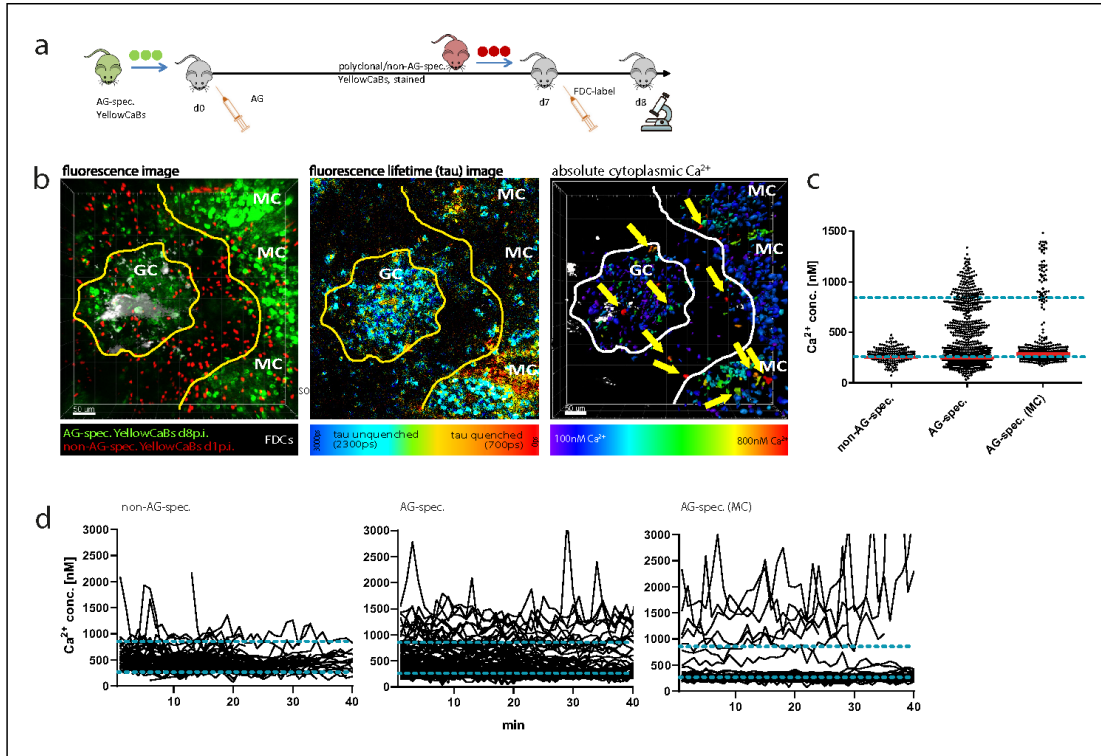
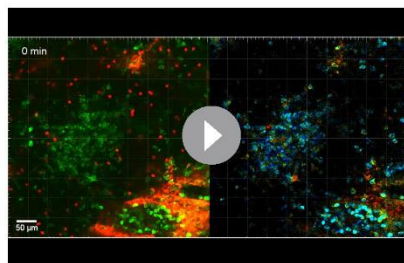


**Figure 5.** Determination of absolute calcium concentration by intravital fluorescence lifetime imaging of germinal center (GC) B cell populations. (a) Cell transfer and immunization strategy for intravital imaging of antigen (AG)-specific and polyclonal YellowCaB cells. (b) Left: maximum intensity projection of a z-stack, intravitaly imaged GC, and medullary cords (MCs). B cells were distinguished as polyclonal, non-AG-specific YellowCaB cells (red), AG-specific YellowCaB cells, and AG-specific cells inside the MC. Middle: color-coded fluorescence lifetime image with lifetimes of unquenched eCFP depicted in blue and lifetimes of quenched eCFP in red. Right: 3D-rendered, color-coded z-stack showing absolute calcium concentrations in B cell subsets in GC and MC. Yellow arrows point to cells containing high cytoplasmic calcium. (c) Bulk analysis of absolute calcium concentrations in segmented single-cell objects from B cell subsets at any given time point measured. The dynamic range of the genetically encoded calcium indicator (GECI) TN-XXL is indicated by blue dashed lines. (d) Time-resolved analysis of calcium concentrations in tracked segmented objects corresponding to B cell subsets in (c). 2 frames per minute. Non-AG-specific YellowCaB cells (left,  $n = 92$  tracks); AG-specific YellowCaB cells (middle,  $n = 169$  tracks); and extrafollicular AG-specific YellowCaB cells in MC (right,  $n = 69$  tracks). The dynamic range of the GECI TN-XXL is indicated by blue dashed lines. The online version of this article includes the following figure supplement(s) for figure 5:

**Figure supplement 1.** Mean calcium concentration and SD in non-antigen (AG)-specific and AG-specific YellowCaB cells distinguished by localization.

(66 kDa) into mice that had been adoptively transferred with B1-8<sup>hi</sup> (AG-specific) YellowCaB cells and recorded absolute calcium concentrations within the GC by intravital FLIM. Antigens up to 70 kDa have been reported to be transported into the follicles via conduits in less than 5 min (Rozenaal et al., 2009). Accordingly, AG-specific GC YellowCaB cells significantly upregulated cytoplasmic calcium after AG injection within minutes (Figure 6a, top panel, Figure 6—figure supplement 1). To test if this concentration increase could be explained via BCR-dependent AG recognition, we pre-injected the inhibitor of Bruton's tyrosine kinase (BTK) ibrutinib (Hendriks et al., 2014), which blocks BCR downstream activation, in a control group. BTK inhibition could abrogate the increase in mean cytoplasmic calcium after additional injection of NP-BSA (Figure 6a, bottom panel) and even seemed to downregulate baseline signals (Figure 6—figure supplement 1). In addition, we found that also in 48 hr LPS/ interleukin 4 (IL-4)-cultured B1-8-plasma



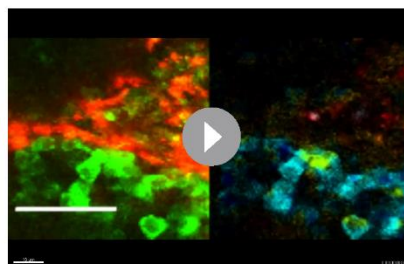
**Video 2.** Side-by-side depiction of fluorescence, fluorescence lifetime imaging, and cell-based phasor data of intravitaly imaged germinal center (day 8 p.i.), single z-plane. Left: fluorescence data with antigen (AG)-specific YellowCaB cells (green) and stained non-AG-specific YellowCaB cells transferred 1 day prior to imaging (red; autofluorescence of capsule also visible in the same channel). 4 fps, scale bar 50  $\mu\text{m}$ . Middle: false color-coded presentation of fluorescence lifetime  $\tau$  (0–3000 ps, see range scale in *Figure 5b*). 4 fps, scale bar 50  $\mu\text{m}$ . Right: raw cell-based phasor plot with cells segmented according to fluorescence and spatial distribution, subsets indicated. 4 fps.

<https://elifesciences.org/articles/56020#video2>

YellowCaB cells crowding the SCS space were found to have multiple contact sites to SCSM. Some B cells were observed to migrate along the SCS, possibly scanning for antigenic signals (*Video 4*). Bulk analysis of YellowCaB cells and their colocalization with SCSM showed that the calcium concentration in YellowCaB cells with direct contact to SCSM reaches values that are more than doubled compared to values in cells that were not in contact, and that calcium concentration is positively cor-

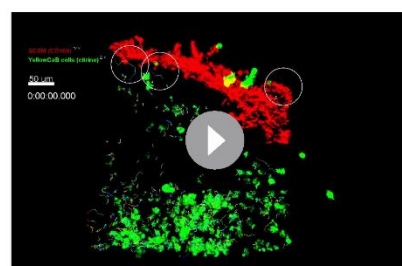
relates to calcium concentration in SCSM. In response to NP-BSA blasts, an increase in calcium was detectable after addition of NP-BSA (*Figure 6—figure supplement 2*), suggesting that stimulation via AG remains possible in at least a proportion of these differentiated B cells.

These results led us to investigate the possible sources of AG abundance outside of GCs and their effect on calcium in B cells. Earlier studies proposed that one possible AG source in lymph nodes are subcapsular sinus macrophages (SCSM) (*Junt et al., 2007; Moran et al., 2018; von Andrian and Mempel, 2003*). We tested if SCSM contacts could be the cause of elevated calcium levels in extrafollicular B cells. We intravitaly imaged wild-type host mice that have been adoptively transferred with B1-8<sup>hi</sup>:YellowCaB cells and received an injection of efluor660-labeled anti-CD169 antibody together with the usual FDC labeling 1 day prior to analysis. We concentrated on the area beneath the capsule, identified by second harmonic generation signals of collagen fibers in this area. Thresholds of colocalization between CD169<sup>+</sup> macrophages and TN-XXL<sup>+</sup> YellowCaB cells are described in *Figure 6—figure supplement 3*. Together, these methods led to a 3D visualization of the SCS with CD169 stained macrophages, lined up in close proximity (*Figure 6b*). AG-specific YellowCaB cells were detected clustering in GCs nearby. Extrafollicular



**Video 3.** Detail of *Video 2* within medullary cords and side-by-side depiction of fluorescence and fluorescence lifetime imaging data, single z-plane. Left: fluorescence data with antigen-specific YellowCaB cells (green) and autofluorescence of capsule (red). 4 fps, scale bar 50  $\mu\text{m}$ . Right: false color-coded presentation of fluorescence lifetime  $\tau$  (0–3000 ps, see range scale in *Figure 5b*). 4 fps.

<https://elifesciences.org/articles/56020#video3>



**Video 4.** 3D projection of intravital imaging of germinal center and subcapsular sinus. YellowCaB cells (green, with track lines) and subcapsular sinus macrophages (red), stained by CD169 in vivo labeling. White circles highlight antigen-specific B cells migrating along subcapsular space. 4 fps, scale bar 50  $\mu\text{m}$ .

<https://elifesciences.org/articles/56020#video4>

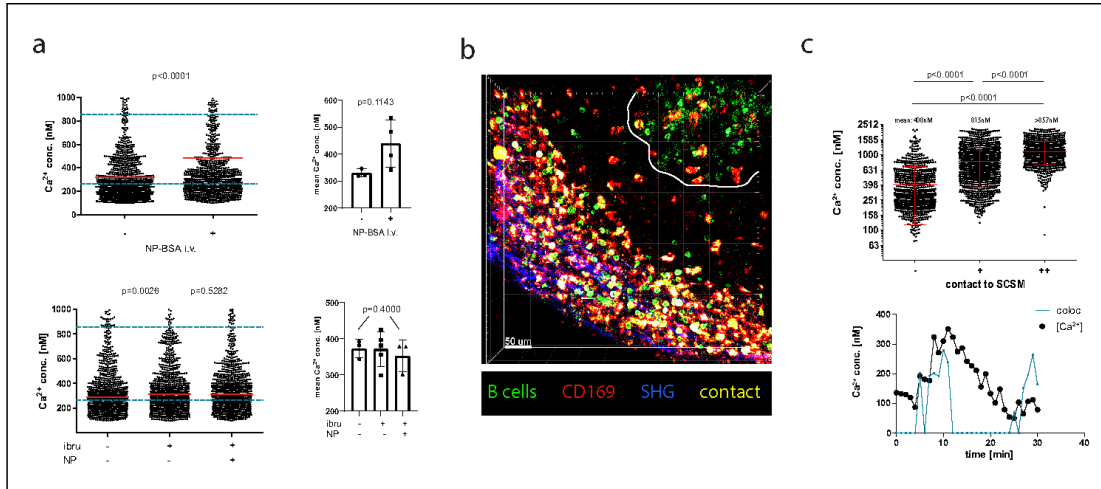


**Figure 6.** Antigen dependency of calcium elevation in germinal center (GC) and extrafollicular B cells. (a) Top panel: absolute calcium concentrations measured in antigen (AG)-specific GC B cells before and after in vivo injection of NP-BSA. Exemplary results (left) and pooled data from three imaged mice (right). Bottom panel: absolute calcium concentrations measured in AG-specific GC B cells before and after in vivo injection of the Bruton's tyrosine kinaseinhibitor ibrutinib, followed by injection of NP-BSA. Exemplary results (left) and pooled data from three imaged mice (right). (b) z-stack of intravitaly imaged lymph node with GC (white line) and subcapsular sinus (indicated by SHG, blue). CD169<sup>+</sup> macrophages (red, contacts [yellow], YellowCaB cells [green]). Size 500 × 500 × 78 μm. Scale bar 60 μm. (c) Top: Fluorescence lifetime imaging measurement of mean absolute calcium concentration of YellowCaB cells showing no (-), transient (+), or strong (++) overlap with CD169<sup>+</sup> signal. n = 1000, ANOVA analysis, mean and SD. Bottom: Single-cell track of a YellowCaB cell making transient contact to a macrophage; blue: colocalization intensity (AU); black: change of absolute calcium concentration.

The online version of this article includes the following figure supplement(s) for figure 6:

**Figure supplement 1.** Calcium concentration change detected by in vivo fluorescence lifetime imaging measurements over time, exemplary single germinal center (GC) B cell tracks, before and after injection(s) of compounds.

**Figure supplement 2.** Absolute calcium concentration of fluorescence lifetime imaging measured after NP-BSA stimulation of ex vivo lipopolysaccharide-induced plasmablasts.

**Figure supplement 3.** Colocalization histogram and exponential fit for analysis of colocalization between CD169<sup>+</sup> macrophages and extrafollicular YellowCaB cells.

related with contact strength (Figure 6c, top). Single-cell tracking and simultaneous analysis of absolute calcium concentration and colocalization intensity revealed that the increase of cytoplasmic calcium is a direct cause of B-cell-to-SCSM contacts (Figure 6c, bottom). We conclude that contacts of B cells to SCSM could induce elevation of B cell cytoplasmic calcium concentrations, presumably due to antigenic activation, with the absolute concentrations being dependent on the contact strength.

## Discussion

Intravital imaging technologies have contributed greatly to a better understanding of the dynamic processes in GCs. AG-capture, cycling between zones, and development of clonality patterns have been made visible by two-photon microscopic techniques (Hauser et al., 2007; Suzuki et al., 2009; Tas et al., 2016; Victora et al., 2010). Furthermore, important functional in vivo data like signaling in T helper cells have been collected using a calcium-sensitive protein (Kyratsous et al., 2017; Shulman et al., 2014).

However, calcium mobilization within GC B cells was mostly investigated via *ex vivo* analysis of sorted cells after adoptive transfer and immunization, or BCR activation was measured using a non-reversible BCR signaling reporter like Nur77, altogether neglecting calcium flux (Khalil *et al.*, 2012; Mueller *et al.*, 2015). These data suggested that BCR signaling in the GC is reduced. However, no statement was made about the dynamics and timely coordination of (even small) calcium pulses and the relation to their microenvironment. In fact, a recent study confirmed that BCR signals play a central role in positive selection and display a fragile interdependence with costimulatory events (Luo *et al.*, 2018).

BCR-regulating surface proteins like CD22 or sialic acid-binding immunoglobulin-type lectins have been related to development of autoimmunity and point out BCR-mediated calcium flux as an important component, not only during B cell development but also in their differentiation to effector cells (Hoffmann *et al.*, 2007; Jellusova *et al.*, 2010; Müller and Nitschke, 2014; Nitschke and Tsu-bata, 2004; O'Keefe *et al.*, 1999). Apart from regulating gene transcription, cytosolic calcium mobilized has been shown to be essential for F-actin remodulation and B cell spreading on antigen presenting cells (Maus *et al.*, 2013). Furthermore, cytosolic calcium concentration is closely linked to metabolic reprogramming of activated B cells and their cell fate (Boothby and Rickert, 2017; Caro-Maldonado *et al.*, 2014). It has been shown that SOCE is acting directly on the mitochondrial capability to import cytosolic calcium (Shanmughapriya *et al.*, 2016). In mitochondria, calcium is regulating ATP production through increase of glycolysis and fatty acid oxidation, processes for which activated and GC B cells have high demands, although there is controversy as to which of the two metabolic pathways predominates in GC B cells (Griffiths and Rutter, 2009; Jellusova *et al.*, 2017; Maus *et al.*, 2017; Weisel *et al.*, 2020).

For flexible analysis of calcium mobilization in cells of the CD19<sup>+</sup> lineage, we developed a novel transgenic reporter system and image processing approach, enabling quantification of cytosolic calcium concentrations. The FRET-based GEC1 TN-XXL can be used stably in moving, proliferating, and differentiating lymphocytes, and the reversibility of the sensor makes it suitable for longitudinal intravital measurements. Switching from ratiometric acquisition of FRET-donor and FRET-acceptor fluorescence intensities to measuring FRET-donor fluorescence lifetime enabled quantification of calcium concentrations in absolute numbers.

A first advantage of FRET-FLIM in tissue is that different photobleaching or scattering properties of the fluorophores can be neglected. We further decided to perform all analyses based on the phasor approach that circumvents the problem of multiexponential fluorescence decays we encounter measuring a two-fluorophore FRET-based GEC1 in tissue. For titration of TN-XXL, we used lysate of YellowCaB plasma blasts. Besides TN-XXL affinity, also eCFP fluorescence lifetime itself may be influenced by large shifts in *pH* value, ionic strength, oxygenation, or temperature. We ensured that these parameters were similar in lysates and cells, except for the temperature, which was at room temperature for calibration. Temperature was reported to only slightly change the fluorescence lifetime of a CFP variant (cerulean) (Laine *et al.*, 2012). However, for accuracy purposes and in order to exclude such artifacts when determining cytosolic calcium levels in B lymphocytes within lymph nodes of YellowCaB mice, we adapted the phasor-based calibration strategy proposed by Celli *et al.*, 2010 for the use of Calcium Green in skin samples to our data. In this way, we were able to reliably determine absolute values of cytosolic calcium concentrations in B cells within lymph nodes.

In our set-up, we have shown that TN-XXL in B cells has suitable sensitivity and fast reversibility. This key factor made it possible to observe repeated and partially sustained calcium elevation in the cytoplasm, showing that B cells are able to collect sequential signals, possibly up to a certain threshold, which determines their fate.

In support of that, B cellular calcium concentration must not constitutively exceed a certain value in order to prevent mitochondrial depolarization (Akkaya *et al.*, 2018; Bouchon *et al.*, 2000; Niiro and Clark, 2002). Gradual calcium elevation could be a mechanistic link for that. For example, calcium levels of >1  $\mu\text{M}$  over the duration of >1 hr have been reported to be damaging to other cell types, such as neurons (Radbruch *et al.*, 2015; Siffrin *et al.*, 2015). Accordingly, stimulation of AG receptors via large doses of soluble AG can lead to tolerogenic apoptosis in GC B cells, which could be explained by uninhibited calcium influx (Nossal *et al.*, 1993; Pulendran *et al.*, 1995). Since apoptosis is the default fate for B cells in the GC reaction (Mayer *et al.*, 2017), CD40 and TLR signaling might contribute to limiting cytoplasmic calcium concentrations, and thus promote survival of B cell

clones with appropriate BCR affinity (Akkaya et al., 2018; Eckl-Dorna and Batista, 2009; Pone et al., 2015; Pone et al., 2012; Pone et al., 2010; Ruprecht and Lanzavecchia, 2006). For CD40 signaling in immature B cells, this has been confirmed (Nguyen et al., 2011). Our data does show that TLR signaling can attenuate calcium flux in stimulated B cells, while CD40 can either attenuate or augment the calcium response (Figure 2). Whether the different outcomes of CD40 stimulation are dependent on the affinity of the BCR and its efficiency in presenting AG (Schwickert et al., 2011; Shulman et al., 2013) will be subject of further studies.

Measuring absolute calcium concentration in GC B cells after administration of soluble AG in vivo, we could detect an increase of B cell calcium that is attenuated by BCR inhibitor ibrutinib, showing that BCR-mediated calcium increase is substantially contributing to calcium heterogeneity in the GC. However, the interpretation of the data should not neglect other causes of calcium elevation, given the multifaceted role of this second messenger. Therefore, it is likely that apart from BCR signaling, also other events, like binding of non-AG ligands and stress-related calcium release from internal stores, contribute to an overall cytosolic calcium increase, which needs to be regulated in order to prevent a damaging calcium overload. Causes for stress-related cytosolic calcium elevations in cells can be hypoxia, a condition reported to be present within GCs (Jellusova et al., 2017); nutrient deprivation, which mostly will affect highly proliferative cells like GC B cells; or ER-calcium release as a result of the unfolded protein response that is indispensable in plasma cells (Díaz-Bulnes et al., 2020; Høyer-Hansen and Jäättelä, 2007; Lam and Bhattacharya, 2018). The complex interaction of factors makes an exact characterization of the absolute calcium concentration in various B cell subsets crucial in order to obtain information about their regulation and containment. This characterization should preferably be done intravitaly since any manipulation of cells can result in enormous non-physiological variations of cytosolic calcium levels.

For the first time, we determined absolute values of B cell cytoplasmic calcium concentrations during the GC reaction within living mice. It appears that BCR AG specificity and state of differentiation are closely related to distinct degrees of heterogeneity of calcium concentrations. Notably, heterogeneity was also evident in extrafollicular B cells in the SCS region, as well as in plasma blasts. The latter actually reach the highest calcium concentrations within the B cell compartment of the lymph node. We also observed an increase of cytoplasmic calcium in plasma blasts after stimulation with specific AG in vitro. These data are in line with a report of residual BCR signaling occurring in antibody-secreting cells (Pinto et al., 2013), which challenges the finding that B cells completely downregulate their surface BCR during differentiation to plasma cells (Manz et al., 1998). Our experiments were done in short-lived plasma blasts, not LLPC, for which the situation could be different. Therefore, an investigation of possible BCR signaling in LLPC is of high interest. Stimulation with the chemokine CXCL12, which has previously been shown to induce migration of antibody-secreting cells (Fooksman et al., 2010; Hauser et al., 2002), resulted only in a minor increase of cytoplasmic calcium in plasma blasts in our hands.

In B cells that have exited the GC, ongoing calcium flux might reflect reactivation. We confirmed that B cells in contact to SCSM had significantly higher cytosolic calcium concentrations. These are possibly attributed to BCR signaling since the SCS has been proposed as a site of reactivation of memory B cells via AG (Moran et al., 2018).

The YellowCaB system provides a tool for measuring calcium as ubiquitous, universal cellular messenger, integrating signals from various pathways, including chemokine receptor signaling and intrinsic calcium release or BCR-triggered activation. Importantly, changes in mitochondrial membrane potential and/or the integrity of the ER also lead to varying calcium concentrations within the cytoplasm since both act as major intracellular calcium buffering organelles (Kass and Orrenius, 1999). A close connection between mitochondrial calcium homeostasis, altered reactive oxygen species production, and the expression of plasma cell master transcription factor BLIMP1, as well as changes in metabolism, has been reported previously (Jang et al., 2015; Shanmugapriya et al., 2019). We have recently applied phasor-FLIM of endogenous NAD(P)H fluorescence for mapping of metabolic enzyme activities in cell cultures (Leben et al., 2019). The combination of this technique with FLIM-based intravital calcium analysis will help to further dissect immunometabolic processes in B cells, as well as in short-lived plasma cells and LLPCs in vivo.

## Materials and methods

## Key resources table

Reagent type (species) or resource	Designation	Source or reference	Identifiers	Additional information
Mouse	R26CAG-TNXXLflo <sub>x</sub>	<i>Mank et al., 2008</i>	-	Plasmid available at addgene (#45797)
Mouse	CD19 cre	<i>Rickert et al., 1997</i>	Stock# 004126 jaxmice	
Mouse	B1-8 <sup>hi</sup> gh	<i>Shih et al., 2002a</i>	Stock# 007775 jaxmice	
Antibody	Rabbit anti-GFP-Alexa488 polyclonal	Rockland, in-house coupling DRFZ Berlin	Cat# 600-401-215	1:200
Antibody	Rat anti-CD21/35-Fab-Atto590 7G6	DRFZ Berlin	-	10 µg/mouse
Antibody	Hamster anti-IgD-Alexa594 11.26 c	DRFZ Berlin	-	-
Antibody	Rat anti-CD21/35-Alexa647 7G6	DRFZ Berlin	-	-
Antibody	Rat anti-CD19-Cy5 1D3	DRFZ Berlin	-	-
Antibody	Rat anti-CD40 3/23	BD Pharmingen	Cat# 553788	As indicated
Antibody	Goat anti-IgM-F(ab) <sub>2</sub> polyclonal	Southern Biotech	Cat#1023-01	As indicated
Antibody	Rat anti-kappa 187.1	DRFZ Berlin	-	As indicated
Recombinant DNA reagent	CpG	Tib Molbiol Berlin	Request #1668 and 1826 sequence ID: 1746437/8	As indicated
Peptide, recombinant protein	Peanut-agglutinin, biotinylated	Vector Biolabs	Cat# B-1075-5	1:200
Other	Lipopolysaccharide (LPS) from <i>Escherichia coli</i>	Sigma	Cat# L4391	As indicated
Peptide, recombinant protein	NP-CGG ratio > 20	Biosearch Technologies	Cat# N-5055C-5-BS	10 µg/mouse
Peptide, recombinant protein	Streptavidin-Alexa555	Thermo Fisher Scientific	Cat# S32355	1:2000
Other	X-Rhod-1	Molecular Probes	Cat# X14210	Manufacturer's protocol
Software, algorithm	Python 2.7	Python Software Foundation		
Software, algorithm	MATLAB	MathWorks		
Software, algorithm	Imaris	Bitplane		
Software, algorithm	Phasor-based-numerical analysis of eCFP lifetime data	Own work, <a href="https://github.com/ulbrica/Phasor-FLIM.git">https://github.com/ulbrica/Phasor-FLIM.git</a> ; swk:1:rev:8ae5bfc17ec019fcc8ec7e4627442646e52cc3c5; <i>Ulbricht, 2021</i> .		

## Mice

Mice carrying a STOP cassette flanked by two loxP sites upstream of the region encoding for the TN-XXL biosensor (Mank *et al.*, 2008) in the ROSA26 locus were obtained from F. Kirchhoff, Saarland University, Homburg. YellowCaB mice were generated by crossing those mice with the *Cd19<sup>cre/cre</sup>* strain (Rickert *et al.*, 1997) and maintained on a C57Bl/6 background. Only YellowCaB mice heterozygous for Cre were used to avoid deletion of CD19. Mice with monoclonal NP-specific BCR (B1-8<sup>hi</sup>:YellowCaB) were generated by crossing of YellowCaB mice with B1-8<sup>hi</sup> mice (Shih *et al.*, 2002b). All mice were bred in the animal facility of the DRFZ. All animal experiments were approved by Landesamt für Gesundheit und Soziales, Berlin, Germany, in accordance with institutional, state, and federal guidelines.

## Cells

Primary splenocytes were isolated from whole spleens of YellowCaB mice or B1-8<sup>hi</sup>:YellowCaB mice in 1 × PBS and erythrocytes lysed. B cells were negatively isolated using the Miltenyi murine B cell isolation kit via magnetic-assisted cell sorting (MACS), leaving B cells untouched in order not to pre-stimulate them.

## Staining and flow cytometry

Single-cell suspensions were prepared and stained according to the guidelines for flow cytometry and cell sorting in immunological studies (Cossarizza *et al.*, 2019). To simultaneously assess calcium influx with a dye-based method, we stained whole splenocytes or isolated B cells with the calcium-sensitive dye X-Rhod-1 (Invitrogen). X-Rhod-1 is a single-fluorophore calcium reporter molecule that enhances its fluorescence intensity upon calcium binding in a range of 0–40 μM up to 100 times at a wavelength of 600 nm. Measurements were carried out at a BD Fortessa flow cytometer. TN-XXL expression was checked assessing positive fluorescence in a 525 ± 25 nm channel after 488 nm excitation on a MACSQuant flow cytometer.

## Perfusion chamber

All in vitro experiments were carried out in Krebs–Ringer solution containing 6 mM Ca<sup>2+</sup> at 37°C. Cells were stimulated with anti-mouse IgM-F(ab)<sub>2</sub> (Southern Biotech), ionomycin (4 μM, Sigma), anti-CD40 antibody (BD), LPS (20 μg/ml, Sigma), or CpG (10 μg/ml, TIB Molbiol Berlin). Cell culture imaging experiments with ionomycin stimulation were performed using an open perfusion chamber system. Buffer solution was pumped through the heated chamber containing a poly-D-lysine-coated glass slide on which freshly and sterile isolated YellowCaB cells were grown for approximately 1 hr. Ionomycin was added in the flow-through buffer supply. The lag time for the volume to arrive at the imaging volume was determined for each set-up and considered for analysis of ΔR/R over time. Anti-IgM-F(ab)<sub>2</sub> antibody was given directly to cells within the open chamber in between acquisition time points. To visualize the reversibility of the sensor despite antibody still present, the experiment was performed in an open culture system without media exchange through a pump. To analyze if YellowCaB cells could repeatedly be stimulated, experiments were performed under continuous perfusion. Buffer flow was switched off with stimulation for several minutes and switched on again to dilute antibody out again for a second stimulation.

For analysis, regions of interest were determined based on randomly chosen single cells. Intensity density values of the raw citrine signal were divided by the intensity density values of the raw eCFP signal and related to the baseline ratio of the signals before stimulation.

## Cell transfers, immunization, and surgical procedures

B cells from spleens of YellowCaB mice were negatively isolated using the Miltenyi murine B cell isolation kit via MACS. 5 × 10<sup>6</sup> cells were transferred to a host mouse with a transgenic BCR specific for an irrelevant AG (myelin oligodendrocyte glycoprotein). When NP-specific B cells were analyzed, B cells from spleens of B1-8<sup>hi</sup>:YellowCaB mice were transferred to wildtype C57Bl/6 mice. Host mice were immunized in the right footpad with 10 μg NP-CGG in complete Freund's adjuvant 24 hr after B cell transfer. After 6–8 days p.i., FDCs were labeled with Fab-Fragment of CD21/35-Atto590 or CD21/35-Alexa647 (in-house coupling) into the right footpad. Polyclonal B cells from YellowCaB mice were stained with a red fluorescent dye (CellTracker Deep Red, ThermoFisher) and

adoptively transferred. 24 hr later, the popliteal lymph node was exposed for two-photon imaging as described before (Ulbricht *et al.*, 2017). Briefly, the anesthetized mouse is fixed on a microscope stage custom-made for imaging the popliteal lymph node. The mouse is shaved and incisions are made to introduce fixators that surround the spine and the femoral bone. The mouse is thus held in a planar position to the object table. The right foot is fixed by a wire allowing to increase the tension on the leg to position the lymph node parallel to the imaging set-up. A small incision is made to the popliteal area. The lymph node is exposed after freeing it from surrounding adipose tissue. A puddle around the lymph node is formed out of insulating silicon compound, then filled with NaCl and covered bubble-free with a cover slide.

For intravital application of AG, 500  $\mu\text{g}$  NP-BSA were administered i.v. after acquiring 10 time steps of baseline FLIM signal (four mice). To check for BCR specificity of calcium elevation recorded after AG injections, BTK inhibitor ibrutinib was pre-injected i.v. before AG application at 3.75 mg/kg and recorded in a control group of three mice. Technically, measurements were paused for injections for about 5 min. For accurate comparison of baseline calcium levels with calcium levels after injections, we imaged the same GC before and after. Therefore, measurements are always to be treated as separate measurements and it is not possible to track individual cells before and after an injection. However, the mean calcium elevation in the presented subset of cells can be visualized. For better comparability, we have chosen to present a time course that virtually combines two consecutive measurements in the same GC into one (Figure 5—figure supplement 1). Up to 22 individual cell tracks were randomly chosen after gating out overlapping signals from macrophages, filtering for maximum track duration and completeness of the series of events (absolute calcium value in the center of the segmented object).

### Intravital and live cell imaging and image analysis

Imaging experiments of freshly isolated B cells were carried out using a Zeiss LSM 710 confocal microscope. Images were acquired measuring 200–600 frames with one frame/3 s frame rate while simultaneously detecting eCFP and citrine signals at an excitation wavelength of 405 nm.

For intravital two-photon ratiometric imaging, z-stacks were acquired over a time period of 30–50 min with image acquisition every 30 s. eCFP and citrine were excited at 850 nm by a fs-pulsed Ti:Sa laser, and fluorescence was detected at  $466 \pm 30$  nm or  $525 \pm 25$  nm, respectively. Fluorescence signals of FDCs were detected in a  $593 \pm 20$  nm channel. For experiments including macrophage staining, the fluorescence data has been unmixed for a possible overlap of the TN-XXL-citrine signal with that of the injected marker to prevent false-positive colocalization analysis between the red efluor660 coupling of anti-CD169 and the green fluorescence of TN-XXL in the  $525 \pm 25$  nm channel (Rakhymzhan *et al.*, 2017).

For intravital FLIM experiments, eCFP fluorescence lifetime was measured with a time-correlated single-photon counting system (LaVision Biotec, Bielefeld, Germany). The fluorescence decay curve encompassed 12.4 ns (80 MHz laser repetition rate) with a time resolution of 55 ps. The pixel dwell time was  $4 \times 5 \mu\text{s}$ , allowing to detect photons from 1600 laser pulses for the fluorescence decay. The fluorescence decay, while being multiexponential, may be approximated by a bi-exponential function containing the two monoexponential decays of unquenched CFP and of FRET-quenched CFP, respectively. The phasor approach allows us to display the data prior to data interpretation graphically, that is, prior to the decision on the multiexponentiality of the CFP decay function, and was primarily used for the FRET-FLIM data evaluation. Similar to fluorescence intensity two-photon experiments, we performed time-lapse FRET-FLIM measurements and repeated the described acquisition every 30 s.

### Analysis of two-photon data

For ratiometric analysis of two-photon data, fluorescence signals were corrected for spectral overlap (the eCFP to citrine ratio in  $525 \pm 25$  nm channel is 0.52/0.48) and refined by taking into account the sensitivity of photomultiplier tubes (0.37 for  $466 \pm 30$  nm and 0.4 for  $525 \pm 25$  nm). Ratiometric FRET for in vivo experiments was calculated accordingly as

$$FRET = \frac{1,2 \cdot ch2}{2,7 \cdot ch1 + 2,5 \cdot ch2} \cdot 100 \quad (12)$$

Evaluation of FLIM data was performed using the phasor approach (Digman *et al.*, 2008; Leben *et al.*, 2018). Briefly, the fluorescence decay in each pixel of the image is Fourier-transformed at a frequency of 80 MHz and normalized, resulting into a phase vector, with the origin at (0|0) in a Cartesian system, pointing into a distinct direction within a half-circle centered at (0.5|0) and a radius of 0.5. For pure substances, vectors end directly on the half-circle, for mixtures of two on a connecting segment between the respective pure lifetimes and within a triangle, if three substances are present, and so on. The distance between several fluorescence lifetimes on the half-circle is naturally distributed logarithmically, with the longest lifetimes closer to the origin. In the case of TN-XXL, the extremes are the unquenched CFP fluorescence (2312 ps) and the eCFP fluorescence completely quenched by FRET (744 ps). The location of the measured lifetime on the connecting line can directly be translated into the amount of either eCFP state and thus to a corresponding calcium concentration in each pixel of the image.

At low signal-to-noise ratio values, the FLIM signal of the donor with a large contribution of electronic noise is shifted towards the origin of coordinates in the phasor plot, indicative for the infinite lifetime of noise. In non-fluorescent medium, we measured electronic noise and Gaussian-fitted the histograms of real and imaginary parts. The Gaussian fit of each part gives the mean (distribution center) as well as the full distribution width at half maximum,  $\text{FWHM} = 2\sqrt{2\ln 2}\sigma$ , which was the same for both parts. The width of electronic noise distribution gives the radius within which we expect only noise (Figure 4g). In order to increase the accuracy, we excluded all data points in an area within the radius of  $\frac{3}{4}\text{FWHM} = 0.3$ .

### Titration of TN-XXL construct

Sensor calibration was performed using lysate of cultured, homozygous B1-8<sup>hi</sup>:YellowCaB plasma blasts induced from isolated B1-8<sup>hi</sup>:YellowCaB cells stimulated with LPS/IL-4 for 2 days. Briefly, cells were freeze-thawed in liquid nitrogen 3–4 times and treated with ultrasound for 15 min. Lysate was filtered and cell clumps separated by high-speed centrifugation. Lysis was done at two equal shares in a sufficiently small volume of calcium-free calibration buffer (Life Technologies) or calcium-saturated (39  $\mu\text{M}$  CaEGTA), respectively. Calcium buffer concentrations measured were achieved by dilution of 39  $\mu\text{M}$ -buffered cell lysate with 0  $\mu\text{M}$ -buffered cell lysate. Sample concentrations were loaded into glass microscope slides with recess, covered, and their fluorescence was measured at the two-photon microscope in a time-resolved manner. Focus was adjusted to a z-position with maximal photon counting numbers, as ensured by acquisition of proper decay curves. In time domain, the eCFP mean fluorescence lifetimes  $\tau$  at various free calcium concentrations were determined by approximating the corresponding fluorescence decay curves  $F(t)$  acquired with our TCSPC-based FLIM detector to a monoexponential function containing background  $y_0$ :  $F(t) = y_0 + A \cdot e^{-t/\tau}$ . Fitting was performed iteratively using a Levenberg–Marquardt gradient algorithm (Rinnenthal *et al.*, 2013).

### Statistical information

Time-dependent FRET curve analysis shows representative graphs for the number of analyzed cells and independent experiments given. For multiple curve analysis, mean is shown and SD indicated in each data point. For column analysis, one-way ANOVA with Bonferroni multiple comparison test was applied with a confidence Interval of 95%.

### Data availability

All raw data and analyzed data shown here are stored on institutional servers. Imaging source data and raw Excel files have been deposited at <https://datadryad.org> under DOI: 10.5061/dryad.cc2fqz63d.

### Acknowledgements

We thank Patrick Thiemann, Vivien Theissig, and Manuela Ohde for animal caretaking. We thank Robert Günther for excellent surgical assistance and Peggy Mex for cell isolations and stainings. We thank Ralf Uecker for microscope facility services. We further thank Mathis Richter, who provided support with the SNR-based quality check of imaging data and their evaluation. This study has been

supported by the Deutsche Forschungsgemeinschaft (DFG) TRR130, project 17 (to AEH and HR) and C01 (to AEH and RAN), and DFG SFB 1444, project 14 (to AEH and RAN).

## Additional information

### Competing interests

Frank Kirchhoff: Reviewing editor, *eLife*. The other authors declare that no competing interests exist.

### Funding

Funder	Grant reference number	Author
Deutsche Forschungsgemeinschaft	TRR130 P17	Helena Radbruch Anja E Hauser
Deutsche Forschungsgemeinschaft	TRR130 C01	Raluca A Niesner Anja E Hauser
Deutsche Forschungsgemeinschaft	TRR130 P04	Lars Nitschke
Deutsche Forschungsgemeinschaft	SFB1444 P14	Raluca A Niesner Anja E Hauser

The funders had no role in study design, data collection and interpretation, or the decision to submit the work for publication.

### Author contributions

Carolin Ulbricht, Conceptualization, Data curation, Formal analysis, Validation, Visualization, Methodology, Writing - original draft; Ruth Leben, Data curation, Software, Formal analysis, Validation, Investigation, Visualization, Methodology, Writing - review and editing; Asylkhan Rakhymzhan, Data curation, Software, Formal analysis, Investigation, Methodology; Frank Kirchhoff, Resources; Lars Nitschke, Resources, Methodology; Helena Radbruch, Supervision, Funding acquisition, Writing - original draft; Raluca A Niesner, Conceptualization, Resources, Data curation, Software, Formal analysis, Supervision, Funding acquisition, Validation, Investigation, Visualization, Methodology, Project administration, Writing - review and editing; Anja E Hauser, Conceptualization, Resources, Formal analysis, Supervision, Funding acquisition, Validation, Investigation, Methodology, Project administration, Writing - review and editing

### Author ORCIDs

Carolin Ulbricht  <https://orcid.org/0000-0003-2983-6242>

Asylkhan Rakhymzhan  <https://orcid.org/0000-0003-3152-1557>

Anja E Hauser  <https://orcid.org/0000-0002-7725-9526>

### Ethics

Animal experimentation: The study was approved by the Berlin Landesamt für Gesundheit und Soziales under the registration # G00158/16. All surgeries and experimental procedures were conducted following the principle of minimization of suffering and 3R means were used where possible.

### Decision letter and Author response

Decision letter <https://doi.org/10.7554/eLife.56020.sa1>

Author response <https://doi.org/10.7554/eLife.56020.sa2>

## Additional files

### Supplementary files

- Source code 1. Annotated Python-based code for phasor analysis.
- Transparent reporting form

**Data availability**

Source data for flow cytometric Analysis, in vitro confocal imaging, ratiometric in vivo Imaging and fluorescence lifetime in vivo Imaging are deposited at Dryad Digital Repository 10.5061/dryad.cc2fqz63d. Analyzed absolute calcium concentration for all cells measured out of 5 experiments have also been deposited there. Source code for phasor based analysis of fluorescence lifetime data has been provided with full submission upload and is available to the public via github (<https://github.com/ulbrica/Phasor-FLIM>; <https://archive.softwareheritage.org/swh:1:rev:8ae5bfc17ec019fcc8ec7e4627442646e52cc3c5>).

The following dataset was generated:

Author(s)	Year	Dataset title	Dataset URL	Database and Identifier
Ulbricht C, Leben R, Rakhymzhan A, Kirchhoff F, Nitschke L, Radbruch H, Niesner RA, Hauser AE	2021	Intravital quantification reveals dynamic calcium concentration changes across B cell differentiation stages	<a href="https://doi.org/10.5061/dryad.cc2fqz63d">https://doi.org/10.5061/dryad.cc2fqz63d</a>	Dryad Digital Repository, 10.5061/dryad.cc2fqz63d

**References**

- Akkaya M, Traba J, Roesler AS, Miozzo P, Akkaya B, Theall BP, Sohn H, Pena M, Smelkinson M, Kabat J, Dahlstrom E, Dorward DW, Skinner J, Sack MN, Pierce SK. 2018. Second signals rescue B cells from activation-induced mitochondrial dysfunction and death. *Nature Immunology* **19**:871–884. DOI: <https://doi.org/10.1038/s41590-018-0156-5>, PMID: 29988090
- Baba Y, Matsumoto M, Kurosaki T. 2014. Calcium signaling in B cells: regulation of cytosolic Ca<sup>2+</sup> increase and its sensor molecules, STIM1 and STIM2. *Molecular Immunology* **62**:339–343. DOI: <https://doi.org/10.1016/j.molimm.2013.10.006>, PMID: 24246800
- Berek C, Berger A, Apel M. 1991. Maturation of the immune response in germinal centers. *Cell* **67**:1121–1129. DOI: [https://doi.org/10.1016/0092-8674\(91\)90289-B](https://doi.org/10.1016/0092-8674(91)90289-B), PMID: 1760840
- Boothby M, Rickert RC. 2017. Metabolic regulation of the immune humoral response. *Immunity* **46**:743–755. DOI: <https://doi.org/10.1016/j.immuni.2017.04.009>, PMID: 28514675
- Bouchon A, Kramer PH, Walczak H. 2000. Critical role for mitochondria in B cell receptor-mediated apoptosis. *European Journal of Immunology* **30**:69–77. DOI: [https://doi.org/10.1002/1521-4141\(200001\)30:1<69::AID-IMMU69>3.0.CO;2-#](https://doi.org/10.1002/1521-4141(200001)30:1<69::AID-IMMU69>3.0.CO;2-#), PMID: 10602028
- Caro-Maldonado A, Wang R, Nichols AG, Kuraoka M, Milasta S, Sun LD, Gavin AL, Abel ED, Kelsoe G, Green DR, Rathmell JC. 2014. Metabolic reprogramming is required for antibody production that is suppressed in anergic but exaggerated in chronically BAFF-exposed B cells. *The Journal of Immunology* **192**:3626–3636. DOI: <https://doi.org/10.4049/jimmunol.1302062>, PMID: 24616478
- Celli A, Sanchez S, Behne M, Hazlett T, Gratton E, Mauro T. 2010. The epidermal Ca<sup>2+</sup> gradient: measurement using the phasor representation of fluorescent lifetime imaging. *Biophysical Journal* **98**:911–921. DOI: <https://doi.org/10.1016/j.bpj.2009.10.055>, PMID: 20197045
- Chen Y, Müller JD, So PT, Gratton E. 1999. The photon counting histogram in fluorescence fluctuation spectroscopy. *Biophysical Journal* **77**:553–567. DOI: [https://doi.org/10.1016/S0006-3495\(99\)76912-2](https://doi.org/10.1016/S0006-3495(99)76912-2), PMID: 10388780
- Chen Y, Mills JD, Periasamy A. 2003. Protein localization in living cells and tissues using FRET and FLIM. *Differentiation* **71**:528–541. DOI: <https://doi.org/10.1111/j.1432-0436.2003.07109007.x>, PMID: 14686950
- Cossarizza A, Chang HD, Radbruch A, Acs A, Adam D, Adam-Klages S, Agace WW, Aghaepour N, Akdis M, Allez M, Almeida LN, Alvisi G, Anderson G, André I, Annunziato F, Anselmo A, Bacher P, Baldari CT, Bari S, Barnaba V, et al. 2019. Guidelines for the use of flow cytometry and cell sorting in immunological studies (second edition). *European Journal of Immunology* **49**:1457–1973. DOI: <https://doi.org/10.1002/eji.201970107>, PMID: 31633216
- Crabtree GR, Olson EN. 2002. NFAT signaling: choreographing the social lives of cells. *Cell* **109 Suppl**:S67–S79. DOI: [https://doi.org/10.1016/S0092-8674\(02\)00699-2](https://doi.org/10.1016/S0092-8674(02)00699-2), PMID: 11983154
- da Silva AC, de Souza KW, Machado RC, da Silva MF, Sant'Anna OA. 1998. Genetics of immunological tolerance: I. bidirectional selective breeding of mice for oral tolerance. *Research in Immunology* **149**:151–161. DOI: [https://doi.org/10.1016/S0923-2494\(98\)80298-8](https://doi.org/10.1016/S0923-2494(98)80298-8), PMID: 9628396
- Díaz-Bulnes P, Saiz ML, López-Larrea C, Rodríguez RM. 2020. Crosstalk between hypoxia and ER stress response: a key regulator of macrophage polarization. *Frontiers in Immunology* **10**:1–16. DOI: <https://doi.org/10.3389/fimmu.2019.02951>
- Digman MA, Caiolfa VR, Zamai M, Gratton E. 2008. The phasor approach to fluorescence lifetime imaging analysis. *Biophysical Journal* **94**:L14–L16. DOI: <https://doi.org/10.1529/biophysj.107.120154>, PMID: 17981902

- Eckl-Dorna J, Batista FD. 2009. BCR-mediated uptake of antigen linked to TLR9 ligand stimulates B-cell proliferation and antigen-specific plasma cell formation. *Blood* **113**:3969–3977. DOI: <https://doi.org/10.1182/blood-2008-10-185421>, PMID: 19144984
- Elson D, Requejo-Isidro J, Munro I, Reavell F, Siegel J, Suhling K, Tadrour P, Benninger R, Lanigan P, McGinty J, Talbot C, Treanor B, Webb S, Sandison A, Wallace A, Davis D, Lever J, Neil M, Phillips D, Stamp G, et al. 2004. Time-domain fluorescence lifetime imaging applied to biological tissue. *Photochemical & Photobiological Sciences* **3**:795–801. DOI: <https://doi.org/10.1039/b316456j>, PMID: 15295637
- Fooksman DR, Schwickert TA, Victora GD, Dustin ML, Nussenzweig MC, Skokos D. 2010. Development and migration of plasma cells in the mouse lymph node. *Immunity* **33**:118–127. DOI: <https://doi.org/10.1016/j.immuni.2010.06.015>, PMID: 20619695
- Geiger A, Russo L, Gensch T, Thestrup T, Becker S, Hopfner KP, Griesinger C, Witte G, Griesbeck O. 2012. Correlating calcium binding, Förster resonance energy transfer, and conformational change in the biosensor TN-XXL. *Biophysical Journal* **102**:2401–2410. DOI: <https://doi.org/10.1016/j.bpj.2012.03.065>, PMID: 22677394
- Gitlin AD, Mayer CT, Oliveira TY, Shulman Z, Jones MJ, Koren A, Nussenzweig MC. 2015. Humoral immunity. T cell help controls the speed of the cell cycle in germinal center B cells. *Science* **349**:643–646. DOI: <https://doi.org/10.1126/science.1254919>, PMID: 26184917
- Griffiths EJ, Rutter GA. 2009. Mitochondrial calcium as a key regulator of mitochondrial ATP production in mammalian cells. *Biochimica Et Biophysica Acta (BBA) - Bioenergetics* **1787**:1324–1333. DOI: <https://doi.org/10.1016/j.bbabi.2009.01.019>
- Hauser AE, Debes GF, Arce S, Cassese G, Hamann A, Radbruch A, Manz RA. 2002. Chemotactic responsiveness toward ligands for CXCR3 and CXCR4 is regulated on plasma blasts during the time course of a memory immune response. *The Journal of Immunology* **169**:1277–1282. DOI: <https://doi.org/10.4049/jimmunol.169.3.1277>
- Hauser AE, Junt T, Mempel TR, Sneddon MW, Kleinstein SH, Henrickson SE, von Andrian UH, Shlomchik MJ, Haberman AM. 2007. Definition of germinal-center B cell migration in vivo reveals predominant intrazonal circulation patterns. *Immunity* **26**:655–667. DOI: <https://doi.org/10.1016/j.immuni.2007.04.008>, PMID: 17509908
- Hendriks RW, Yuvaraj S, Kil LP. 2014. Targeting Bruton's tyrosine kinase in B cell malignancies. *Nature Reviews Cancer* **14**:219–232. DOI: <https://doi.org/10.1038/nrc3702>, PMID: 24658273
- Hiepe F, Dörner T, Hauser AE, Hoyer BF, Mei H, Radbruch A. 2011. Long-lived autoreactive plasma cells drive persistent autoimmune inflammation. *Nature Reviews Rheumatology* **7**:170–178. DOI: <https://doi.org/10.1038/nrrheum.2011.1>, PMID: 21283146
- Hoffmann A, Kerr S, Jellusova J, Zhang J, Weisel F, Wellmann U, Winkler TH, Kneitz B, Crocker PR, Nitschke L. 2007. Siglec-G is a B1 cell-inhibitory receptor that controls expansion and calcium signaling of the B1 cell population. *Nature Immunology* **8**:695–704. DOI: <https://doi.org/10.1038/ni1480>, PMID: 17572677
- Hoyer-Hansen M, Jäättelä M. 2007. Connecting endoplasmic reticulum stress to autophagy by unfolded protein response and calcium. *Cell Death & Differentiation* **14**:1576–1582. DOI: <https://doi.org/10.1038/sj.cdd.4402200>, PMID: 17612585
- Jameson DM, Gratton E, Hall RD. 1984. The measurement and analysis of heterogeneous emissions by multifrequency phase and modulation fluorometry. *Applied Spectroscopy Reviews* **20**:55–106. DOI: <https://doi.org/10.1080/05704928408081716>
- Jang K-J, Mano H, Aoki K, Hayashi T, Muto A, Nambu Y, Takahashi K, Itoh K, Taketani S, Nutt SL, Igarashi K, Shimizu A, Sugai M. 2015. Mitochondrial function provides instructive signals for activation-induced B-cell fates. *Nature Communications* **6**:1–13. DOI: <https://doi.org/10.1038/ncomms7750>
- Jellusova J, Wellmann U, Amann K, Winkler TH, Nitschke L. 2010. CD22 x Siglec-G double-deficient mice have massively increased B1 cell numbers and develop systemic autoimmunity. *The Journal of Immunology* **184**:3618–3627. DOI: <https://doi.org/10.4049/jimmunol.0902711>, PMID: 20200274
- Jellusova J, Cato MH, Apgar JR, Ramezani-Rad P, Leung CR, Chen C, Richardson AD, Conner EM, Benschop RJ, Woodgett JR, Rickert RC. 2017. Gsk3 is a metabolic checkpoint regulator in B cells. *Nature Immunology* **18**:303–312. DOI: <https://doi.org/10.1038/ni.3664>, PMID: 28114292
- Jellusova J. 2018. Cross-talk between signal transduction and metabolism in B cells. *Immunology Letters* **201**:1–13. DOI: <https://doi.org/10.1016/j.imlet.2018.11.003>, PMID: 30439477
- Junt T, Moseman EA, Iannacone M, Massberg S, Lang PA, Boes M, Fink K, Henrickson SE, Shayakhmetov DM, Di Paolo NC, van Rooijen N, Mempel TR, Whelan SP, von Andrian UH. 2007. Subcapsular sinus macrophages in lymph nodes clear lymph-borne viruses and present them to antiviral B cells. *Nature* **450**:110–114. DOI: <https://doi.org/10.1038/nature06287>, PMID: 17934446
- Kass GE, Orrenius S. 1999. Calcium signaling and cytotoxicity. *Environmental Health Perspectives* **107** Suppl 1:25–35. DOI: <https://doi.org/10.1289/ehp.99107s125>, PMID: 10229704
- Khalil AM, Cambier JC, Shlomchik MJ. 2012. B cell receptor signal transduction in the GC is short-circuited by high phosphatase activity. *Science* **336**:1178–1181. DOI: <https://doi.org/10.1126/science.1213368>, PMID: 22555432
- Kyratsous NI, Bauer IJ, Zhang G, Pesic M, Bartholomäus I, Mues M, Fang P, Wörner M, Everts S, Ellwart JW, Watt JM, Potter BVL, Hohlfield R, Wekerle H, Kawakami N. 2017. Visualizing context-dependent calcium signaling in Encephalitogenic T cells in vivo by two-photon microscopy. *PNAS* **114**:E6381–E6389. DOI: <https://doi.org/10.1073/pnas.1701806114>, PMID: 28716943
- Laine R, Stuckey DW, Manning H, Warren SC, Kennedy G, Carling D, Dunsby C, Sardini A, French PM. 2012. Fluorescence lifetime readouts of Troponin-C-based calcium FRET sensors: a quantitative comparison of CFP

- and mTFP1 as donor fluorophores. *PLOS ONE* **7**:e49200. DOI: <https://doi.org/10.1371/journal.pone.0049200>, PMID: 23152874
- Lakowicz JR, Szmajdzinski H, Nowaczyk K, Johnson ML. 1992. Fluorescence lifetime imaging of free and protein-bound NADH. *PNAS* **89**:1271–1275. DOI: <https://doi.org/10.1073/pnas.89.4.1271>
- Lam WY, Bhattacharya D. 2018. Metabolic links between plasma cell survival, secretion, and stress. *Trends in Immunology* **39**:19–27. DOI: <https://doi.org/10.1016/j.it.2017.08.007>, PMID: 28919256
- Le Marois A, Suhling K. 2017. Quantitative Live Cell FLIM Imaging in Three Dimensions BT - Multi-Parametric Live Cell Microscopy of 3D Tissue Models. In: Dmitriev R. I (Ed). *Multi-Parametric Live Cell Microscopy of 3D Tissue Models*. Cham: Springer International Publishing. p. 31–48.
- Leben R, Ostendorf L, van Koppen S, Rakhymzhan A, Hauser A, Radbruch H, Niesner R. 2018. Phasor-Based endogenous NAD(P)H fluorescence lifetime imaging unravels specific enzymatic activity of neutrophil granulocytes preceding NETosis. *International Journal of Molecular Sciences* **19**:1018. DOI: <https://doi.org/10.3390/ijms19041018>
- Leben R, Köhler M, Radbruch H, Hauser AE, Niesner RA. 2019. Systematic enzyme mapping of cellular metabolism by Phasor-Analyzed Label-Free NAD(P)H fluorescence lifetime imaging. *International Journal of Molecular Sciences* **20**:5565. DOI: <https://doi.org/10.3390/ijms20225565>
- Levitt JA, Poland SP, Krstajic N, Pfisterer K, Erdogan A, Barber PR, Parsons M, Henderson RK, Ameer-Beg SM. 2020. Quantitative real-time imaging of intracellular FRET biosensor dynamics using rapid multi-beam confocal FLIM. *Scientific Reports* **10**:5146. DOI: <https://doi.org/10.1038/s41598-020-61478-1>, PMID: 32198437
- Li N, Sul JY, Haydon PG. 2003. A calcium-induced calcium influx factor, nitric oxide, modulates the refilling of calcium stores in astrocytes. *The Journal of Neuroscience* **23**:10302–10310. DOI: <https://doi.org/10.1523/JNEUROSCI.23-32-10302.2003>, PMID: 14614089
- Luo W, Weisel F, Shlomchik MJ. 2018. B cell receptor and CD40 signaling are rewired for synergistic induction of the c-Myc transcription factor in germinal center B cells. *Immunity* **48**:313–326. DOI: <https://doi.org/10.1016/j.immuni.2018.01.008>, PMID: 29396161
- Mank M, Reiff DF, Heim N, Friedrich MW, Borst A, Griesbeck O. 2006. A FRET-based calcium biosensor with fast signal kinetics and high fluorescence change. *Biophysical Journal* **90**:1790–1796. DOI: <https://doi.org/10.1529/biophysj.105.073536>, PMID: 16339891
- Mank M, Santos AF, Dörenberger S, Mrcic-Flogel TD, Hofer SB, Stein V, Hendl T, Reiff DF, Levelt C, Borst A, Bonhoeffer T, Hübener M, Griesbeck O. 2008. A genetically encoded calcium indicator for chronic in vivo two-photon imaging. *Nature Methods* **5**:805–811. DOI: <https://doi.org/10.1038/nmeth.1243>, PMID: 19160515
- Manz RA, Löhning M, Cassese G, Thiel A, Radbruch A. 1998. Survival of long-lived plasma cells is independent of antigen. *International Immunology* **10**:1703–1711. DOI: <https://doi.org/10.1093/intimm/10.11.1703>, PMID: 9846699
- Maus M, Medgyesi D, Kiss E, Schneider AE, Enyedi A, Szilágyi N, Matkó J, Sármay G. 2013. B cell receptor-induced Ca<sup>2+</sup> mobilization mediates F-actin rearrangements and is indispensable for adhesion and spreading of B lymphocytes. *Journal of Leukocyte Biology* **93**:537–547. DOI: <https://doi.org/10.1189/jlb.0312169>, PMID: 23362305
- Maus M, Cuk M, Patel B, Lian J, Ouimet M, Kaufmann U, Yang J, Horvath R, Hornig-Do HT, Chrzanoska-Lightowlers ZM, Moore KJ, Cuervo AM, Feske S. 2017. Store-Operated Ca<sup>2+</sup> entry controls induction of lipolysis and the transcriptional reprogramming to lipid metabolism. *Cell Metabolism* **25**:698–712. DOI: <https://doi.org/10.1016/j.cmet.2016.12.021>, PMID: 28132808
- Mayer CT, Gazumyan A, Kara EE, Gitlin AD, Golijanin J, Viant C, Pai J, Oliveira TY, Wang Q, Escolano A, Medina-Ramirez M, Sanders RW, Nussenzweig MC. 2017. The microanatomic segregation of selection by apoptosis in the germinal center. *Science* **358**:eaao2602. DOI: <https://doi.org/10.1126/science.aao2602>, PMID: 28935768
- Moran I, Nguyen A, Khoo WH, Butt D, Bourne K, Young C, Hermes JR, Biro M, Gracie G, Ma CS, Munier CML, Luciani F, Zaunders J, Parker A, Kelleher AD, Tangye SG, Croucher PI, Brink R, Read MN, Phan TG. 2018. Memory B cells are reactivated in subcapsular proliferative foci of lymph nodes. *Nature Communications* **9**:1–14. DOI: <https://doi.org/10.1038/s41467-018-05772-7>
- Mossakowski AA, Pohlman J, Bremer D, Lindquist R, Millward JM, Bock M, Pollok K, Mothes R, Viohl L, Radbruch M, Gerhard J, Bellmann-Strobl J, Behrens J, Infante-Duarte C, Mähler A, Boschmann M, Rinnenthal JL, Fuchtemeier M, Herz J, Pache FC, et al. 2015. Tracking CNS and systemic sources of oxidative stress during the course of chronic neuroinflammation. *Acta Neuropathologica* **130**:799–814. DOI: <https://doi.org/10.1007/s00401-015-1497-x>, PMID: 26521072
- Mueller J, Matloubian M, Zikherman J. 2015. Cutting edge: an in vivo reporter reveals active B cell receptor signaling in the germinal center. *The Journal of Immunology* **194**:2993–2997. DOI: <https://doi.org/10.4049/jimmunol.1403086>, PMID: 25725108
- Müller JD, Chen Y, Gratton E. 2000. Resolving heterogeneity on the single molecular level with the Photon-Counting histogram. *Biophysical Journal* **78**:474–486. DOI: [https://doi.org/10.1016/S0006-3495\(00\)76610-0](https://doi.org/10.1016/S0006-3495(00)76610-0)
- Müller J, Nitschke L. 2014. The role of CD22 and Siglec-G in B-cell tolerance and autoimmune disease. *Nature Reviews Rheumatology* **10**:422–428. DOI: <https://doi.org/10.1038/nrrheum.2014.54>, PMID: 24763061
- Murakoshi H, Lee SJ, Yasuda R. 2008. Highly sensitive and quantitative FRET-FLIM imaging in single dendritic spines using improved non-radiative YFP. *Brain Cell Biology* **36**:31–42. DOI: <https://doi.org/10.1007/s11068-008-9024-9>, PMID: 18512154

- Negulescu PA, Krasieva TB, Khan A, Kerschbaum HH, Cahalan MD. 1996. Polarity of T cell shape, motility, and sensitivity to antigen. *Immunity* **4**:421–430. DOI: [https://doi.org/10.1016/S1074-7613\(00\)80409-4](https://doi.org/10.1016/S1074-7613(00)80409-4), PMID: 8630728
- Nguyen YH, Lee KY, Kim TJ, Kim SJ, Kang TM. 2011. CD40 Co-stimulation inhibits sustained BCR-induced ca signaling in response to Long-term antigenic stimulation of immature B cells. *The Korean Journal of Physiology and Pharmacology* **15**:179–187. DOI: <https://doi.org/10.4196/kjpp.2011.15.3.179>, PMID: 21860597
- Niiri H, Clark EA. 2002. Regulation of B-cell fate by antigen-receptor signals. *Nature Reviews Immunology* **2**: 945–956. DOI: <https://doi.org/10.1038/nri955>, PMID: 12461567
- Nitschke L, Tsubata T. 2004. Molecular interactions regulate BCR signal inhibition by CD22 and CD72. *Trends in Immunology* **25**:543–550. DOI: <https://doi.org/10.1016/j.it.2004.08.002>, PMID: 15364057
- Nossal GJ, Karvelas M, Pulendran B. 1993. Soluble antigen profoundly reduces memory B-cell numbers even when given after challenge immunization. *PNAS* **90**:3088–3092. DOI: <https://doi.org/10.1073/pnas.90.7.3088>, PMID: 8464928
- O'Keefe TL, Williams GT, Batista FD, Neuberger MS. 1999. Deficiency in CD22, a B cell-specific inhibitory receptor, is sufficient to predispose to development of high affinity autoantibodies. *Journal of Experimental Medicine* **189**:1307–1313. DOI: <https://doi.org/10.1084/jem.189.8.1307>, PMID: 10209047
- Ojaniemi M, Glumoff V, Harju K, Liljeroos M, Vuori K, Hallman M. 2003. Phosphatidylinositol 3-kinase is involved in Toll-like receptor 4-mediated cytokine expression in mouse macrophages. *European Journal of Immunology* **33**:597–605. DOI: <https://doi.org/10.1002/eji.200323376>, PMID: 12616480
- Pinto D, Montani E, Bolli M, Garavaglia G, Sallusto F, Lanzavecchia A, Jarrossay D. 2013. A functional BCR in human IgA and IgM plasma cells. *Blood* **121**:4110–4114. DOI: <https://doi.org/10.1182/blood-2012-09-459289>, PMID: 23550036
- Pone EJ, Zan H, Zhang J, Al-Qahtani A, Xu Z, Casali P. 2010. Toll-like receptors and B-cell receptors synergize to induce immunoglobulin class-switch DNA recombination: relevance to microbial antibody responses. *Critical Reviews in Immunology* **30**:1–29. DOI: <https://doi.org/10.1615/CritRevImmuno.v30.i1.10>, PMID: 20370617
- Pone EJ, Zhang J, Mai T, White CA, Li G, Sakakura JK, Patel PJ, Al-Qahtani A, Zan H, Xu Z, Casali P. 2012. BCR-signalling synergizes with TLR-signalling for induction of AID and immunoglobulin class-switching through the non-canonical NF- $\kappa$ B pathway. *Nature Communications* **3**:712–767. DOI: <https://doi.org/10.1038/ncomms1769>, PMID: 22473011
- Pone EJ, Lou Z, Lam T, Greenberg ML, Wang R, Xu Z, Casali P. 2015. B cell TLR1/2, TLR4, TLR7 and TLR9 interact in induction of class switch DNA recombination: modulation by BCR and CD40, and relevance to T-independent antibody responses. *Autoimmunity* **48**:1–12. DOI: <https://doi.org/10.3109/08916934.2014.993027>, PMID: 25536171
- Pulendran B, Kannourakis G, Nouri S, Smith KG, Nossal GJ. 1995. Soluble antigen can cause enhanced apoptosis of germinal-centre B cells. *Nature* **375**:331–334. DOI: <https://doi.org/10.1038/375331a0>, PMID: 7753199
- Radbruch H, Bremer D, Mothes R, Günther R, Rinnenthal JL, Pohlen J, Ulbricht C, Hauser AE, Niesner R. 2015. Intravital FRET: probing cellular and tissue function in vivo. *International Journal of Molecular Sciences* **16**: 11713–11727. DOI: <https://doi.org/10.3390/ijms160511713>, PMID: 26006244
- Rakhymzhan A, Leben R, Zimmermann H, Günther R, Mex P, Reismann D, Ulbricht C, Acs A, Brandt AU, Lindquist RL, Winkler TH, Hauser AE, Niesner RA. 2017. Synergistic strategy for multicolor Two-photon microscopy: application to the analysis of germinal center reactions in vivo. *Scientific Reports* **7**:7101. DOI: <https://doi.org/10.1038/s41598-017-07165-0>, PMID: 28769068
- Ranjit S, Malacrida L, Jameson DM, Gratton E. 2018. Fit-free analysis of fluorescence lifetime imaging data using the phasor approach. *Nature Protocols* **13**:1979–2004. DOI: <https://doi.org/10.1038/s41596-018-0026-5>, PMID: 30190551
- Ren H, Teng Y, Tan B, Zhang X, Jiang W, Liu M, Jiang W, Du B, Qian M. 2014. Toll-like receptor-triggered calcium mobilization protects mice against bacterial infection through extracellular ATP release. *Infection and Immunity* **82**:5076–5085. DOI: <https://doi.org/10.1128/IAI.02546-14>, PMID: 25245808
- Rickert RC, Roes J, Rajewsky K. 1997. B lymphocyte-specific, Cre-mediated mutagenesis in mice. *Nucleic Acids Research* **25**:1317–1318. DOI: <https://doi.org/10.1093/nar/25.6.1317>, PMID: 9092650
- Rinnenthal JL, Börnchen C, Radbruch H, Andresen V, Mossakowski A, Siffrin V, Seelemann T, Spiecker H, Moll I, Herz J, Hauser AE, Zipp F, Behne MJ, Niesner R. 2013. Parallelized TCSPC for dynamic intravital fluorescence lifetime imaging: quantifying neuronal dysfunction in neuroinflammation. *PLOS ONE* **8**:e60100. DOI: <https://doi.org/10.1371/journal.pone.0060100>, PMID: 23613717
- Rooszendaal R, Mempel TR, Pitcher LA, Gonzalez SF, Verschoor A, Mebius RE, von Andrian UH, Carroll MC. 2009. Conduits mediate transport of low-molecular-weight antigen to lymph node follicles. *Immunity* **30**:264–276. DOI: <https://doi.org/10.1016/j.immuni.2008.12.014>, PMID: 19185517
- Ruprecht CR, Lanzavecchia A. 2006. Toll-like receptor stimulation as a third signal required for activation of human naive B cells. *European Journal of Immunology* **36**:810–816. DOI: <https://doi.org/10.1002/eji.200535744>, PMID: 16541472
- Saijo K, Mecklenbräuker I, Santana A, Leitger M, Schmedt C, Tarakhovskiy A. 2002. Protein kinase C beta controls nuclear factor kappaB activation in B cells through selective regulation of the I $\kappa$ B kinase alpha. *Journal of Experimental Medicine* **195**:1647–1652. DOI: <https://doi.org/10.1084/jem.20020408>, PMID: 12070292
- Schwickert TA, Victora GD, Fooksman DR, Kamphorst AO, Mugnier MR, Gitlin AD, Dustin ML, Nussenzweig MC. 2011. A dynamic T cell-limited checkpoint regulates affinity-dependent B cell entry into the germinal center.

- Journal of Experimental Medicine* **208**:1243–1252. DOI: <https://doi.org/10.1084/jem.20102477>, PMID: 21576382
- Scott TG, Spencer RD, Leonard NJ, Weber G. 1970. Synthetic spectroscopic models related to coenzymes and base pairs. V. emission properties of NADH. studies of fluorescence lifetimes and quantum efficiencies of NADH, AcPyADH, [reduced acetylpyridineadenine dinucleotide] and simplified synthetic models. *Journal of the American Chemical Society* **92**:687–695. DOI: <https://doi.org/10.1021/ja00706a043>
- Shanmugapriya K, Kim H, Kang HW. 2019. In vitro antitumor potential of astaxanthin nanoemulsion against Cancer cells via mitochondrial mediated apoptosis. *International Journal of Pharmaceutics* **560**:334–346. DOI: <https://doi.org/10.1016/j.ijpharm.2019.02.015>, PMID: 30797074
- Shanmughapriya S, Rajan S, Hoffman NE, Guo S, Kolesar JE, Hines KJ, Ragheb J, Jog R, Caricchio R, Baba Y, Zhou Y, Kaufman B, Joseph Y, Kurosaki T, Gill DL, Madesh M, Long M, Tao S, Vega D, Jiang T, et al. 2016. Ca<sup>2+</sup> signals regulate mitochondrial metabolism by stimulating CREB-mediated expression of the mitochondrial Ca<sup>2+</sup> uniporter mcu. *Science Signaling* **8**:444–454. DOI: <https://doi.org/10.1126/scisignal.2005673>
- Shih TA, Meffre E, Roederer M, Nussenzweig MC. 2002a. Role of BCR affinity in T cell dependent antibody responses in vivo. *Nature Immunology* **3**:570–575. DOI: <https://doi.org/10.1038/ni803>, PMID: 12021782
- Shih TA, Roederer M, Nussenzweig MC. 2002b. Role of antigen receptor affinity in T cell-independent antibody responses in vivo. *Nature Immunology* **3**:399–406. DOI: <https://doi.org/10.1038/ni776>, PMID: 11896394
- Shulman Z, Gitlin AD, Targ S, Jankovic M, Pasqual G, Nussenzweig MC, Victora GD. 2013. T follicular helper cell dynamics in germinal centers. *Science* **341**:673–677. DOI: <https://doi.org/10.1126/science.1241680>, PMID: 23887872
- Shulman Z, Gitlin AD, Weinstein JS, Lainez B, Esplugues E, Flavell RA, Craft JE, Nussenzweig MC. 2014. Dynamic signaling by T follicular helper cells during germinal center B cell selection. *Science* **345**:1058–1062. DOI: <https://doi.org/10.1126/science.1257861>, PMID: 25170154
- Siffrin V, Birkenstock J, Luchtman DW, Gollan R, Baumgart J, Niesner RA, Griesbeck O, Zipp F. 2015. FRET based ratiometric Ca<sup>2+</sup> imaging to investigate immune-mediated neuronal and axonal damage processes in experimental autoimmune encephalomyelitis. *Journal of Neuroscience Methods* **249**:8–15. DOI: <https://doi.org/10.1016/j.jneumeth.2015.04.005>, PMID: 25864804
- Strickler SJ, Berg RA. 1962. Relationship between absorption intensity and fluorescence lifetime of molecules. *The Journal of Chemical Physics* **37**:814–822. DOI: <https://doi.org/10.1063/1.1733166>
- Su TT, Guo B, Kawakami Y, Sommer K, Chae K, Humphries LA, Kato RM, Kang S, Patrone L, Wall R, Teitell M, Leitges M, Kawakami T, Rawlings DJ. 2002. PKC-β controls ixb kinase lipid raft recruitment and activation in response to BCR signaling. *Nature Immunology* **3**:780–786. DOI: <https://doi.org/10.1038/ni823>, PMID: 12118249
- Suzuki K, Grigorova I, Phan TG, Kelly LM, Cyster JG. 2009. Visualizing B cell capture of cognate antigen from follicular dendritic cells. *Journal of Experimental Medicine* **206**:1485–1493. DOI: <https://doi.org/10.1084/jem.20090209>, PMID: 19506051
- Tas JM, Mesin L, Pasqual G, Targ S, Jacobsen JT, Mano YM, Chen CS, Weill JC, Reynaud CA, Browne EP, Meyer-Hermann M, Victora GD. 2016. Visualizing antibody affinity maturation in germinal centers. *Science* **351**:1048–1054. DOI: <https://doi.org/10.1126/science.aad3439>, PMID: 26912368
- Tolar P, Hanna J, Krueger PD, Pierce SK. 2009. The constant region of the membrane immunoglobulin mediates B cell-receptor clustering and signaling in response to membrane antigens. *Immunity* **30**:44–55. DOI: <https://doi.org/10.1016/j.immuni.2008.11.007>, PMID: 19135393
- Ulbricht C, Lindquist RL, Tech L, Hauser AE. 2017. Tracking plasma cell differentiation in living mice with Two-Photon microscopy. *Methods in Molecular Biology* **1623**:37–50. DOI: [https://doi.org/10.1007/978-1-4939-7095-7\\_3](https://doi.org/10.1007/978-1-4939-7095-7_3), PMID: 28589345
- Ulbricht C. 2021. Phasor-FLIM. *Software Heritage*. swh:1:rev:8ae5bfc17ec019fcc8ec7e4627442646e52cc3c5. <https://archive.softwareheritage.org/swh:1:rev:8ae5bfc17ec019fcc8ec7e4627442646e52cc3c5>
- Victora GD, Schwickert TA, Fooksman DR, Kamphorst AO, Meyer-Hermann M, Dustin ML, Nussenzweig MC. 2010. Germinal center dynamics revealed by multiphoton microscopy with a photoactivatable fluorescent reporter. *Cell* **143**:592–605. DOI: <https://doi.org/10.1016/j.cell.2010.10.032>, PMID: 21074050
- Victora GD, Nussenzweig MC. 2012. Germinal centers. *Annual Review of Immunology* **30**:429–457. DOI: <https://doi.org/10.1146/annurev-immunol-020711-075032>, PMID: 22224772
- von Andrian UH, Mempel TR. 2003. Homing and cellular traffic in lymph nodes. *Nature Reviews Immunology* **3**:867–878. DOI: <https://doi.org/10.1038/nri1222>, PMID: 14668803
- Weisel FJ, Mullett SJ, Elsner RA, Menk AV, Trivedi N, Luo W, Wikenheiser D, Hawse WF, Chikina M, Smita S, Conter LJ, Joachim SM, Wendell SG, Jurczak MJ, Winkler TH, Delgoffe GM, Shlomchik MJ. 2020. Germinal center B cells selectively oxidize fatty acids for energy while conducting minimal glycolysis. *Nature Immunology* **21**:331–342. DOI: <https://doi.org/10.1038/s41590-020-0598-4>, PMID: 32066950

## Appendix B

### B.1. Python script

The following code script was written in Python 2.7.12 using the spyder 3.0.2 Scientific Python Development Environment and Anaconda 4.2.0 (64-bit package (default, Jun 29 2016, 11:07:13 [MSC v.1500 64 bit (AMD64)] a free and open-source distribution of the Python programming language for scientific computing.

This algorithm loads, preprocesses and analyzes the FLIM data, but is exclusively designed to process FLIM data recorded with the software Inspector Pro version 2.0.8 provided by La Vision BioTec GmbH. This restriction applies primarily to the import of raw data, which are provided as images in \*.tiff stacks containing 76, 153, 227 or 455 images, depending on the microscope and binning setting chosen. The mathematics of the phasor approach is not affected and is the same as presented by (Digman et al. 2008).

The preprocessing includes the Gaussian blurring, the offset compensation, the pixel rejection by thresholding and the moving of the exponential part of the curve to the beginning so that the transformation starts at the maximum of the curve. A number of GUIs (graphical user interfaces) ask for the exact parameters to be used for the preprocessing and analysis. For example, the sigma for the Gaussian blur can be chosen or the pixel value below which no analysis should take place (threshold).

The analysis part transfers the time-domain raw TCSPC decay stack to the virtual phase domain by calculating the discrete Fourier Transformation numerically (phasor approach) and creates a 3D-histogram of the generated datapoints. The output includes the unblurred sum image of the TCSPC stack (= intensity image), the fluorescence lifetime image, the images of the real and imaginary parts as well as the phasor plot and stores them in a individually created folder.

Furthermore the algorithm is able to loop over all TCSPC raw data contained in a single folder in order to analyze i.e. a z-Stack and/ or the frames of a film.

Using the last GUI, the user can select a scale that represents the markings of the positions of the specific lifetimes in the phasor plot in addition to the representation of the phasor cloud by points or contour lines. For the scaling there are the options of:

- a) The NAD(P)H scale, which marks the free NAD(P)H, the range of the metabolic enzymes bound to NAD(P)H shown as a broad band and the NADPH oxidase,
- b) The NAD(P)H scale is similar to the one in a but includes the specified phasor positions of several, prominent NAD(P)H-dependent enzymes (enzyme fingerprint represented in the colors which are also used for the enzyme mapping).

c) The FRET scale (Förster resonance energy transfer). Whether the construct was CerT-NL (Rinnenthal et al. 2013) or TN-XXL (Geiger et al. 2012).

d) The marks of the lifetimes 0–20 ns in 1 ns steps, to illustrate the logarithmic nature of the phasor plot. The “zero” is actually 0.001 ns, because there is no zero in a logarithmic representation.

e) No scale

If the option b NAD(P)H scale with enzyme fingerprint was chosen, the algorithm calculates the enzyme assignment and activity as described in (Leben et al. 2019) and puts out the enzyme map as well as the enzyme activity map.

### Code:

```
print "ready"

import numpy as np
import math
from matplotlib.backends.backend_tkagg import FigureCanvasTkAgg
from matplotlib.figure import Figure
from PIL import Image
from scipy.ndimage import gaussian_filter
import Tkinter as tk
import tkFileDialog
import os

print "steady"
np.warnings.filterwarnings('ignore')

#####
## -- GUI -- ##
#####
## ++ choose file ++ ##
root1 = tk.Tk()
root1.filename = tkFileDialog.askopenfilename()
filename = root1.filename

directory = os.path.split(filename)[0]
directory = str(directory)

baseFolder = os.path.abspath(os.path.join(directory, os.pardir))

rawdataFolder = os.path.basename(directory)
stopFolder = rawdataFolder.find("raw")
folder = rawdataFolder[0:stopFolder-1]

allfiles = [f for f in os.listdir(directory)
            if os.path.isfile(os.path.join(directory, f))]

## ++ choose 2PM & binning ++ ##
v = tk.IntVar()
v.set(1)
options = [
    ("old 2PM + binning1 [153]",153),
```

```

        ("old 2PM + binning2 [76]", 76),
        ("new 2PM + binning1 [455]", 455),
        ("new 2PM + binning2 [227]", 227)
    ]

def showChoice():
    global timesteps
    timesteps = v.get()
    # == number of images in time stack

for txt, val in options:
    tk.Radiobutton(root1,
                   text=txt,
                   padx = 20,
                   variable=v,
                   command=showChoice,
                   value=val).pack(anchor=tk.W)

button = tk.Button(root1, text="OK", fg="red", command=root1.destroy)
button.pack(side="bottom")

root1.mainloop()

print " ", timesteps, "timesteps"

### ++ tip sigma & offset ++ ##
root2 = tk.Tk()

sigma = 2
offset = 10
thresh = 0

def show_entry_fields():
    global sigma, offset, thresh
    sigma = e1.get()
    sigma = int(sigma)
    offset = e2.get()
    offset = int(offset)
    thresh = e3.get()
    thresh = int(thresh)

labelA = tk.Label(root2, text="gaussian blur: sigma = [2]")
labelA.grid(row = 0)
labelB = tk.Label(root2, text="number of steps used for offset [10]:")
labelB.grid(row = 1)
labelC = tk.Label(root2, text="threshold - pixelvalue in SUM-image [0]:")
labelC.grid(row = 2)

e1 = tk.Entry(root2)
e2 = tk.Entry(root2)
e3 = tk.Entry(root2)

e1.grid(row = 0, column = 1)
e2.grid(row = 1, column = 1)
e3.grid(row = 2, column = 1)

button1 = tk.Button(root2, text='use', command=show_entry_fields)
button1.grid(row=3, column=1, sticky=tk.W, pady=4)

button2 = tk.Button(root2, text='OK', fg="red", command=root2.destroy)
button2.grid(row=3, column=0, sticky=tk.W, pady=4)

root2.mainloop()

```

```

print " sigma = ", sigma
print " offset = ", offset
print " threshold = ", thresh
print "go "

### ++ choose running variable ++ ##
root4 = tk.Tk()
label1 = tk.Label(root4, text = "which part in filename is running?")
label1.grid(row=0, column=0, columnspan=3, sticky=tk.W, pady=4)

substring = [["none", 0, 0],
             ["Time Time", 5, 8],
             ["Axis0000", 18, 5],
             ["xyz-Table Upright z", 18, 5],
             ["C00", 0, 3]]

def runV():
    global AA
    AA = [var1.get(), var2.get(), var3.get(), var4.get(), var5.get()]
    AA = np.asarray([index for index, value in enumerate(AA) if value == 1])
    print ""
    print "running variables:"
    for ii in range(len(AA)): print " ", substring[AA[ii]][0]

tauName = ""
realName = ""
imagName = ""
def imaris_yes():
    global tauName, realName, imagName, AA, taus
    tauName = "Ch222"
    realName = "Ch000"
    imagName = "Ch111"
    taus = 1000
    print "for Imaris"
    runV()

def imaris_no():
    global tauName, realName, imagName, taus
    tauName = "tauImage"
    realName = "real"
    imagName = "imag"
    taus = 1
    runV()

var1 = tk.IntVar()
check1 = tk.Checkbutton(root4, text=substring[0][0], variable=var1)
check1.grid(row=1, sticky=tk.W)

var2 = tk.IntVar()
check2 = tk.Checkbutton(root4, text=substring[1][0], variable=var2)
check2.grid(row=2, sticky=tk.W)

var3 = tk.IntVar()
check3 = tk.Checkbutton(root4, text=substring[2][0], variable=var3)
check3.grid(row=3, sticky=tk.W)

var4 = tk.IntVar()
check4 = tk.Checkbutton(root4, text=substring[3][0], variable=var4)
check4.grid(row=4, sticky=tk.W)

var5 = tk.IntVar()
check5 = tk.Checkbutton(root4, text=substring[4][0], variable=var5)

```

```

check5.grid(row=5, sticky=tk.W)

label2 = tk.Label(root4, text = "Do you plan to use IMARIS?")
label2.grid(row=8, columnspan=3, sticky=tk.W, pady=4)

button3 = tk.Button(root4, text='yes', command=imaris_yes)
button3.grid(row=9, column = 0, sticky=tk.W, pady=4)

button4 = tk.Button(root4, text='no', command=imaris_no)
button4.grid(row=9, column = 1, sticky=tk.W, pady=4)

button5 = tk.Button(root4, text='Ok', fg="red", command=root4.destroy)
button5.grid(row=9, column = 2, sticky=tk.W, pady=4)

tk.mainloop()

fq = 80E6 # modulation frequency [Hz]
w = 2*math.pi*fq

def reS(tau):
    return 1/(1+(w*tau)**2)

def ims(tau):
    return w*tau/(1+(w*tau)**2)

#####
## -- NAD(P)H fingerprint -- ##
#####
tau_free = 0.450E-9 # unbound (free) NAD(P)H -- all in sec --

tau_MDH = 1.2400E-9 # malate dehydrogenase
tau_HADH = 1.360E-9 # hydroxyacyl-coenzyme-A dehydrogenase
tau_LDH = 1.600E-9 # lactate dehydrogenase
tau_G6PDH = 2.005E-9 # glucose-6-phosphate dehydrogenase
tau_SDH_1 = 2.010E-9 # sorbitol dehydrogenase (NADH)
tau_GAPDH = 2.050E-9 # glyceraldehyde 3-phosphate dehydrogenase
tau_IDH = 2.170E-9 # Isocitrate dehydrogenase
tau_SDH_2 = 2.260E-9 # sorbitol dehydrogenase (NADPH)
tau_CTBP1_PDH = 2.470E-9 # C-terminal binding protein 1 & pyruvate dehy.
tau_iNOS = 2.550E-9 # inducible nitric oxide synthase
tau_ADH = 2.600E-9 # alcohol dehydrogenase

tau_NOX = 3.650E-9 # NADPH oxidases family (NOX1-4, DUOX1,2)

list_tau = (tau_free, tau_MDH, tau_HADH, tau_LDH, tau_G6PDH, tau_SDH_1,
            tau_GAPDH, tau_IDH, tau_SDH_2, tau_CTBP1_PDH, tau_iNOS,
            tau_ADH, tau_NOX)

labels_tau = ('free', 'MDH', 'HADH', 'LDH', 'G6PDH', 'SDH (NADH)',
             'GAPDH', 'IDH', 'SDH (NADPH)', 'CTBP1/PDH', 'iNOS',
             'ADH', 'NOX')

colors_tau = ((0.0, 0.0, 1.0), (0.0, 0.518, 0.0),
             (0.0, 0.675, 0.322), (0.0, 0.914, 0.082),
             (0.0, 1.0, 0.0), (0.514, 1.0, 0.0),
             (0.859, 1.0, 0.0), (1.0, 1.0, 0.0),
             (1.0, 1.0, 0.498), (1.0, 0.957, 0.0),
             (1.0, 0.714, 0.0), (1.0, 0.553, 0.0),
             (1.0, 0.0, 0.0))

def fingerprint():
    for num in range(0,len(list_tau)):

```

```

ax.plot(reS(list_tau[num]), imS(list_tau[num]), marker='o',
        markersize=8, color=colors_tau[num], linestyle='none',
        label=labels_tau[num])

#####
## -- define plotting functions -- ##
#####
fs = 15 # fontsize plot

def enzymRegion():
    ## -- enzym region -- ##
    rEnzy = []
    iEnzy = []
    for x in range(77, 108):
        rEnzy.append((1+math.cos(math.radians(x)))/2)
        iEnzy.append((math.sin(math.radians(x)))/2)

    ax.plot(rEnzy, iEnzy, 'k-', linewidth=5)

def NADPHscale():
    ## -- free -- ##
    ax.plot(reS(tau_free), imS(tau_free), 'ko')
    ax.text(reS(tau_free), imS(tau_free), "free",
            va = 'bottom', ha = 'left', rotation = 45, fontsize=fs)

    ## -- meta. enzymes -- ##
    tau_enzym = 2026E-12 # middle of enzym region
    ax.text(reS(tau_enzym)-0.11, imS(tau_enzym)+0.02, "meta. enzymes",
            va = 'bottom', ha = 'left', fontsize=fs)

    ## -- NOX region -- ##
    ax.plot(reS(tau_NOX), imS(tau_NOX), 'ko')
    ax.text(reS(tau_NOX)-0.01, imS(tau_NOX)+0.01, "NOX",
            va = 'bottom', ha = 'left', rotation = 45, fontsize=fs)

    ax.plot()

def FRETscale_CertNL():
    tau_quen = 693E-12 # CerT-NL; Rinnenthal et al., 2013
    tau_unquen = 2225E-12

    ax.plot(reS(tau_quen), imS(tau_quen), 'ko')
    ax.text(reS(tau_quen), imS(tau_quen), "quen.",
            va = 'bottom', ha = 'left',
            rotation = 45, fontsize=fs)

    ax.plot(reS(tau_unquen), imS(tau_unquen), 'ko')
    ax.text(reS(tau_unquen), imS(tau_unquen), "unquen.",
            va = 'bottom', ha = 'left',
            rotation = 45, fontsize=fs)

    ax.plot()

def FRETscale_TNXXL():
    # -- TN-XXL; Griesbeck et al. -- ##
    tau_quen = 735E-12 # tau1 from suppl tab 1 ECFP
    tau_inter = 1260E-12 # from text
    tau_unquen = 2350E-12 # tau_ave from suppl tab 1 ECFP

    ax.plot(reS(tau_quen), imS(tau_quen), 'ko')
    ax.text(reS(tau_quen), imS(tau_quen), "quen.",
            va = 'bottom', ha = 'left',
            rotation = 45, fontsize=fs)

```

---

```

ax.plot(res(tau_inter), imS(tau_inter), 'ko')
ax.text(res(tau_inter), imS(tau_inter), "inter.",
        va = 'bottom', ha = 'left',
        rotation = 45, fontsize=fs)

ax.plot(res(tau_unquen), imS(tau_unquen), 'ko')
ax.text(res(tau_unquen), imS(tau_unquen), "unquen.",
        va = 'bottom', ha = 'left',
        rotation = 45, fontsize=fs)

def tauMark():
    tau_mark = (0.001E-9, 1E-9, 2E-9, 3E-9, 4E-9, 5E-9, 6E-9, 7E-9,
               8E-9, 9E-9, 10E-9, 11E-9, 12E-9, 13E-9, 14E-9, 15E-9)

    tau_text = ("0ns", "1ns", "2ns", "3ns", "4ns", "5ns", "6ns", "7ns",
               "8ns", "9ns", "10ns")

    for index in range(len(tau_mark)):
        ax.plot(res(tau_mark[index]), imS(tau_mark[index]), marker='o',
                markersize=7, color='#bebebe', linestyle='none')
        #ax.text(res(tau_mark[index])+0.01, imS(tau_mark[index])+0.001,
        #tau_text[index], va = 'bottom', ha = 'left',
        #fontsize=12, color='#bebebe')

    ax.plot()

def layout():
    global real, imag, scale
    real = []
    imag = []
    for x in range(0, 180):
        real.append((1+math.cos(math.radians(x)))/2)
        imag.append((math.sin(math.radians(x)))/2)

    ax.plot(real, imag, 'k-')
    ax.set_xlim(0, 1)
    ax.set_ylim(0, 0.6)

    ax.set_xlabel('real', fontsize=fs)
    ax.set_ylabel('imaginary', fontsize=fs)

    if scale == 1:
        NADPHscale()
        enzymRegion()

    elif scale == 2:
        NADPHscale()
        fingerprint()

    elif scale == 3:
        FRETscale_CertNL()

    elif scale == 4:
        FRETscale_TNXXL()

    elif scale == 5:
        tauMark()

    else: pass

```

---

---

```

def contour():
    global upCL, lowCL, cf, counts1, levels, extent
    if n == 0:
        upCL = e.get()
        upCL = int(upCL)
        lowCL = e2.get()
        lowCL = int(lowCL)
    else:
        upCL
        lowCL

    canvas=FigureCanvasTkAgg(fig, master=root4)
    canvas.get_tk_widget().grid(row=6, column=0, columnspan = 4)
    ax.clear()

    counts1, ybins1, xbins1 = np.histogram2d(eTAU[:,1], eTAU[:,0], bins=80)
    ex = [xbins1.min(), xbins1.max(), ybins1.min(), ybins1.max()]
    levels = np.arange(lowCL, upCL, 0.01*upCL)
    cf = ax.contour(counts1, levels, linewidths=1, cmap='plasma', extent=ex)

    layout()

def dots():
    global upCL, lowCL, cf, counts1, levels, ex
    if n == 0:
        upCL = e.get()
        upCL = int(upCL)
        lowCL = e2.get()
        lowCL = int(lowCL)
    else:
        upCL
        lowCL

    canvas=FigureCanvasTkAgg(fig, master=root4)
    canvas.get_tk_widget().grid(row=6, column=0, columnspan = 4)
    ax.clear()

    ax.plot(eTAU[:,0], eTAU[:,1], color = '#130789', marker='.',
            linestyle='none', markersize=0.7, zorder=-1)

    counts1, ybins1, xbins1 = np.histogram2d(eTAU[:,1], eTAU[:,0], bins=80)
    ex = [xbins1.min(), xbins1.max(), ybins1.min(), ybins1.max()]
    levels = np.arange(100, upCL, 10)

    cf = ax.contourf(counts1, levels, linewidths=1, cmap='plasma', extent=ex)
    layout()

#####
## -- defining enzyme mapping functions-- ## optional!
#####
# ++ vector: angle & length ++ #
def angle(P1, P2):
    a = (P1[1] - P2[1]) / (P1[0] - P2[0])
    return np.degrees(np.arctan(a)) # in degree

def lenVec(P1, P2):
    diff_r = P2[0] - P1[0]
    diff_i = P2[1] - P1[1]
    return np.sqrt(np.square(diff_r) + np.square(diff_i))

def quot(data, enzy):
    return angleStore_data[data] / angleStore_enzy[enzy]

```

---

---

```

sh = Image.open(directory + '/' + allfiles[0])
sh = sh.convert('F')
sh = np.asarray(sh)

# -- measued free NAD(P)H [180411] -- #
re_free = 0.881
im_free = 0.197

sigma_free = 0.02
radius = sigma_free*3          # free radius

ones = np.ones(sh.shape)
RE_free = ones*re_free
IM_free = ones*im_free

ones3d = np.ones((len(list_tau), len(sh[0]), len(sh[1])))

# ++ loop over all enzymes ++ # measured free NADH --> enzyme vector
lengthStore_enz = []
angleStore_enz = []
for enzy in range(0, len(list_tau)):
    mx_reS_enz = ones*reS(list_tau[enzy])
    mx_imS_enz = ones*imS(list_tau[enzy])
    alpha2 = angle([mx_reS_enz, mx_imS_enz], [RE_free, IM_free])
    angleStore_enz.append(alpha2)
    length2 = lenvec([mx_reS_enz, mx_imS_enz], [RE_free, IM_free])
    lengthStore_enz.append(length2)

angleStore_enz = np.asarray(angleStore_enz)
lengthStore_enz = np.asarray(lengthStore_enz)

angleStore_data = np.zeros((len(allfiles), len(sh[0]), len(sh[1])))
angleStore_data.fill(np.nan)

lengthStore_data = angleStore_data.copy()

#####
## -- image read-in -- ##
#####
for n in range(0, len(allfiles)):
    print ""
    print "wait, I'm reading stack ", n, "..."

    st = allfiles[n]
    stop_dateC = st.find("_DC-TCSPC")
    # stop_dateC = st.find("_TDC")

    if stop_dateC < 0:
        dateCells = st[0:-4]
    else:
        dateCells = st[9:stop_dateC]

    if substring[AA[0]][0] == "none":
        uStrich = ""
    else: uStrich = "_"

    crt = ""
    for ix in range(len(AA)):
        start = st.find(substring[AA[ix]][0]) + substring[AA[ix]][1]
        stop = start + substring[AA[ix]][2]

```

---

---

```

        #print st.find(substring[AA[ix]][0]), start, stop, st[start:stop],
        crt += "_" + st[start:stop]

print " ", dateCells + crt
print ""

img = Image.open(directory + '/' + allfiles[n])
shape = img.convert('F')
shape = np.asarray(shape)
shape = shape.shape

## -- without mask -- ##
mask = np.ones(shape)

## -- predefined IJ-mask -- ##
##imgM = Image.open("conva_800nm_P0_BB30_woDC_TDC_maskIJ.tif")
##mask = imgM.convert('F')
##mask = np.asarray(mask)

signal = []
signalG = []
meanG = []
mean = []
for k in range(0,timesteps):
    img.seek(k)
    data = img.convert('F')
    signal.append(np.array(data))
    g = 1000*(gaussian_filter(data, sigma=sigma)*mask)
    signalG.append(np.array(g))
    meanG.append(np.average(signalG[k]))

S = np.array(signal)
S = np.sum(S, axis=0)

sumFile = baseFolder + '/' + str(folder) + '_unblurredSUM/'
if not os.path.exists(sumFile):
    os.makedirs(sumFile)

img00 = Image.fromarray(S)
img00.save(sumFile + dateCells + crt + ustrich + 'unblursUM.tif')

N = np.array(signalG[0:offset])      # average of 1st 10 images of stack
N = np.average(N)                    # as offset --> subtracted
N = np.ones(shape)*N

datalist = ((np.array(signalG)-N)*np.greater(np.array(signalG)-N,0)
            *np.greater(S, thresh))
            #subtracts noise & negative values = 0 & thresholds

#####
## -- sampling time and used datapoints -- ##
#####
dt = 12.24E-9/timesteps
t = []
for k in range(0, timesteps):
    t.append(k*dt)

A = []
for k in range(meanG.index(max(meanG)), timesteps):
    A.append(datalist[k])

```

---

```

#####
## -- phasor approach -- ##
#####
Re = []
Im = []
TAU = []
for k in range(len(A)):
    Re.append(A[k]*math.cos(w*t[k]))
    Im.append(A[k]*math.sin(w*t[k]))

DFTr = (sum(Re)/sum(A))*np.greater(sum(Re),0)
DFTi = (sum(Im)/sum(A))*np.greater(sum(Im),0)
TAU = (1/w)*(DFTi/DFTr)*1E12 # lifetime in [ps]

#####
## -- tau image -- ## --> tau in ps
#####
# upper = 15000.0 # upper border of tau
# lower = 10.0 # lower border of tau
tau = TAU#*(np.less(TAU,upper)*np.greater(TAU,lower)*mask)

analyFile = (baseFolder + '/' + str(folder) + '_analy_sig'
            + str(sigma) + '-off' + str(offset) + '-th' + str(thresh))

tauFile = analyFile + '/tauImages/'
if not os.path.exists(tauFile):
    os.makedirs(tauFile)

img1 = Image.fromarray(tau) # tauImage
img1.save(tauFile + dateCells + crt + uStrich + tauName + '.tif')

#####
## -- phasor plot -- ##
#####
RE = DFTr#*(np.less(TAU,upper)*np.greater(TAU,lower)*mask)
IM = DFTi#*(np.less(TAU,upper)*np.greater(TAU,lower)*mask)

realFile = analyFile + '/real/'
if not os.path.exists(realFile):
    os.makedirs(realFile)

real = Image.fromarray(RE*tausi) # real part image
real.save(realFile + dateCells + crt + uStrich + realName + '.tif')

imagFile = analyFile + '/imag/'
if not os.path.exists(imagFile):
    os.makedirs(imagFile)

imag = Image.fromarray(IM*tausi) # imag part image
imag.save(imagFile + dateCells + crt + uStrich + imagName + '.tif')

eTAU = [] # removes zeros from matrix & forms matrix to 1D
for y in range (len(RE)):
    for x in range (len(RE[0])):
        if RE[y][x]!=0 and IM[y][x]!=0 and
            np.isnan(TAU[y][x])==False:
            eTAU.append((RE[y][x], IM[y][x], x, y, tau[y][x]))
        else: pass

eTAU = np.asarray(eTAU)

```

```

### -- contoured 2d histogram -- ###
root4=tk.Tk()

fig = Figure(figsize=(5,3))
ax=fig.add_axes([0,0,1,1])

v = tk.IntVar()
v.set(1)

options = [
    ("NAD(P)H",1),
    ("NAD(P)H with enzymes",2),
    ("FRET (CerT-NL)",3),
    ("FRET (TN-XXL)",4),
    ("tau 0-20ns",5),
    ("no scale",6)
]

def ShowChoice():
    global scale
    scale = v.get()
    print scale

def close():
    root4.destroy()

if n == 0:
    label3 = tk.Label(root4, text = "Tipp contour levels in
                                phasorPlot")
    label3.grid(row=0, column=0, columnspan=4, sticky=tk.W, pady=4)

    label4 = tk.Label(root4, text = "lower level (e.g. 0): ")
    label4.grid(row=1, column=0, sticky=tk.W, pady=4)

    e2 = tk.Entry(root4, width = 10)
    e2.grid(row=1, column=2)

    label5 = tk.Label(root4, text = "upper level (e.g. 500): ")
    label5.grid(row=2, column=0, sticky=tk.W, pady=4)

    e = tk.Entry(root4, width = 10)
    e.grid(row=2, column=2)

    radio1 = tk.Radiobutton(root4, text=options[0][0], variable=v,
                            command>ShowChoice, value=options[0][1])
    radio1.grid(row = 3, column = 0)

    radio2 = tk.Radiobutton(root4, text=options[1][0], variable=v,
                            command>ShowChoice, value=options[1][1])
    radio2.grid(row = 3, column = 1)

    radio3 = tk.Radiobutton(root4, text=options[2][0], variable=v,
                            command>ShowChoice, value=options[2][1])
    radio3.grid(row = 4, column = 0)

    radio4 = tk.Radiobutton(root4, text=options[3][0], variable=v,
                            command>ShowChoice, value=options[3][1])
    radio4.grid(row = 4, column = 1)

    radio4 = tk.Radiobutton(root4, text=options[4][0], variable=v,

```

```

        command>ShowChoice, value=options[4][1])
radio4.grid(row = 5, column = 0)
radio5 = tk.Radiobutton(root4, text=options[5][0], variable=v,
        command>ShowChoice, value=options[5][1])
radio5.grid(row = 5, column = 1)
label6 = tk.Label(root4, text = "select your preferred plot
        type:")
label6.grid(row=6, column=0, columnspan=5, sticky=tk.W, pady=5)
plotbutton1 = tk.Button(master=root4, text="contour",
        command=contour)
plotbutton1.grid(row=7, column=1)
plotbutton2 = tk.Button(master=root4, text="dots", command=dots)
plotbutton2.grid(row=7, column=2)
OKbutton = tk.Button(master=root4, text="OK", fg="red",
        command=root4.destroy)
OKbutton.grid(row=7, column=32)
tk.mainloop()
else:
    contour() or dots()
    close()

fig.gca().set_aspect('equal', adjustable='box') # scales plot axis
if contour == True:
    fig.colorbar(cf, ax=ax, shrink = 0.8)
else: pass

plotFile = analyFile + '/phasorPlots/'
if not os.path.exists(plotFile):
    os.makedirs(plotFile)

# ax.legend(bbox_to_anchor=(0,1.02,1,0.2), loc="lower left",
mode="expand",
# borderaxespad=0, ncol=3, numpoints=1, scatterpoints = 1)

fig.savefig(plotFile + dateCells + crt + uStrich + 'phasorPlot.png',
        dpi = 300, bbox_inches='tight')#, transparent=True)

img.close()

#####
## -- optional enzyme & activity mapping -- ##
#####
if scale == 2: # NAD(P)H scale with enzyme fingerprint
    quotStore = np.zeros((len(list_tau), len(sh[0]), len(sh[1])))
    quotStore.fill(np.nan)

    sqSubStore = np.zeros((len(list_tau), len(sh[0]), len(sh[1])))
    sqSubStore.fill(np.nan)

    length1 = lenVec([RE, IM], [re_free, im_free])
    lengthStore_data[n] = length1

    alpha1 = angle([RE, IM], [RE_free, IM_free])
    angleStore_data[n] = alpha1

    for enzy in range(0, len(list_tau)):

```

---

```

        sqSubStore[enzy] = np.sqrt(np.square(quot(n, enzy) - ones))
    invSqSub, mxSUM, probStore = [], [], []
    invSqSub = 1/sqSubStore
    mxSUM = ones3d[:] * invSqSub.sum(axis=0)
    probStore = 100 * 1 / (sqSubStore * mxSUM) # assignment probability in %

    ## -- probability compare -- ##
    prob_max_ix = np.argmax(probStore, axis=0) * np.greater(length1,
radius)
    # finds index of max = enzyme index --> with lenDiscriminator
    prob_max_ix1 = prob_max_ix + ones

    ## -- with discriminating free corridor -- ##
    prob_max_ix1 = prob_max_ix1.astype(float)

    for jx in range(len(RE)):
        for ix in range(len(RE[0])):
            if np.isnan(RE[jx, ix]) == True or np.isnan(IM[jx,
ix]) == True:
                prob_max_ix1[jx, ix] = np.nan
            else:
                prob_max_ix1[jx, ix] = prob_max_ix1[jx, ix]

    mapFile = analyFile + '/enzymeMaps/' + 'enzymes/'
    if not os.path.exists(mapFile):
        os.makedirs(mapFile)

    img01 = Image.fromarray(prob_max_ix1.astype(float))
    img01.save(mapFile + dateCells + crt + uStrich + 'enzy.tif')

    ## -- vector length map -- ##
    lenSt_enzy = np.zeros(prob_max_ix.shape)
    lenSt_data = np.zeros(prob_max_ix.shape)

    prob_max_ix = prob_max_ix.astype(float)
    for x in range(len(prob_max_ix[0])):
        for y in range(len(prob_max_ix[1])):
            lenSt_data[y][x] = lengthStore_data[n,y,x]
            if np.isnan(prob_max_ix[y][x]) == True:
                lenSt_enzy[y][x] = np.nan
            else:
                e = int(prob_max_ix[y][x])
                lenSt_enzy[y][x] = lengthStore_enzy[e,y,x]

    RatioVecLen = []
    RatioVecLen = 100 * lenSt_data / lenSt_enzy
    RatioVecLen = RatioVecLen * np.greater(length1, radius)

    VecLenFile = analyFile + '/enzymeMaps/' + 'activity/'
    if not os.path.exists(VecLenFile):
        os.makedirs(VecLenFile)

    img02 = Image.fromarray(RatioVecLen)
    img02.save(VecLenFile + dateCells + crt + uStrich + 'activ.tif')

else: pass

print ""
print "Finished!!"

```

---

## **Appendix C**

### **C.1. curriculum vitae**

*For reasons of data protection, the curriculum vitae is not published in the electronic version.*

## **C.2. Finanzierungquellen, Interessenskonflikte, Selbstständigkeitserklärung**

### **Finanzierungsquellen**

Die Arbeiten wurden finanziell unterstützt durch die Deutsche Forschungsgemeinschaft unter dem Vorhaben FOR2165 (NI1167/4-2) und TRR130 (C01).

### **Interessenskonflikte**

Es besteht kein Interessenskonflikt durch finanzielle Unterstützung der Arbeit, durch externe Projektfinanzierung – Sach- oder Personalmittel – die über Motivation oder Bias auf die Arbeit Einfluss genommen haben könnten.

### **Selbstständigkeitserklärung**

Hiermit bestätige ich, Ruth Leben, dass ich die vorliegende Arbeit selbstständig angefertigt habe. Ich versichere, dass ich ausschließlich die angegebenen Quellen und Hilfen in Anspruch genommen habe und die vorliegende Dissertation bisher nicht in dieser oder leicht abgewandelter Form in einem anderen Promotionsverfahren eingereicht wurde.

Berlin,

23.11.2021, Ruth Leben

---

Datum, Unterschrift

---